The Dissertation Committee for Lixin Gong
Certifies that this is the approved version of the following dissertation:

THE COMPRESSIVE RESPONSE OF OPEN-CELL FOAMS

Committee:

Kyriakides, Stelios, supervisor

Liechti, Kenneth M.

Becker, Eric B.

Ravi-Chandar, K.

Kraynik, Andrew M.

THE COMPRESSIVE RESPONSE OF OPEN-CELL FOAMS

by

Lixin Gong, BS

Dissertation

Presented to the Faculty of the Graduate School of
The University of Texas at Austin
in Partial Fulfillment
of the Requirements
for the Degree of

Doctor of Philosophy

The University of Texas at Austin
May, 2005

ACKNOWLEDGEMENTS

I would like to express my sincere gratitude to my advisor, Professor Stelios Kyriakides, for all his teaching, guidance and support throughout my graduate studies. His knowledge, experience and deep understanding of the subject helped me through every step to accomplish this research. I would also like to thank Professor Eric B. Becker for his precious advice in the finite element method, Dr. Andrew Kraynik for his help in foam morphology and the surface evolver, and Professor Nicolas Triantafyllidis for helping me develop the Bloch wave method. Thanks also go to the other committee members for reviewing this dissertation.

A special thanks to my family for all their supports and love accompany me through these PhD. pursuing years. A great owe to my loving wife, Yingcong Tan, for her unconditional love and understanding.

I would like to thank Rob Green for his excellent lab work, and thank Jim Williams for his help in the experiments.

The financial support of the National Science Foundation through Grant CMS-0245485 and the Air Force Office of Scientific Research through Grant No. F49620-98-1-0145 is acknowledged with thanks. Gratitude also goes to *Foamex Corporation* for providing the open-cell foam specimens and useful technical information.

Lixin Gong

The University of Texas at Austin

May 2005

THE COMPRESSIVE RESPONSE OF OPEN-CELL FOAMS

Publication No._____________

Lixin Gong, Ph.D.
The University of Texas at Austin, 2005

Supervisor: Stelios Kyriakides

The compressive response of many cellular materials is characterized by a nearly linear elastic regime, which terminates into a limit load. This is followed by an extensive load plateau that is responsible for their excellent energy absorption characteristics. The end of the plateau is usually followed by a second branch of stiff response. This study uses experiment and analysis to illustrate how the cell microstructure and the properties of the base material govern these mechanical characteristics for a class of foams.

The experiments are conducted on polyester urethane open-cell foams of several cell sizes. They include: measurement of the compressive response of the foams, characterization of the foam microstructure, and measurement of the mechanical properties of foam ligaments. It was found that for such materials the onset of instability and the subsequent localization occur due to buckling of the microstructure.

The foam is idealized to be periodic using the space-filling Kelvin cell assigned the major geometric characteristics found in the foams tested. Several modeling levels are used to analyze the different aspects of this complex mechanical behavior. Beam-type models are used to develop closed form expressions for the initial elastic moduli. The onset of instability is established numerically using models involving either a single or stacks of fully periodic characteristic cells. Large scale models are used to reproduce all aspects of the compressive response including crushing.

In the rise direction the prevalent instability exhibits a long wavelength mode that leads to a limit load, an indication that localization is possible. By contrast, in the transverse direction the buckling mode is local to the characteristic cell and has a stable postbuckling response. For more general loadings the Bloch wave method is employed to establish the onset of instability. For such general loadings a rich variety of buckling modes are identified that are affected by the anisotropy and the multiaxiality of the loads.

The crushing response is simulated by considering finite size microsections that allow localized deformation to develop. Ligament contact is approximated by limiting the amount a cell can collapse in the direction of the applied load. This arrests local collapse and causes it to spread to neighboring material at a nearly constant stress level as in the experiments. The crushing stress and the extent of the stress plateau can be evaluated by using this pseudo-contact scheme.

Table of Contents

NOMENCLATURE

A	ligament cross sectional area
A_o	$= A(0)$
C_A	$\left(\sqrt{3} - \frac{\pi}{2}\right)$
C_I	$I_y \big/ A^2$
C_J	$J/2I_y$
C_M	material constant
$C_i \quad i = 1,3$	integrals of $f(\xi)$
$D_i \quad i = 1,3$	material constants
E	Young's modulus of base material
E^*, E_1^*, E_2^*	foam axial moduli
$f(\xi)$	ligament cross sectional area distribution function
G	shear modulus of base material
$G^*, G_{12}^*, G_{23}^*, G_{13}^*$	foam shear moduli
H, H_1, H_2	foam block dimensions
h, h_1, h_2	cell dimensions
I_x, I_y	ligament cross sectional second moments of area
J	ligament cross sectional torsion constant
k	spring stiffness
ℓ	ligament length
M, N, T, V	moment, axial force, torque and shear force
N	number of cells in a column

r	radius of Plateau borders
r_o	$= r(0)$
$\bar{r}$	$= r/\ell$
U	strain energy
u_i	displacement degrees of freedom
α	$= \tan^{-1}\lambda$
β	shear correction factor
$\Delta\varepsilon_P$	stress plateau extent
Δ_o	imperfection amplitude
$\delta,\ \delta_1,\ \delta_2$	axial shortening
$\dot{\delta}$	shortening rate
ε	strain
θ_i	rotational degrees of freedom
κ^*	foam bulk moduli
λ	cell anisotropy parameter
ν	Poisson’s ratio of base material
$\nu^*, \nu_{12}^*, \nu_{21}^*, \nu_{23}^*$	foam Poisson’s ratios
ρ	density of base material
ρ^*	foam density
$\sigma, \sigma_1, \sigma_2$	stress component
$\bar{\sigma}$	mean stress
σ_C	critical stress
σ_I	initiation stress

σ_L	limit stress
σ_P	propagation stress
υ	foam volume
υ_o	undeformed foam volume
ξ	x/ℓ
ψ	contact spring gap

CHAPTER 1

INTRODUCTION

Cellular materials come in either fluid or solid form and consist of cells packed together to fill space. Their cells consist of interconnected networks of ligaments, membranes, plates or shells which form their edges and faces. Two and three dimensional cellular solids are available. Honeycombs pack polygons in a plane and as a result are two-dimensional. Solid foam is one of the most common three-dimensional cellular materials. It consists of networks of space-filling polyhedra. In some foams the polyhedra faces are open (*open-cell foams*) in which case the solid is contained in the edges. In other foams the faces are covered with plates or membranes (*closed cell foams*) and each cell is sealed off from its neighbors.

Cellular materials are abundant in nature. Examples include many woods, iris leafs, cork, stalks of plants, cancellous bone, sponge, coral, etc (Gibson and Ashby, 1997). Many fruits and vegetables such as apples and potatoes have a cellular microstructure too. Several man-made foods such as bread, cakes, chocolate bars, flake cereals and snack foods also have cellular microstructures.

Synthetic cellular materials which mimic nature became increasingly popular from 1950 onwards. Today they are everywhere in our lives. From polystyrene cups to NASA space-shuttle insulation tiles, synthetic cellular materials have became one of the most widely used man-made classes of materials. They can be made from all classes of materials: polymers, metals, carbon, ceramics, glass, paper etc. Figure 1.1 shows photographs of two man-made open-cell foams: a polyester urethane foam and an aluminum alloy foam. They both illustrate how polyhedra are packed in space to form a structurally sound and load bearing network.

1.1 Making Cellular Solids

1.1.1 Polymeric foams

In 1941 Otto Bayer and coworkers first produced flexible polyurethane foam in the laboratory (Bayer, 1947). The first industrial plant production of flexible polyurethane foam started in Germany in 1952. Since then polymer foams have become a multi-billion-dollar industry. According to the study from *Business Communication Company, Inc*. (Forman, 2001) the U.S. market for polymeric foams is projected to be more than 8.5 billion pounds by 2006.

The foaming of polymeric materials can be carried out by mechanical, chemical or physical means. Some of the most commonly used methods are the following (Frisch and Saunders, 1972):

1. Using chemical blowing agents to generate either nitrogen or carbon dioxide or both during thermal decomposition by application of heat or as a result of the exothermic heat of reaction during polymerization (ICI Ltd., 1971).
2. Mechanically whipping gases (frothing) into a polymer system (melt, solution, or suspension), which hardens either by catalytic action or heat or both, thus entrapping the gas bubbles in the matrix (Schwencke, 1954).
3. Volatilizing low-boiling liquids (fluorocarbons or methylene chloride) within

the polymer mass by application of heat or as a result of the exothermic heat of reaction during polymerization (Kraemer, 1967).

4. Mixing isocyanate with water, thus releasing carbon dioxide and forming bubbles during reaction (ICI Australia & New Zealand Ltd., 1969).
5. Reducing pressure in the system, thus expanding gas dissolved in a polymer mass (Alderson JR, 1945).
6. Incorporating hollow microspheres, which may consist of either glass or plastic beads, into a polymer mass (Wong and Mahoney, 1994).
7. Expansion of gas-filled beads in a polymer mass by application of heat (Cleland, 1962).

1.1.2 Metal Foams

In 1943 the first metal foam was attempted by adding mercury to molten aluminum by Sosnik (Sosnik, 1948). In 1956 Elliot replaced mercury by foaming agents generating gas by thermal decomposition (Elliot, 1956). In 1959 Allen invented the powder compact foaming (PCF) route for manufacturing metallic foams (Allen, 1963) and the basic processing techniques were thus completed. From then on several additional techniques for manufacturing metallic foams have been developed. At the present the main metal foaming techniques can be categorized under one of the following six process-routes (Ashby *et al.*, 2000):

1. Injecting gases (such as air, carbon dioxide, oxygen, inert gases) into molten Al-SiC or Al-Al_2O_3 alloys (or Al, Mg) to create bubbles (Stuart, 1959). This is the least expensive approach. The produced foams have relative density

ranging from 0.03 to 0.1, and closed cell pores with diameters between 5 and 20 mm.

2. Mixing a foaming agent (TiH_2) into a molten alloy (Al alloy), thus generating bubbles by thermal decomposition, and controlling the pressure while cooling (Elliot, 1956). Products by this means have relative densities from 0.2 to as low as 0.07. The cells have sizes from 0.5 to 5 mm and are closed.
3. Introducing foaming agents into metals in the solid state by mixing and consolidating powders, followed by heating into the mushy state when the foaming agent releases gases, expanding the material (Al, Zn, Fe, Pb, Au) (Baumeister and Schrader, 1992). The relative density of the created foam can be as low as 0.08. The foam has closed cells with diameters that range from 1 to 5 mm.
4. Using a wax or a polymeric foam as precursor to create a ceramic mold. Then the precursor is burned out and the mold is filled with a molten metal or metal powder slurry and allowed to cool. The mold material is then removed leaving behind the metal equivalent of the original polymeric foam (Shroyer, 1960). These are subsequently sintered. This method is used to produce open-cell foams with pore sizes of 1-5 mm and relative densities as low as 0.05.
5. Vapor phase deposition or electrodeposition of metals onto an open-cell polymeric foam precursor which is subsequently burned out, leaving hollow cell ligaments (Babjak *et al.*, 1990). This method produces the lowest relative density (0.02-0.05) foams with open pore sizes in the 100-300 μm diameter range.

6. Sintering of hollow metal spheres, which can be made by inert gas atomization, or from a slurry composed of a decomposable precursor such as TiH_2, together with organic binders and solvents, or from polymer spheres coated with a metal slurry and sintered (Wang, 1982). With this process, relative densities as low as 0.05 are feasible with pore sizes ranging from 100 μm to several millimeters.

1.1.3 Carbon, graphite and other foams

Carbon foams were first developed by researchers in the 1960's as a reticulated vitreous carbon (RVC) foam. Ford (1964) produced carbon foams by carbonizing thermosetting organic polymer foams through a simple heat treatment. Then Googin *et al.* (1967) reported the first process dedicated to controlling the structure and material properties of carbon and graphite foams by varying the precursor material (partially cured urethane polymer). In the 1970's, research was primarily aimed at producing carbon foams from alternative precursors. For example, Klett produced the first carbon foams from cork, a natural cellular precursor (Klett, 1975). In the early 1990's, researchers at the Wright Patterson Air Force Base Materials Lab produced mesophase-derived graphitic foams for the first time, specifically for replacing expensive 3-D woven fiber performs in polymer composites and as replacements for honeycomb materials (Hager *et al.*, 2000). In the mean time, Ultramet Corp. performed research on RVC foam and used chemical vapor deposition (CVD) as a technique to place pyrolytic graphite on the glassy carbon ligament of RVC, producing 3-D carbon structures with high-modulus ligaments (Richard *et al.*, 1992).

Ceramic foams can be produced by dipping the polymer foam in a slurry containing an appropriate binder and ceramic phases, followed by pressureless sintering at elevated temperatures (Schwartzwalder and Somers, 1963). Foam glass can be made by mixing glass powder and foaming agent (such as H_2S), followed by sintering, thus forming closed bubbles (Hubscher, 1954).

1.2 Applications of Cellular Solids

Natural cellular materials have been used by man throughout history. Now with the fast development of foaming techniques, synthetic cellular materials have been utilized in most aspects of modern life (Gibson and Ashby, 1997). Due to their light weight and high stiffness characteristics, cellular solids are broadly used as lightweight structural components. For example they are often used as cores in sandwich plates and shells, which is one of the most effective weight saving design options for structures in a variety of applications. Their exceptional ability to absorb large amounts of energy at nearly constant pressure suggests applications ranging from packing, cushioning to shock mitigation devices as automobile bumpers and helicopter seats.

Polymeric foams and glass foams have very low thermal conductivity and thus are ideal for thermal insulation applications in food containers, in refrigerators, on the space shuttle booster rockets, etc. Carbon foams and ceramic foams are outstanding candidates for developing low-density composites with high-temperature performance, which are ideal for applications in jet engine nacelles and rocket nozzles. As mentioned above, polymeric and carbon foams are also used as precursors or templates to produce other foams, such as metal foams and ceramic foams. Open-cell metal foams have high surface area to volume ratio, which make them ideal for use in compact heat exchangers.

Cellular materials can also be used as acoustic materials for noise absorption or inversely in sound fidelity systems. Noise absorption applications include: aircraft ventilation ducts, portable compressors and power units, panels for automobiles, marine application, etc. Sound fidelity applications include: earphones, microphone covers, and stereo speaker grilles.

Other applications of foams include filters and fluid flow limiting devices, catalyst supports, fluid flow damping conduit, magnetic shielding, vibration damping, storage media, fuel cells, biomedical prostheses, internally-cooled shape memory actuators, air batteries, protective permeable membranes and sheathes, artificial skin, non-slip surfaces for trays, tables and floors, etc.

1.3 Outline of the Present Study

As the use of cellular solids increased the need for relating the microstructure and the property of the base material to the mechanical properties of the foams became increasingly more important. Gent and Thomas (1963), Ko (1965), Shaw and Sata (1966), Dement'ev and Tarakanov (1970a, 1970b), Patel and Finnie (1970) took the first steps in this direction by trying to relate the initial elastic properties to the microstructure. More recent works include those of Gibson *et al*. (1982, 1989, 1997), Kraynik (1996), Warren and Kraynik (1988, 1997), Weaire and Hutzler (1999), Zhu *et al*. (1997), Laroussi *et al*. (2002).

Gibson and Ashby's book (1997) gives an excellent review of the state of the art as well as basic information on cellular materials. Although a lot of work has been accomplished in this area, the prediction of the overall mechanical response based on cell geometry and base material properties is rather crude, and the understanding of the behavior beyond the linear elastic range is still far from mature. The present work aims to understand and model the main aspects of the mechanical behavior of open-cell foams.

The general characteristics of the compressive response of many foams are illustrated in Figure 1.1. Shown is the compressive stress (σ = force/undeformed area) vs. the applied displacement normalized by the height of the specimen (δ/H) for an open-cell polymeric foam. The response consists of a nearly linear elastic regime with modulus E^* which terminates into a limit load (σ_I). This is followed by a load plateau ($\overline{\sigma}_P$) which extends to an average strain ($\Delta\overline{\varepsilon}_P$) of about 50% followed by a second stiff branch. The polymer in question is a viscoelastic solid so on unloading a hysteresis is traced. The hysteresis loop remains open at zero load but with time, as the material relaxes, it closes at the origin. The relatively low stress maximum and the extended stress plateau are responsible for the excellent energy absorption characteristics of such foams while the recovery of deformation makes them useful in cushioning. The objective of this thesis is to (a) understand the physics governing this type of response and (b) to develop models for predicting its main variables $\{E^*,\ \sigma_I,\ \overline{\sigma}_P,\ \Delta\overline{\varepsilon}_P\}$.

Some guidance as to what is behind such material responses comes from the work of Papka and Kyriakides on honeycombs under in-plane compression (1994, 1998a, 1998b, 1998c, 1999a, 1999b). In this setting honeycombs are two-dimensional counterparts of foams. A typical compressive stress-displacement response of a polycarbonate honeycomb with circular cells in a hexagonal packing is shown in Fig. 1.3a. A sequence of corresponding deformed configurations are shown in Figure 1.3b (Papka and Kyriakides, 1998a). The response exhibits the same three-regime behavior seen in the loading part of the foam response in Fig. 1.2. Initially, the response is stiff and nearly linear and all the cells deform symmetrically about vertical axes passing through their centers (configuration ①). The response then becomes progressively softer until a local load maximum develops. This marks the beginning of the second regime. Beyond this point, deformation starts to localize in a narrow zone (configuration ②). The deformation of these cells weakens their neighbors which collapse next. This process is then repeated as the crushed region propagates through the specimen as seen in configurations ③-⑦. As the crushing front(s) propagate through the specimen, the load remains relatively constant. Eventually, all the cells collapse and the load increases sharply (*densification*).

Local collapse involves a shear-type mode illustrated in Figure 1.4. The undeformed configuration is identified as ⓪. In configuration ①, the cells deform symmetrically while in configuration ② the onset of unsymmetric deformation is observed. Configuration ③ and ④ show the cells at increasing stages of collapse while in ⑤ the cell walls come into contact arresting further local deformation.

The clear two-dimensional pictures and video recordings of these events showed for the first time that the first load peak represents the onset of an instability which subsequently localizes. Contact arrests the local collapse making its spreading to neighboring cells energetically preferred. This should have some correspondence to the microstructural events underlying the foam response in Figure 1.2. One of our aims is to establish this correspondence.

Papka and Kyriakides were able to reproduce the measured honeycomb responses to a great degree of accuracy using micromechanics. The keys to their success were the accurate modeling of the microstructure coupled with appropriate modeling of the nonlinear constitutive behavior of the base materials (polycarbonate and aluminum alloys). They demonstrated that the properties of interest can be established using models of increasing complexity. For example, the elastic properties and the onset of the instability can be found from relatively small characteristic cell type analyses. Figure 1.5 shows the calculated $\sigma - \delta/L$ response of a microsection. The initial elastic regime and the onset of the shear-type buckling are captured with accuracy. They subsequently used large scale finite size honeycomb domains representative of those used in their experiments to reproduce all aspects of the response including the stress plateau and densification. One of their predictions is included in Figure 1.3 along with its experimental counterpart. The comparison of the two is seen to very favorable. The modeling part of the present study will be guided by the technique developed in these pioneering works.

CHAPTER 2

FOAM PROCESSING AND MORPHOLOGY

The foams analyzed in this study are reticulated flexible polyester urethane foams manufactured by *Foamex*. They are filter foams (SIF) with completely open and relatively uniform cells. They were selected because they could be obtained in a variety of cell sizes in approximately the same material system. Results from five such foams with nominal sizes of 3, 10, 20, 45 and 100 pores per inch (ppi) will be considered. Following is an outline of the processing followed by a study of the morphology of the foams.

2.1 Processing

The evolution of a flexible urethane foam is a complicated process involving many ingredients and multiple simultaneous reactions and processes. The basic ingredients of flexible urethane foams of the type considered in this study are ester resin (or polyol), diisocyanate, water, catalysts and surfactants. The structure, molecular weight, composition and functionality of the isocyanate or polyol play significant roles in determining the final properties of the polymer. (e.g., Artavia and Macosko, 1994; Priester and Turner, 1994; Foamex, 2003).

The ingredients are introduced in a controlled manner in a mixer (in some cases air is added). CO_2 released from the isocyanate-water reaction forms bubbles which expand. Simultaneously, the chemical reaction which is highly exothermic (75-160°C temperature rise) produces a crosslinked polyester urethane network (gelling reaction). The pressure in the gas bubbles causes expansion resulting in volume increase of 40-50 times. The packing of the bubbles is decided during the expansion. When their volume fraction exceeds about 75% their walls start to intersect forming polyhedra. Fully developed polyhedra consist of a framework of interconnected slender ligaments which serve as channels of flow. The sides of the polyhedra are covered with thin membranes. Eventually the polymer starts to gel and at this time the gas bubbles rupture the thin membranes opening the cells. What is left behind is illustrated in the micrograph in Figure 2.1.

The mechanical properties of a cured foam depend both on the cell morphology and on the material within the cell ligaments. During the foaming process, the reaction chemistry has important implications on the properties of the material. The timing of the cell opening is crucial in getting structurally sound materials. The catalysts help adjust the foaming chemistry and time while the surfactants help mix incompatible components in the reaction and stabilize bubble expansion. The process is relatively fast lasting between 2-4 minutes. Cell size is determined by the surfactant type and amount as well as by the mixing speed and back pressure. In some of the foams the membranes are removed by mechanical shock while in others they are removed chemically. The foams analyzed are polyester urethane material systems with approximately the following composition by weight: ester resin 100 parts, diisocyanate 43-50 parts, water 3.3-3.8 parts, surfactant 1-4 parts and catalysts 0.5-2.0 parts.

2.2 Morphology

The nominal pore sizes of the foams analyzed were: 3, 10, 20, 45 and 100 ppi. Measured cell sizes appear in Table 2.1 ($\bar{h}_1$ and $\bar{h}_2$ are the average cell heights in the rise and transverse directions respectively based on 20-30 measurements for each foam). This type of foam is used in filtering where a high degree of uniformity and cleanliness of the cellular microstructure (or low *polydispersity* -- Kraynik (2003)) is a requirement. Included in Table 2.1 are the maximum and minimum values of cell diameters measured in each foam. As a measure of polydispersity we have chosen the ratio of one standard deviation (Σ_{h_1}) of the measured values of h_1 to the average value $\bar{h}_1$ of the measurements. The results in Table 2.1 show that, with one exception, this ratio is less than 0.1 which confirms that the microstructure is unusually uniform for polymeric foams. This is achieved by the amount and type of surfactant used, as well as by the mixer speed and back pressure.

The five foams had relative densities (ρ^* / ρ) ranging between approximately 2.2-2.8% (Table 2.1); in other words their relative densities have the same order of magnitude. This, coupled with the relatively uniform cell sizes in each foam, indicated that the microstructure might scale with cell size. This was indeed found to be true, at least to the first order, from comparisons of the microstructures of the 5 foams analyzed using optical and scanning electron microscopy. An example of such a comparison is shown in Figure 2.2, where optical micrographs of three foams [(a) 3 ppi, (b) 10 ppi and (c) 45 ppi], enlarged by different amounts to make the cells approximately the same size, are shown.

Table 2.1 Geometric parameters of reticulated polyester urethane foams analyzed

Foam ppi	$\bar{h}_1$ in (mm)	$h_1\|$min-max in (mm)	$\frac{\Sigma_{h_1}}{\bar{h}_1}$	$\bar{h}_2$ in (mm)	$h_2\|$min-max in (mm)	λ	Σ_λ	$\frac{\rho^*}{\rho}$ (%)
3	0.365 (9.27)	0.201-0.427 (5.11-10.8)	0.122	0.257 (6.53)	0.183-0.334 (4.65-8.48)	1.432	0.157	2.18
10	0.292 (7.42)	0.263-0.328 (6.68-8.33)	0.066	0.218 (5.54)	0.185-0.262 (4.70-6.65)	1.360	0.082	2.47
20	0.170 (4.32)	0.153-0.185 (3.9-4.7)	0.050	0.132 (3.35)	0.118-0.145 (3.00-3.68)	1.281	0.035	2.36
45	0.0714 (1.81)	0.064-0.084 (1.6-2.1)	0.070	0.0566 (1.44)	0.050-0.064 (1.27-1.63)	1.256	0.071	2.44
100	0.0302 (0.767)	0.025-0.034 (0.64-0.86)	0.079	0.0244 (0.610)	0.020-0.027 (0.508-0.696)	1.233	0.043	2.82

$\rho \approx 0.0432$ lb/in^3 (1.19 g/cm^3); $\Sigma_x \equiv$ standard deviation.

The microstructures are seen to be similar supporting its scaling with cell size.

2.2.1 Cells

The cell morphology was found to be in general disordered consisting of a variety of cell shapes. Matzke, in his classic work (1946) in which he characterized 600 soap bubbles in a foam he assembled, reported a great variety of irregular polyhedra. We conducted a similar study which involved 30 cells extracted from the 3 ppi foam. The results are summarized in Table 2.2 Polyhedra with 9 to 17 faces were found with the average number of faces being 13.7. This matches exactly the corresponding average number reported by Matzke. The most numerous (7) polyhedra were 14-sided with 15 and 13 sides following. Once again the trend matches that reported by Matzke. The faces had 3 to 7 edges with 5 edges being the dominant and the average number being 4.94 edges per face. This compares to Matzke's average of 5.12 edges per face. We attribute this difference to the much larger number of samples in Matzke's study.

The cells of Matzke's foam did not have any preferential orientation because of the special way the soap foam was assembled (constructed manually bubble-by-bubble). The foams analyzed in this study exhibited some anisotropy in the shapes of the cells in the form of elongation along the rise direction (see Figure 2.2). The anisotropy was quantified for each foam by comparing the maximum height of cells to their lateral dimensions ($\lambda = h_1/h_2$; e.g. see Table 2.2). The mean values of the λs of the five foams analyzed are reported in Table 2.1. (Note that these values are not determined from $\bar{h}_1/\bar{h}_2$). They vary from

Table 2.2 Geometric characteristics of cells of a 3ppi polyester urethane foam [†]

Polyester Urethane Open Cell Foam				Number of Edges				
No.	$\bar{h}_1$	λ	Number of faces	3	4	5	6	7
1	0.360	1.443	13	0	1	10	2	0
2	0.361	1.243	15	0	3	7	4	1
3	0.395	1.506	14	0	4	7	2	1
4	0.409	1.560	17	0	3	10	3	1
5	0.349	1.475	14	0	4	4	6	0
6	0.400	1.452	16	2	4	5	4	1
7	0.405	1.427	14	0	3	8	3	0
8	0.391	1.484	16	0	2	8	6	0
9	0.406	1.468	16	0	3	8	3	2
10	0.427	1.546	17	1	3	8	4	1
11	0.357	1.264	15	1	2	9	3	0
12	0.397	1.586	12	0	0	12	0	0
13	0.427	1.793	15	1	4	5	5	0
14	0.334	1.487	11	0	2	8	1	0
15	0.394	1.634	12	0	5	5	2	0
16	0.366	1.511	14	0	5	5	4	0
17	0.365	1.498	10	1	4	5	0	0
18	0.201	1.065	9	0	7	2	0	0
19	0.334	1.292	14	1	2	9	2	0
20	0.351	1.614	11	0	2	8	1	0
21	0.355	1.121	14	0	2	7	5	0
22	0.352	1.455	13	0	4	6	3	0
23	0.410	1.599	17	1	7	5	3	1
24	0.368	1.505	13	0	6	5	2	0
25	0.320	1.285	13	0	4	8	1	0
26	0.318	1.296	14	0	2	8	4	0
27	0.375	1.340	15	0	6	3	6	0
28	0.321	1.285	12	1	2	7	2	0
29	0.378	1.361	15	0	3	8	4	0
30	0.326	1.369	11	0	4	4	3	0
AVG	**0.365**	**1.432**	**13.7**	**4.94 Edges/Face**				

[†] The measurements in this table were performed by Robert Green.

about 1.43 to 1.23 with the values decreasing with cell size. (Huber and Gibson (1988) reported similar values of anisotropy for a group of polyurethane foams.)

2.2.2 Ligaments

The nearly linear members which form the edges of the polyhedra, often called struts, will be referred to as ligaments. Ligaments were surgically extracted from the three coarser foams and used to establish their geometry. Figure 2.3a shows a SEM micrograph of a typical ligament. Several ligaments were potted in a wax compound and sectioned along the length using a microtome. The thin cross sections were photographed using microscope and their area was measured by using the software *NIH Image*. Figure 2.3b shows a set of cross sections obtained in this manner.

The ligaments are nearly linear and have the characteristic three-cusp hypocycloid cross section (*Plateau borders*). Each curved side approximately lies in a 2-D plane, which means the ligament is not twisted. The area of the cross section increases as the junctions (nodes) with other ligaments on either end are approached.

The coarseness of the 3 ppi foam enabled measurement of geometric properties with relative ease. Table 2.3 lists 60 measurments of ligament length (ℓ). The mean value of the measurements was 0.123 in while the standard deviation was 0.039 in. Table 2.4 lists 14 values of measured mid-span cross sectional areas (A_o) along with their mean values and standard deviation.

Table 2.3 Measured ligament lengths in 3ppi foam [†]

Ligament No.	ℓ in	Ligament No.	ℓ in
1	0.039	31	0.117
2	0.042	32	0.120
3	0.057	33	0.125
4	0.064	34	0.125
5	0.077	35	0.125
6	0.082	36	0.125
7	0.082	37	0.127
8	0.083	38	0.130
9	0.088	39	0.133
10	0.091	40	0.134
11	0.093	41	0.136
12	0.094	42	0.140
13	0.094	43	0.142
14	0.095	44	0.148
15	0.096	45	0.150
16	0.096	46	0.151
17	0.096	47	0.155
18	0.099	48	0.155
19	0.099	49	0.159
20	0.100	50	0.163
21	0.100	51	0.164
22	0.103	52	0.167
23	0.105	53	0.172
24	0.106	54	0.176
25	0.107	55	0.177
26	0.108	56	0.187
27	0.108	57	0.195
28	0.112	58	0.201
29	0.114	59	0.205
30	0.116	60	0.219
$\bar{\ell}$	0.123	Σ_{ℓ}	0.039

[†] The measurements in this table were performed by Robert Green.

Table 2.4 Ligament cross sectional area at mid-span (3ppi) †

Ligament No.	A_o in$^2 \times 10^{-6}$
1	98
2	102
3	104
4	104
5	107
6	113
7	119
8	119
9	125
10	131
11	127
12	134
13	134
14	156
$\overline{A}_o$	119.5
Σ_{A_o}	16.25

† The measurements in this table were performed by Robert Green.

More detailed measurements of cross sectional area distribution were performed on 5 ligaments of different lengths extracted from a couple of the foams. The results are summarized in Table 2.5. In Figure 2.4 the cross sectional area $A(\xi)$ normalized by the value at mid-span, A_o, is plotted against the normalized length. The data were fitted with the following symmetric function:

$$A(\xi) = A_o f(\xi) = A_o\left(a\xi^4 + b\xi^2 + 1\right), \qquad \xi = x/\ell. \tag{2.1}$$

The constants $a = 86$ and $b = 1$ were found to yield a good fit of the data.

2.2.3 Nodes

Figure 2.6 shows micrographs of three ligament nodes taken from the 100 and 45 ppi foams. They are all junctions of four ligaments which are by far the most commonly occurring ones. The edges of neighboring ligaments are seen to be co-planar. Furthermore, the plane formed passes through the centers of the ligament cross sections. The nodes are seen to have smooth curved surfaces while simultaneously they are significant concentrations of material. This and the nonunifomity of the ligament cross sections will have to be appropriately represented in modeling.

Representation of the ligaments as simple uniform cross section Bernoulli-Euler beams, adopted in most modeling efforts to date, is an oversimplification appropriate only for foams of the lowest relative densities (ρ^*/ρ ~ 0.1% or less—Kraynik, 2003).

Table 2.5 Measured variation of cross sectional area along the length for 5 ligaments †

No. (size)	ℓ in	A_o in$^2 \times 10^{-6}$	Variation of ligament cross sectional area alog ligament length										
1 (10ppi)	0.095	84.6	ξ	-0.41	-0.32	-0.23	-0.14	-0.05	0.04	0.13	0.21	0.30	0.39
			$A(\xi)/A_o$	5.3	2.3	1.3	1.2	1.0	1.0	1.1	1.2	2.0	4.0
2 (10ppi)	0.118	70.7	ξ	-0.50	-0.38	-0.27	-0.15	-0.03	0.09	0.21	0.32	0.44	0.50
			$A(\xi)/A_o$	6.6	2.8	1.4	1.1	1.0	1.1	1.2	1.6	4.2	6.6
3 (3ppi)	0.170	156	ξ	-0.36	-0.24	-0.12	0.01	0.13	0.26	0.38	--	--	--
			$A(\xi)/A_o$	2.6	1.3	1.0	1.0	1.1	1.2	2.8	--	--	--
4 (3ppi)	0.200	119	ξ	-0.37	-0.25	-0.13	-0.01	0.12	0.24	0.36	--	--	--
			$A(\xi)/A_o$	3.0	1.2	0.98	1.0	1.0	1.2	2.1	--	--	--
5 (3ppi)	0.210	107	ξ	-0.38	-0.23	-0.09	0.06	0.20	0.35	--	--	--	--
			$A(\xi)/A_o$	2.7	1.2	1.0	1.0	1.2	1.8	--	--	--	--

† The measurements in this table were performed by Robert Green.

CHAPTER 3

EXPERIMENTS

Several mechanical tests were performed on the five polyester-urethane foams analyzed in Chapter 2. These include compression and crushing tests in the rise and transverse directions as well as material tests on individual ligaments. This chapter presents the facilities and procedures used and the and results from these experiments.

3.1. Compression Experiments on Foam Blocks

Compression tests on foam blocks were performed in an Instron 4507 screw-type testing machine using the experimental set up shown in Figure 3.1. The specimens were compressed between parallel rigid platens with ground surfaces, under constant displacement rates (Figure 3.2). Tests were performed at various constant displacement rates ($\dot{\delta}$). The load was measured via an 1000 lb load cell and the displacement by the machine encoder. The two variables were monitored via a computer operated data acquisition system. In some of the experiments the deformation in the front face of the foam block was monitored by a low magnification microscope mounted on a video camera. The video system and the computer were run synchronously.

3.1.1 Rise Direction Compression Experiments

Figure 3.3a shows a typical engineering stress-shortening response ($\sigma_1 - \delta_1 / H_1$) response recorded in a compression test performed along the rise direction of the 3ppi foam bock. The foam was crushed at a rate of $\dot{\delta}_1 / H_1 = 3.8 \times 10^{-3}$ s^{-1}. Figure 3.3b shows a set of photographs of the specimen during crushing recovered from the video. The response has the general features common to many cellular materials (Gibson and Ashby, 1982, 1989, 1997; Papka and Kyriakides, 1994, 1998a). Initially, it is relative stiff and nearly linear. The material deforms nearly uniformly. At higher stresses the response starts to soften and eventually a limit load is reached. Following the local stress maximum the specimen buckles in an overall manner, which can be seen in the configurations as a bowing of the edges on the left and right. Simultaneously, deformation localizes in a banded manner. The bands showed up at what is best described as randomly located sites on the cross section monitored while the stress remained essentially unchanged. The number of bands multiplied while at some sites the bands broadened and coalesced with neighboring ones. This surface deformation pattern is qualitatively similar to that reported in Wang *et al.* (2000) who used a digital image correlation technique to establish the evolution of events (see also Bastawros *et al.* 2000). Although surface deformation patterns do not necessarily represent bulk material behavior, the randomness of the locations of bands is a distinctly different feature from the one or two well defined collapse fronts seen in in-plane crushing experiments on honeycombs (e.g., Papka & Kyriakides, 1998a). This may be a characteristic of the more complex space filling foam microstructure but, more probably, is due to the more random distribution of larger geometric irregularities in foams than in the polymeric honeycomb of Papka and Kyriakides. Despite this difference, during the main evolution of localized deformation, the stress traced essentially a plateau in both cases. At an average “strain” about 45%, the response develops a positive slope once more as the material enters the *densification* regime.

Similar compression experiments in the rise direction were performed on all 5 foams. The responses and recorded are similar as were the corresponding deformation patterns including overall bowing of the blocks. Figure 3.4 shows a comparison of five such responses recorded at a displacement rate of $\dot{\delta}_1 / H_1 = 7.5 \times 10^{-3} \mathrm{s}^{-1}$. The main variables of these responses $\{E_1^*,\ \sigma_I,\ \bar{\sigma}_{1P},\ \Delta\bar{\varepsilon}_{1P}\}$ are listed in Table 3.1. The table shows that the values of σ_{1I} and $\bar{\sigma}_{1P}$ increases somewhat as the pore sizes of the foams decreases from 3ppi to 100ppi (note that these variables are also influenced by the cell anisotropy). The extents of the stress plateaus are around 45% for all cases. The elastic moduli of the foams vary to some degree but no discernable pattern can be established just from the experimental measurements. Differences are partly due to the relatively small variations in relative density but also to differences in the anisotropy which was found to get reduced with cell size.

3.1.2 Transverse Direction Compression Experiments

The cell anisotropy causes a difference between the compressive response in the rise direction (x_1) and directions normal to it (transverse direction, say, x_2).

Table 3.1 Material parameters of reticulated polyester urethane foams investigated [†]
($\dot{\delta}$ given in Fig. 3.4 and Fig. 3.5b)

Foam ppi	λ	$\frac{\rho^*}{\rho}$ (%)	$\frac{E_1^*}{E}$ (%)	σ_{1I} psi (kPa)	$\bar{\sigma}_{1P}$ psi (kPa)	$\Delta\bar{\varepsilon}_p$ (%)	$\frac{E_2^*}{E}$ (%)	σ_{2I} psi (kPa)
3	1.432	2.18	0.227	0.584 (4.03)	0.56 (3.9)	46	0.0701	0.386 (2.66)
10	1.360	2.47	0.181	0.65 (4.48)	0.62 (4.3)	44	0.0707	0.522 (3.60)
20	1.281	2.36	0.200	0.71 (4.9)	0.69 (4.8)	47	--	--
45	1.256	2.44	0.215	0.84 (5.8)	0.83 (5.7)	47	0.103	0.645 (4.45)
100	1.233	2.82	0.229	0.92 (6.3)	0.90 (6.2)	45	0.128	0.568 (3.92)

$E \approx 10$ ksi (69 MPa); $\nu = 0.49$

† The measurements in this table were performed by Robert Green.

The initial part of the transverse response is significantly more compliant (see comparison in Figure 3.5a). In addition, neither a stress peak nor a stress plateau is traced as the response remains monotonically increasing. Interestingly, the bowing of the sides seen in Figure 3.3b did not take place. The block deformed symmetrically with a slight barreling at the top and bottom edges due to friction developed between the foam and the platens. These differences indicate that deformation is probably uniform when the foam is crushed in the lateral direction.

Figure 3.5b shows the loading part of the transverse direction responses measured in four of our foams. The general trends are similar to those of the 45ppi foam (see similar results in Figure 2a of Huber and Gibson, 1988). The initial moduli measured in these responses are listed in Table 3.1 under E_2^*. They vary between values that are 33-50% of moduli E_1^*. An estimate of the stress at the initiation collapse (σ_{2I}) was obtained as follows. The initial elastic part of the response was extrapolated and the linear part of the response just after the knee was also fitted linearly as shown in Figure 3.6. The stress at the intersection of the two lines was designated as σ_{2I}. σ_{2I} values for the four foams analyzed are listed in Table 3.1. They are lower than the corresponding σ_{1I} by factors ranging between approximately 1.25 to 1.62. And they are seen to be of similar order of magnitude. Differences are partly due to the relatively small variations in relative density but also to differences in the anisotropy, which was found to get reduced with cell size.

3.1.3 Effect of Rate of Crushing

The mechanical properties of the foam polymeric material depend on the rate of loading (viscoelastic behavior). This reflects also on the compressive response of the foam. Figure 3.7a shows a set of rise direction responses of 3ppi foam measured at displacement rates spanning four decades. As the rate increases the initial modulus stiffens, the load maximum increases and the whole stress plateau moves to a higher stress level. Compression experiments at displacement rates spanning four decades were also performed on other foams. The initial moduli of the measured responses are listed in Table 3.2. The results demonstrate that a complete modeling of the foam requires a viscoelastic characterization of the polymer.

3.1.4 Mullins' Effect

The elastomeric polymer also exhibits Mullins' effect (1948, 1969) which implies that the material response in the first load cycle is stiffer from subsequent cycles. Figure 3.7b shows how this affects the compressive response of the foam. Shown are results from six load-unload cycles with a 5 minute relaxation time between each cycle. The first cycle produces the highest initial modulus and load plateau. The second cycle exhibits a significant drop in the plateau stress while subsequently the reduction per cycle is relatively small. By the 6th cycle the material has essentially been stabilized and the responses repeat. We found that the material recovers fully after a wait of about 48 hours and the highest response is repeated. All test results presented in this study are from fully rested foams.

Table 3.2 Material parameters of reticulated polyester urethane foams under compression at displacement rates spanning four decades †

Foam ppi	$\dot{\varepsilon}$ s^{-1}	E_1^* psi (kPa)	σ_I psi (kPa)	$\bar{\sigma}_p$ psi (kPa)
3	1.0×10^{-5}	11.51 (79.36)	--	--
	1.0×10^{-4}	12.42 (85.63)	--	--
	1.0×10^{-3}	13.26 (91.42)	--	--
	1.0×10^{-2}	16.15 (111.4)	--	--
3 †	7.5×10^{-5}	18.43 (127.1)	0.513 (3.54)	0.503 (3.47)
	7.5×10^{-4}	20.90 (144.1)	0.539 (3.72)	0.528 (3.64)
	7.5×10^{-3}	22.90 (157.9)	0.586 (4.04)	0.567 (3.91)
	7.5×10^{-2}	21.70 (149.6)	0.650 (4.48)	0.628 (4.33)
10	1.0×10^{-4}	14.97 (103.2)	--	--
	1.0×10^{-3}	17.89 (123.3)	--	--
	1.0×10^{-2}	19.39 (133.7)	--	--
45	1.0×10^{-5}	16.56 (114.2)	--	--
	1.0×10^{-4}	18.93 (130.5)	--	--
	1.0×10^{-3}	20.48 (141.2)	--	--
	1.0×10^{-2}	21.74 (149.9)	--	--
100	1.0×10^{-5}	19.75 (136.2)	--	--
	1.0×10^{-4}	20.21 (139.3)	--	--
	1.0×10^{-3}	23.18 (159.8)	--	--
	1.0×10^{-2}	24.88 (171.5)	--	--

† The measurements in this part were performed by Robert Green.

3.2 Base Material Experiments

Some foam chemists believe that the polymer flow resulting from the foaming process may cause preferential alignment of the long molecules of the material along the ligaments. These characteristics may not be easily achievable in bulk material. Thus, it is preferable that the mechanical properties of the polymer be measured directly from foam ligaments. This is a relatively difficult task because of the small sizes and the small loads involved and because of the relatively large strains that the ligaments must be stretched to. A small microscope testing stage, suitably modified, was used to tests ligaments from the 3ppi foam (Figure 3.8a).

The overall lengths of such ligaments were of the order of 0.12 in (3 mm) and the load required is of the order of 20 g. The stage was equipped with a 500 g load cell and a miniature LVDT for measuring the displacement. Closed loop control was added to it so that it can run at selected rates either in load or displacement control. The nodes of the ligament were bonded to two small plates, which were then clamped in the device. The ligaments were tested at different displacement rates.

Several 3ppi foam ligaments were tested in the microscope testing stage. Three typical stress-strain results were chosen to be discussed here. Figures 3.8b, 3.8c and 3.8d show the corresponding sets of load-unload stress-strain results up to a strain of about 20%. The tests were conducted at a strain rate of $\dot{\varepsilon} = 7.5 \times 10^{-3}$ s^{-1}. The material is rubber-like and exhibits Mullins' effect in the first loading cycle but subsequently the response stabilizes. In this strain range, after the first cycle the material is almost linearly elastic. The slender hysteresis loops traced are mainly due to rate dependence. The main parameters of three tests are listed in Table 3.3. In the title row, ℓ is the undeformed ligament length,

ℓ_o is the length of the middle part of the undeformed ligament, which is between the two clampers, A_o is the mid-span cross sectional area and E is the Young's modulus measured from the first loading cycle.

Table 3.3 Material parameters of the ligaments in the uniaxial stress-strain tests †

Ligament No.	ℓ in	ℓ_o in	A_o in$^2 \times 10^{-6}$	E ksi (MPa)
1	0.195	0.134	102.0	10.0 (69.0)
2	0.197	0.141	125.4	7.49 (51.6)
3	0.211	0.135	103.9	6.13 (42.3)

† The measurements in this table were performed by Robert Green.

The small size of the ligaments, the nonuniform and special shape of their cross section, small initial curvature in the ligaments, difficulties in clamping the ends, and uncertainty about the exact size of the test section all contribute uncertainties to these measurements. They are thus to be considered of qualitative value. Furthermore, it is not known to what extent the mechanical properties of the four foams with smaller cells differ from the one tested. Since all the imperfection factors tend to decrease the measured Young's modulus from the true value, the largest measurement $E \approx$ 10.0 ksi (69 MPa) is chosen as the Young's modulus of the base material to be used in the models that follow.

CHAPTER 4

LINEARLY ELASTIC BEHAVIOR

Efforts to model foam mechanical behavior are numerous although most are limited to the prediction of just the initial elastic constants (e.g., elastic modulus, Poisson’s ratio and shear modulus). The most representative models assume some cellular microstructure (usually regular), treat the ligaments as beam columns, and use elementary strength of materials to evaluate the deformation of representative microsections. Early examples of such models include Gent and Thomas (1963) who used a cubical cell limited to just axial deformations; Ko (1965) used a cell microstructure motivated by hexagonal packing of bubbles and calculated properties correctly; Menges and Knipschild (1975) used a part of a cell to show that both bending and membrane deformation affect the properties; Gibson and Ashby (1982, 1997) used a cubical cell in which ligaments bend to get the correct order of magnitude dependence of the elastic constants on the relative density.

4.1 Kelvin Cell Foam Model

The aim of the present effort is to model all major aspects of the compressive response of open-cell foams seen in Figures 1.2 and 3.5. The geometry will be idealized to be periodic by adopting the regular, 14-sided polyhedron of Lord Kelvin shown in Figure 4.1a (Thompson, 1887), which will be referred to as the *Kelvin cell*. The cell is space filling and consists of 6 squares and 8 hexagons with all edges being of the same length (ℓ). In this case the cell dimension is $h = 2\sqrt{2}\ell$.

Prediction of elastic constants of Kelvin cell foams has been performed amongst others by Dement'ev and Tarakanov (1970a, 1970b), Warren and Kraynik (1997), Zhu *et al.* (1997) and Pradel (1998). The ligaments were considered as Bernoulli-Euler beams of various cross sections (squares, circles, equilateral triangles, Plateau borders). The present study builds on these results by considering the effect of the following additional factors:

(a) Ligaments with nonuniform Plateau borders cross sections are considered.

(b) The foam is allowed to be anisotropic.

(c) The amount of material in the nodes is represented more accurately.

(d) The effect of shear deformation is considered in beam models.

For simplicity, in this first effort at the problem, the material rate dependence and the small initial nonlinearity observed in the uniaxial tests on ligaments will be neglected. The material will be assumed to be linearly elastic with modulus E and Poisson's ratio ν. All foams tested will be assumed to be made of the same material with the two material constants coming from the best estimates based on the measurements made on the 3 ppi ligaments (E= 10 ksi (69 MPa) and $\nu = 0.49$).

4.1.1 Ligament Geometry

The ligaments have length ℓ (Figure 4.1b) and a three-cusp hypocycloid cross section as shown in Figure 4.2 and 4.1b. The cross section is defined by the radius $r(\xi)$ ($\xi = x/\ell$, $-0.5 \le \xi \le 0.5$, and $r_o = r(0)$). The cross sectional area varies along the length according to the empirical expression (2.1). The area and moments of inertia of this section are given by (derived in Appendix A):

$$A = \left(\sqrt{3} - \frac{\pi}{2}\right) r^2 \equiv C_A r^2, \quad I_y = I_z = \frac{1}{24}(20\sqrt{3} - 11\pi) r^4 = 0.003479 r^4. \qquad (4.1)$$

The volume of the solid is governed by the geometric variables (ℓ, r_o). They will appear in the elastic moduli through their ratio $r_o/\ell \equiv \bar{r}$.

4.1.2 Anisotropy

Most polymeric foams exhibit some anisotropy in the form of elongation of the cells in the rise direction. This type of anisotropy is introduced to our Kelvin cell foam in the following arbitrary but simple manner. All ligaments with a projection in the x_1-direction are elongated to $\ell / \sqrt{2}\cos\alpha$ $(\alpha \ge \pi/4)$ while the length of ligaments in the plane normal to x_1 remains ℓ. This change makes the height of the cell $h_1 = 2\sqrt{2}\ell\tan\alpha$ while the width remains $h_2 = 2\sqrt{2}\ell$. Thus, the anisotropy parameter λ becomes

$$\lambda = \frac{h_1}{h_2} = \tan\alpha, \quad \alpha \ge \frac{\pi}{4}. \qquad (4.2)$$

Figure 4.3 shows the effect of this anisotropy on a cluster of Kelvin cells. The space-filling character of the cell is retained but the cells are elongated in the x_1-direction. (Dement’ev and Tarakanov 1970b) used a similar geometric distortion of the Kelvin cell to represent anisotropy.)

4.1.3 The Characteristic Cell

Because of the regularity and periodicity of the microstructure chosen, a characteristic cell can be identified. This is the smallest geometric unit, which can be used to assemble the infinitely large material domain by invoking periodicity at its boundaries. The characteristic cell of the anisotropic Kelvin foam is shown in Figure 4.4. It is also shown in red color in the isotropic and anisotropic clusters of Kelvin cells in Figures 4.1 and 4.4 respectively. Most of the mechanical properties of interest can be evaluated by considering either the characteristic cell or an assembly of characteristic cells along with appropriate periodicity conditions. The periodicity conditions will be given later in §4.3.

4.1.4 Volume of Material at Nodes

In the majority of the analytical models for elastic properties of foams mentioned above, the ligaments are represented as slender beams of length ℓ, with uniform cross section (A). The beams rigidly connect to each other at the nodes. The volume of the beam is represented as $A\ell$. In other words, the intersection of the beams at the nodes is neglected. For our non-uniform beams this approach results in the following expression for the volume of all the ligaments in an anisotropic characteristic cell

$$V_{solid} = 8C_{V\ell}\left(1+\frac{\sqrt{2}}{\cos\alpha}\right)A_o\ell = 8C_{V\ell}C_A\left(1+\frac{\sqrt{2}}{\cos\alpha}\right)r_o^2\ell \qquad (4.3)$$

where

$$C_{V\ell} = \int_{-1/2}^{1/2} f(\xi)d\xi \quad (= 2.1583 \text{ for (2.1)})$$

and C_A is given in (4.1). The total volume of the characteristic cell is

$$V_{cell} = 16\sqrt{2}\ell^3 \tan\alpha \tag{4.4}$$

so the expression for the relative density of anisotropic Kelvin foams is:

$$\frac{\rho^*}{\rho} = 0.369\left[\frac{\sqrt{2}+\cos\alpha}{3\sin\alpha}\right]\left(\frac{r_o}{\ell}\right)^2, \quad \alpha \geq \frac{\pi}{4} \tag{4.5}$$

where ρ^* is the density of the foam and ρ is the density of the base material. The square bracket in (4.5) reduces to 1 for the isotropic case ($\alpha = \pi/4$). If the ligaments are assumed to have uniform cross sections along their length, the expression for the relative density becomes

$$\frac{\rho^*}{\rho} = 0.171\left[\frac{\sqrt{2}+\cos\alpha}{3\sin\alpha}\right]\left(\frac{r_o}{\ell}\right)^2, \quad \alpha \geq \frac{\pi}{4}. \tag{4.6}$$

The proportionality of the relative density to the second power of r_o/ℓ $(\equiv \bar{r})$, repeats for beams of other cross sectional shapes by replacing it with a corresponding nondimensional geometric variable.

Dement'ev and Tarakanov (1970a) avoided the problem of material distribution at the nodes by making their nodes rigid and of fixed volume. The deformable beams then connect to the surface of a node rather than to its center. The issue was also noted in Gibson and Ashby (1982) but was neglected in most of their subsequent works.

In the present study the excess material at the nodes was removed (strictly for the purposes of calculating the volume of the ligaments). This was done by cutting the corners at the ends of the beams with appropriately chosen smooth surfaces. The details of this process appear in Appendix B. Figure 4.4 shows a node generated by this process. Although not a perfect match it is seen to be a good approximation of actual foam nodes like those in Figure 2.5.

Taking into account the material removed results in a new relationship between the relative density and $\bar{r}$. For isotropic foams the relationship is shown graphically in Figure 4.6 where it is compared to Eq. (4.5). For the corrected foam the relative density is proportional to $\bar{r}^{1.739}$ which makes the difference with Eq. (4.5) quite significant. The amount of material removed depends on the area distribution function $A(\xi)$ and must be calculated for each case separately. The case of uniform cross section is included in Figure 4.6 for comparison. In this case the correction for the volume at the nodes has a smaller effect.

Corrections of relative density were performed for several anisotropic cases also. In all cases Eq. (2.1) was adopted for $A(\xi)$. The uncorrected relative densities and the corresponding $\bar{r}$s and corrected relative densities are listed in Table 4.1. The range of uncorrected relative densities is chosen from 1% to 11%. After correction, the corresponding new relative densities are between 0.77% and 6%. A powerlaw relationship (fit) was established for foam relative density of this type.

$$\frac{\rho^*}{\rho} = k\left(\frac{r_o}{\ell}\right)^n \tag{4.7}$$

Results for various values of λ are listed in Table 4.2. Included for comparison are results for the uniform cross section ligament.

Table 4.1 Comparison of relative density w/o correction

λ	1.0		1.1		1.2		1.3		1.4	
$\frac{\rho^*}{\rho}$ (%) (no corr.)	$\frac{r_o}{\ell}$	$\frac{\rho^*}{\rho}$ (%) (w. corr,)	$\frac{r_o}{\ell}$	$\frac{\rho^*}{\rho}$ (%) (w. corr,)	$\frac{r_o}{\ell}$	$\frac{\rho^*}{\rho}$ (%) (w. corr,)	$\frac{r_o}{\ell}$	$\frac{\rho^*}{\rho}$ (%) (w. corr,)	$\frac{r_o}{\ell}$	$\frac{\rho^*}{\rho}$ (%) (w. corr,)
1.0	0.165	0.775	0.170	0.775	0.174	0.775	0.178	0.777	0.182	0.778
2.0	0.233	1.431	0.240	1.430	0.247	1.432	0.252	1.435	0.257	1.439
3.0	0.285	2.031	0.294	2.030	0.302	2.032	0.309	2.037	0.315	2.044
4.0	0.329	2.593	0.340	2.591	0.349	2.595	0.357	2.602	0.364	2.612
5.0	0.368	3.127	0.380	3.124	0.390	3.128	0.399	3.137	0.407	3.150
7.0	0.436	4.129	0.449	4.124	0.461	4.129	0.472	4.142	0.482	4.162
9.0	0.494	5.064	0.509	5.057	0.523	5.063	0.535	5.080	0.546	5.105
11.0	0.546	5.948	0.563	5.938	0.578	5.944	0.592	5.964	0.604	5.995

Table 4.2 Fit parameters for corrected relative density power law relationship to $\bar{r}$ for variable cross section ligaments

λ	n	k
1	1.7392	0.1803
1.1	1.7426	0.1791
1.2	1.7433	0.1637
1.3	1.7449	0.1580
1.4	1.7474	0.1350
Unif. Xsc	1.8968	0.1395

4.1.5 Effect of Shear Deformation

The foams of interest have relative density in the range of 1-5%. Ligaments of foams with even this small solid content are not very slender. As a result, when treated as beams, a Timoshenko type correction should be included for the additional deformation resulting from shear stresses. The calculations that follow are energy based and thus the correction is introduced in the strain energy due to shear force as follows:

$$U_S = \int_{-1/2}^{1/2} \beta \frac{V^2(\xi)}{2GA} \ell d\xi \qquad \text{where} \qquad \beta = \frac{A}{I_y^2} \int_z \frac{Q^2(z)}{b(z)} dz . \tag{4.8}$$

The second integral is over the cross section of the ligament shown in Figure 4.2 with Q being the first moment of area about the $y-$axis ($b(z) \equiv$ width). For this cross section β = 1.24.

4.2 Beam Models for Elastic Constants

The elastic moduli can be evaluated in closed form by treating the ligaments as Bernoulli-Euler beams and including the effect of axial and shear deformations. A representative microsection of the anisotropic foam can be found for each loading of interest as shown in Appendix C. For example, Figure C.1 shows a free-body diagram of a microsection used to establish the elastic modulus in the rise direction E_1^* and Poisson's ratio ν_{12}^*. Figure C.3 shows the free-body diagram appropriate for evaluating the bulk modulus κ^* (b), and Figure C.4 the one for the shear modulus G_{13}^*. Drawn in bold lines are the parts that are considered in each case. Free-body diagrams for each of the remaining constants appear in Appendix C (see also Zhu *et al.* (1997) who considered similar microsections of isotropic foams).

The axial force (N), bending moment (M), shear force (V), and torque (T) in each ligament are established in terms of the applied far field loads. The corresponding strain energy is then given by:

$$U = \int_{-1/2}^{1/2} \frac{N^2(\xi)}{2EA(\xi)} \ell d\xi + \int_{-1/2}^{1/2} \frac{M^2(\xi)}{2EI(\xi)} \ell d\xi + \int_{-1/2}^{1/2} \beta \frac{V^2(\xi)}{2GA(\xi)} \ell d\xi + \int_{-1/2}^{1/2} \frac{T^2(\xi)}{2GJ(\xi)} \ell d\xi \tag{4.9}$$

where the sectional properties A and I are given in Eq. (4.1) and E and G are the Young's and shear moduli of the linearly elastic base material. The torsion rigidity based on elasticity (includes effect of warping) is given by

$$GJ = G \times 0.0021 r^4 \tag{4.10}$$

(Warren *et al.*, 1997). For uniaxial compression and hydrostatic pressure loadings, ligaments do not twist and the last term in (4.9) drops out.

The analysis associated with these models is somewhat lengthy but straightforward. Details are presented at Appendix C. The most general expressions for the elastic constants are listed in Table 4.3 with definitions of auxiliary constants given in Table 4.4. They are expressed in terms of the geometric variable $\bar{r}$, the anisotropy λ $(=\tan\alpha)$, the elastic base material constants (E,ν), constants C_i that depend on the cross sectional area distribution function $f(\xi)$, and constants D_i chosen for algebraic convenience. In case either a different cross sectional area is selected, or a different $f(\xi)$, then constants C_i in Table 4.4 must be reevaluated. Because the correction for the material at the nodes depends on the anisotropy, it is not possible to present general moduli expressions for anisotropic foams in terms of the relative density as in common practice.

Simpler versions of the elastic constants with the effect of shear neglected (β = 0) appear Table 4.5. Results for two degenerate cases, the isotropic foam, and the isotropic foam with uniform ligament cross section ($f=1$) are listed in Table 4.6. Isotropy simplifies the expressions significantly. When in addition $f=1$, comparison with results of previous works becomes possible. Zhu *et al.* (1997) developed expressions for $\{E^*,\nu^*,G^*,\kappa^*\}$ for general cross section beams. Their results match the present ones for beams of general cross section if the effect of shear, the correction for the material at the nodes, and the warping correction of the torsion rigidity are neglected. The same is true for similar results

Table 4.3 Elastic constants of anisotropic Kelvin cell foams with shear effect

	Anisotropic-NonUniform XSC With Shear Effect
$\frac{\rho^*}{\rho}$	$k\ \bar{r}^n$
$\frac{E_1^*}{E}$	$\frac{C_I C_A^2 \sin\alpha\ \bar{r}^4}{C_1 + 2\left(\sin^2\alpha + 2\beta(1+\nu)\cos^2\alpha\right) C_I C_A C_2\ \bar{r}^2}$
$\frac{E_2^*}{E}$	$\frac{\frac{2}{\lambda} C_I C_A^2\ \bar{r}^4}{C_1(\frac{\lambda^2}{\cos\alpha}+\sqrt{2}) + C_I C_A C_2\left(\sqrt{2}+2\cos\alpha+2\beta(1+\nu)(2\lambda\sin\alpha+\sqrt{2})\right)\ \bar{r}^2}$
ν_{12}^*	$\frac{\lambda^2}{2}\left(\frac{C_1 - 2\left(1-2\beta(1+\nu)\right)C_I C_A C_2 \cos^2\alpha\ \bar{r}^2}{C_1+2\left(\sin^2\alpha+2\beta(1+\nu)\cos^2\alpha\right)C_I C_A C_2\ \bar{r}^2}\right)$
ν_{21}^*	$\frac{\frac{C_1}{\cos\alpha} + \left(4\beta(1+\nu)-2\right)C_I C_A C_2\cos\alpha\ \bar{r}^2}{C_1(\frac{\lambda^2}{\cos\alpha}+\sqrt{2}) + C_I C_A C_2 (2 cos\alpha + \sqrt{2} + 2\beta(1+\nu)(2\lambda\sin\alpha+\sqrt{2}))\ \bar{r}^2}$
ν_{23}^*	$\frac{C_1 + \left(2\beta(1+\nu)-1\right)C_I C_A C_2\ \bar{r}^2}{C_1\left(1+\frac{\lambda^2}{\sqrt{2}\cos\alpha}\right) + \left(\sqrt{2}\cos\alpha + 1 + 2\beta(1+\nu)(\sqrt{2}\lambda\sin\alpha+1)\right)C_I C_A C_2\bar{r}^2}$
$\frac{\kappa^*}{E}$	$\frac{C_I C_A^2\ \bar{r}^4}{\frac{\cos^2 2\alpha}{\sin\alpha\cos^4\alpha}C_1 + \left((8\sin\alpha+2\sqrt{2}\lambda)+4\beta(1+\nu)\frac{\cos^2 2\alpha}{\sin\alpha\cos^2\alpha}\right)C_I C_A C_2\ \bar{r}^2}$
$\frac{G_{12}^*}{E}$	$\frac{2\lambda C_I C_A^2\ \bar{r}^4}{\frac{D_1}{\cos^3\alpha} + 2\sqrt{2}\lambda^2 D_2 + 2C_I C_A C_2\ \bar{r}^2[\frac{1}{\lambda^2}+2\beta(1+\nu)(\frac{1}{\cos\alpha}+\sqrt{2}\lambda^2)]}$
$\frac{G_{23}^*}{E}$	$\frac{\cos^3\alpha C_I C_A^2\ \bar{r}^4}{\lambda\{D_3 + 2\sqrt{2}\cos^3\alpha C_I C_A C_2[1+\frac{\sqrt{2}(1+\nu)\beta}{\cos\alpha}]\ \bar{r}^2\}}$

Table 4.4a Geometric and other constants which appear in elastic moduli in Table 4.3 and Table 4.5

	Anisotropic/Non-Uniform XSC
C_A	$\left(\sqrt{3}-\frac{\pi}{2}\right)$
C_I	$\frac{I_y}{A^2}=0.1338$
C_J	$\frac{J}{2I_y}=0.3018$
C_1	$\int_{-1/2}^{1/2}\frac{\xi^2 d\xi}{f(\xi)^2}=0.0168241$
C_2	$\int_{-1/2}^{1/2}\frac{d\xi}{f(\xi)}=0.654375$
C_3	$\int_{-1/2}^{1/2}\frac{d\xi}{f(\xi)^2}=0.520105$
C_M	$\dfrac{\dfrac{(1+\nu)\cos\alpha}{C_J+(1+\nu)}+\dfrac{(1+\nu)(1+\lambda^2)}{2\sqrt{2}\left[C_J+(1+\nu)\lambda^2\right]}}{1+\dfrac{2\sqrt{2}(1+\nu)\cos\alpha}{C_J+(1+\nu)}+\dfrac{(1+\nu)(1+\lambda^2)}{C_J+(1+\nu)\lambda^2}}$
D_1	$C_1+\frac{(1+\nu)(1-2\sqrt{2}C_M)\lambda^2}{4\left[C_J+(1+\nu)\lambda^2\right]}C_3$
D_2	$C_1+\frac{(1+\nu)(1-2\sqrt{2}C_M)}{4\left[C_J+(1+\nu)\right]}C_3$
D_3	$C_1+\frac{(1+\nu)\cos\alpha}{4\left[\lambda C_J\sin\alpha+(1+\nu)(\sqrt{2}+\cos\alpha+\sqrt{2}\lambda^2)\right]}C_3$

Table 4.4b Geometric and other constants which appear in elastic moduli in Table 4.6

	Isotropic/Non-Uniform XSC	Isotropic/Uniform XSC
C_A	$\left(\sqrt{3}-\frac{\pi}{2}\right)$	$\left(\sqrt{3}-\frac{\pi}{2}\right)$
C_I	$\frac{I_y}{A^2}=0.1338$	$\frac{I_y}{A^2}=0.1338$
C_J	$\frac{J}{2I_y}=0.3018$	$\frac{J}{2I_y}=0.3018$
C_1	$\int_{-1/2}^{1/2}\frac{\xi^2 d\xi}{f(\xi)^2}=0.0168241$	$\frac{1}{12}$
C_2	$\int_{-1/2}^{1/2}\frac{d\xi}{f(\xi)}=0.654375$	1
C_3	$\int_{-1/2}^{1/2}\frac{d\xi}{f(\xi)^2}=0.520105$	1
C_M	$\frac{\sqrt{2}(1+v)}{C_J+5(1+v)}$	$\frac{\sqrt{2}(1+v)}{C_J+5(1+v)}$
D_1	$C_1+C_3\frac{(1+v)}{4[C_J+5(1+v)]}$	$\frac{1}{12}+\frac{(1+v)}{4[C_J+5(1+v)]}$
D_2	$C_1+C_3\frac{(1+v)}{4[C_J+5(1+v)]}$	$\frac{1}{12}+\frac{(1+v)}{4[C_J+5(1+v)]}$
D_3	$C_1+C_3\frac{(1+v)}{4[C_J+5(1+v)]}$	$\frac{1}{12}+\frac{(1+v)}{4[C_J+5(1+v)]}$

Table 4.5 Elastic constants of anisotropic Kelvin cell foams without shear effect

	Anisotropic/Non-Uniform XSC
$\frac{\rho^*}{\rho}$	$k\ \bar{r}^n$
$\frac{E_1^*}{E}$	$\frac{C_I C_A^2 \sin\alpha\ \bar{r}^4}{C_1 + 2C_I C_A C_2 \sin^2\alpha\ \bar{r}^2}$
$\frac{E_2^*}{E}, \frac{E_3^*}{E}$	$\frac{2C_I C_A^2 \cos\alpha\ \bar{r}^4}{\lambda\left[C_1(\lambda^2 + \sqrt{2}\cos\alpha) + C_I C_A C_2 (2\cos^2\alpha + \sqrt{2}\cos\alpha)\ \bar{r}^2\right]}$
ν_{12}^*	$\frac{\lambda^2}{2}\left(\frac{C_1 - 2C_I C_A C_2 \cos^2\alpha\ \bar{r}^2}{C_1 + 2C_I C_A C_2 \sin^2\alpha\ \bar{r}^2}\right)$
ν_{21}^*	$\frac{C_1 - 2C_I C_A C_2 \cos^2\alpha\ \bar{r}^2}{C_1(\lambda^2 + \sqrt{2}\cos\alpha) + (2\cos^2\alpha + \sqrt{2}\cos\alpha) C_I C_A C_2\ \bar{r}^2}$
ν_{23}^*	$\frac{C_1 - C_I C_A C_2\ \bar{r}^2}{C_1\left(1 + \frac{\lambda^2}{\sqrt{2}\cos\alpha}\right) + (\sqrt{2}\cos\alpha + 1) C_I C_A C_2\, \bar{r}^2}$
$\frac{\kappa^*}{E}$	$\frac{C_I C_A^2\ \bar{r}^4}{\frac{\cos^2 2\alpha}{\sin\alpha\cos^4\alpha} C_1 + (8\sin\alpha + 2\sqrt{2}\lambda) C_I C_A C_2\ \bar{r}^2}$
$\frac{G_{12}^*}{E}, \frac{G_{13}^*}{E}$	$\frac{2\sin\alpha\cos^2\alpha C_I C_A^2\ \bar{r}^4}{D_1 + 2\sqrt{2} D_2 \sin^2\alpha\cos\alpha + 2C_I C_A C_2\ \bar{r}^2}$
$\frac{G_{23}^*}{E}$	$\frac{\cos^3\alpha C_I C_A^2\ \bar{r}^4}{\lambda(D_3 + 2\sqrt{2}\cos^3\alpha C_I C_A C_2\ \bar{r}^2)}$

Table 4.6 Elastic constants of isotropic Kelvin cell foams without shear effect

	Isotropic/Non-Uniform XSC	Isotropic/Uniform XSC
$\dfrac{\rho^*}{\rho}$	$k\ \bar{r}^n$	$k\ \bar{r}^n$
$\dfrac{E_1^*}{E}$	$\dfrac{C_I C_A^2\ \bar{r}^4}{\sqrt{2}(C_1 + C_I C_A C_2\ \bar{r}^2)}$	$\dfrac{12 C_I C_A^2\ \bar{r}^4}{\sqrt{2}(1 + 12 C_I C_A\ \bar{r}^2)}$
$\dfrac{E_2^*}{E}, \dfrac{E_3^*}{E}$	$\dfrac{C_I C_A^2\ \bar{r}^4}{\sqrt{2}(C_1 + C_I C_A C_2\ \bar{r}^2)}$	$\dfrac{12 C_I C_A^2\ \bar{r}^4}{\sqrt{2}(1 + 12 C_I C_A\ \bar{r}^2)}$
ν_{12}^*	$\dfrac{1}{2} - \left(\dfrac{C_I C_A C_2\ \bar{r}^2}{C_1 + C_I C_A C_2\ \bar{r}^2}\right)$	$\dfrac{1}{2} - \left(\dfrac{12 C_I C_A\ \bar{r}^2}{1 + 12 C_I C_A\ \bar{r}^2}\right)$
ν_{21}^*	$\dfrac{1}{2} - \left(\dfrac{C_I C_A C_2\ \bar{r}^2}{C_1 + C_I C_A C_2\ \bar{r}^2}\right)$	$\dfrac{1}{2} - \left(\dfrac{12 C_I C_A\ \bar{r}^2}{1 + 12 C_I C_A\ \bar{r}^2}\right)$
ν_{23}^*	$\dfrac{1}{2} - \left(\dfrac{C_I C_A C_2\ \bar{r}^2}{C_1 + C_I C_A C_2\ \bar{r}^2}\right)$	$\dfrac{1}{2} - \left(\dfrac{12 C_I C_A\ \bar{r}^2}{1 + 12 C_I C_A\ \bar{r}^2}\right)$
$\dfrac{\kappa^*}{E}$	$\dfrac{\sqrt{2} C_A}{12 C_2}\ \bar{r}^2$	$\dfrac{\sqrt{2} C_A}{12}\ \bar{r}^2$
$\dfrac{G_{12}^*}{E}, \dfrac{G_{13}^*}{E}$	$\dfrac{C_I C_A^2\ \bar{r}^4}{2\sqrt{2}(D_1 + C_I C_A C_2\ \bar{r}^2)}$	$\dfrac{C_I C_A^2\ \bar{r}^4}{2\sqrt{2}\left(\dfrac{1}{12} + \dfrac{(1+\nu)}{4[C_J + 5(1+\nu)]} + C_I C_A\ \bar{r}^2\right)}$
$\dfrac{G_{23}^*}{E}$	$\dfrac{C_I C_A^2\ \bar{r}^4}{2\sqrt{2}(D_1 + C_I C_A C_2\ \bar{r}^2)}$	$\dfrac{C_I C_A^2\ \bar{r}^4}{2\sqrt{2}\left(\dfrac{1}{12} + \dfrac{(1+\nu)}{4[C_J + 5(1+\nu)]} + C_I C_A\ \bar{r}^2\right)}$

developed by Pradel (1998) (quoted in Laroussi *et al.*, 2002). If in addition axial deformations are neglected, results in Warren and Kraynik (1997) match the present ones. The expression for E_1^* including the effect of anisotropy in Dement'ev and Tarakanov (1970b) is also in agreement with the present results under the simplifying assumptions of their model. The quantitative effect of the additional factors considered in the present models on the elastic constants will be discussed in §4.4.

4.3 Numerical Models

4.3.1 Beam Element Model

The elastic constants can also be evaluated numerically using the characteristic cell shown in Figure 4.4. The periodicity conditions can be expressed as follows: Let the three pairs of opposite bounding faces of the cell be $(\partial R_{i1}, \partial R_{i2})\ \ i = 1,2,3$. The displacements and rotations of points on these faces are respectively denoted by (u_{i1}, u_{i2}) and $(\theta_{i1}, \theta_{i2})\ \ i = 1,2,3$. The following relationships of degrees of freedom are prescribed for points on each pair of faces $(\partial R_{i1}, \partial R_{i2})\ \ i = 1,2,3$:

$$\begin{aligned} &u_{i1} - u_{i2} = u_{i1}^{ref} - u_{i2}^{ref} \quad i = 1,2,3 \\ &\theta_{i1} - \theta_{i2} = 0 \quad i = 1,2,3 \end{aligned} \tag{4.11}$$

where u_{ij}^{ref} are displacements of conjugate points on opposite sides chosen as reference points (e.g., (A_1, A_2), (C_1, C_2), etc.).

The characteristic cell is discretized with finite elements within the nonlinear code ABAQUS using beam element. The area of each element is based on the symmetric function $f(\xi)$ as follows:

$$\begin{aligned}
f(\xi) &= 1 & 0 \le |\xi| \le 0.2, \\
f(\xi) &= 1.482 & 0.2 < |\xi| \le 0.3, \\
f(\xi) &= 2.574 & 0.3 < |\xi| \le 0.4, \\
f(\xi) &= 4.993 & 0.4 < |\xi| \le 0.5.
\end{aligned} \qquad (4.12)$$

Convergence tests were performed for the elastic modulus (E_1^*) by considering two types of space beam elements B31 (2-noded linear element, shear deformable) and B32 (3-noded quadratic element, shear deformable) and using different number of elements in each ligament. Based on the results listed in Table 4.7, the model with 7 B32 elements per ligament is the most accurate and efficient model. The resultant model has 24 ligaments, 168 elements, 363 nodes (330 nodes by user) and a total of 1980 variables.

Table 4.7 Convergence test results of Young’s modulus in ABAQUS model.

No. of Elements in a Ligament	$\frac{E^*}{E}$ (%) (B31)	$\frac{E^*}{E}$ (%) (B32)
7	0.11411	0.11225
14	0.11271	0.11225
20	0.11229	0.11225

By using the *beam general section* feature the sectional characteristics of each beam $\{A, I_y, J\}$ are prescribed to correspond to the values in (4.1) and (4.10). In addition, the beam is made to be shear-deformable with the shear factor given in Eq. (4.8).

4.3.2 Solid Element Model

The characteristic cell was also discretized with solid elements using C3D15V prisms and C3D27 brick elements (Figure 4.7). The philosophy behind generating the mesh was to closely match the geometry of the corresponding beam element model. As mentioned above, parts of the beams were removed in the neighborhood of the nodes in order to correctly represent the material distribution in the actual foam. The removed material depends on the relative density. For the solid model, part of the ligaments was assigned the area distribution $f(\xi)$, while the node was a smooth version of the corresponding beam node with the material removed (note that the two can not match exactly). As a result, for the relative densities considered $0.01 \le \rho^* / \rho \le 0.06$, the length of the mid-section of the ligament obeying $f(\xi)$ ranges from 0.664ℓ to 0.34ℓ.

Figure 4.5b shows a 3-D model node and one ligament. Although it compares well with the beam model node shown in Figure 4.5a it is not a perfect match. The part identified by $\mathrm{B-B'}$ has the $f(\xi)$ area distribution. This part was modeled with 32 prism elements. Each node was modeled with 16 prisms and 8 brick elements. The triangular prisms have 18 nodes and the bricks 27 nodes all with 3 degrees of freedom. Full integration was used for both. The full cell has

1,056 elements and a total of 23,814 degrees of freedom, which makes it computationally considerably more expensive than the beam model.

4.4 Elastic Moduli Predictions

4.4.1 Effect of Extension and Shear Deformation

The performance of the various beam models is illustrated in Figure 4.8 where predictions of the elastic modulus E^* as a function of the relative density are compared for the isotropic foam. Shown are results from the inextensional Bernoulli-Euler beam (B-E), the extensional beam (B-E Exte.), the shear deformable beam, and from the FE model using B32 elements. In all cases the beam cross section varies according to Eq. (2.1). The stiffest model is the inextensional B-E. The effect of extensionality increases with ρ^*. At relative densities of about 3% and 5% the inextensional model modulus is respectively 10% and 20% higher than the extensional model. The shear deformation plays an even more important role and can only be neglected for foams of relative densities of less than 1%. For example, at relative densities of about 3% and 5% the modulus of the shear deformable beam is only 74% and 62% respectively of the corresponding beam that precludes shear deformations. Included in the figure are results generated by the FE model. Since this beam model has the same features as the analytic extensional and shear deformable model it yields results, which are in excellent agreement with the latter.

A second set of comparisons appears in Figure 4.9. Here the elastic modulus and shear modulus of the isotropic foam predicted by the extensional beam, the FE B32 and the 3D models are compared. As pointed out above, the difference between the B-E and the FE B32 model is due to the effect of shear. The 3-D model is somewhat stiffer than the B32 model (Figure 4.9a). We attribute this small difference mainly to the fact that the node geometry was somewhat different in the two models.

4.4.2 Effect of Nonuniform Cross-section Distribution

The FE beam model will now be used to examine the importance of some of the realistic aspects of foams introduced in this work. Figure 4.10 shows the effect of the cross sectional variation of foam ligaments on the elastic constants of the isotropic Kelvin foam. Foams with Plateau border cross sections with uniform and nonuniform (Eq. (2.1)) cross sections are compared. The effect of cross sectional variation is very significant with the nonuniform cross section foam being generally stiffer. For example, at a relative density of 2% the nonuniform foam Young's modulus (Figure 4.10a) is nearly 69% higher than the uniform foam while at 5% relative density the difference increases to 74%. The Young's modulus to first order is governed by beam bending and, as a result, it is proportional to $\bar{r}^4$. The nonunifomity of the ligaments reduces $\bar{r}$ for a given relative density as shown in Figure 4.6. However, the nonunifomity makes the ligament stiffer by about a factor of 5 (difference between C_1 and 1/12 in Table 4.4), which has a stronger effect than the difference in $\bar{r}$.

The difference between the two sets of results is significant but smaller for the shear modulus (Figure 4.10b). The bulk modulus (Figure 4.10c) is relatively unaffected by this redistribution of material primarily because it is governed by axial deformation which is less sensitive to this change. By contrast, Poisson's ratio is slightly reduced by cross sectional nonunifomity (Figure 4.10d). This stiffening effect carries through to anisotropic foams as well.

4.4.3 Effect of Cell Anisotropy

The effect of cell anisotropy in the elastic properties is illustrated in Figure 4.11 where results for λ = 1, 1.2 and 1.4 are presented for foams with nonuniform cross section. The modulus in the x_1-direction increases (Figure 4.11a) while the one in the x_2-direction decreases (Figure 4.11b). For example, at a relative density of 3%, λ of 1.2 and 1.4 result in an increase in E_1^* of 36% and 69% respectively and a corresponding decrease in E_2^* of 17% and 35%. The equations in Table 4.3 show that these changes are directly related to the geometric variable λ.

The shear moduli $G_{12}^* = G_{13}^*$ remain unaffected (Figure 4.11c) by λ whereas G_{23}^* get reduced as λ increases (Figure 4.11d). Figure 4.11e shows that bulk modulus also gets reduced as λ increases. For the isotropic case κ^* is governed by membrane deformations (Table 4.6). Anisotropy makes κ^* depend also on bending deformations, which generally reduce the stiffness. Poisson's ratio ν_{12}^* is seen in Table 4.3 to be proportional to λ^2; as a result it increases significantly with λ as demonstrated in Figure 4.11f. By contrast ν_{21}^* (Figure 4.11g) and ν_{23}^* (Figure 4.11h) are reduced as λ increases.

4.4.4 Comparison of Measured and Calculated Elastic Moduli

Table 4.8 shows a direct comparison of the measured and calculated ($\hat{E}_i^*$, i =1,2) values of these moduli using the formulas in Table 4.3 (including the effect of shear). The predicted moduli are somewhat smaller than the measured values with the biggest difference being 33% for the 3ppi foam. This favorable comparison suggests that the idealizations made in the geometry of the model foam are reasonable. It also confirms that factors included in the present analysis such as axial and shear deformations, the nonuniformity of the ligament cross sections and the material distribution at the nodes are essential in getting this level of agreement between measurements and predictions.

table 4.8 Comparison of measured and calculated foam elastic moduli

Foam ppi	λ	$\frac{\rho^*}{\rho}$ (%)	$\frac{E_1^*}{E}$ (%)	$\frac{\hat{E}_1^*}{E}$ (%)	$\frac{E_2^*}{E}$ (%)	$\frac{\hat{E}_2^*}{E}$ (%)
3	1.432	2.18	0.227	0.152	0.0701	0.0535
10	1.360	2.47	0.181	0.181	0.0707	0.0749
20	1.281	2.36	0.200	0.151	--	0.0747
45	1.256	2.44	0.215	0.156	0.103	0.0819
100	1.233	2.82	0.229	0.203	0.128	0.113

CHAPTER 5

ONSET OF INSTABILITY AND POSTBUCKLING RESPONSE

The compression experiments on polyester urethane foams showed that the material response is governed by instabilities. Furthermore, a distinct difference between the response in the rise and transverse directions was observed. The difference was present in all five foams tested and has been attributed to the cell anisotropy present in this class of foams. In this chapter we use models with Kelvin cells to explore first the onset of instability and subsequently to establish the postbuckling behavior of the material. The models use either a single or an assemblage of Kelvin cells with appropriate periodicity conditions. Uniaxial compression in the rise and transverse directions is examined.

5.1 ABAQUS Model

The microstructure of the model foams is idealized to be periodic using the space filling Kelvin cell with the geometric characteristics developed in Chapter 4. In other words, the ligaments are assumed to be straight with Plateau border cross sections with the nonuniform cross sectional area distribution given in Eq. (2.1). The ligaments will be modeled as shear-deformable beams using ABAQUS's B32 quadratic element. The cell will exhibit the type of anisotropy shown in Figure 4.3 and Eq. (4.2), and the relative density quoted will incorporate the correction introduced in Chapter 4 (Eq. (4.7)) for the extra material at the nodes. The basic building block of the models is the characteristic cell shown in Figure 4.4, with the periodicity conditions given in Eqs. (4.11). From convergence studies (see Table 5.1) we decide to assign 8 B32 elements per ligament. This discretization provides sufficient accuracy while keeping numerical calculation at a manageable size. Unless otherwise stated the area distribution in the eight elements will be as follows

$$\begin{aligned} f(\xi) &= 1 && 0 \le |\xi| \le 0.2, \\ f(\xi) &= 1.482 && 0.2 < |\xi| \le 0.3, \\ f(\xi) &= 2.574 && 0.3 < |\xi| \le 0.4, \\ f(\xi) &= 4.993 && 0.4 < |\xi| \le 0.5 \end{aligned} \tag{4.12}$$

where $f(\xi)$ is the symmetric function given in Eq. (2.1). The base material is again assumed to be linearly elastic, time independent and isotropic with modulus E and Poisson's ratio ν (values given in Table 3.1)

Table 5.1 Convergence test for the critical stress of beam model

B32 Model	No. of Elements in a Ligament	7	8	14	16
$\lambda = 1$ $N = 1$	$\frac{\sigma_C}{E} \times 10^3$	0.16929	0.16683	0.16683	0.16668
$\lambda = 1.3$ $N = 12$	$\frac{\sigma_{1C}}{E} \times 10^3$	0.15775	0.15738	0.15738	0.15735

5.2 Rise Direction

5.2.1 Critical Stress and Buckling Mode

In all such calculations we first consider one characterisitc cell with periodicity on all edges. Uniaxial compression is accomplished by prescribing incrementally the relative displacement (δ_1) between the upper and lower periodic boundaries. The average stress σ_1 required to produce this deformation is the force normalized by the initial cross sectional area of the cell ($h_2 \times h_2$). Figure 5.1a shows the calculated stress-displacement response for an anisotropic foam ($\lambda = 1.3$) with relative density of 2.5%. Initially (OAB), the foam deforms uniformly and symmetrically about a vertical axis through the center of the cell (inset shows side view of the deformed characteristic cell). The response is stiff but increasingly nonlinear because of the increasingly larger deflections of the ligaments. The foam elastic modulus quoted in Chapter 4 (E_1^*) corresponds to the slope at the origin and is $E_1^* / E = 0.00176$.

At some point along OAB the first eigenvalue is identified indicating that an alternate equilibrium configuration is possible. Naturally, because of the size of the domain chosen and periodicity conditions imposed, this mode of buckling is at the cell level and takes the form shown in Figure 5.2 under *N* = 1 and 2. In microstructures with the extent of periodicity such as that of the Kelvin foam, buckling modes involving more than one cell are possible and must be investigated. To this end we conduct similar calculations and eigenvalue checks for columns of *N* characterisitc cells with periodicity conditons at the top, bottom, and sides. For the present microstructure *N* = 2 yields the same first eigenvalue and mode, but for $N = 3$ the eigenvalue is smaller and the mode changes to the one shown in Figure 5.2. Increasing the number of cells to 4, 6, 8 and 12 reduces further the critical stress and increases the mode wavelength. Figure 5.3a illustrates the drop in critical stress with N. For $N > 12$ the critical stress remains unchanged although the mode wavelength increases. Similar calculations are performed for wider columns (number of characteristic cells in the x_2 or x_3 directions is increased). It was found that this does not affect the critical stress and the corresponding mode. The same insensitivity is observed when the column is made wider in both directions simultaneously. Thus, the critical stress is taken to be the plateau value in Figure 5.3a and is identified on the response in Figure 5.1a as σ_{1C}.

The behavior described indicates that the periodic foam admits a long wavelength buckling mode rather than one limited to the cell level. This finding is in concert with the bowing observed in the compressed foam block shown in Figure 3.3b. The long wave mode is to be contrasted with that of honeycombs under in-plane crushing (Papka and Kyriakides, 1994, 1998a) where the buckling mode was at the cell level.

Interestingly the neighborhood just beyond the critical stress contains many eigen values and modes similar to the ones shown in Figure 5.2. This richness in closely packed buckling modes is a characteristic that indicates sensitivity to a variety of imperfections, a subject that will be discussed Chapter 8.

5.2.2 Postbuckling Response

We next examine the postbuckling response corresponding to the long wavelength mode associated with σ_{1C}. The mode is assigned an amplitude and applied as an initial imperfection to a column of characteristic cells of sufficient height ($N = 12$ is selected here). The periodicity conditions applied to the perfect geometry are maintained. The microsection is then compressed in the x_1-direction by prescribing incrementally δ_1. Results for the case with imperfection amplitude of $\Delta_o/\ell = 0.25$ are included in Figure 5.1a ($\Delta_o = |u_o(x)|_\infty$ and $u_o(x)$ is the imperfection). The initial and several deformed configurations corresponding to points marked with solid bullets on the response are shown in Figure 5.1c. Initially the response follows that of the perfect case. As σ_{1C} is approached, the domain is distorted (see configurations ① and ②) resulting in reduction of its stiffness. With further distortion the imperfect case response increasingly deviates from the perfect case and reaches a limit load (stress) at an average strain of about 17.6%. Subsequently, the stress decreases with deformation. The deformed configurations in Figure 5.1c show the progressive growth of the buckled configuration. These calculations were performed with just one column of characteristic cells. It is worth noting that increasing the width of the characteristic domain did not change the calculated response.

The fact that a limit load instability is traced in the response of this strictly periodic microstructure, indicates that localized deformation patterns will probably be energetically preferred if the periodicity conditions are relaxed to some degree. This possibility will be examined in chapter 8. (Note that the possibility of contact between ligaments of deforming cells was precluded in this calculation.)

5.3 Transverse Direction

5.3.1 Critical Stress and Buckling Mode

We repeat the process for uniaxial compression in the transverse direction (x_2). Again we start with one characteristic cell with periodicity conditions on all of its sides and prescribe incrementally the relative displacement (δ_2) between the two sides normal to the x_2-direction. The calculated $\sigma_2 - \delta_2$ response is shown in Figure 5.4a. Initially the deformation involves symmetric crushing of the cell as shown in the inset. As mentioned earlier the initial modulus is much smaller than the corresponding one in the rise direction ($E_2^* = 0.475 E_1^*$). At larger strains the response again becomes increasingly nonlinear due to geometric distortion of the cells. The first eigen value occurs at point A at a stress of σ_{2C}. Two views of the corresponding buckling mode are shown in Figure 5.4b. The mode is limited to just one characteristic cell (for clarity the microsection shown includes six cells).

We next conduct similar compression tests on columns with N characteristic cells where N is progressively increased as described above. Unlike the rise direction the calculated critical stress and the corresponding mode were found to be insensitive to N. This is illustated in Figure 5.3b where the critical stress is plotted as a function of N. The critical stress and mode were also found to be insensitive to the width of the column analyzed. This implies that in this direction the prevalent buckling mode is the local one shown in Figure 5.4b (several cells are included for clarity).

5.3.2 PostBuckling Response

The buckling mode corresponding to σ_{2C} with amplitude $\Delta_o = 0.01\ell$ is now applied as an imperfection to the characteristic cell and the compression test is repeated keeping the same periodicity conditions. The imperfect cell response initially follows that of the perfect one. It starts to deviate from it as σ_{2C} is approached. Deformed configurations corresponding to points marked on the response are shown in Figure 5.4c. In configuration ① nonsymmetric deformation is visible and it is seen to grow in configurations ② and ③. In contrast to the rise direction, this response maintains a positive slope to large values of average strain. We note again that increasing the width of the characteristic domain does not alter the response. This overall behavior indicates that this deformation pattern will also be maintained in a larger domain in which the periodicity conditions are relaxed.

In summary, the compressive behavior in the rise and transverse directions of the anisotropic Kelvin cell foam are distinctly different. In the rise direction the foam buckles into a long wavelength mode. The postbuckling behavior of this mode exhibits a limit load instability, which in a less constrained domain is expected to result in localized collapse. Both the long wave buckling mode and localized crushing were observed in the rise direction crushing tests on the five foams tested. In the transverse direction the critical buckling modes is at the cell level and postbuckling response is monotonically increasing and stable. These general features were also observed in the transverse direction crushing experiments: the long wavelength buckling mode was absent and the response remained a monotone.

5.4 Solid Element Models

The critical stress was calculated in a similar manner using the characteristic cell model discretized with solid elements as described in §4.3b (C3D15V prisms and C3D27 bricks; mesh shown in Figure 4.7). The same periodicity conditions (4.11) were applied to the models in these buckling analyses. The difference here is that the models have about one order of magnitude more degrees of freedon than the beam models. As a result they are more difficult to use especially when multicell domains need to analyzed.

In the rise direction, the stress-displacment response is slightly harder than that of the beam model as shown in Figure 5.5 for the same generic foam used above (E_1^* / E 0.00209 vs. 0.00176). The critical stress was found to correspond to the same long wavelength buckling mode (shown in Figure 5.5b). However the critical stress for N = 12 was found to be 29.2% lower than the corresponding value from the beam model. Two main factors contribute to this difference. The first is the more accurate representation of the node compliance afforded by the solid model. The second is related to cell ligament cross sectional distortion resulting from prebuckling bending. The solid model captures this distorsion whereas beam models do not.

The trivial compressive response calucated by the solid element model and beam model are compared in Figure 5.6. In the transverse direction, the modulus from the solid element model is E_2^*/E 0.00101 vs. 0.00083 for the beam model. The critical stress of the solid model was found to be associated with the same local cell mode as the beam model (see Figure 5.6b where for clarity the microsection shown includes three cells). The comparison of the critical stresses in transverse direction between beam element model and solid element model is shown in Figure 5.6a. The critical stress value is 29.5% lower than the value in Figure 5.4a.

As pointed out in Chapter 4, the solid element model is prohibitively computationally expensive. It was thus decided to limit its use to only bifurcation stress calculations for the major cases analyzed.

5.5 Isotropic Foam

In view of the differences introduced by anisotropy to the idealized foam, it is worthwhile to also examine the compressive behavior of the isotropic case ($\lambda = 1$). The compressive response of the perfect case is shown in Figure 5.7a. The initial elastic modulus is $E^*/E = 0.001123$ which lies between the E_1^* and E_2^* values calculated for $\lambda = 1.3$. The critical stress is found to correspond to a long wavelength mode. Figure 5.8 shows how σ_C varies with the number of cells in the column analyzed. The buckling stress drops as *N* increases but at a much slower rate than it did for the anisotropic case. For *N* > 12 the buckling stress does not change. The buckling mode corresponding to *N* = 12 shown in Figure 5.7b is similar to the one seen earlier in Figure 5.1b. As in the other two cases, the critical stress yielded by the solid FE model is 17.4% lower. The same long wavelength mode shown in Figure 5.7b is associated with the critical stress.

Included in Figure 5.7a is the compressive response of the imperfect case where the buckling mode for $N = 12$ is used as initial imperfection (amplitude $\Delta_o = 0.45\ell$). The response exhibits a limit load indicating again that localized crushing can be expected to take place in the isotropic foam also.

The onset of instability in Kelvin cell foams was previously investigated by Laroussi *et al.* (2002). Their foam was linearly elastic, isotropic, with ligaments of uniform circular cross section. The ligament was modeled as shear deformable beams. In most calculations the foam had a relative density of 0.06. The characteristic cell adopted was somewhat different from the one used in this study but, because in most stability calculations an assemblage of such cells was used, this difference may be inconsequential. The main thrust of the work was the use of a variation of the Bloch wave method of Triantafyllidis *et al.* to establish stability envelopes in different multi-axial spaces. Uniaxial compression was also discussed and a long wavelength buckling mode was found to occur. The postbuckling behavior of this case was not discussed. Because of the many differences in the assumed microstructure and in the modeling scheme adopted, direct comparison with the present results is difficult and will not be attempted. In the cases discussed by these authors perturbation was applied to the initial geometry rather than the deformed one. Since instability occurs at average strains well beyond 10%, this will contribute to some difference between the critical stresses yielded by their schemes and the present one.

5.6 Parametric Study of Critical Stress

5.6.1 r_o/ℓ *and* ρ^*/ρ

The procedure described in the previous section was used to calculate the critical bifurcation stress as a function of the geometric parameter r_o/ℓ for foams of anisotropy values λ ranging from 1 to 1.4. The variable r_o/ℓ was varied so that the relative density ρ^*/ρ was in the range of 0.01 to 0.06. In all cases the ligament cross sectional variation was in accordance with $f(\xi)$ in Eq. (2.1). As a result, ρ^*/ρ is related to r_o/ℓ through a power law with the constants given in the Table 4.2. The calculated critical stresses were fitted to power law expressions as follows:

$$\frac{\sigma_C}{E} = k_{\bar{r}}\left(\frac{r_o}{\ell}\right)^{n_{\bar{r}}} \qquad \text{and} \qquad \frac{\sigma_C}{E} = k_{\bar{\rho}}\left(\frac{\rho^*}{\rho}\right)^{n_{\bar{\rho}}} \tag{5.1}$$

Critical stress calculated for two representative cases ($\lambda = 1$ and 1.3) for the rise direction (σ_{1C}) are plotted in log-log scale against r_o/ℓ in Figure 5.9. The plots confirm that the critical stress is indeed a power law function of r_o/ℓ. The numerical results of the fits are listed in Table 5.2. It is of interest to observe that in the corresponding strictly linear problem $n_{\bar{r}} = 4$. If in addition the material distribution at the nodes is neglected then $n_{\bar{\rho}} = 2$ as suggested by Gibson and Ashby (1982, 1997). By contrast, in the present calculations $n_{\bar{r}} < 4$ because of the nonlinearity of the problem. In addition, $n_{\bar{\rho}} > 2$ and both $n_{\bar{r}}$ and $n_{\bar{\rho}}$ depend on the anisotropy variable λ.

Table 5.2 Fit parameters for powerlaw relationships between the critical stress (σ_{1C}) and r_o/ℓ and ρ^*/ρ

λ	$n_{\bar{r}}$	$k_{\bar{r}}$	$n_{\bar{\rho}}$	$k_{\bar{\rho}}$
1	3.8071	0.011918	2.272	0.6825
1.1	3.8447	0.011241	2.288	0.7286
1.2	3.8612	0.010184	2.298	0.7425
1.3	3.8712	0.009122	2.299	0.7577
1.4	3.8842	0.008414	2.307	0.7185

A similar parametric study was conducted for the bifurcation stress in the transverse direction (σ_{2C}). In all cases the mode corresponding to the critical stress was local to the characteristic cell (similar to results in Figure 5.4). A sample of σ_{2C} results for $\lambda = 1.3$ is plotted against r_o/ℓ in Figure 5.9. They are lower than the corresponding σ_{1C} values but have nearly the same exponent $n_{\bar{r}}$.

5.6.2 Imperfection Δ_o/ℓ

The limit stress of the imperfect microstructure is a more realistic estimate of the maximum load capacity of the material. It is thus worth establishing its imperfection sensitivity. Figure 5.10a shows for example how the imperfection amplitude affects the response of the case analyzed in Figure 5.1. Increase of the imperfection makes the microstructure more compliant and lowers the limit load. The limit stress (σ_{1L}) from similar calculations normalized by the bifurcation stress of the perfect structure is plotted against Δ_o/ℓ in Figure 5.11 (dashed line). Its imperfection sensitivity is seen to be quite significant.

Calculations of imperfect microstructures similar to the ones presented in Figure 5.10 were performed for the five foams used in the experiments (using their individual values of r_o/ℓ and λ). In each case the imperfection corresponded to the mode of the critical stress but its amplitude, Δ_o, was varied. The calculated limit stresses are plotted against Δ_o/ℓ in Figure 5.11. The imperfection sensitivity of the normalized limit stress of the different foams is seen to be similar.

Included in Table 5.3 are calculated limit stresses for the five foams tested for imperfection amplitudes of $\Delta_o/\ell = 1$ and 2. The predictions are now seen to be much closer to the measured values approaching them from above. This illustrates that an even more accurate prediction of the measured initiation stress will have to involve models with a more accurate representation of the actual microstructure with all its imperfections.

Figure 5.10b shows how the amplitude of the initial imperfection affects the postbuckling response in the transverse direction. The behavior is typical of structures with a stable postbuckling behavior. The imperfection makes the response more compliant. It rounds and lowers the knee in the neighborhood of the bifurcation point. In view of the results we conclude that the difference between the calculated bifurcation stress and the experimental knee stress can again be attributed to geometric imperfections including the irregularity of the microstructure of the actual foams.

Table 5.3 Comparison of measured and calculated critical stresses

Foam ppi	λ	$\frac{\rho^*}{\rho}(\%)$	$\frac{\sigma_{1I}}{E}\times 10^3$	$\frac{\sigma_{1C}}{E}\times 10^3$	$\frac{\sigma_{1L}}{E}\times 10^3$ $(\Delta_o/\ell = 1)$	$\frac{\sigma_{1L}}{E}\times 10^3$ $(\Delta_o/\ell = 2)$	$\frac{\sigma_{2I}}{E}\times 10^3$	$\frac{\sigma_{2C}}{E}\times 10^3$
3	1.432	2.18	0.0584	0.1083	0.0841	0.0681	0.0386	0.1062
10	1.360	2.47	0.0650	0.1466	0.1187	0.1000	0.0522	0.1093
20	1.281	2.36	0.0710	0.1350	0.1097	0.0923	--	0.1065
45	1.256	2.44	0.0840	0.1459	0.1183	0.0993	0.0645	0.1175
100	1.233	2.82	0.0920	0.2054	0.1656	0.1384	0.0568	0.1687

It is of interest to compare the critical bifurcation stresses calculated for the five foams tested with the measured limit stresses (σ_{1I} and σ_{2I} in Table 3.1). The calculated and measured values are listed in Table 5.3. σ_{2I} are lower than the corresponding σ_{1I} by factors ranging between approximately 1.25 to 1.62. The calculated critical stresses σ_{2C} are lower than the corresponding σ_{1C} by factors ranging between approximately 1.02 to 1.34. In all cases the predicted critical stress is higher by about a factor of 2, which is not surprising. The actual microstructure is irregular and has significant geometric imperfections. In addition, test in which the foam is compressed between rigid platens mask to some degree the actual compressive strength because of the interaction between the edges of the foam and the platens. Another factor contributing to this difference are idealizations introduced by the beam models, which make the microstructure stiffer. As demonstrated above, solid FE models which are more representative of actual foams yield lower critical stresses.

CHAPTER 6

BLOCH WAVE METHOD

An important variable for open-cell foams is the first bifurcation or critical stress and the corresponding mode. This is particularly important in the foams being considered in this study because, as we have seen, the critical stress does not differ significantly from the plateau stress. In Chapter 5 it was demonstrated that the complexity of foam microstructures requires that bifurcation checks be made to increasingly larger domains with multiples of the characteristic cell. The critical mode can be local to the cell, it can involve several cells, or it can involve many cells. Even for just uniaxial compression along the rise and transverse directions considered in Chapter 5, this process is lengthy if done mannually. When more general multiaxial loadings are considered the task of estabilishing a stability surface in an appropriate stress space can be daunting.

Triantafyllidis and co-workers (Geymonat *et al.*, 1993; Schraad, and Triantafyllidis, 1997a,b) developed an efficient, robust numerical method for establishing the onset of instability in periodic structures under general loading conditions based on Bloch wave theory. The characteristic cell with the appropriate periodicity conditions is loaded incrementally along a given loading path. Using Bloch wave theory and the stiffness matrix of the unit cell, one can investigate the stability of the infinite periodic medium against all possible bounded perturbations and establish the critical conditions.

The periodicity of our Kelvin cell foam and the numerous checks, which must be performed to establish the critical condition, make the problem an excellent candidate for application of this method. In this chapter the method is tailored to the present microstructure using the characteristic cell developed in Chapter 5 (developed in Gong, Kyriakides and Triantafyllidis, 2005).

6.1 Bloch Wave Stability Calculations

We consider the stability of the infinite periodic foam under general loading following a specific path. We will use the incremental response of the unit cell to this loading, and seek to identify the first instance equilibria different from the trivial one become possible. The unit cell is the one shown in Figure 4.4 descretized as described in §5.1.

Let $\mathbf{K}(\Lambda)$ be the global tangent stiffness matrix of the characteristic cell (unconstrained, i.e. before applying B.C.), where Λ is a normalized load parameter. It can be written as

$$\mathbf{K}(\Lambda)=\begin{bmatrix}\mathbf{K}_{11} & \mathbf{K}_{12} & \mathbf{K}_{1\mathrm{I}} \\ \mathbf{K}_{21} & \mathbf{K}_{22} & \mathbf{K}_{2\mathrm{I}} \\ \mathbf{K}_{\mathrm{I}1} & \mathbf{K}_{\mathrm{I}2} & \mathbf{K}_{\mathrm{II}}\end{bmatrix}, \tag{6.1}$$

where $\mathbf{K}_{\alpha\beta}$ are stiffness submatrices corresponding to nodes on the three opposite pairs of cell surfaces $(\partial R_{i1}, \partial R_{i2})$, $i=1,2,3$ (subscripts 1 and 2 represent the face pair) and internal nodes are represented by subscript I. So, for example, $\mathbf{K}_{11}$ is a 36×36 matrix for the six nodes (A_1, B_1), (C_1, D_1), (E_1, F_1) on surfaces

∂R_{i1} (see Figure 4.4). Each node has 6 degrees of freedom constituting vector $\mathbf{u}_1$ with 36 components. $\mathbf{K}_{22}$ is a similar stiffness matrix corresponding to (A_2, B_2), (C_2, D_2), (E_2, F_2) on surfaces ∂R_{i2} and degrees of freedom $\mathbf{u}_2$ (also with 36 components). $\mathbf{K}_{12}$ and $\mathbf{K}_{21}$ are cross stiffness matrices relating $\mathbf{u}_1$ and $\mathbf{u}_2$. $\mathbf{K}_{\mathrm{II}}$ (2196×2196) is the stiffness matrix of the (366) internal nodes with corresponding (2196) degrees of freedom $\mathbf{u}_{\mathrm{I}}$.

Let $\tilde{\mathbf{u}} = \{\tilde{\mathbf{u}}_1, \tilde{\mathbf{u}}_2, \tilde{\mathbf{u}}_{\mathrm{I}}\}^{\mathrm{T}}$ be the displacement increments along a bifurcated equilibrium path starting at the critical point and $\tilde{\mathbf{F}} = \{\tilde{\mathbf{F}}_1, \tilde{\mathbf{F}}_2, \mathbf{0}\}^{\mathrm{T}}$ be the corresponding force increments. Then incremental equilibrium requires that

$$\mathbf{K}(\Lambda)\tilde{\mathbf{u}} = \tilde{\mathbf{F}}. \tag{6.2}$$

The internal degrees of freedom $\tilde{\mathbf{u}}_{\mathrm{I}}$ can be evaluated from (6.2) as

$$\tilde{\mathbf{u}}_{\mathrm{I}} = -\mathbf{K}_{\mathrm{II}}{}^{-1}\left[\mathbf{K}_{\mathrm{I}1}\tilde{\mathbf{u}}_1 + \mathbf{K}_{\mathrm{I}2}\tilde{\mathbf{u}}_2\right]. \tag{a}$$

Substituting (a)$\rightarrow$(6.2) results in

$$\begin{bmatrix} \hat{\mathbf{K}}_{11} & \hat{\mathbf{K}}_{12} \\ \hat{\mathbf{K}}_{21} & \hat{\mathbf{K}}_{22} \end{bmatrix} \begin{Bmatrix} \tilde{\mathbf{u}}_1 \\ \tilde{\mathbf{u}}_2 \end{Bmatrix} = \begin{Bmatrix} \tilde{\mathbf{F}}_1 \\ \tilde{\mathbf{F}}_2 \end{Bmatrix}, \tag{6.3}$$

where

$$\begin{aligned} \hat{\mathbf{K}}_{11} &= \mathbf{K}_{11} - \mathbf{K}_{1\mathrm{I}}\mathbf{K}_{\mathrm{II}}{}^{-1}\mathbf{K}_{\mathrm{I}1}, \\ \hat{\mathbf{K}}_{12} &= \mathbf{K}_{12} - \mathbf{K}_{1\mathrm{I}}\mathbf{K}_{\mathrm{II}}{}^{-1}\mathbf{K}_{\mathrm{I}2}, \\ \hat{\mathbf{K}}_{21} &= \mathbf{K}_{21} - \mathbf{K}_{2\mathrm{I}}\mathbf{K}_{\mathrm{II}}{}^{-1}\mathbf{K}_{\mathrm{I}1}, \\ \hat{\mathbf{K}}_{22} &= \mathbf{K}_{22} - \mathbf{K}_{2\mathrm{I}}\mathbf{K}_{\mathrm{II}}{}^{-1}\mathbf{K}_{\mathrm{I}2}. \end{aligned} \tag{b}$$

Because of the periodicity of the cell we can assume that the bifurcation mode admits the following form (Bloch, 1928)

$$\tilde{\mathbf{u}}(\mathbf{x}) = \mathbf{U}(\mathbf{x})\exp\left[i\left(\frac{m_1 x_1}{h_1} + \frac{m_2 x_2}{h_2} + \frac{m_3 x_3}{h_3}\right)\right], \tag{6.4}$$

where h_i and $m_i/h_i,\ i = 1,3$ are the dimensions of the sides of the characteristic cell and the wave numbers respectively. $\mathbf{U}(\mathbf{x})$ is a periodic function with the same spatial periodicity as the unit cell, i.e.

$$\mathbf{U}(x_1 + n_1 h_1, x_2 + n_2 h_2, x_3 + n_3 h_3) = \mathbf{U}(x_1, x_2, x_3), \tag{c}$$

where n_i are arbitrary integers. In view of (6.4) nodes on opposite sides will have

$$\tilde{\mathbf{u}}_2 = \boldsymbol{\mu}\tilde{\mathbf{u}}_1 \qquad \text{and} \qquad \tilde{\mathbf{F}}_2 = -\boldsymbol{\mu}\tilde{\mathbf{F}}_1, \tag{6.5}$$

where

$$\mu = \begin{bmatrix} \mathrm{e}^{im_1}\mathbf{I} & \mathbf{0} & \mathbf{0} \\ \mathbf{0} & \mathrm{e}^{im_2}\mathbf{I} & \mathbf{0} \\ \mathbf{0} & \mathbf{0} & \mathrm{e}^{im_3}\mathbf{I} \end{bmatrix}, \ \dim(\mathbf{I}) = 12. \tag{d}$$

Substituting (6.5) $\rightarrow$(6.3) results in

$$\begin{bmatrix} \hat{\mathbf{K}}_{11} & \hat{\mathbf{K}}_{12} \\ \hat{\mathbf{K}}_{21} & \hat{\mathbf{K}}_{22} \end{bmatrix} \begin{bmatrix} \mathbf{I} & \mathbf{0} \\ \mathbf{0} & \mu \end{bmatrix} \begin{Bmatrix} \tilde{\mathbf{u}}_1 \\ \tilde{\mathbf{u}}_1 \end{Bmatrix} = \begin{bmatrix} \mathbf{I} & \mathbf{0} \\ \mathbf{0} & \mu \end{bmatrix} \begin{Bmatrix} \tilde{\mathbf{F}}_1 \\ -\tilde{\mathbf{F}}_1 \end{Bmatrix}. \tag{6.6}$$

Multiplying both sides of (6.6) by $[\mathbf{I} \quad \bar{\mu}]$, where $\bar{\mu}$ is the complex conjugate of μ (i.e., $\bar{\mu}\mu = \mathbf{I}$), gives

$$[\mathbf{I} \quad \bar{\mu}]\begin{bmatrix} \hat{\mathbf{K}}_{11} & \hat{\mathbf{K}}_{12} \\ \hat{\mathbf{K}}_{21} & \hat{\mathbf{K}}_{22} \end{bmatrix}\begin{bmatrix} \mathbf{I} & \mathbf{0} \\ \mathbf{0} & \mu \end{bmatrix}\begin{Bmatrix} \tilde{\mathbf{u}}_1 \\ \tilde{\mathbf{u}}_1 \end{Bmatrix} = [\mathbf{I} \quad \bar{\mu}]\begin{bmatrix} \mathbf{I} & \mathbf{0} \\ \mathbf{0} & \mu \end{bmatrix}\begin{Bmatrix} \tilde{\mathbf{F}}_1 \\ -\tilde{\mathbf{F}}_1 \end{Bmatrix}, \qquad \text{(e)}$$

which results in

$$\overset{\circ}{\mathbf{K}}(\Lambda,\mu)\tilde{\mathbf{u}}_1 = [\mathbf{I} \quad \bar{\mu}]\begin{bmatrix} \hat{\mathbf{K}}_{11} & \hat{\mathbf{K}}_{12} \\ \hat{\mathbf{K}}_{21} & \hat{\mathbf{K}}_{22} \end{bmatrix}\begin{bmatrix} \mathbf{I} \\ \mu \end{bmatrix}\tilde{\mathbf{u}}_1 = \left[\hat{\mathbf{K}}_{11} + \hat{\mathbf{K}}_{12}\mu + \bar{\mu}\hat{\mathbf{K}}_{21} + \bar{\mu}\hat{\mathbf{K}}_{22}\mu\right]\tilde{\mathbf{u}}_1 = \mathbf{0}. \qquad (6.7)$$

Here $\overset{\circ}{\mathbf{K}}(\Lambda, m_1, m_2, m_3)$ is a 36×36 Hermitian matrix (i.e., real eigen values) with zero determinant. Thus, we prescribe m_i and seek the lowest value of $\Lambda(m_i)$ for which $\det|\overset{\circ}{\mathbf{K}}| = 0$. The process is repeated for a broad range of $m_i \in [0,\pi]$ (note cubic symmetry of cell) and the critical bifurcation load is

$$\Lambda_C = \min_{m_1,m_2,m_3} \Lambda(m_i) \qquad \text{at } m_i = m_i^c. \qquad (6.8)$$

The corresponding bifurcation mode is given by

$$\tilde{\mathbf{u}}(\mathbf{x}) = \mathbf{U}(\mathbf{x})\exp\left[i\left(\frac{m_1^c x_1}{h_1} + \frac{m_2^c x_2}{h_2} + \frac{m_3^c x_3}{h_3}\right)\right]. \qquad (6.9)$$

Two cases are distinguished: either the dimensionless wave numbers at criticality m_i^c are different from 0 (or $2n\pi$) (modes involving a finite number of cells) or they are in the neighborhood of 0. In the latter case two different types of modes coexist: either strictly periodic modes--local to the cell--($m_i^c = 0$ or $2n\pi$) or long wavelength modes ($m_i^c \to 0$). For the strictly periodic modes ($\tilde{\mathbf{u}}_2 = \tilde{\mathbf{u}}_1$) one should be careful to constrain (6.7) against rigid body translation, thus removing the singularity from $\det|\overset{\circ}{\mathbf{K}}| = 0$. For $m_i^c \to 0$, the limit of $\det|\overset{\circ}{\mathbf{K}}| = 0$ has to be taken analytically and corresponds to the loss of ellipticity of the homogenized tangent moduli of the structure.

6.2 Homogenized Moduli Of Kelvin Cell Foam

For the long wavelength mode ($m_i^c \to 0$) in Bloch wave method, the limit of the critical load Λ_C can be solved analytically by evaluating the homogenized tangent moduli of the infinite periodic structure under the same loading path.

We construct special functions $\overset{ij}{\boldsymbol{\chi}}$ for the six degrees of freedom of all nodes of the characteristic cell, which correspond to unit normal (ε_{ii}, no sum) and shear ($\varepsilon_{ij},\ i \neq j$) strains as follows:

$$\overset{ij}{\chi} = \left\{ \overset{ij}{\chi}_1, \overset{ij}{\chi}_2, \overset{ij}{\chi}_{\mathbf{I}} \right\}^T, \ (ij) = 1,2,3. \qquad (6.10)$$

For each node (N)

$$\overset{ij}{\boldsymbol{\chi}}(N) = \begin{Bmatrix} \overset{ij}{\boldsymbol{\chi}}_k \\ \overset{ij}{\boldsymbol{\chi}}_r \end{Bmatrix}^T \qquad (k = 1,2,3)\ (r = 4,5,6), \qquad (f)$$

where subscript k represents the displacements and r the rotations. For the displacement degrees of freedom

$$\overset{ij}{\chi}_k = \delta_{ik} x_j + \overset{ij}{\upsilon}_k, \tag{g}$$

where $\mathbf{x}$ are the coordinates of the nodes, $\overset{ij}{\upsilon}_k$ are periodic functions

$$\left(\overset{ij}{\upsilon}_k \Big|_1 = \overset{ij}{\upsilon}_k \Big|_2 \right)$$

and

$$\overset{ij}{\chi}_k \Big|_2 = \overset{ij}{\chi}_k \Big|_1 + \delta_{ik} h_j, \tag{h}$$

where $\bullet|_1$ and $\bullet|_2$ refer to opposite sides of the characteristic cell (the second term on the RHS is only present for surfaces with normals acting in the j-direction). For the rotational degrees of freedom

$$\overset{ij}{\chi}_r \Big|_2 = \overset{ij}{\chi}_r \Big|_1 . \tag{i}$$

Applying Eq. (6.10) to the unit cell, where the internal degrees of freedom are condensed out as in (a), results in

$$\begin{bmatrix} \hat{\mathbf{K}}_{11} & \hat{\mathbf{K}}_{12} \\ \hat{\mathbf{K}}_{21} & \hat{\mathbf{K}}_{22} \end{bmatrix} \begin{Bmatrix} \overset{ij}{\boldsymbol{\chi}}_1 \\ \overset{ij}{\boldsymbol{\chi}}_2 \end{Bmatrix} = \begin{Bmatrix} \overset{ij}{\mathbf{F}}_1 \\ \overset{ij}{\mathbf{F}}_2 \end{Bmatrix}. \tag{j}$$

Using (h), (i) and $\overset{ij}{\mathbf{F}}_2 = -\overset{ij}{\mathbf{F}}_1$ in (j) and multiplying both sides by $[\mathbf{I} \quad \mathbf{I}]$ ($\mathbf{I}$ is a 36×36 unit matrix) yields

$$[\mathbf{I} \quad \mathbf{I}]\begin{bmatrix} \hat{\mathbf{K}}_{11} & \hat{\mathbf{K}}_{12} \\ \hat{\mathbf{K}}_{21} & \hat{\mathbf{K}}_{22} \end{bmatrix}\begin{Bmatrix} \overset{ij}{\boldsymbol{\chi}}_1 \\ \overset{ij}{\boldsymbol{\chi}}_1 + \left\langle \delta_{ik} h_j \right\rangle \end{Bmatrix} = [\mathbf{I} \quad \mathbf{I}]\begin{Bmatrix} \overset{ij}{\mathbf{F}}_1 \\ -\overset{ij}{\mathbf{F}}_1 \end{Bmatrix}$$

or

$$\left[\hat{\mathbf{K}}_{11} + \hat{\mathbf{K}}_{12} + \hat{\mathbf{K}}_{21} + \hat{\mathbf{K}}_{22}\right]\left\{\overset{ij}{\boldsymbol{\chi}}_1\right\} = -\left[\hat{\mathbf{K}}_{12} + \hat{\mathbf{K}}_{22}\right]\left\langle \delta_{ik} h_j \right\rangle, \tag{k}$$

where $\left\langle \delta_{ik} h_j \right\rangle$ are applied to all displacement degrees of freedom of $\overset{ij}{\boldsymbol{\chi}}_1$. This has the solution:

$$\overset{ij}{\boldsymbol{\chi}}_1 = -\left[\hat{\mathbf{K}}_{11} + \hat{\mathbf{K}}_{12} + \hat{\mathbf{K}}_{21} + \hat{\mathbf{K}}_{22}\right]^{-1}\left[\hat{\mathbf{K}}_{12} + \hat{\mathbf{K}}_{22}\right]\left\langle \delta_{ik} h_j \right\rangle. \tag{6.11}$$

From $\overset{ij}{\boldsymbol{\chi}}_1$ evaluate $\overset{ij}{\boldsymbol{\chi}}_2$ and $\overset{ij}{\boldsymbol{\chi}}_{\mathrm{I}}$ and form $\overset{ij}{\boldsymbol{\chi}}$. The incremental moduli of the material at the load Λ can then be evaluated as:

$$L_{ijkl}(\Lambda) = \frac{\overset{ij}{\chi}{}^T \mathbf{K}(\Lambda) \overset{kl}{\chi}}{V}, \tag{6.12}$$

where $V = h_1 h_2 h_3$ is the volume of the unit cell.

Long wavelength instability has been shown (Geymonat *et al.*, 1993) to correspond to the loss of rank one convexity of the above found homogenized moduli of the periodic microstructure, i.e.

$$(L_{ijkl}(\Lambda) n_j n_l) g_k = 0 \quad \text{or} \quad \det | L_{ijkl}(\Lambda) n_j n_l | = 0. \tag{6.13}$$

Define

$$\mathbf{n} = \{\cos\varphi,\ \sin\varphi\cos\psi,\ \sin\varphi\sin\psi\}^{\mathrm{T}} \quad 0 \le \varphi \le \pi,\ 0 \le \psi \le 2\pi. \qquad \text{(l)}$$

Then for each Λ, vary $\{\varphi,\psi\}$ until (6.13) is satisfied. The critical load is the lowest Λ which allows such a solution and the corresponding $\mathbf{n}$ is the direction of the band (see also Rice, 1976).

6.3 RESULTS

Uniaxial compression of one characteristic cell in the rise direction is accomplished by prescribing incrementally the relative displacement (δ_1) between its upper and lower periodic boundaries. Figure 5.1a shows the calculated trivial stress-displacement response for an anisotropic foam ($\lambda = 1.3$) with relative density of 0.025.

The Bloch wave method automates the search for the critical state. The method was implemented in conjunction with the FE code ABAQUS which provided the instantaneous stiffness matrix $\mathbf{K}(\Lambda)$ at different positions along the primary loading path. At each Λ, $m_i \ (i = 1,3)$ are varied from 0 to π and check is made for which values, if any, $\det|\overset{\circ}{\mathbf{K}}| = 0$. The critical value of Λ is the lowest value for which this is the case (see Eq. (6.8)). This search is done by the computer for the stiffness matrices provided by the user for finite increments of Λ. Once buckling is found to occur between two values of Λ, interpolation is used to get close to the critical state.

Figure 6.1a shows the critical stress as a function of the number of cells N in a periodic column for uniaxial loading in the x_1- direction. The Bloch wave method results are drawn with a solid line ($N = 2\pi / m$). They are seen to be in agreement with the discrete results obtained via the manual method described in §5.2.1. From the results it is evident that the periodic foam admits a long wavelength buckling mode for this type uniaxial loading. This finding is in concert with the bowing observed in the compressed foam block shown in Figure 3.3b.

The same process is repeated for uniaxial compression in the transverse direction (x_2). Again we start with one characteristic cell with periodicity conditions on all of its sides and prescribe incrementally the relative displacement (δ_2) between the two sides normal to the x_2-direction. The calculated trivial $\sigma_2 - \delta_2$ response is shown in Figure 5.4a. As we discussed in Chapter 5, in this direction the critical stress and the corresponding mode were found to be insensitive to N. The critical state was also found to be insensitive to the width of the domain analyzed. These results were also confirmed by the Bloch wave method. Results of σ_{2C} as a function of N predicted by the two methods are compared in Figure 6.1b and seen to be in excellent agreement. Thus, the results show that in this direction the prevalent buckling mode is one local to the cell.

σ_C results obtained by the Bloch wave method are plotted against N in Figure 6.2. Included are discrete results obtained by the manual method. The foam again exhibits the long wave mode. The two methods confirm that the foam again exhibits the long wave mode. The two sets of results shown in Figure 6.2 are in excellent agreement. The use of the Bloch wave method for triaxial loading will be discussed next in Chapter 7.

CHAPTER 7

FOAMS UNDER TRIAXIAL LOADING

Porous materials are usually tested under triaxial loading (e.g., Triantafyllou *et al.*, 1988; Deshpande and Fleck, 2000; Gioux *et al.*, 2000). Motivated by this we investigate the stability of our foam under such loading states using the Bloch wave theory method described in Chapter 6. Laroussi *et al.* (2002) used a variation of the Bloch wave method to conduct similar calculations for an isotropic Kelvin cell foam with uniform cross section ligaments. Triantafyllidis and Schraad (1998) used the method to investigate biaxial loading of a honeycomb.

Since the material is elastic, surfaces associated with the loss of stability (*failure surfaces*) are independent of the loading path followed. Because of the shape of the failure surfaces traced in the $J_2 - I_1$ plane, we found it convenient to load the foam under the radial stress loading defined by

$$\{\sigma_1, \sigma_2, \sigma_3\} = \Sigma\{k, 1, 1\}, \quad k \in [1, \infty). \tag{7.1}$$

Thus, $k = 1$ represents pure hydrostatic pressure loading and $k \to \infty$ represents uniaxial compression. k was varied and for each value the critical state was established. The Bloch wave method is invaluable in the conduct of such calculations.

7.1 Prebuckling and PostBuckling Responses

7.1.1 $k = 1$, $\lambda = 1.3$

We first consider a foam under hydrostatic compression ($k = 1$). Figure 7.1a shows the mean stress-change in volume ($\bar{\sigma} - \delta\upsilon$) response for a foam with relative density of 0.025 and λ = 1.3 (in this case $\bar{\sigma} = \Sigma$). The mean stress is normalized by the critical stress under uniaxial loading in the rise direction (σ_{1C}^{*}). The critical stress ($\bar{\sigma}_C$) corresponds to a mode local to a single cell. The postbuckling response was calculated by applying a small initial imperfection to the unit cell corresponding to this buckling mode. The calculated response is shown in the figure while a set of deformed configurations corresponding to the points marked in the response with numbered flags are shown in Figure 7.1b ($x_1 - x_2$ and $x_2 - x_3$ planar views are shown). For clarity a $2 \times 2 \times 2$ microsection is shown although the repetition of the single cell deformation pattern is quite obvious. Once again the response is a monotone indicating that deformation is stable. Because of the anisotropy most of the deformation occurs in the $x_2 - x_3$ plane where some parts of the microstructure are seen to stay intact whereas the surrounding neighboring ligaments collapse by twisting. The pattern in configuration ③ is reminiscent of patterns seen in the equibiaxial crushing experiments and numerical simulations on circular cell honeycombs of Papka and Kyriakides (1999a, 1999b) (see Figure I.11 and II.5b). (Note that no ligament contact was applied in these calculations.)

7.1.2 $k = 1.54,\ \lambda = 1.3$

Next we consider tiaxial loading of the same foam for k = 1.54. Figure 7.2a shows the axial stress-displacement response and Figure 7.2b the corresponding mean stress-change in volume response. Both stress quantities are normalized by σ_{1C}^*. The critical state is marked on the responses by σ_{1C} and $\bar{\sigma}_C$. For this loading the critical buckling mode involves a domain consisting of $2 \times 2 \times 2$ cells. The postbuckling responses corresponding to a small initial imperfection in the form of the critical buckling mode are included in the two figures. Both are monotones indicating that they are stable. However, they exhibit a milder rate of increase than the pure hydrostatic pressure case. Figure 7.2c shows two planar views of a sequence of deformed configurations of the $2 \times 2 \times 2$ cell domain analyzed. The evolution of patterns in both domains is quite complex.

7.1.3 $k = 2.5,\ \lambda = 1.3$

Figure 7.3a and 7.3b show similar responses for k = 2.5 for the same foam. In this case the critical state corresponds to a long wavelength mode. Furthermore, the postbuckling responses of the appropriate domain with a small initial imperfection corresponding to this buckling mode exhibit a limit load instability. Figure 7.3c shows the initial and three deformed configurations corresponding to the points marked on the responses with numbered flags. The domain analyzed consists of a column of 12 characteristic cells with the usual periodicity conditions applied to the top, bottom and sides. Overall, the behavior is similar to that of the uniaxial loading case shown in Figure 5.1. The limit load again implies that if the periodicity conditions are removed deformation will tend to localize.

7.1.4 $\lambda = 1.2$

The domain of the critical buckling mode was found to depend on the foam anisotropy. For example, for $\lambda = 1.2$ and loading state $k = 1.43$, the critical buckling mode involves a domain consisting of $2 \times 1 \times 2$ cells. Figure 7.4a shows the axial stress-displacement response and Figure 7.4b the corresponding mean stress-change in volume response (in this case $\bar{\sigma} = \Sigma(2+k)/3$). Both stress quantities are normalized by σ_{1C}^{*} ($\lambda = 1.2$). The postbuckling responses are seen to be stable and relatively stiff. Two views of the initial and three deformed configurations of the $2 \times 2 \times 2$ microsection are shown in Figure 7.4c.

Similar results for the same value of anisotropy and loading state $k = 1.43$ are shown in Figures 7.5. In this case the critical buckling mode involves a domain consisting of $1 \times 2 \times 2$ cells. The postbuckling responses remain stable but with decreased stiffnesses compared to those of the case in Figure 7.4. The two sets of results illustrate the richness in configurations encountered in multiaxial loading of Kelvin cell foams.

7.2 Failure Surfaces

Additional calculations were conducted for a broad range of k and for each case the critical state was established. The results are summarized in Figure 7.6a in the form of a “failure” envelope in the $\sqrt{3J_2} - I_1$ plane (J_2 is the second invariant of the deviatoric stress tensor and I_1 the first invariant of the stress tensor). The two stress quantities are normalized by the critical stress of the same relative density isotropic foam under uniaxial loading ($\sigma_C(1)$). Interestingly, the shape of the envelope is quite similar to envelopes developed from triaxial tests on aluminum foams by Deshpande and Fleck (2000). At low values of k (and J_2) the critical mode is local to a single cell. At high values of k (and J_2) the instability involves long wavelength modes. For intermediate values of k (and J_2) the critical buckling modes cover a domain consisting a few cells (e.g. $2\times2\times2$, $2\times2\times1$, $1\times2\times2$, $2\times1\times2$ cells). In all cases tested the postbuckling responses of long wavelength modes were found to exhibit a limit load. By contrast, local modes exhibit stable postbuckling behavior.

Similar calculations were performed for foams with the same relative density but different values of anisotropy. The results are summarized in Figure 7.6a. For all anisotropic cases considered the shapes of the failure surfaces are similar. The isotropic case (λ = 1) does not exhibit the single cell buckling modes at low values of k. Overall, increasing λ tends to decrease the critical stress states.

An alternate failure envelope is one involving the lateral stress Σ_C vs. the axial stress σ_{1C} (note that here $\{\sigma_2, \sigma_3\} = \{\Sigma, \Sigma\}$). Both are normalized by the critical stress of the isotropic foam with the same relative density under uniaxial loading ($\sigma_C(1)$). The failure envelopes calculated for five values of anisotropy are shown in Figure 7.6b. Because of the different critical states plotted these envelopes contain additional results not included in Figure 7.6a. Again the shapes of the surfaces are qualitatively similar to experimentally produced “yield” surfaces for aluminum foams in Deshpande and Fleck (2000). The isotropic foam essentially encloses all the others. The same three regimes of buckling modes are identified on each envelope.

CHAPTER 8

CRUSHING RESPONSE

Calculations which go well beyond the onset of instability discussed in the previous chapters must address two important new aspects of the problem. The first is the complication introduced by the eventual contact between the buckling ligaments of the cells. The second issue affects cases where a limit load instability was recorded in the characteristic section analysis. In such cases, localized deformation is a strong possibility. Thus, the domain analyzed must be altered/expanded to allow for localization to develop. Both issues bring challenges to the modeling effort and we will address each separately.

8.1 Ligament Contact

As was clearly demonstrated in the studies of honeycomb crushing (Papka and Kyriakides, 1994, 1998), contact between the collapsing walls of cells played a pivotal role in the load plateau traced under displacement controlled compression. Contact arrests local collapse and, as a consequence, locally stabilizes the microstructure. This in turn causes cells adjacent to the zone of local collapse, hitherto only slightly deformed, to start collapsing. This process repeats until collapse spreads in this manner to the whole specimen. Although less ordered, local collapse of zones of cells also governs the crushing of foams. Experimental observations have also confirmed that collapse of these zones is again terminated by contact between the buckled ligaments. The irregularity of the foam microstructure makes modeling of ligament contact formidable. Indeed, despite the simplifications introduced to the modeling effort by the adoption of the periodic Kelvin cell, modeling of ligament contact remains a complex task which often results in numerical convergence difficulties. We bypassed this difficulty by adopting the following approximation for ligament contact. The corner nodes of all vertical rhombi (squares for $\lambda = 1$) are connected with springs. Thus, for example, points a and B_2 in rhombus abB_2F_2 in Figure 8.1 are connected. The springs (ABAQUS SPRING2) become activated when the vertical distance between the two nodes exceeds a chosen threshold. Once activated the spring force depends only on the vertical distance of the connected nodes, in other words, relative displacement of the nodes in the $x_2 - x_3$ plane is uninhibited. Thus the force in the spring is given by

$$F = \begin{cases} 0, & (u_{1B_2} - u_{1a}) < \psi, \\ k(u_{1B_2} - u_{1a}), & (u_{1B_2} - u_{1a}) \geq \psi, \end{cases} \tag{8.1}$$

where ψ is the gap that must be closed first before the spring is activated and k is the spring constant. The selection of the variables ψ and k and their effect on the results will be discussed below.

8.2 Crushing of A Finite Size Foam Domain

8.2.1 Rise Direction

We now explore the possibility of the model foam developing deformation patterns precluded by the full periodicity conditions prescribed in the previous section. To this end we continue to consider foam with relative density of 0.025 and the same anisotropy of $\lambda = 1.3$. For numerical expediency, we first choose a domain with 8 characteristic cells in the rise direction (x_1) (12 would have been more optimal) and 28 in the transverse direction (x_3) (see undeformed configuration, ⓪, in Figure 8.2b). The domain is one characteristic cell thick (x_2-direction) with periodicity conditions applied to the front and back surfaces. Periodicity conditions are also assumed at the top and bottom edges. Compression is applied along the rise direction by prescribing incrementally the relative displacement between the upper and lower edges. The main difference from calculations in the previous section is that the domain width is finite as the two lateral edges are now let free. An initial imperfection (amplitude $\Delta_o = 0.197\ell$) corresponding to the critical mode of the fully periodic microstructure (of this height) is introduced to the model. (Note that the critical stresses of the fully periodic foam and the one with its sides free are very close.) In addition, the pseudo-contact scheme described above with the parameters $\psi = 0.670\lambda\ell$ and $k = 0.202 C_A E r_o^2 / \ell$ was implemented.

Figure 8.2a shows the calculated average stress-displacement response and Figure 8.2b shows the undeformed and a sequence of deformed configurations corresponding to the points on the response marked with numbered flags. The initial response follows the trivial one closely. At higher stress levels the imperfection is excited (see configuration ①) and nontrivial deformation grows causing a softening in the response. This results in a stress maximum close to configuration ②. As might be expected, freeing the lateral edges makes the limit stress about 5% lower than the corresponding value for the fully periodic domain with the same imperfection value. Subsequent to the stress maximum localized deformation starts to become visible in the concave parts of the free edges in configuration ②. At these sites deformation grows to the levels which cause the contact springs to be activated (see configuration ③). Further local deformation is then inhibited and collapse spreads across to neighboring cells. By configuration ④ highly deformed zones and less deformed ones are distinctly seen in the domain. As this continues contact springs are activated in increasingly more cells resulting in the upturn in the average stress seen to occur around a normalize displacement of 45% (see configuration ⑤).

Drawn with a dashed line in the Figure 8.2a is the corresponding response calculated in the absence of the contact springs. A set of deformed configurations corresponding to the points marked on this response is shown in Figure 8.2c. The two responses are identical up to the limit stress. Thus, the initial and the first two deformed configurations in Figures 8.2b and 8.2c are identical. Following the limit stress, localization starts at the same sites in both models in the concave parts of the free edges. In the absence of the artificial contact, localization results in penetration of the deforming cells which starts to be seen in configuration $\boxed{3}$ in Figure 8.2c. Penetration continues in configurations $\boxed{4}$ and $\boxed{5}$. Clearly penetration, as it develops in this setting, has no stabilizing effect. As a result, firstly the stress keeps decreasing monotonically and secondly the spreading of deformation to neighboring regions observed in Figure 8.2b does not materialize. The free edges have some effect on the two sets of results presented in Figure 8.2. This effect can be reduced by increasing the width of the microsection.

The variable ψ in Eq. (8.1) governs the extent to which individual cells can collapse. Its influence on the overall crushing response is shown in Figure 8.3. It has no influence in the early stages of deformation and on the limit stress, which is governed instead by the imperfection amplitude. Increasing ψ extends the stress plateau and delays the densification stage of the response. In other words, ψ influences the energy absorption capacity of the foam. Other features of the crushing response remain similar to those of the case presented in Figures 8.2a and 8.2b. In the present modeling scheme the value of ψ is chosen so that the experimental values of $\Delta\varepsilon^{p}$ are matched.

In the results shown this far nontrivial deformation was activated by an imperfection corresponding to the mode of the critical stress. It was noted earlier that the Kelvin cell foams analyzed were found to have a quite a large number of eigen values at stresses only slightly higher than the critical stress. This richness in closely packed eigen values and modes indicates that the idealized microstructure may be sensitive to a variety of imperfections. To test this we compressed finite size microsections similar (8×12 cells) but with an initially perfect geometry. These microsections were "disturbed" by two equal and opposite point forces of small amplitude applied at different heights along the two free sides. Figure 8.4a shows stress-axial shortening responses for three such models identified as "I", "II" and "III", disturbed at different locations. The location of the applied point forces is shown in the single deformed configurations from each case in Figure 8.4b. The disturbances destabilized each model at a stress level close to the critical stress of the perfect case. The three responses are close to each other and exhibit a limit load following which deformation localizes. The localization is illustrated in the individual configurations in Figure 8.4b, which correspond to points soon after the respective limit stress. When contact springs are included in such models continued compression results in stress plateaus such as the one in Figures 8.2a and 8.3. The results demonstrate that the microstructure is sensitive to a variety of disturbances.

8.2.2 Transverse Direction

In the transverse direction the response of the fully periodic model is monotonic. Thus, it doesn't have the natural tendency to collapse and localize. This was confirmed by analyzing finite size microsections (6×16 cells) similar to the one described above (see undeformed configuration, ⓪, in Figure 8.5b). Figure 8.5a shows the calculated average stress-displacement response and Figure 8.5b shows the undeformed and a sequence of deformed configurations corresponding to the points on the response marked with numbered flags. In Figure 8.5b the local cell mode of Figure 5.4c is repeated in all cells with the exception of a narrow boundary layer along the free edges. Away from the edges ligament contact does not occur until an average strain has passed 40%. The fully periodic response is thus representative of finite size specimens also up to this strain level.

Drawn with a dashed line in Figure 8.5a is the corresponding response calculated in the absence of the contact springs. A set of deformed configurations corresponding to the points marked on this response is shown in Figure 8.5c. The two responses are identical up to about 20% average strain. Thus, the initial and the first deformed configurations in Figures 8.5b and 8.5c are identical. After that, in the absence of the artificial contact, some localization develops at the free ends and results in penetration of the deforming cells (configurations $\boxed{2}$ and $\boxed{3}$ in Figure 8.5c). But since the microsection is wide enough, this boundary effect does not affect the overall monotonic response.

The influence of variable ψ in Eq. (8.1) on the overall crushing response is shown in Figure 8.6. It has no influence in the early stages of deformation and on the first knee. As was the case in the rise direction, increasing ψ extends the stress plateau and delays the densification stage of the response, and thus increases the energy absorption capacity of the foam.

8.3 Energy Based Prediction of Foam Crushing Stress

It was noted that the response yielded by the fully periodic domain of a single column of characteristic cells does not allow the development of localized deformation nor the stress plateau associated with its spreading. Despite this, the characteristic domain response is worth revisiting. To this end we incorporate into this model the pseudo-contact model discussed above and pursue the solution further into the postbuckling regime. In this case we consider a fully periodic domain consisting of a column of 12 characteristic cells. The calculated response is shown in Figure 8.7a. The initial part of the response is the same as the one in

Figure 5.1a. The domain buckles in the long wavelength mode shown in Figure 8.7b. A limit load instability is developed at an average strain of about 18% and subsequently the stress drops with increasing displacement. The response stabilizes again at an average strain of 42.4% when ligaments come into contact in some cells. A second stable branch develops during which most of the cells have collapsed as seen in configuration ⑤.

This *up-down-up* nature of the response of this characteristic domain is one typical of problems which exhibit propagating instabilities (Ericksen, 1975 Kyriakides, 1993, 2001). The first ascending branch up to the limit stress, represents stable, uncollapsed configurations. The second ascending branch following the local minimum represents collapsed configurations which in this case are associated with the long wavelength buckling of the domain. The two are joined by a third branch which is unstable. For a range of stress levels, cells initially at equilibrium in the first ascending branch, given a large enough disturbance, can snap to the second stable branch. Indeed in this stress regime collapsed and uncollapsed zones of cells can co-exist.

This response is unrealizable in practice as it represents a uniformly collapsing foam. It will be referred to as the *local response* of the material. However, it can be used to evaluate the plateau or crushing stress as follows. Consider a loaded foam domain in which the highly deformed phase has been initiated and coexists with the relatively undeformed phase. Apply a far field displacement so that the highly deformed phase consumes, in a quasi-static fashion, an additional unit volume of the domain. In other words, the unit volume of material moves from equilibrium state a to state c at a constant stress σ_{1P}. If A is the cross sectional area of the domain, the external work done in this process is

$$\sigma_{1P} A(\delta_c - \delta_a).$$

The material is elastic and, as a result, the process is path independent. The collapsed configuration c can be reached by moving along abc at a constant stress due to the propagation of the collapse front as discussed above, or by following the up-down-up response. Thus, the change in strain energy induced can be evaluated from the local response. The change in strain energy between configuration a and c is equal to the external work done yielding

$$\sigma_{1P} A(\delta_c - \delta_a) = \int_{\delta_a}^{\delta_c} \sigma_1(\delta) A d\delta .$$

The plateau stress is then

$$\sigma_{1P} = \frac{1}{(\delta_c - \delta_a)} \int_{\delta_a}^{\delta_c} \sigma_1(\delta) d\delta . \tag{8.2}$$

This equation is satisfied when abc is at a level that makes the shaded area under the response and above the line equal to the shaded area below the line and above the response. σ_{1P} is also called *Maxwell* stress.

For the case shown in Figure 8.7a $\sigma_{1P}/E = 0.140 \times 10^{-3}$. We would like to compare this value with the plateau stress of the finite domain. To accomplish this we performed a compression test on a finite size domain with 12×28 cells. The results of this calculation are shown in Figure 8.8. The results are similar to those in Figure 8.2 for the 8×28 cell domain. The plateau stress is about σ_1/E = 0.128×10^{-3}. As is the case for the limit stress, the free ends tend to lower slightly the plateau stress. It is also interesting to compare the deformed configurations from the two cases at the end of the process. Figure 8.9a shows the deformed configuration at an average strain of about 45% for the finite domain calculation. To accommodate such a comparison we assembled together 28 fully periodic column deformed configurations at the same average strain to generate the domain shown in Figure 8.9b. Although not exactly the same, the similarity between the two deformed patterns is quite clear. This is especially true regarding the distributions of collapsed cells. Small differences are once more due to the influence of the free edges. This influence should be diminishing as the width of the finite domain is increased. The strength of the Maxwell construction is the simplicity with which the crushing strength can be established. By comparison, the finite domain calculation is computationally very intensive indeed.

8.4 Parametric Study of Crushing Stress

8.4.1 Amplitude of Imperfection Δ_o

The postbuckling response and, by extension, the crushing stress are influenced first by the amplitude of the imperfection (Δ_o) adopted and second by the value of the gap variable ψ. The influence of the imperfection amplitude is illustrated in Figure 8.10a which shows responses for four imperfection amplitudes for the same generic foam analyzed in the previous section. (In all cases in this section the domain consists of a fully periodic column of 12 cells.) Increasing the imperfection reduces the limit stress and as a result lowers the crushing stress. Numerical values of these stresses are given in Table 8.1. The difference in σ_{1P} between the smallest and largest imperfections used is about

9%. For this idealized Kelvin cell microstructure the accuracy of σ_{1P} will increase as the imperfection amplitude is decreased. However, as pointed out in §5.6.2, the imperfection amplitude is one way of making the calculated critical stresses approach those measured in actual foams which have irregular microstructures. Thus, the optimal choice of $\varDelta_o$ is left to the user.

Table 8.1 Comparison of calculated critical stresses for foams with four initial imperfection amplitudes ($\lambda = 1.3$, $\rho^* / \rho = 2.5\%$, $\psi / \lambda \ell = 0.670$)

$\frac{\varDelta_o}{\ell}$	$\frac{\sigma_{1C}}{E} \times 10^3$	$\frac{\sigma_{1L}}{E} \times 10^3$	$\frac{\sigma_{1P}}{E} \times 10^3$
0.197	0.156	0.149	0.140
0.246	0.156	0.147	0.139
0.492	0.156	0.138	0.133
0.738	0.156	0.130	0.127

8.4.2 Gap Variable ψ

The effect of the gap variable ψ on such results is illustrated in Figure 8.10b where similar responses are shown for three different values of ψ. This variable does not affect the limit stress but affects the point of recovery of the response. The quantitative effect this has on σ_{1P} is given in Table 8.2. The difference in σ_{1P} between the smallest and largest values of ψ used is about 3.5%.

Table 8.2 Comparison of calculated critical stresses for foams with three gap values ($\lambda = 1.3$, $\rho^*/\rho = 2.5\%$, $\Delta_o/\ell = 0.197$)

$\dfrac{\psi}{\lambda\ell}$	$\dfrac{\sigma_{1C}}{E} \times 10^3$	$\dfrac{\sigma_{1L}}{E} \times 10^3$	$\dfrac{\sigma_{1P}}{E} \times 10^3$
0.536	0.156	0.149	0.145
0.590	0.156	0.149	0.143
0.670	0.156	0.149	0.140

8.4.3 r_o/ℓ

To this end, foams of different r_o/ℓ were analyzed keeping the anisotropy, the imperfection and the gap variables fixed. The results are listed in Table 8.3. (Note that the density of all these foams had been calculated in the course of developing (4.7). For this reason, the relative densities listed in Table 8.3 are slightly different from the values yielded by the fit in (4.7).) The bifurcation stress σ_{1C}, the limit stress σ_{1L} and the crushing stress σ_{1P} are listed in Table 8.3. As expected, σ_{1C} is the largest of the three and σ_{1P} the smallest. The three stresses are also plotted in log-log scales against r_o/ℓ in Figure 8.11. All three follow powerlaw relationships to r_o/ℓ.

8.4.4 Foam Anisotropy λ

The next variable to be varied is the foam anisotropy λ keeping the relative density, the imperfection amplitude and the gap variable ($\psi/\lambda\ell$) constant. Foams with five different values of λ between 1.0 and 1.4 were analyzed. Three of the calculated responses are shown in Figure 8.12 while the main results from

Table 8.3 Comparison of calculated critical stresses for foams of several relative densities(λ = 1.3, $\Delta_o/\ell = 0.246$, $\psi/\lambda\ell = 0.670$)

$\frac{r_o}{\ell}$	$\frac{\rho^*}{\rho}$(%)	$\frac{\sigma_{1C}}{E} \times 10^3$	$\frac{\sigma_{1L}}{E} \times 10^3$	$\frac{\sigma_{1P}}{E} \times 10^3$
0.2185	1.11	0.025	0.0236	0.022
0.3485	2.50	0.156	0.147	0.139
0.4720	4.14	0.506	0.472	0.451
0.5352	5.08	0.810	0.767	0.738
0.5917	5.96	1.170	1.130	1.086

Table 8.4 Comparison of calculated critical stresses for foams of different anisotropy ($\rho^*/\rho = 2.5\%$, $\Delta_o/\ell = 0.492$, $\psi/\lambda\ell = 0.670$)

λ	$\frac{r_o}{\ell}$	$\frac{E_1^*}{E} \times 10^3$	$\frac{\sigma_{1C}}{E} \times 10^3$	$\frac{\sigma_{1L}}{E} \times 10^3$	$\frac{\sigma_{1P}}{E} \times 10^3$
1	0.3222	1.115	0.166	0.147	0.143
1.1	0.3324	1.315	0.165	0.146	0.141
1.2	0.3411	1.512	0.162	0.143	0.137
1.3	0.3485	1.701	0.156	0.138	0.133
1.4	0.3549	1.881	0.152	0.136	0.130

the five cases are summarized in Table 8.4. As reported in Chapter 4, increasing the anisotropy increases the foam modulus E_1^* in the x_1-direction. Thus, for example, when λ = 1.4 the modulus is 69% higher than the isotropic case modulus. This is because the ligaments with a vertical projection have a smaller inclination to the vertical axis. Simultaneously, the length of these ligaments has increased (see Figure 8.1) and, as a result, the critical buckling stress of the foam decreases but by a smaller amount. By contrast, the critical strain decreases quite significantly. In all cases the postbuckling response exhibits a limit load instability. The limit load also decreases as λ is increased essentially for the same reason. The crushing stress decreases with λ more or less in the same mild manner as the other two stresses.

CHAPTER 9

SUMMARY AND CONCLUSIONS

This study has been concerned with the understanding and modeling of the response of open-cell foams to uniaxial and multiaxial compression. A set of polyester urethane foams covering a range of cell sizes and with relative densities in the range of 2.2-2.8% was considered. Their microstructures consist of interconnected frameworks forming cells with nearly straight edges. The cells are irregular polyhedra with 9-17 faces. The average number of faces per cell was found to be 13.7. Faces had anywhere from 3 to 7 sides while the average number of sides per face was close to 5. Cells were found to be elongated in the rise direction, a characteristic common to polymeric foam. The anisotropy ranged from $\lambda \approx 1.43$ for the coarser cell foam, to $\lambda \approx 1.23$ for the finer cell one. Because of the way this particular type of foam is manufactured, variation of cell size within each foam was within a relatively narrow range. In addition, the five microstructures were found to scale with cell size (at least to a first order approximation). Cell ligaments have the characteristic three-cusp, Plateau borders cross-section. Their cross-sectional area was found to vary along the length increasing closer to the cell nodes.

9.1 Uniaxial Compression of Open-Cell Foam

Each of the five foams was compressed between rigid plates at prescribed displacement rates. Tests were performed along the rise and transverse directions. Along the rise direction the foams exhibit a force-displacement response shared with many other cellular materials. It starts with a nearly linear elastic regime; this terminates into a limit load followed by an extensive load plateau. The plateau is followed by a second branch of stiff response.

Because of the cell anisotropy, in the transverse direction the foams were found to be initially more compliant with the modulus being only 1/3 to 1/2 of the corresponding values in the rise direction. Interestingly, the nonlinear part of the response exhibited no load maximum and maintained a monotonically increasing trajectory.

The foams are polymeric and, as a result, they exhibit some viscoelastic characteristics and Mullins' effect. These time-dependent characteristics have been demonstrated but more work is required for a more complete characterization. Uniaxial tests on single ligaments showed that the base material also exhibits a mild nonlinearity.

A sequence of models for predicting all mechanical foam properties of interest has been developed. The foam is idealized to be periodic using the space filling Kelvin cell assigned the geometric characteristics found in the actual foams. The cells are elongated in the rise direction, the ligaments are assumed to be straight, to have Plateau border cross-sections and nonuniform cross-sectional area distributions. The ligaments are modeled as shear-deformable extensional beams. The base material is assumed to be linearly elastic. A special provision is made to account for the way their intersections at the nodes affect the relative density of the model.

9.2 Elastic Constants

Closed form expressions have been developed for all elastic constants of the anisotropic foams by analyzing custom microsections. A characteristic cell of the anisotropic microstructure has also been established. This was discretized with appropriate shear-deformable beam elements. Numerical results derived from the characteristic cell loaded appropriately, were shown to be in agreement with the analytical expressions for the elastic moduli. The axial moduli of the foams used in the experiments are calculated individually. Comparison between measurements and predictions is very favorable.

Based on the results presented, it can be concluded that the Kelvin cell model developed is capable of capturing the initial elastic behavior of the foams analyzed. The results show that the following factors included in the models are important in matching measured constants to predicted values:

a. Membrane deformations of the beams.
b. Shear deformability of the beam.
c. The Plateau border cross-sectional shape and its nonunifomity along the ligament length.
d. Correct accounting of the material distribution at the nodes.

9.3 Onset of Instability

Under compression the Kelvin foam response becomes progressively nonlinear because of ligament bending. The stiff part of the response is terminated by an instability. The onset of the instability was established numerically using models involving either a single or stacks of fully periodic characteristic cells. In the rise direction the critical state involves a long wavelength mode whereas in the transverse direction the mode is local to the cell. Isotropic foams exhibit long wavelength buckling modes. The critical stresses calculated for the five foams tested follow the same trends as the measured limit stresses recorded in the rise direction and the stresses corresponding to the first knee of the transverse direction responses. However, they are higher than both sets of measurements by about a factor of 2. A parametric study of the critical stress revealed it to be a power-law function of the geometric parameter r_o/ℓ. The exponent varied with the degree of anisotropy ranging between 3.81 for the isotropic case and 3.88 for $\lambda = 1.4$. Selected calculations in which the foam was discretized with solid FEs instead, yield 20-30% lower critical stresses. This model was not pursued further because it was unduly computationally expensive.

The complexity of such microstructures requires that bifurcation checks, involving increasingly larger domains with multiples of the characteristic cell, be made in order to identify the prevalent buckling modes. These include modes local to the cell, others involving several cells and others involving many cells. This process can be automated by using Bloch wave theory to establish the critical states. In this thesis a method based on Bloch wave theory developed by Triantafyllidis and co-workers has been tailored to the present microstructure. The method was then used to find the critical states of such foams under uniaxial and a set of triaxial loadings. A rich variety of buckling modes were identified which were shown to be affected by the foam anisotropy and the mutliaxiality of the applied loads.

9.4 Crushing of Foams

Postbuckling calculations were conducted involving fully periodic microsections with initial imperfections corresponding to the mode of the respective critical stress. In the rise direction such a response exhibits a limit load, which is shown to be imperfection sensitive. Calculations involving realistic imperfection amplitudes yield limit stresses that are much closer to the initiation stresses measured in the five foams tested. The presence of a limit stress in the response as well as the long wavelength buckling mode are in agreement with experimental observations.

Similar imperfect cell postbuckling calculations for the transverse direction yield monotonically increasing responses for all values of anisotropy considered ($1 < \lambda \leq 1.4$). The monotonicity of the response as well as the absence of the long wavelength buckling modes is consistent with transverse direction experimental observations.

The presence of a limit load in the rise direction response of fully periodic microsections indicates that, if some of the periodicity constrains are relaxed, localized deformation may develop. To this end finite size microsections with two lateral sides free were analyzed. Localized collapse develops soon after attainment of the limit load. In the foams tested, localized cell crushing is arrested by contact between the ligaments of the buckled cells. In the model, contact is approximated by limiting the amount a cell can collapse in the direction of the applied load. This scheme arrests local collapse and causes it to spread to neighboring material at a nearly constant stress level as in the experiments. The stress picks up again when the whole domain is crushed (densification stage). The extent of the stress plateau is governed by a parameter of the pseudo-contact scheme used.

The crushing stress can also be established from the local response of the fully periodic column of cells. Inclusion of cell ligament contact results in an up-down-up response. This response results in crushed configurations similar to those produced via the computationally more elaborate finite width model. In view of this similarity in the final configurations, an energy balance type argument results in the Maxwell stress which is then associated with the crushing stress.

In conclusion, the results show that the idealized Kelvin cell foam assigned several of the geometric characteristics of the foams tested reproduces some features of the compressive responses well quantatively and others qualitatively. The initial elastic properties of the anisotropic foam were shown to be reproduced by the model quite well. The two types of behavior observed in the rise and transverse directions are consistent with experimental observations.

9.5 Triaxial Compression of Kelvin Cell Foam

The response and stability of Kelvin cell foams under triaxial loads was also analyzed. The results were used to develop failure envelopes for foams with varying anisotropy values in the $\sqrt{3J_2} - I_1$ and $\sigma_{1C} - \Sigma_C$ planes. The envelopes corresponding to the isotropic foam were found to enclose (nearly) those of anisotropic foams. For loading states involving relatively small axial stresses (and J_2) in the rise direction, the critical buckling modes were found to be local to the characteristic cell. For loading states involving relatively high axial stresses (and J_2) in the same direction the prevalent buckling modes had long wavelengths. In the transition between the two regimes criticality was associated with buckling modes involving domains of a few cells. For all cases examined, long wavelength modes exhibited unstable postbuckling behavior leading to localization. Modes local to the characteristic cell, or those involving domains of a few cells, were found to have stable postbuckling responses. This richness in buckling modes is a complexity, which required the automated bifurcation check procedure provided by the Bloch wave method.

9.6 Future Work

In the present study the foam microstructure was idealized to be fully periodic by adopting the Kelvin cell. Real foams have an irregular microstructure. Despite this idealization, measured and calculated axial elastic moduli were found to be in good agreement. This indicates that the moduli are not very sensitive to the exact geometry of the microstucture. On the other hand, the onset of instability is presently about a factor of two higher than the limit loads measured experimentally. We showed that the limit load induced by buckling is imperfection sensitive. To first order the microstructure disorder can be viewed as a geometric imperfection which will contribute to the difference between present predictions and measurements. Thus, the effect of cell morphology on the foam stability requires a more careful examination.

Due to the complexity of the problem, the base material in the numerical model is simply assumed to be linearly elastic. In fact, the base material of the five foams tested in this study shows obvious viscoelastic behavior (e.g., Figure 1.2 and Figure 3.7a). Future extensions of this class of models must also account for this type of rate dependence of the base material. Accounting for viscoelastic effects should also enable examination of the foam response to impact loading.

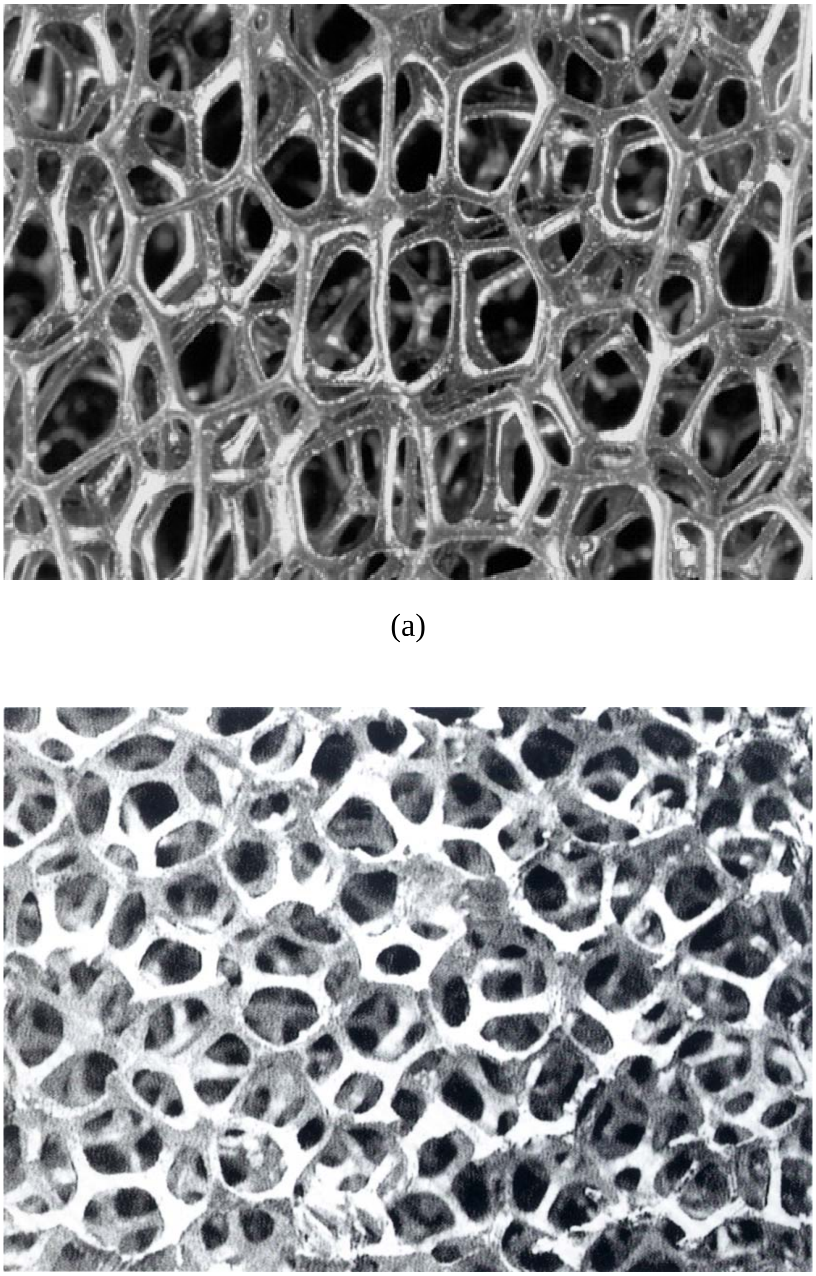

(a)

(b)

Figure 1.1 Synthetic foams manufactured from various materials: (a) polyester urethane; (b) aluminum.

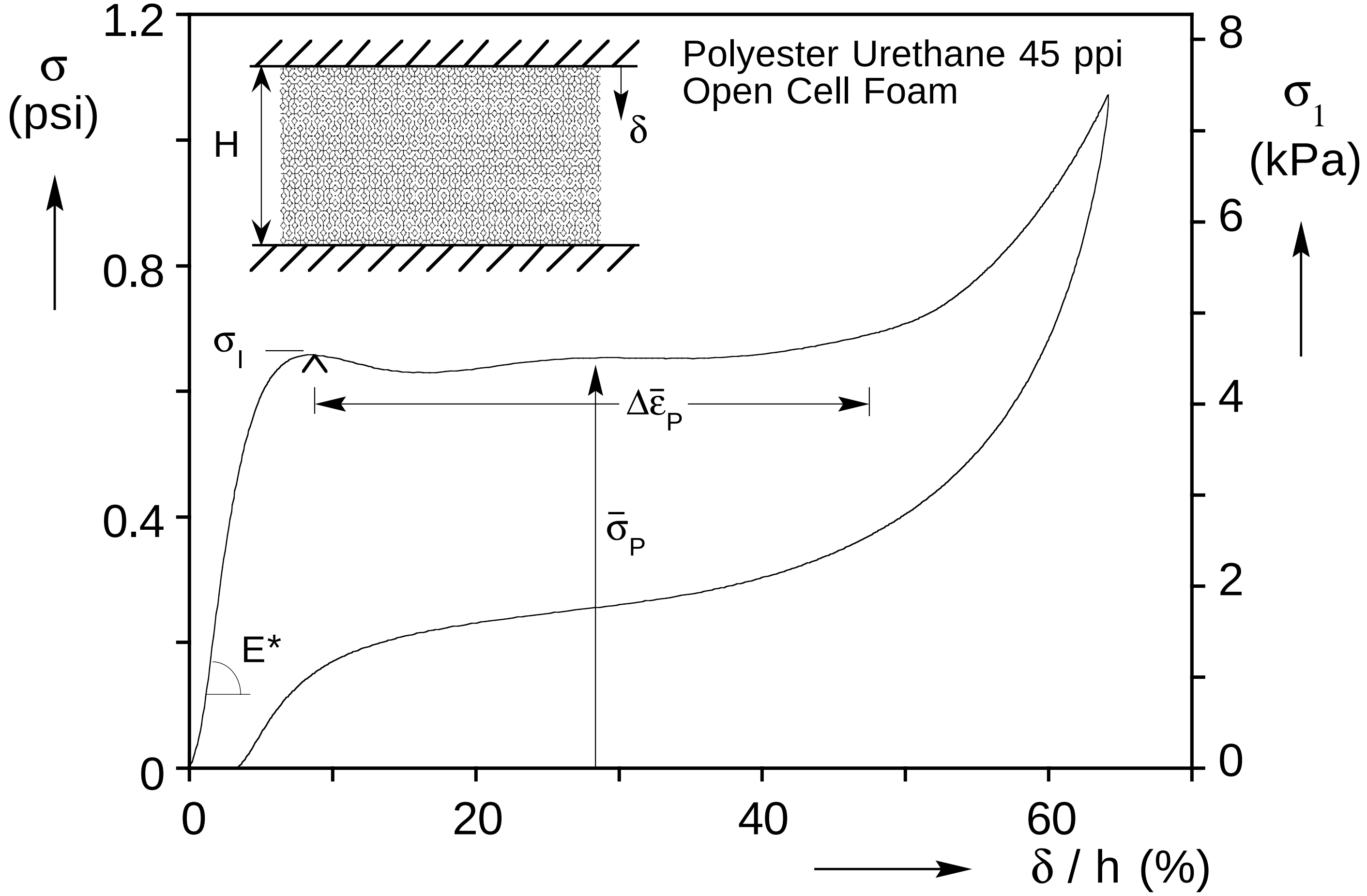

Figure1.2 The compressive response in the rise direction of open-cell foam

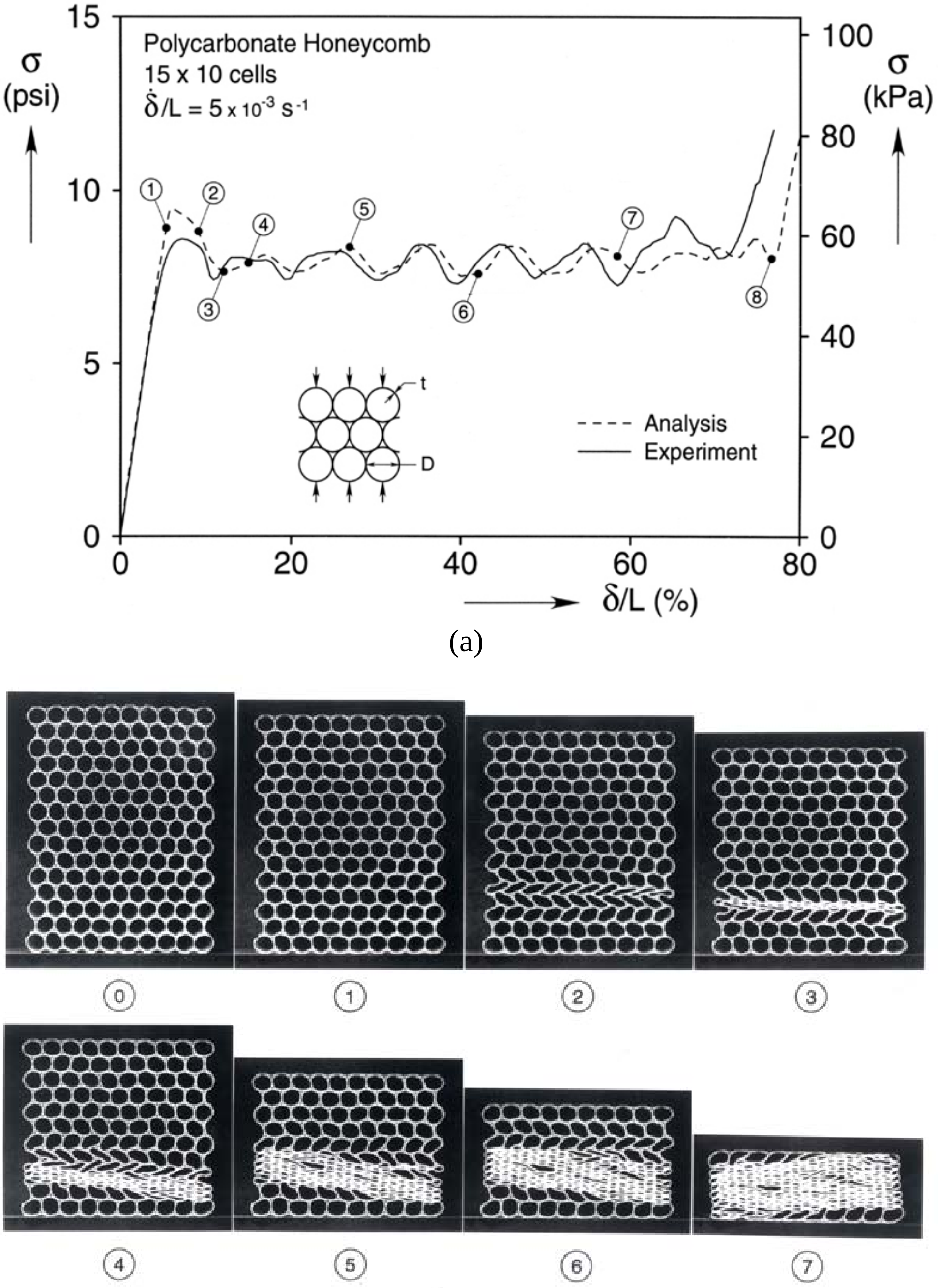

(a)

(b)

Figure 1.3 (a) Force-displacement crushing response of polycarbonate honeycomb. (b) Sequence of deformed configurations corresponding to response in Figure 1.3a.

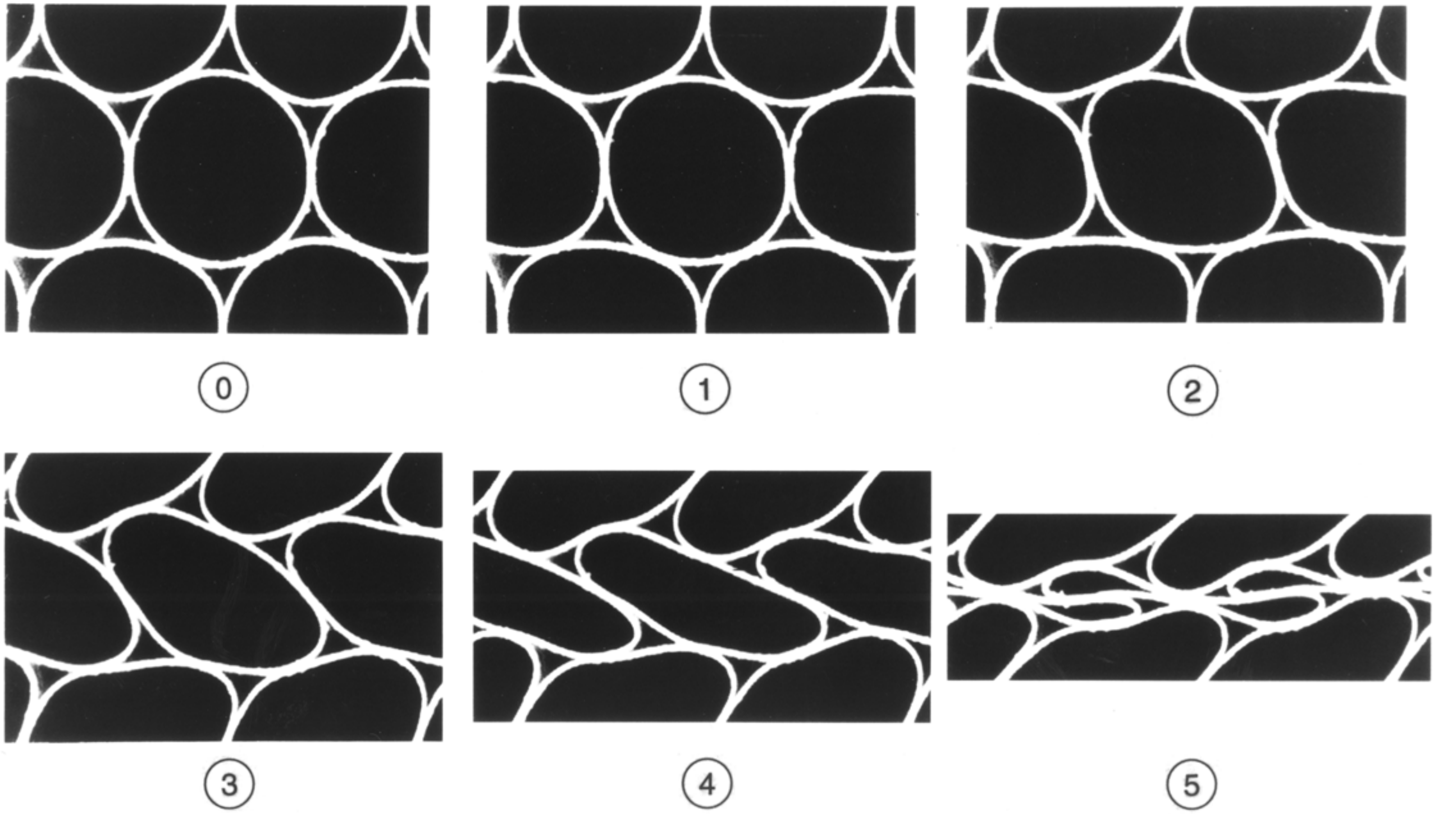

Figure 1.4 Sequence of collapse configurations of a honeycomb cell

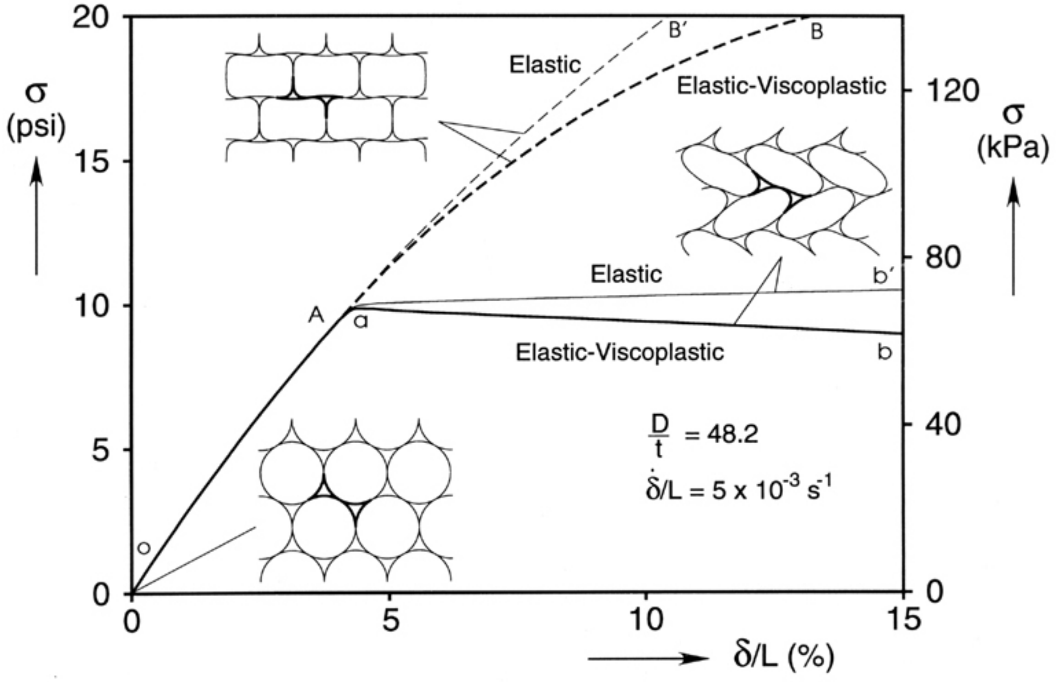

Figure 1.5 Calculated prebuckling and initial postbuckling response of elastic and elastic-viscoplastic microsections.

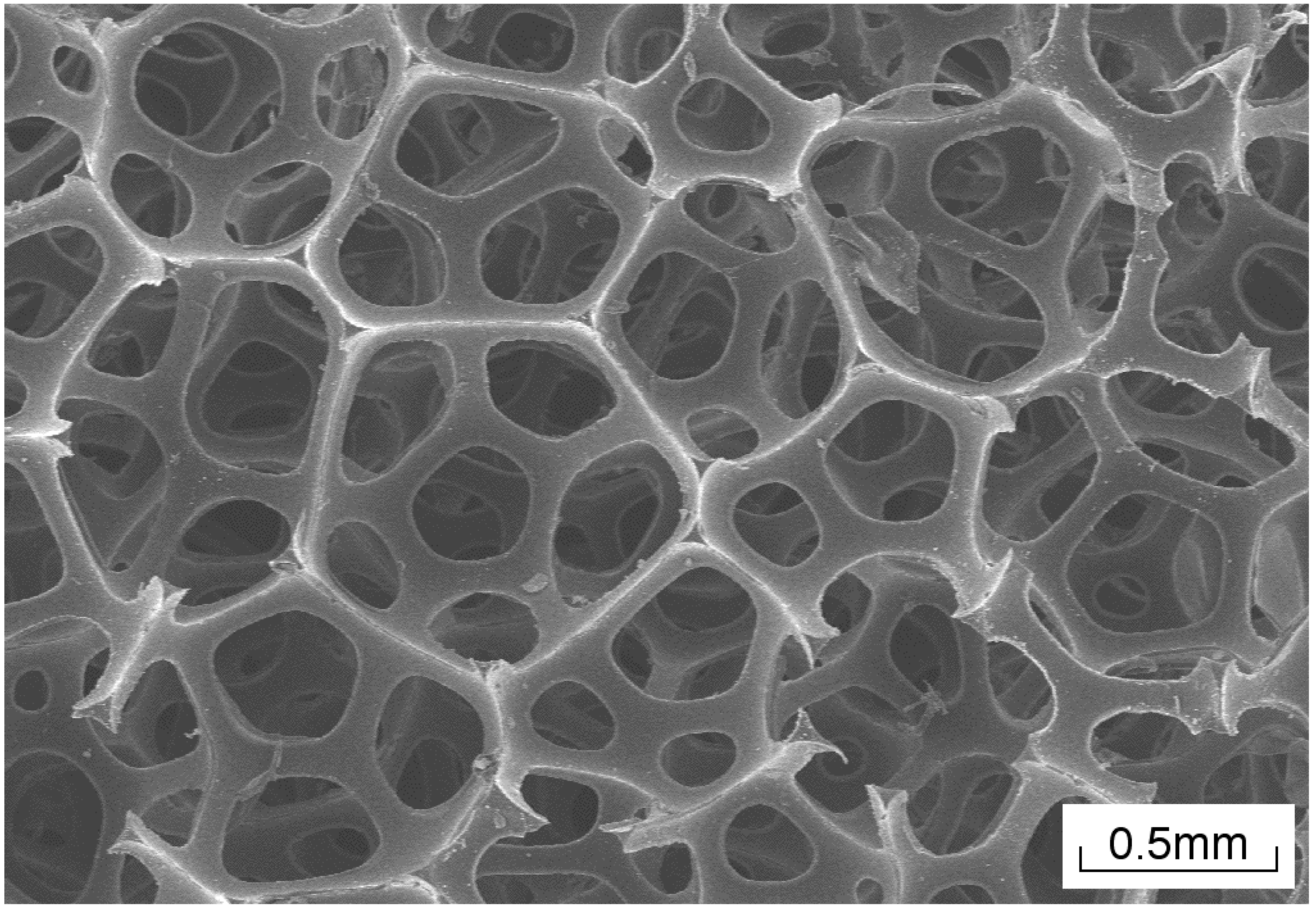

Figure 2.1 Micrograph showing cellular microstructure of a polyester urethane foam (100 ppi)

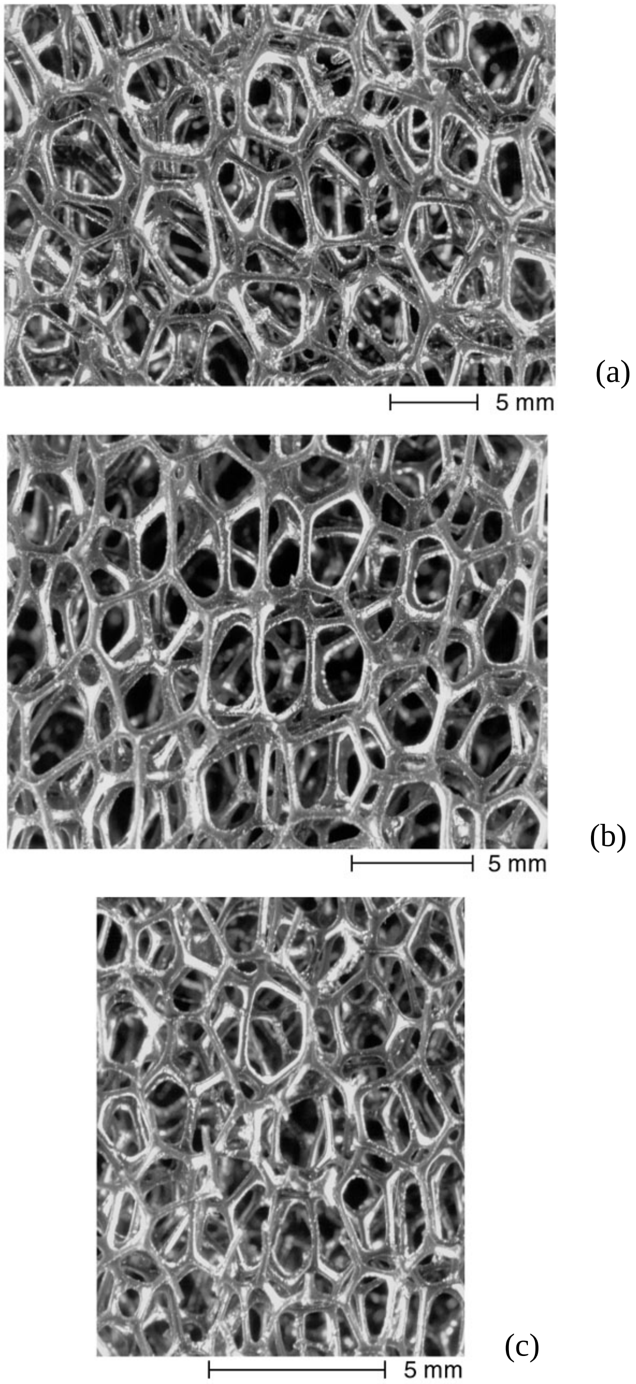

Figure 2.2 Photomicrographs showing side views of 3 different size cells: (a) 3 ppi,(b) 10 ppi and (c) 45 ppi.

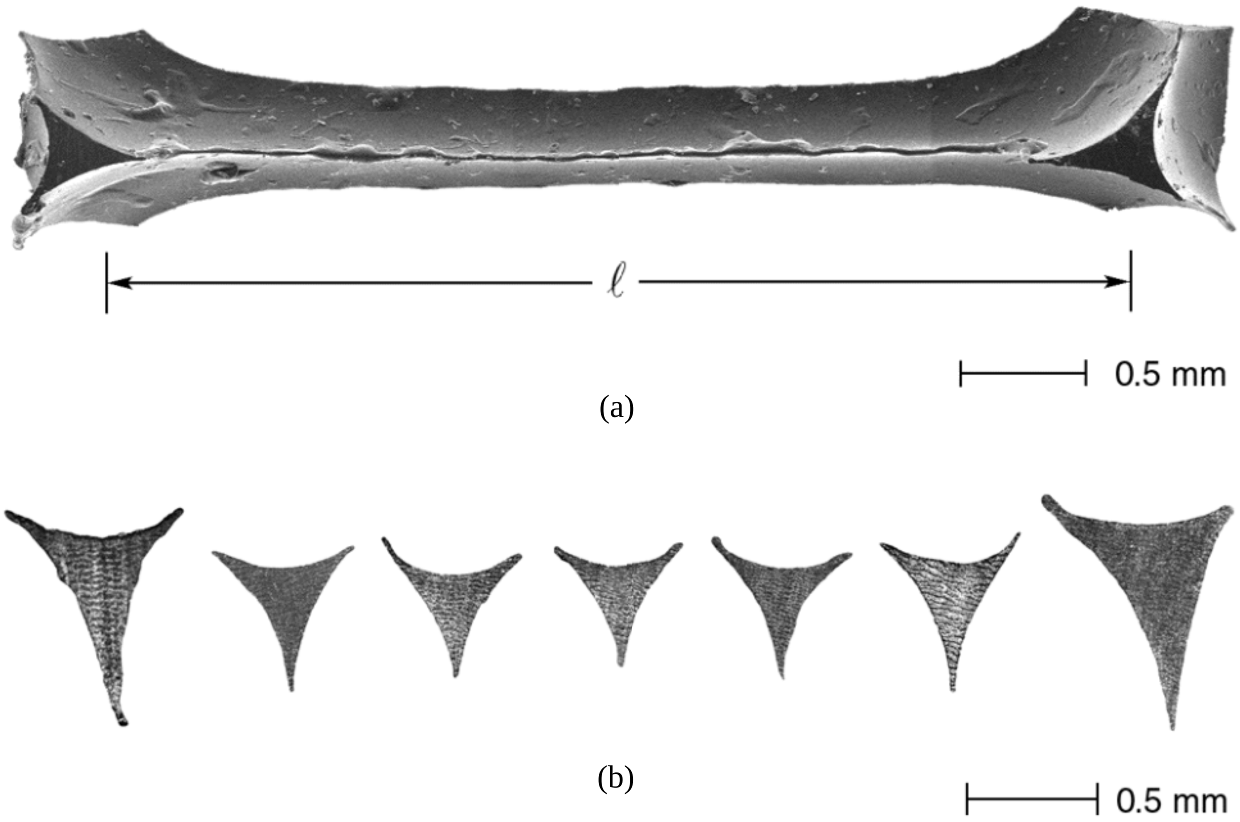

(a)

(b)

Figure 2.3 (a) A typical foam ligament and (b) cross sections taken along its length.

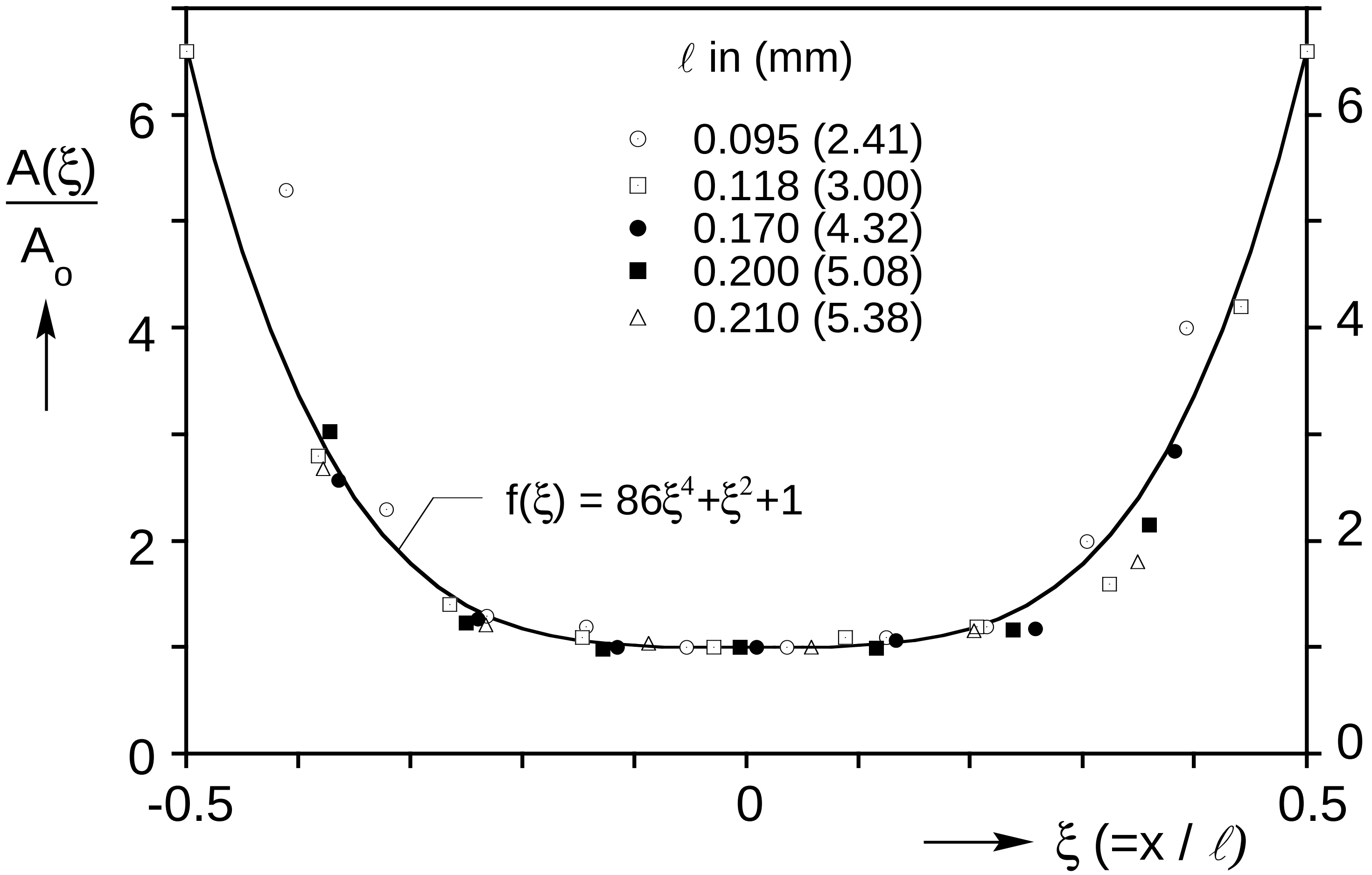

Figure 2.4 Measured variation of ligament cross sectional area along its length fitted with function $f(\xi)$.

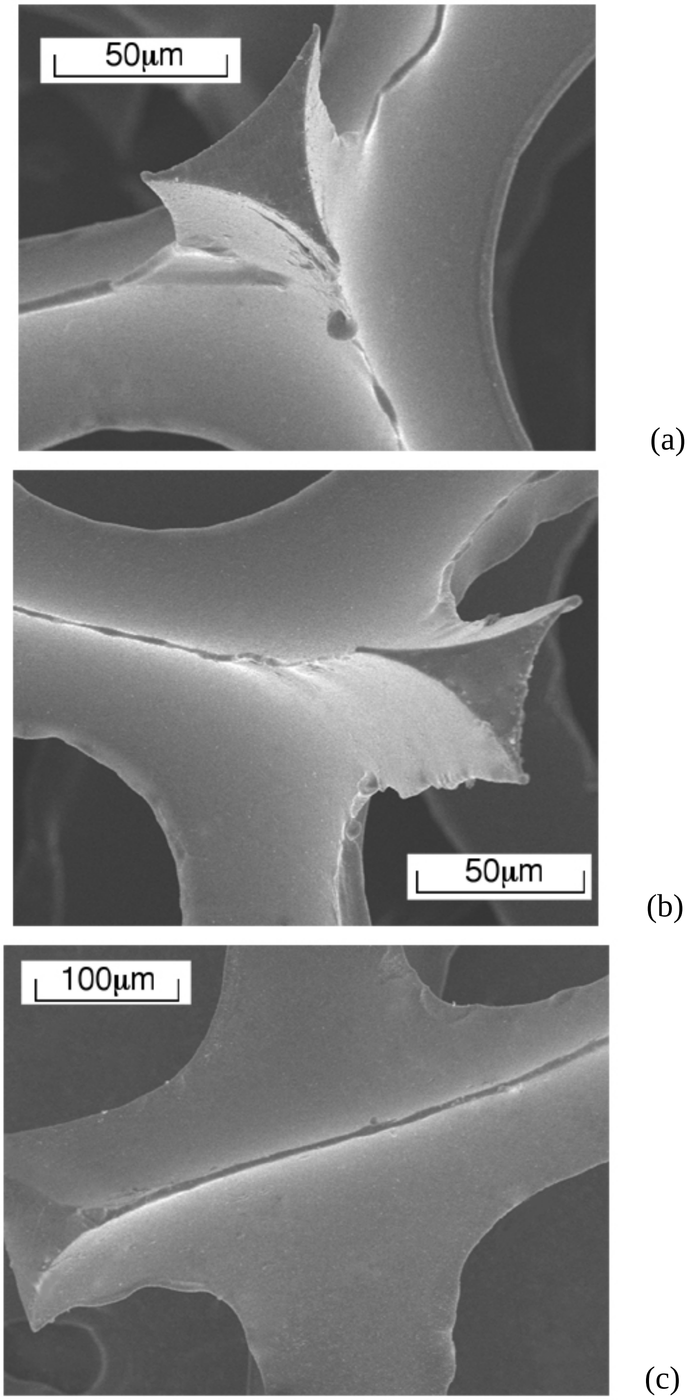

Figure 2.5 Micrographs show three four-ligament foam nodes.

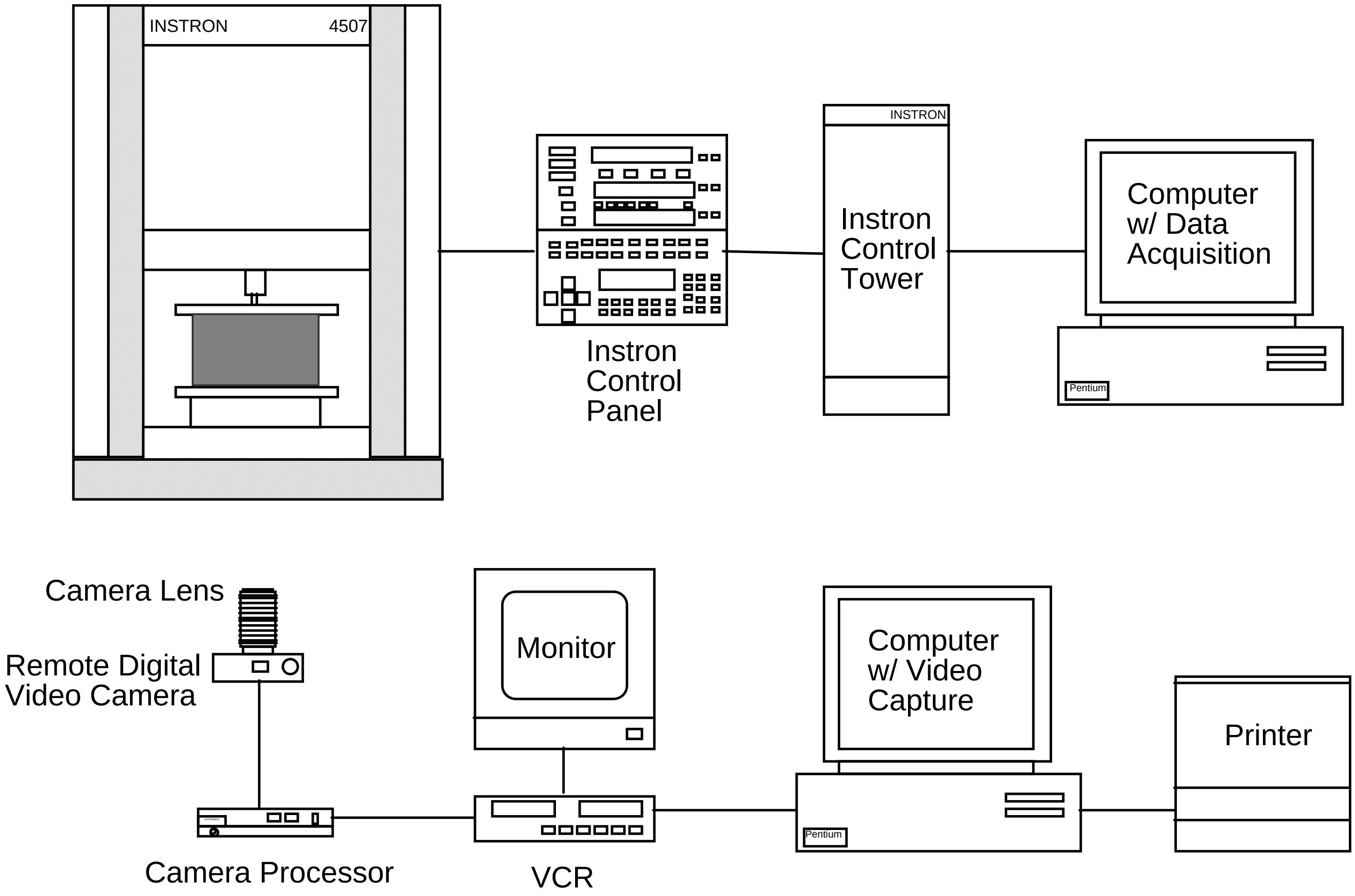

Figure 3.1 Schematic of experimental setup and data acquisition systems

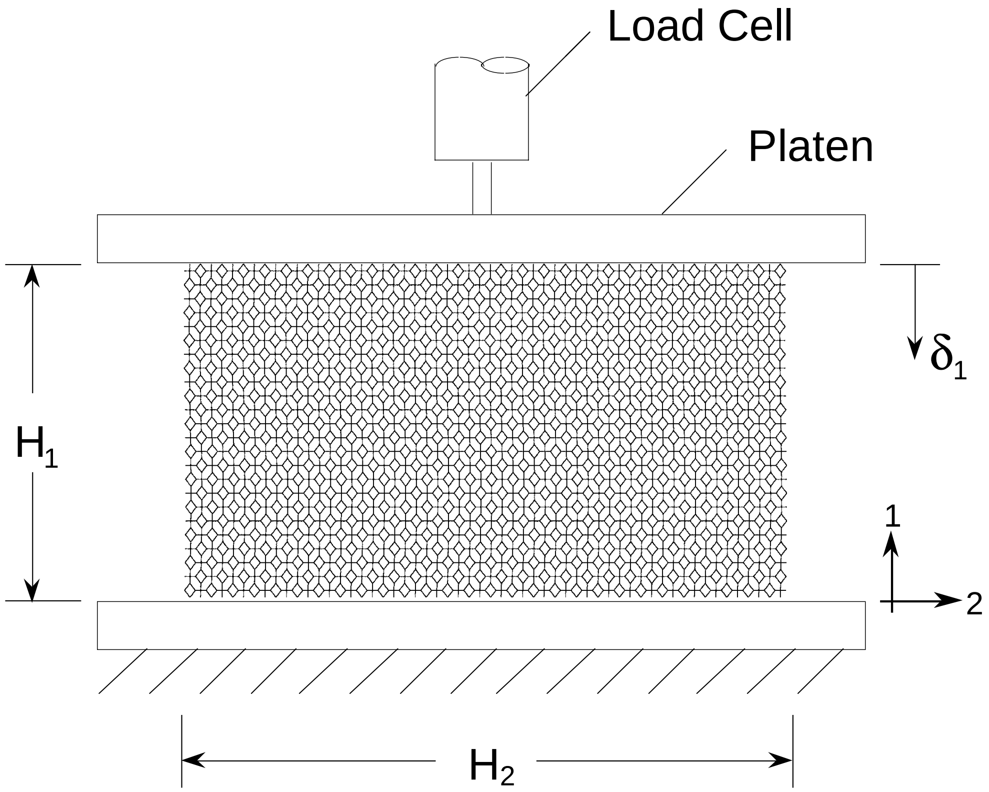

Figure 3.2 Size of reticulated polyester urethane foams under compression experiments

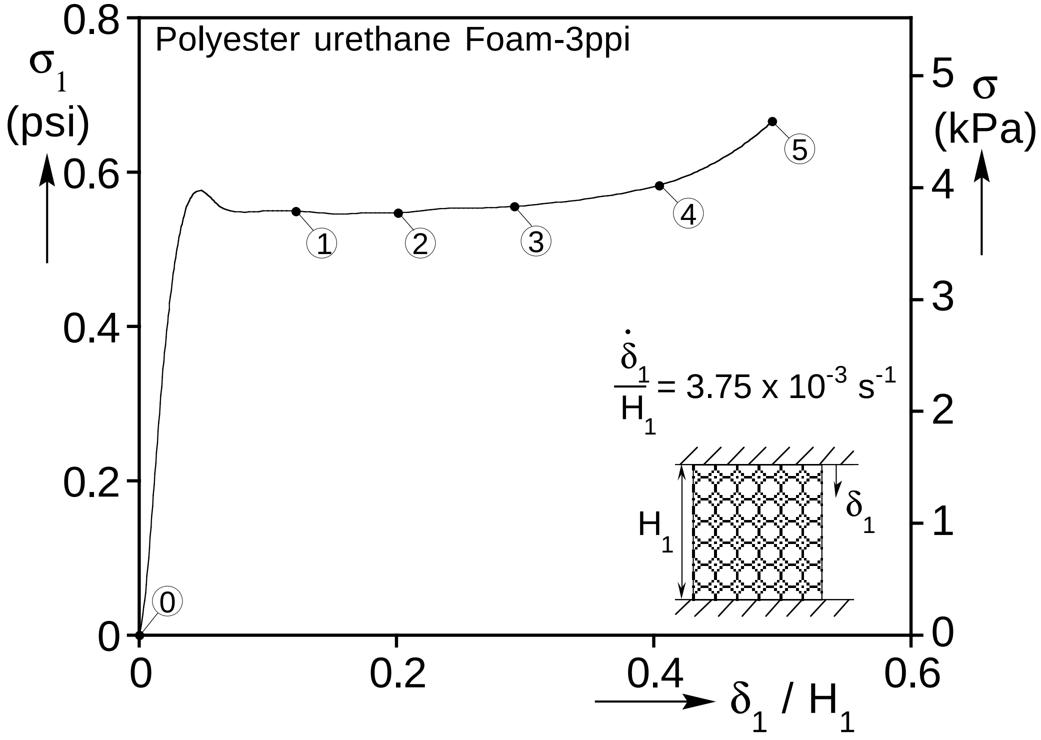

Figure 3.3 (a) Rise direction compressive stress-displacement response from 3ppi foam.

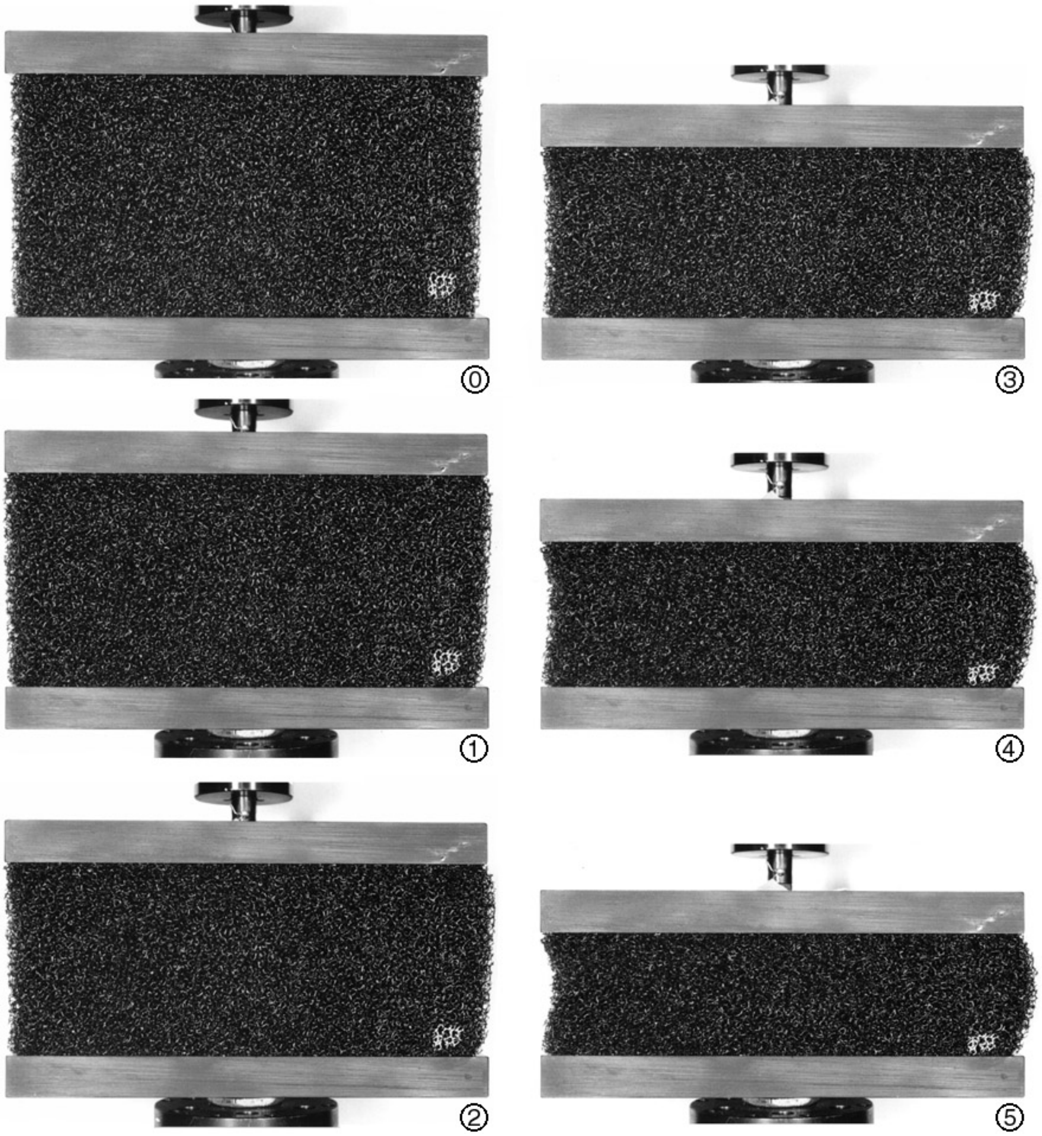

Figure 3.3 (b) The deformed configurations corresponding to the response in Figure 3.3(a)

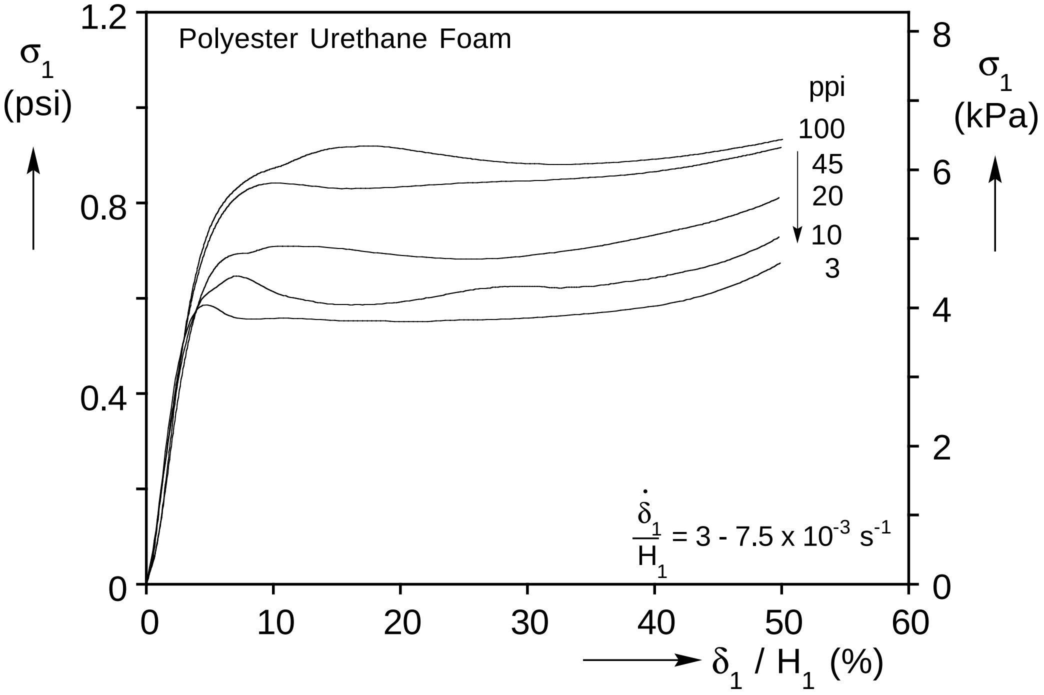

Figure 3.4 Comparison of rise direction compressive stress-displacement responses from foams of five cell sizes.

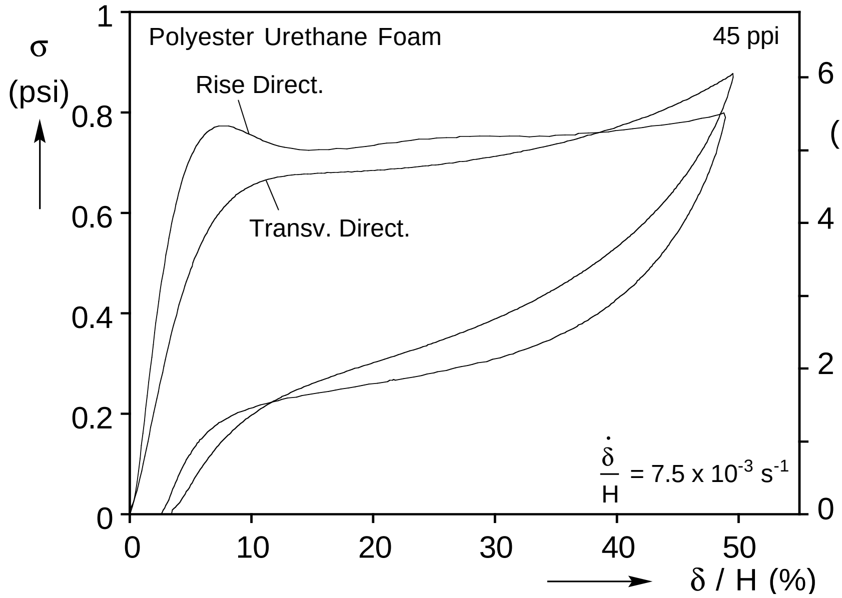

(a)

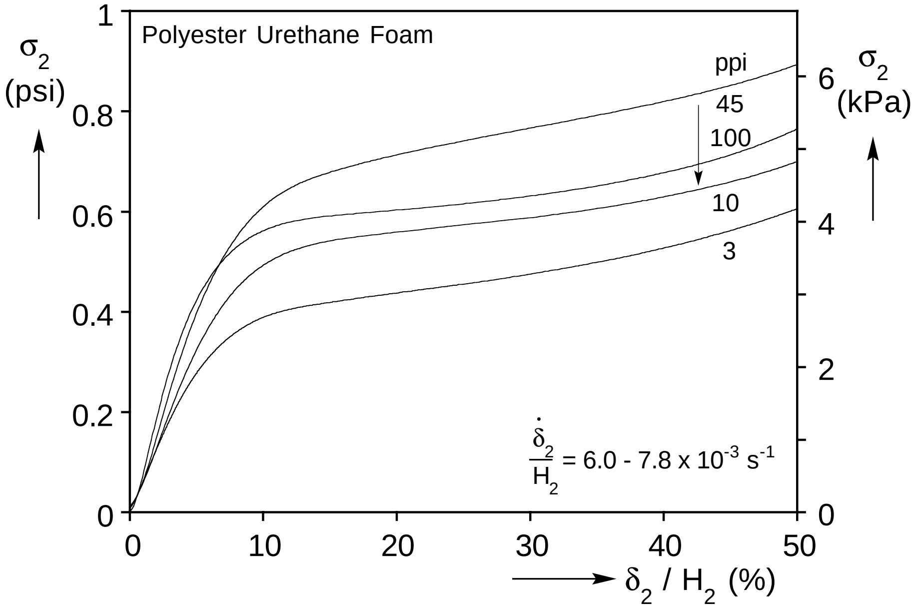

(b)

Figure 3.5 (a) Comparison of rise and transverse direction compressive responses of 45ppi foam. (b) Comparison of transverse direction compressive stress-displacement responses from foams of four cell sizes.

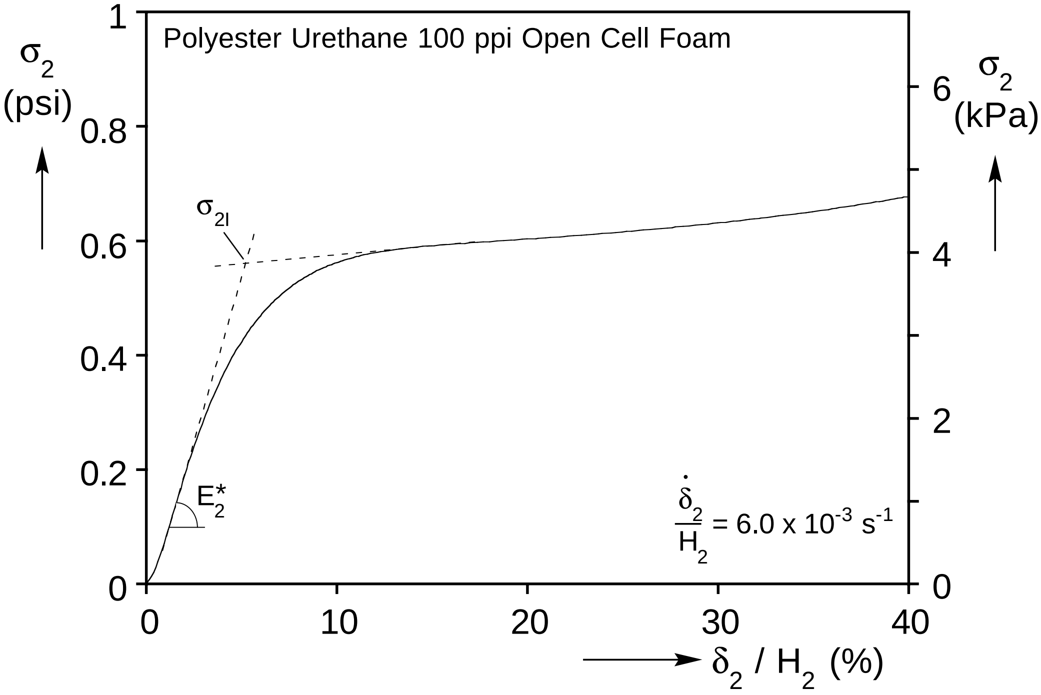

Figure 3.6 Definition of initiation stress for transverse direction responses.

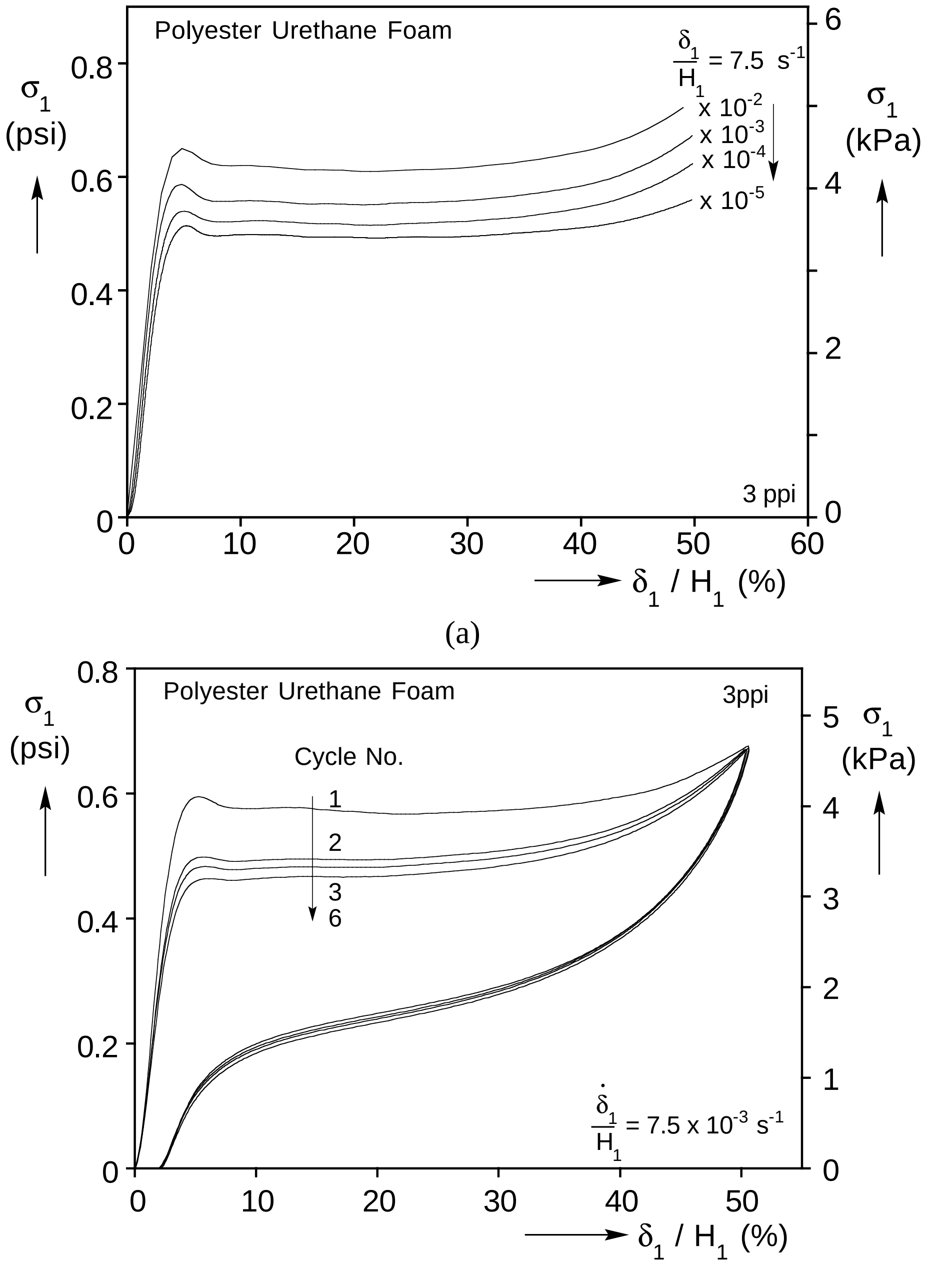

(a)

(b)

Figure 3.7 (a) Effect of crushing rate to compressive response of 3 ppi foam.
(b) Compressive $\sigma - \delta/H$ responses of 3 ppi foam (5 minute rest time allowed between each load cycle).

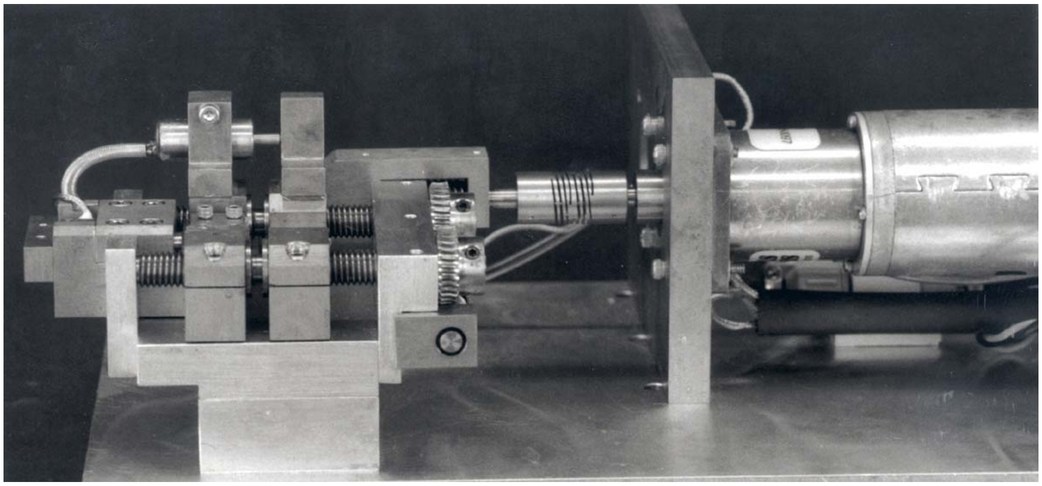

(a)

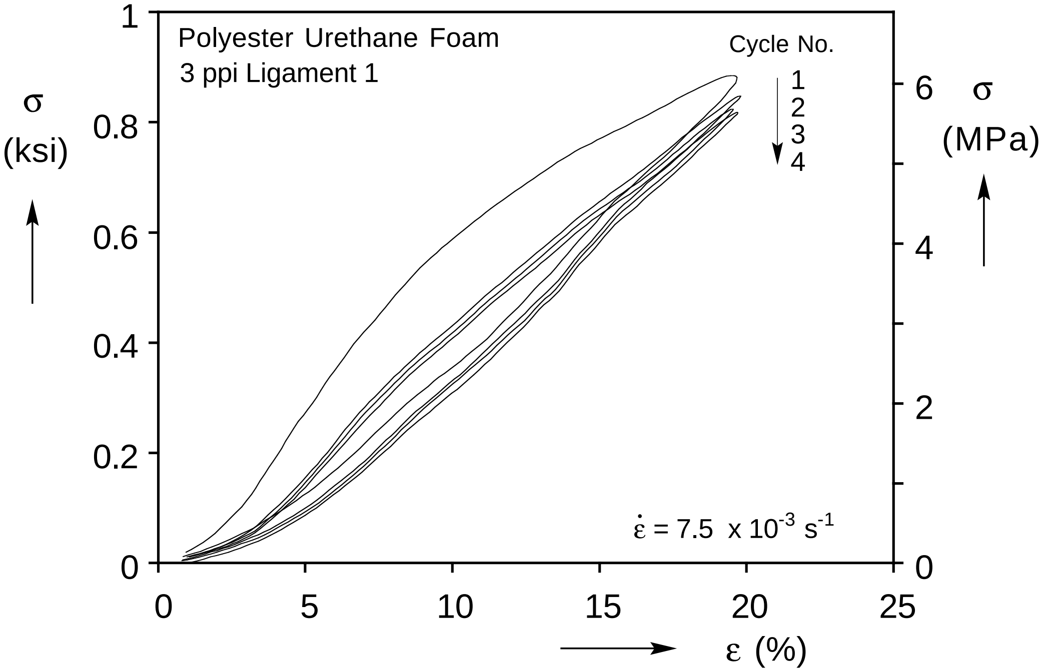

(b)

Figure 3.8 (a) Ligament uniaxial stress-strain testing stage. (b) Uniaxial stress-strain responses measured in ligament 1 (5 minute rest time allowed between each load cycle).

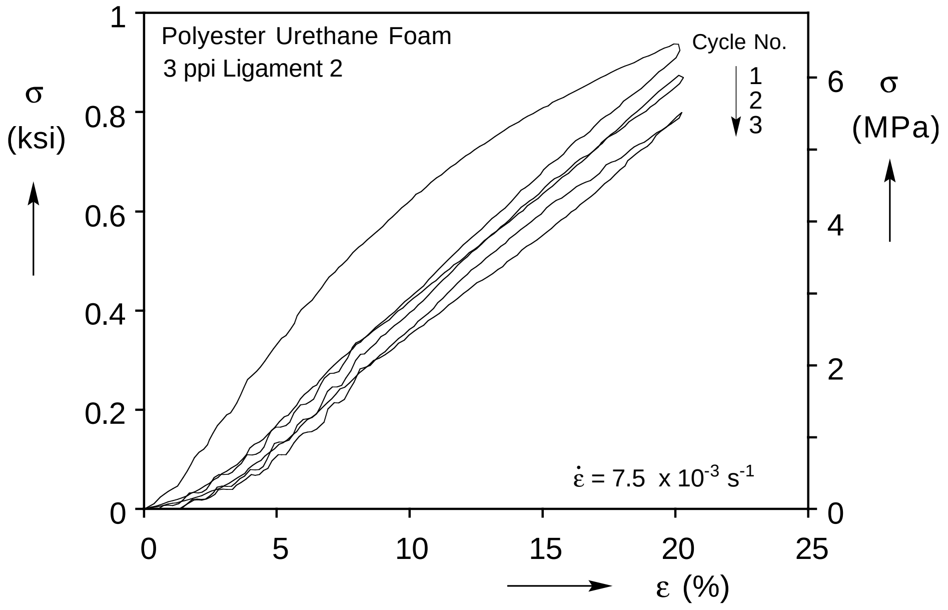

(c)

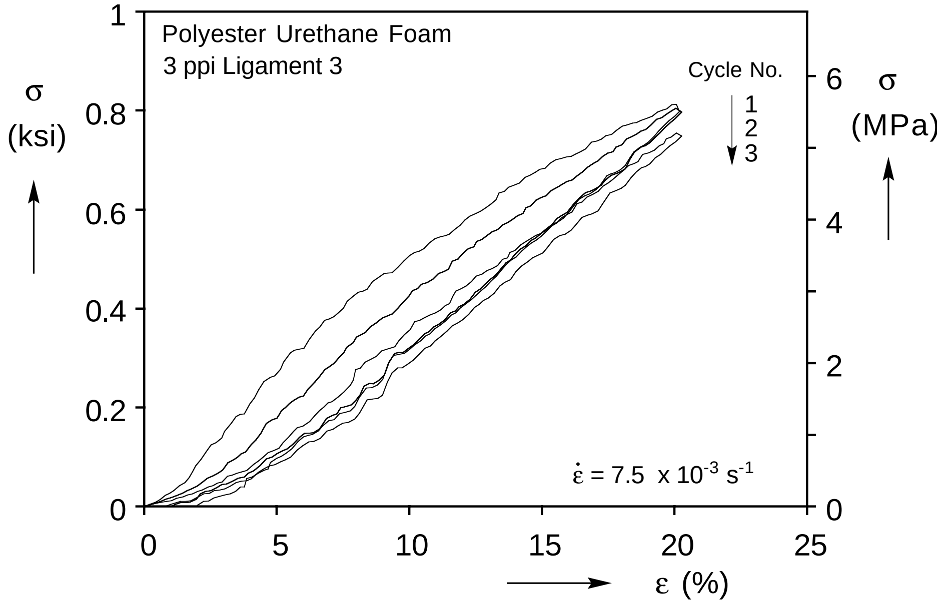

(d)

Figure 3.8 (c) Uniaxial stress-strain responses measured in ligament 2.
(d) Uniaxial stress-strain responses measured in ligament 3.

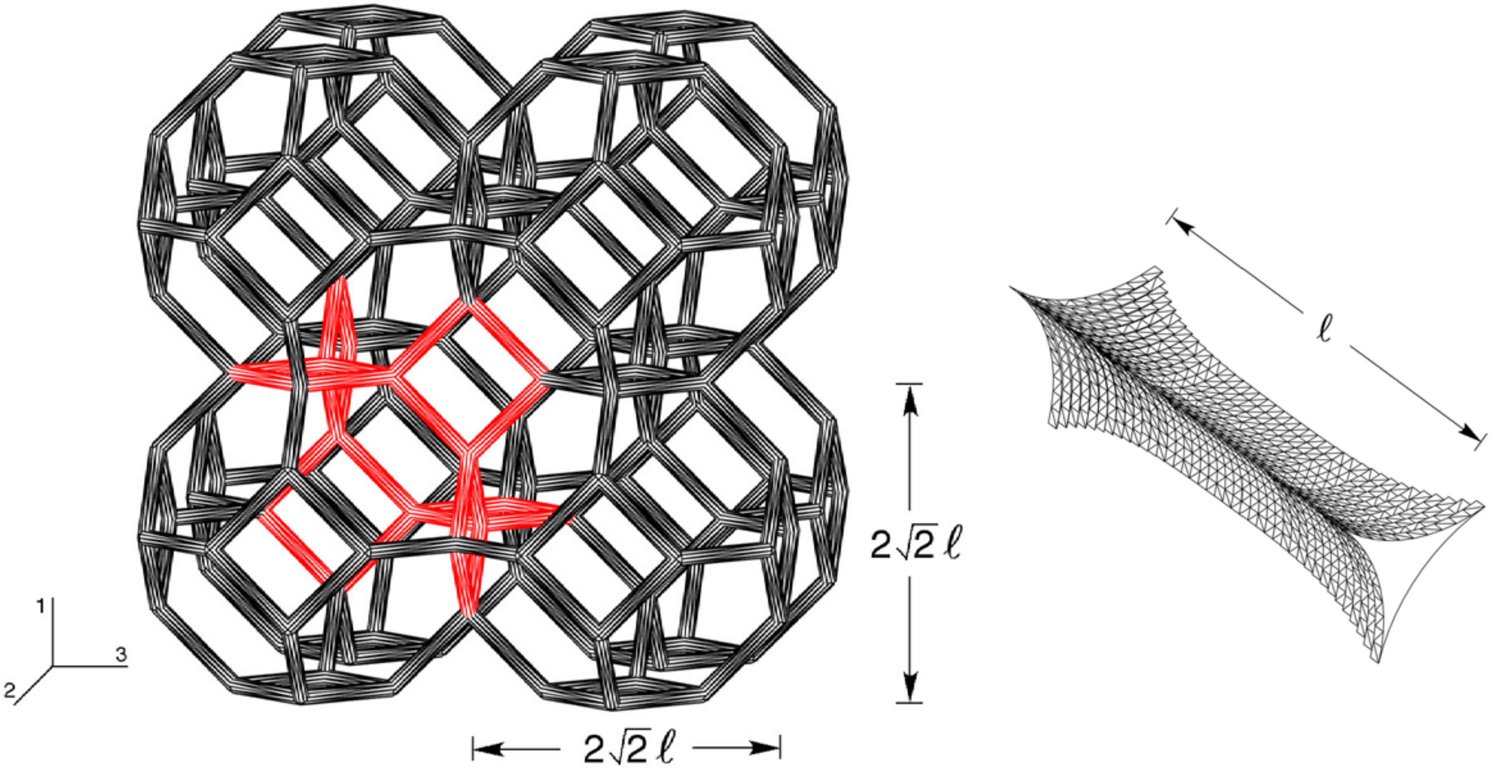

(a)

(b)

Figure 4.1 (a) Cluster of 14-sided Kelvin cells. (b) Geometry of foam ligaments.

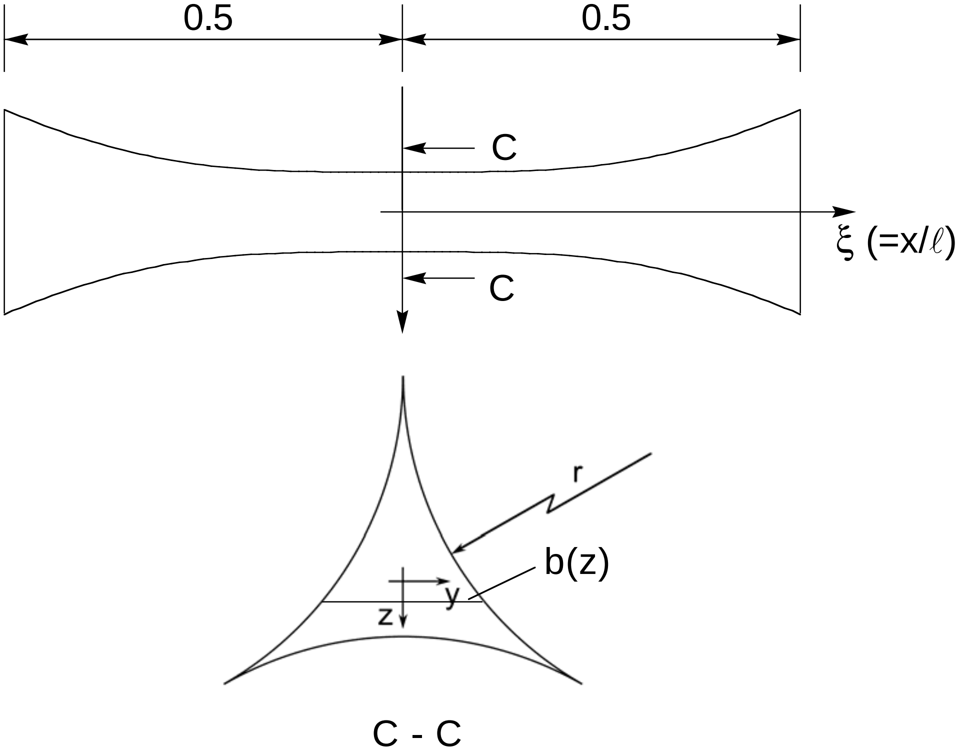

Figure 4.2 Definition of geometry of foam ligaments.

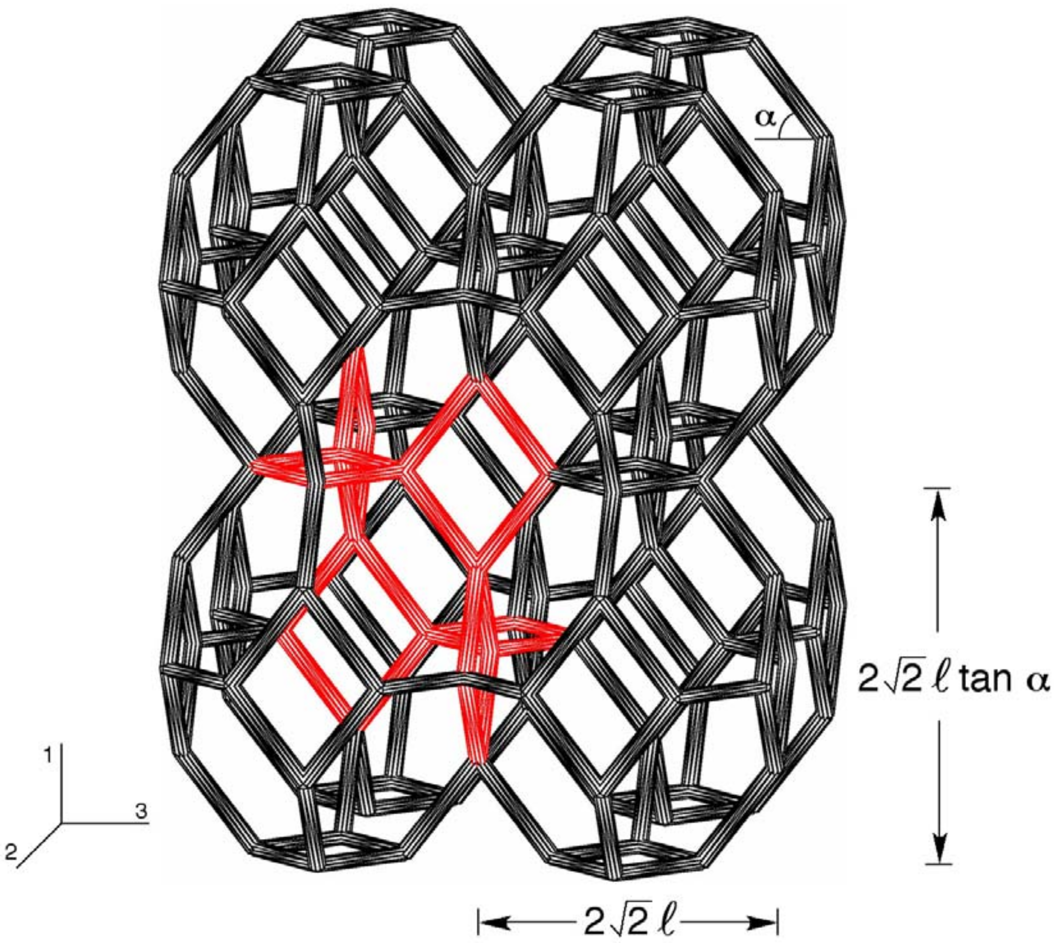

Figure 4.3 Cluster of anisotropic Kelvin cells.

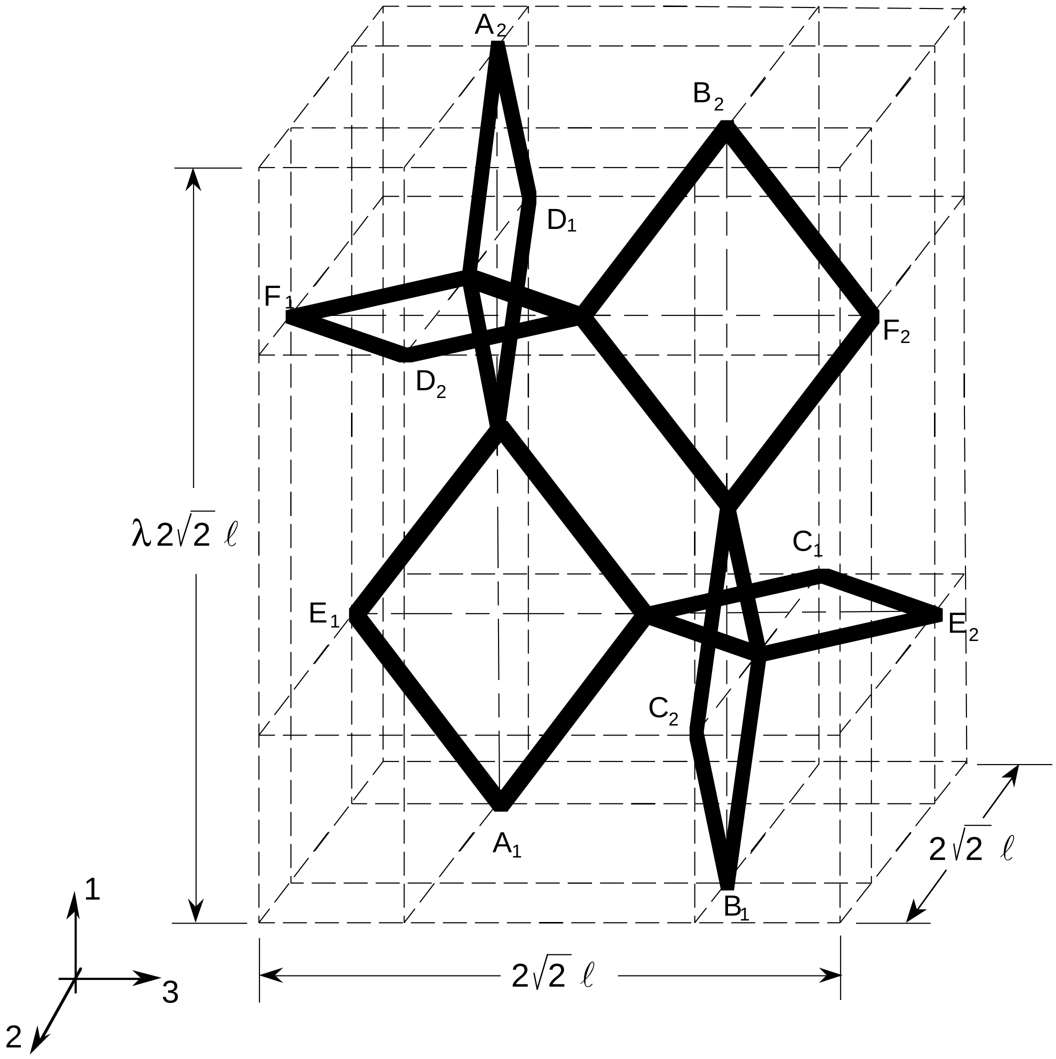

Figure 4.4 The Kelvin foam characteristic cell.

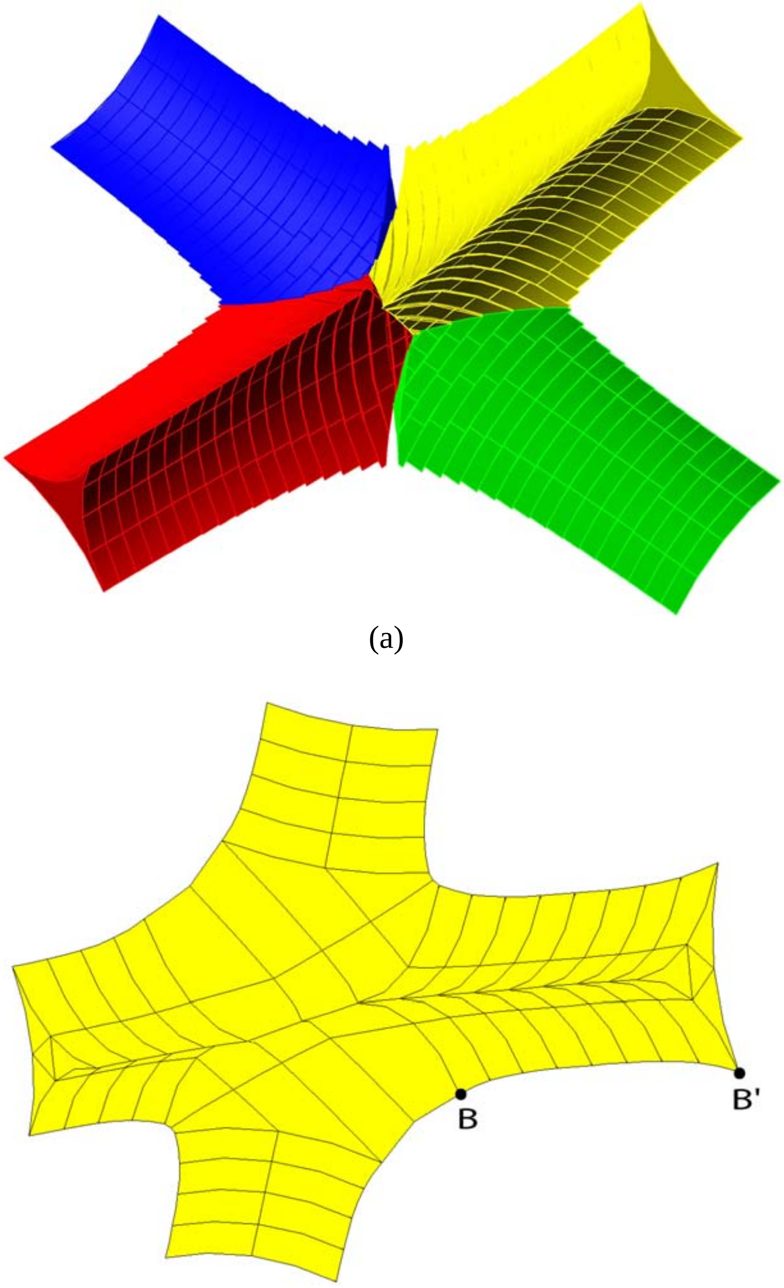

(a)

(b)

Figure 4.5 (a) Kelvin cell node of four converging beam ligaments with intersecting material removed. (b) Same node as represented by solid FEs.

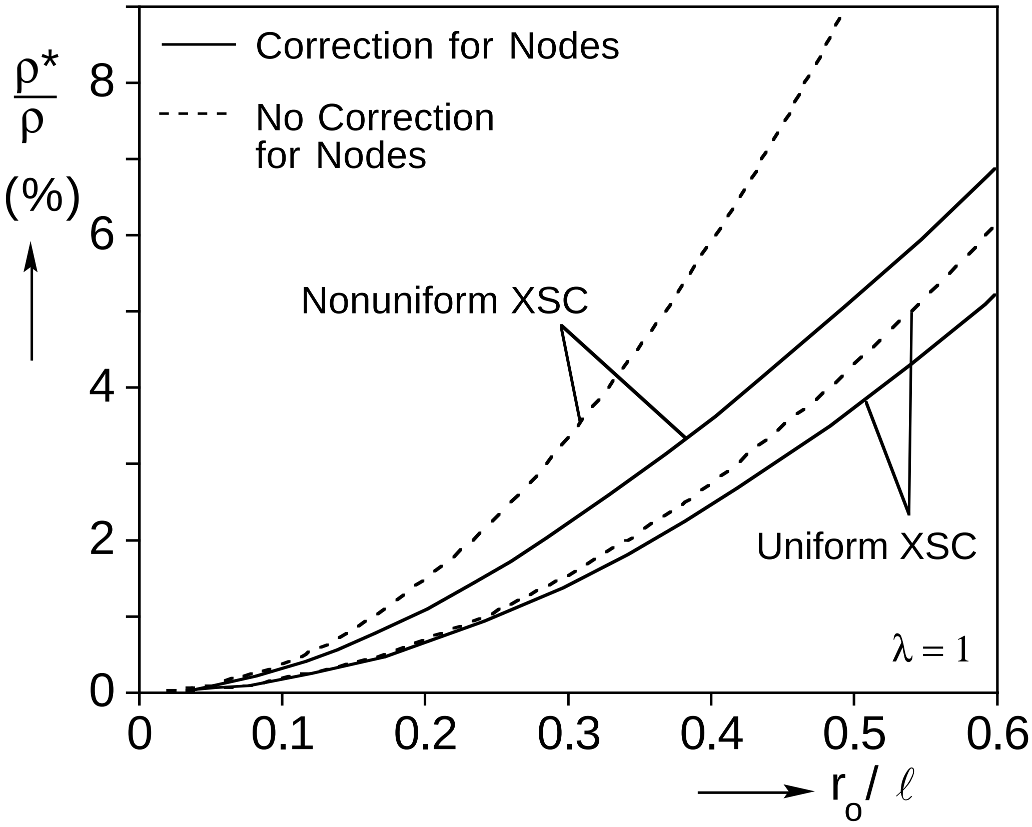

Figure 4.6 Relative density vs. r_o/ℓ for Kelvin cells with and without the correction for the material at the nodes.

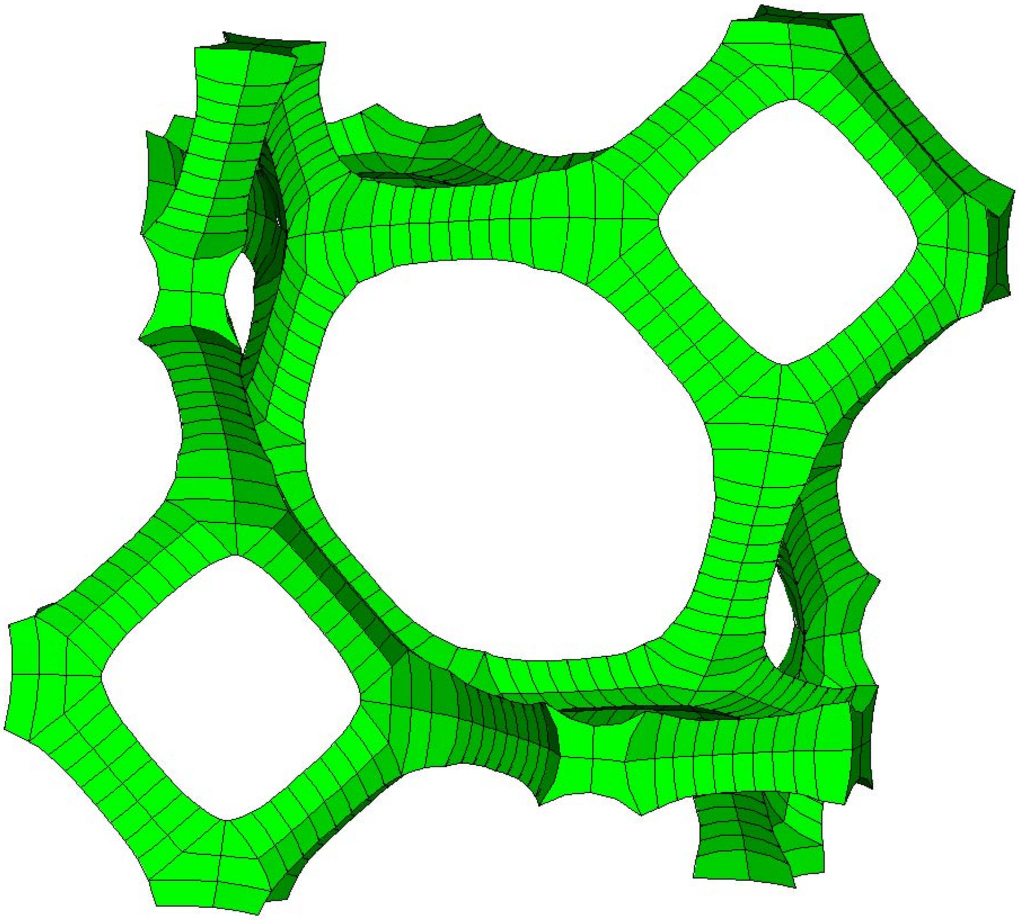

Figure 4.7 The solid element model of a Kelvin foam characteristic cell.

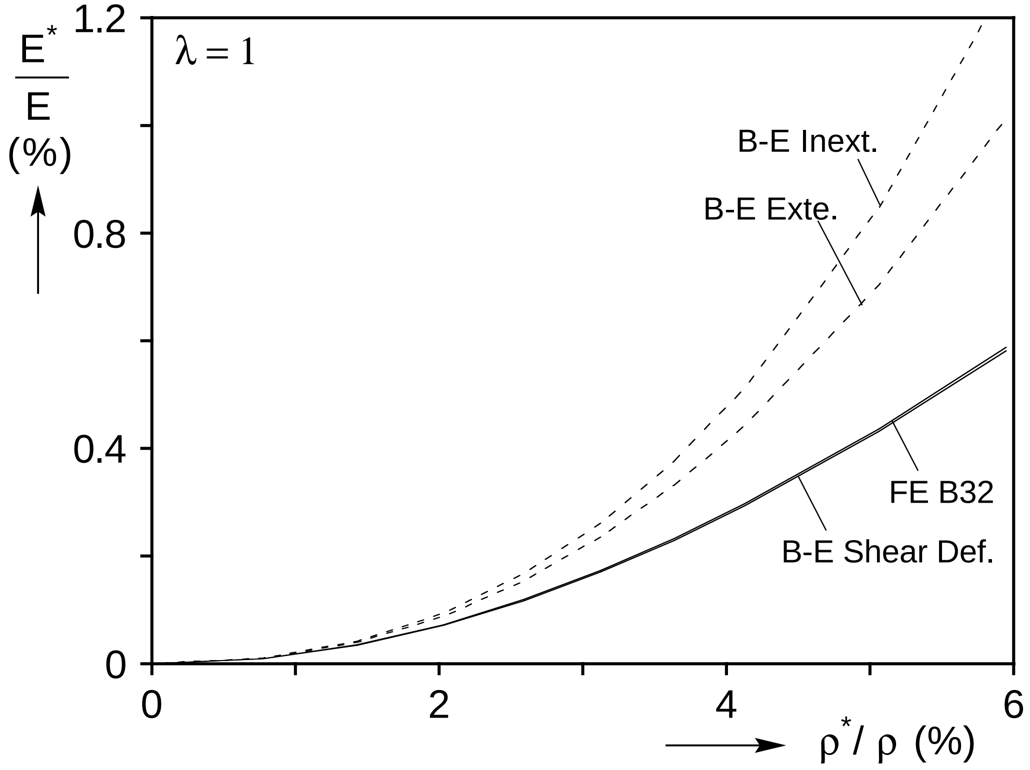

Figure 4.8 Axial moduli vs. relative density calculated by different beam model assumptions.

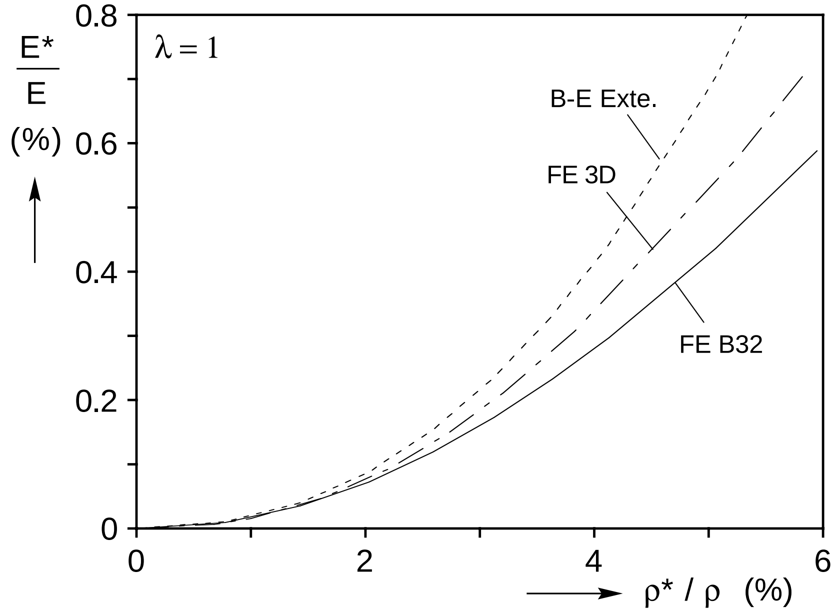

(a)

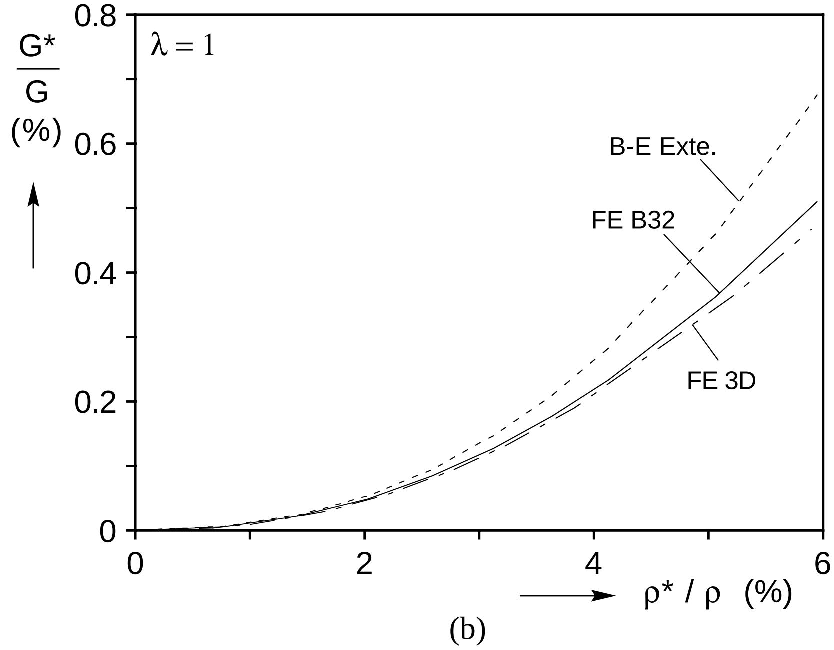

(b)

Figure 4.9 Moduli vs. relative density calculated by beam models and the solid element model. (a) Axial modulus and (b) shear modulus.

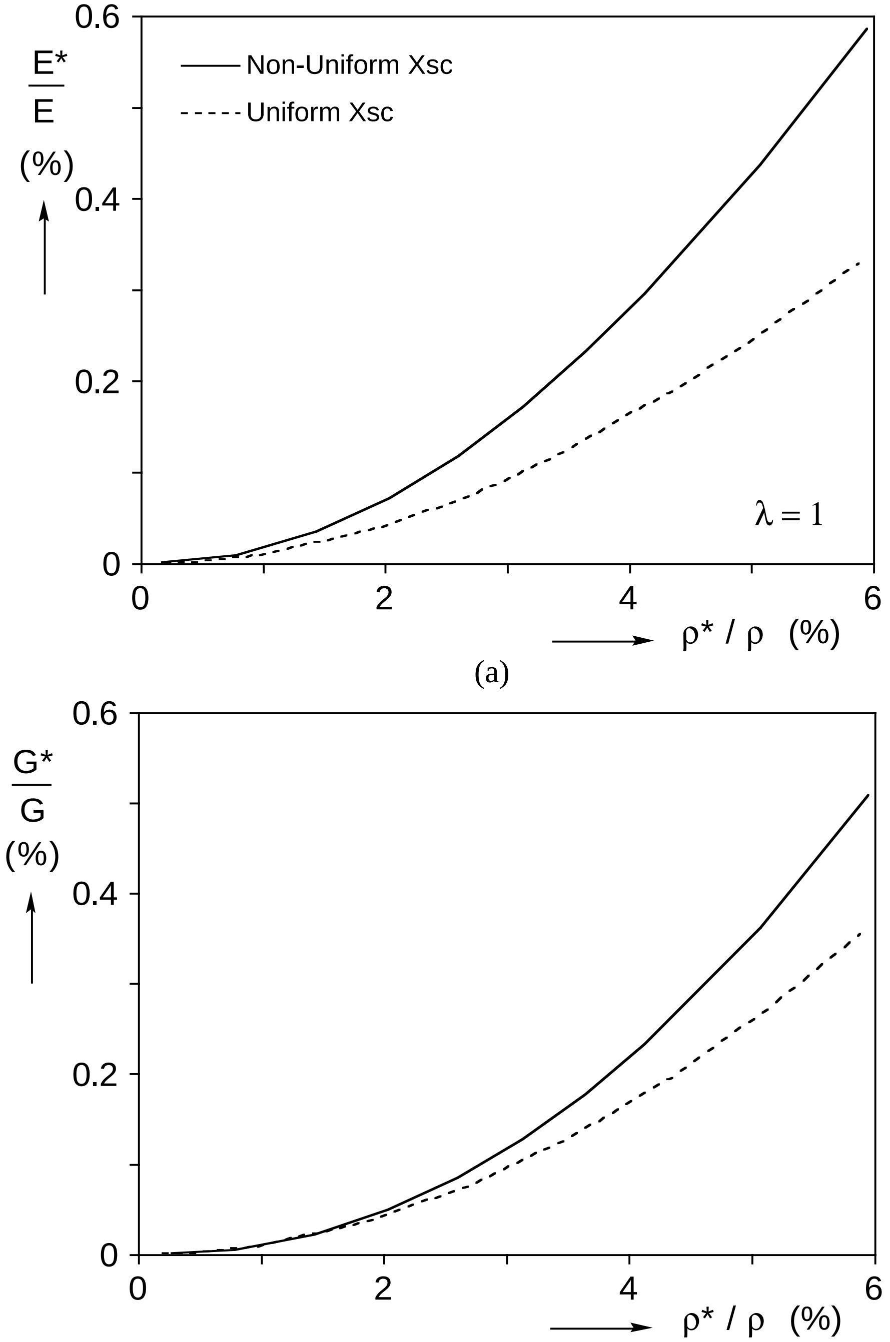

(a)

(b)

Figure 4.10 Material constants vs. relative density for ligaments with uniform and nonuniform cross sectional areas.

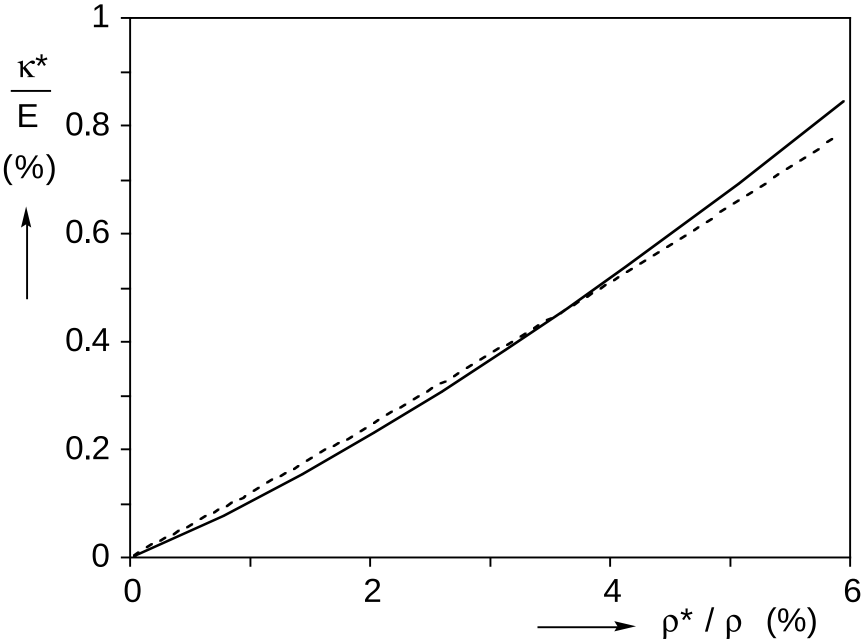

(c)

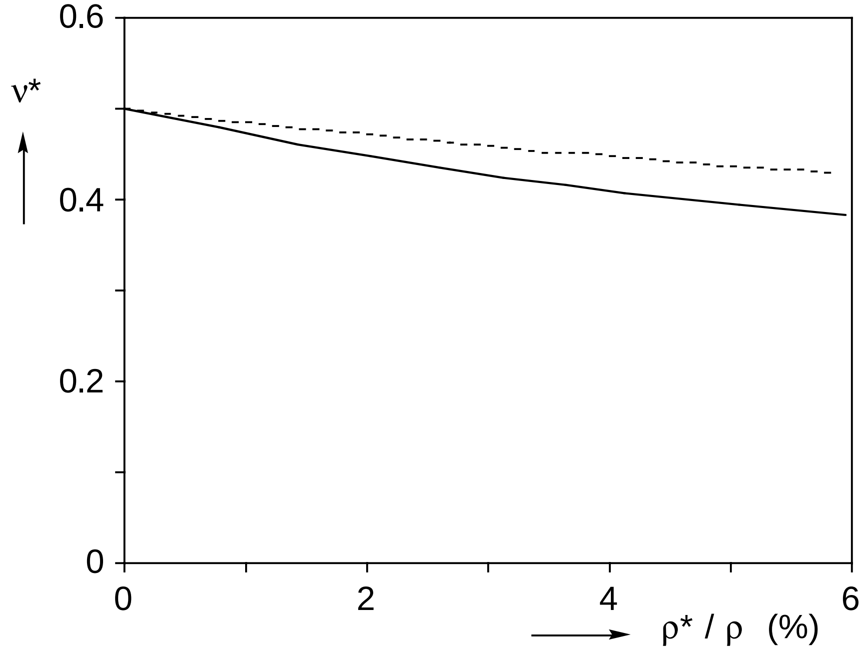

(d)

Figure 4.10 Continue

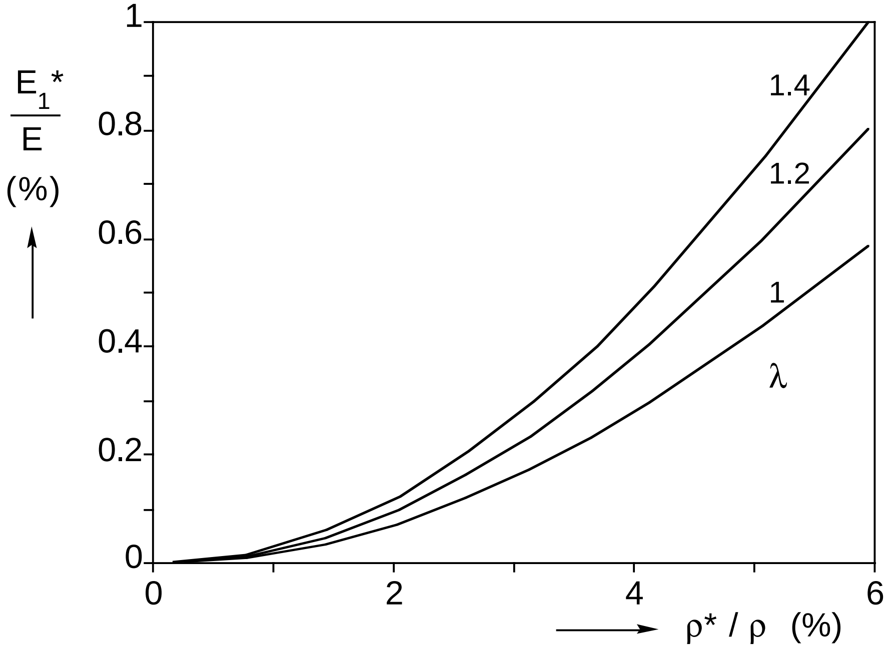

(a)

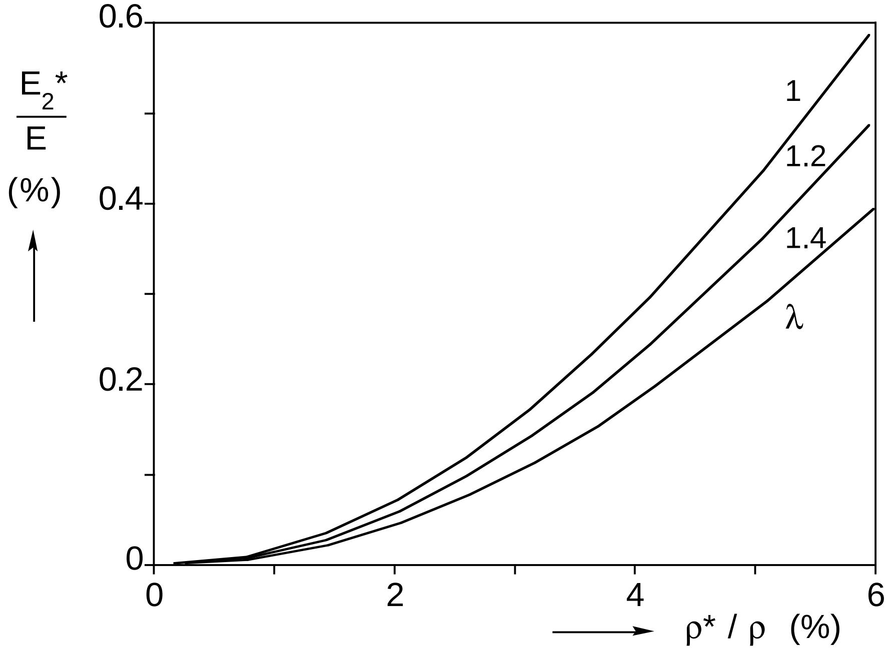

(b)

Figure 4.11 Material constants vs. relative density for foams with different levels of anisotropy.

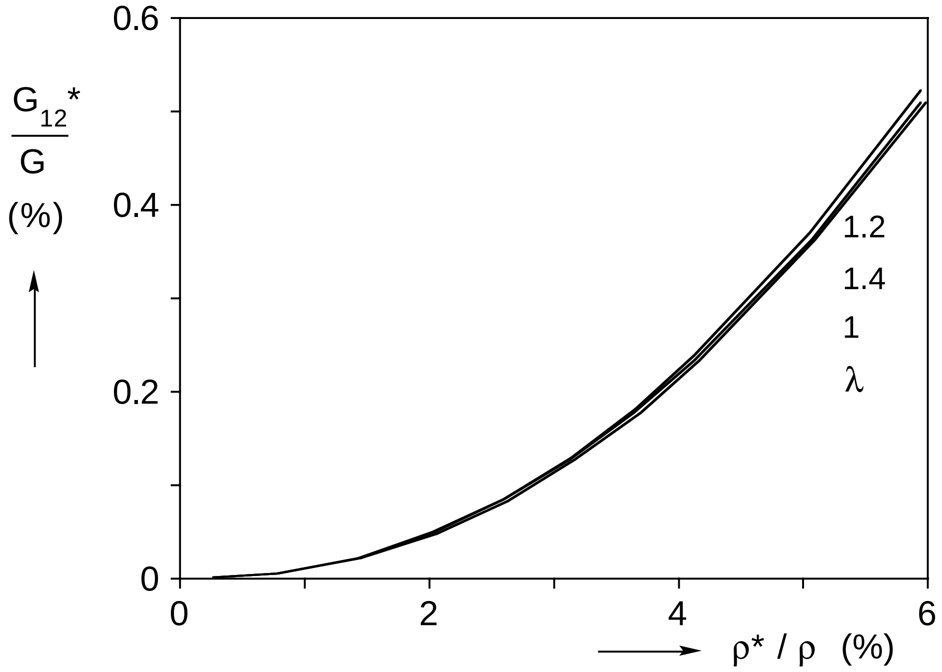

(c)

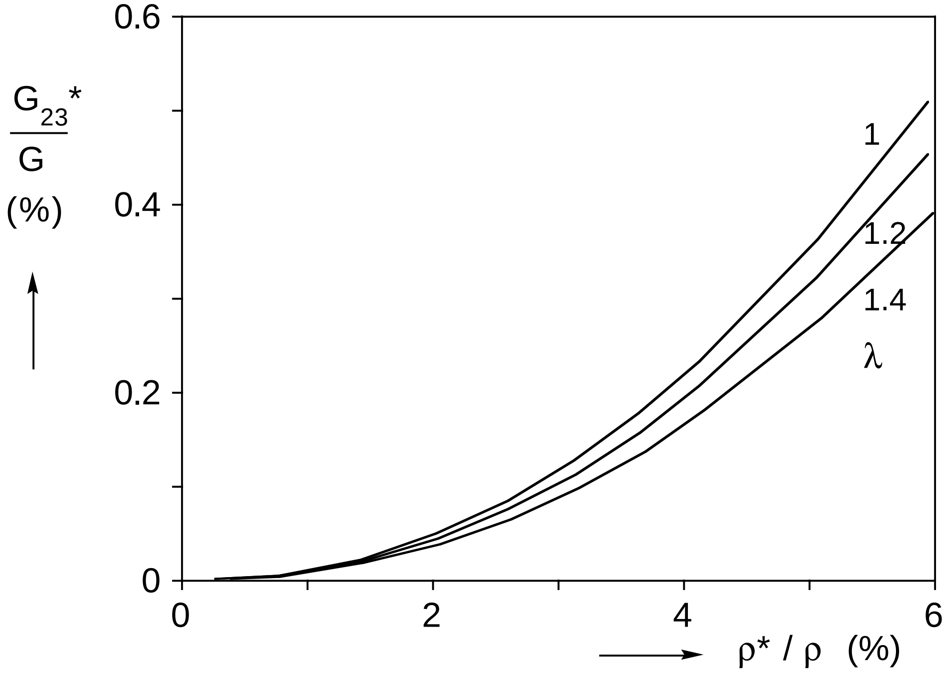

(d)

Figure 4.11 Continued

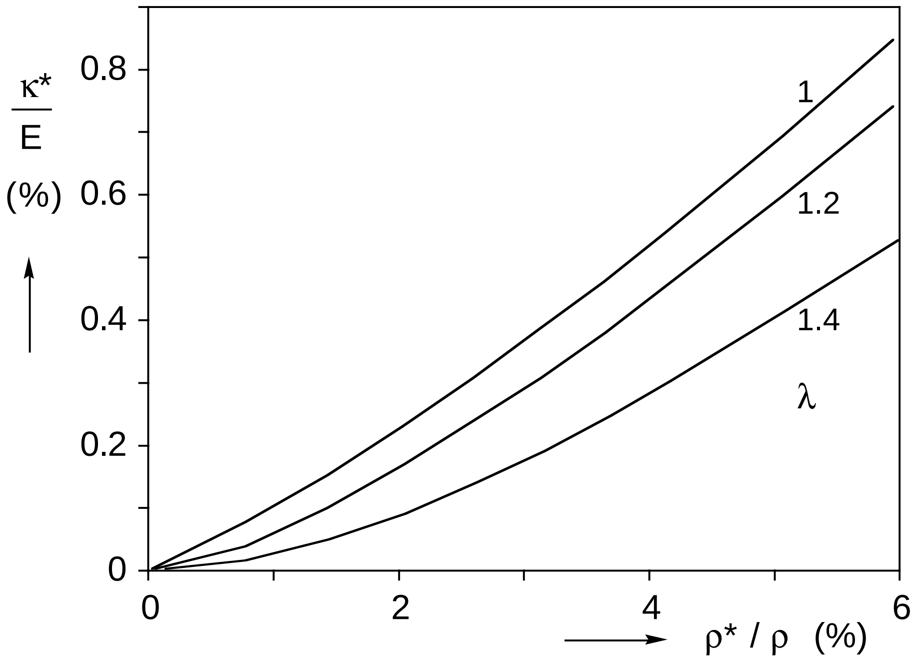

(e)

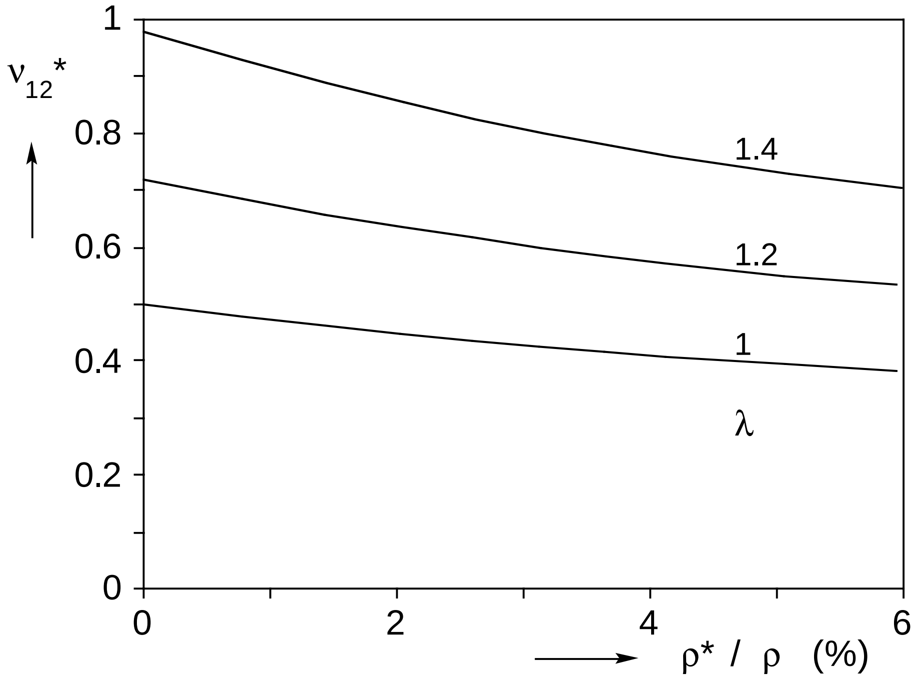

(f)

Figure 4.11 Continued

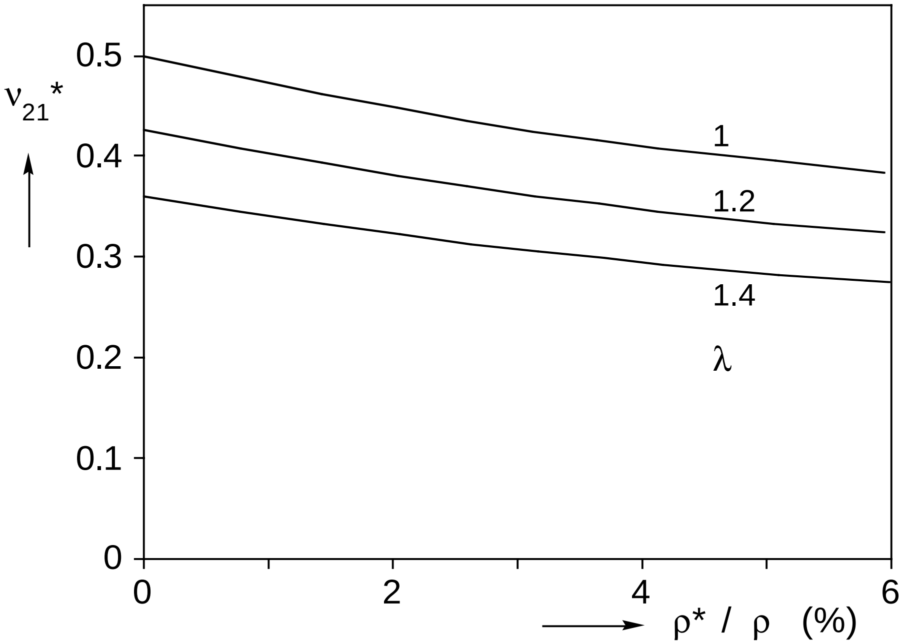

(g)

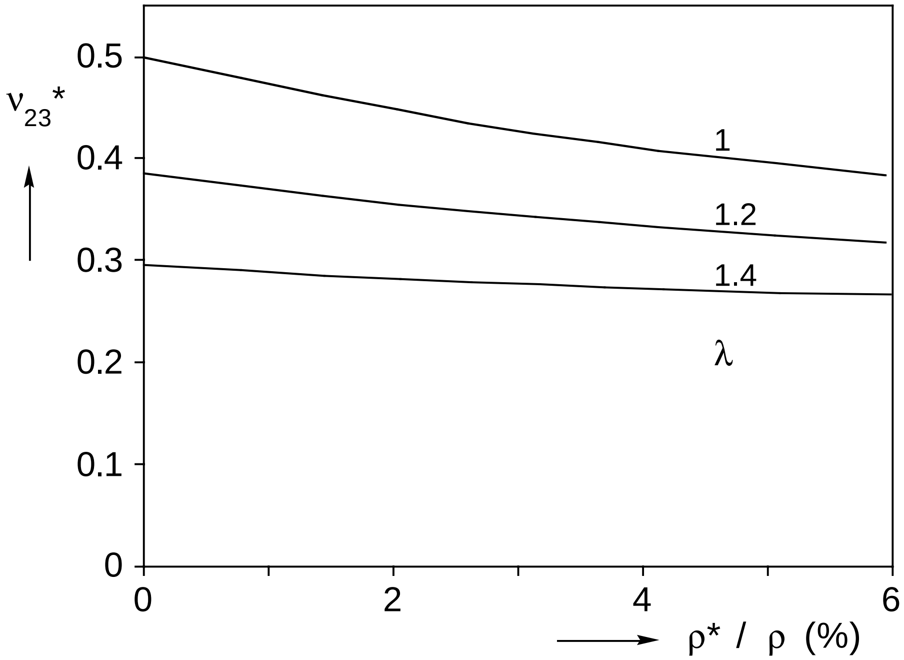

(h)

Figure 4.11 Continued

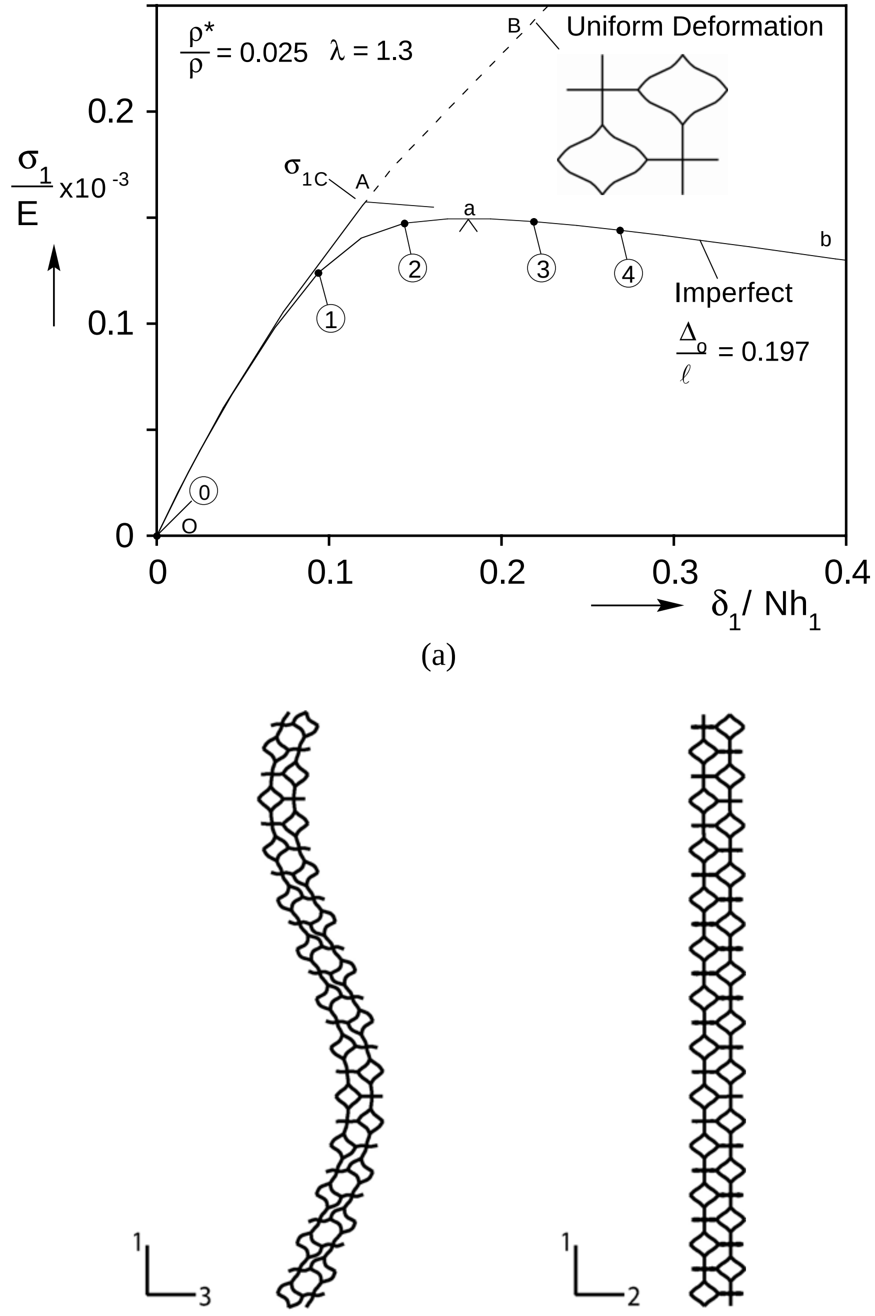

(a)

(b)

Figure 5.1 (a) Calculated rise direction prebuckling and postbuckling stress-shortening responses for fully periodic stacks of Kelvin cells. (b) Long wavelength buckling mode of critical stress.

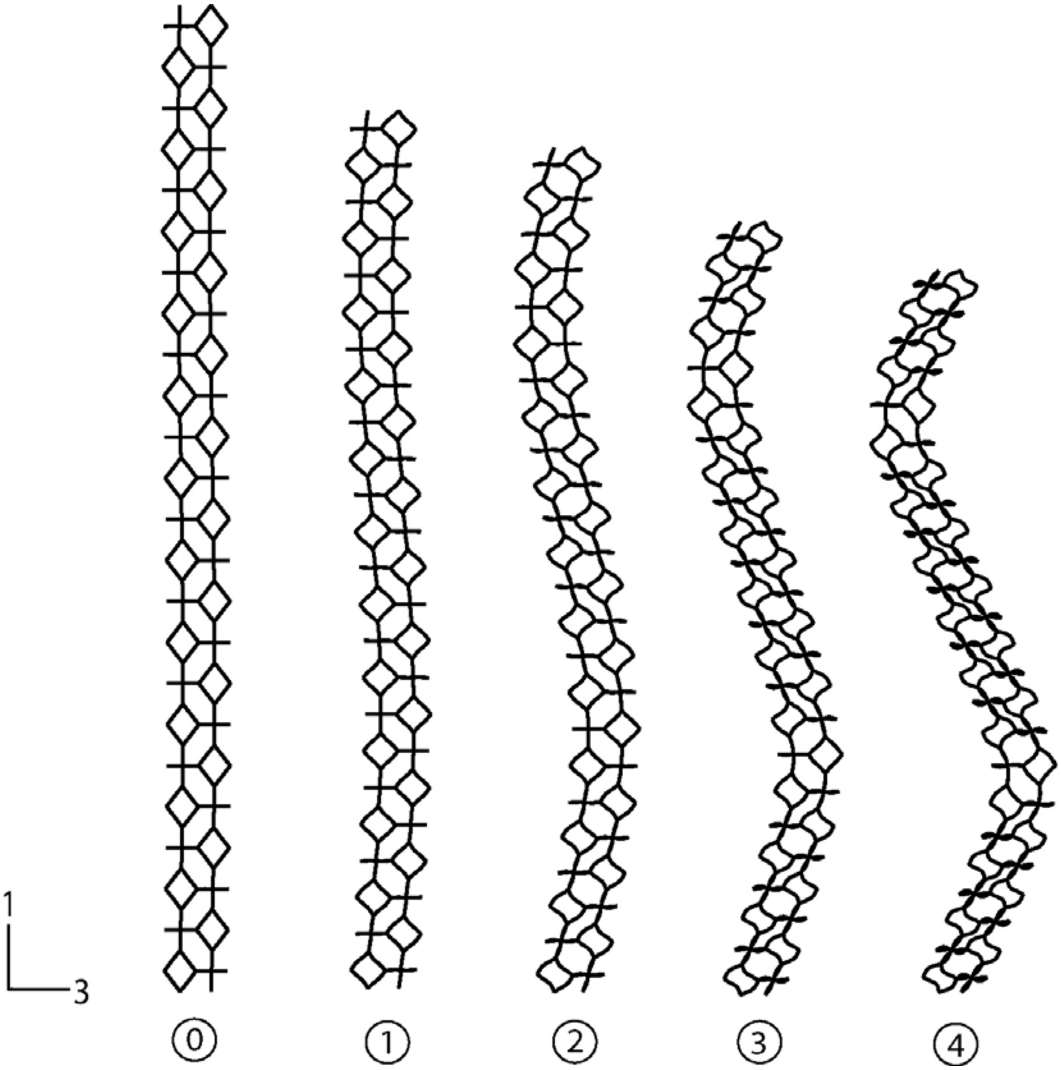

Figure 5.1 (c) Sequence of deformed configurations of long wavelength buckling corresponding to points marked on response in Figure 5.1a.

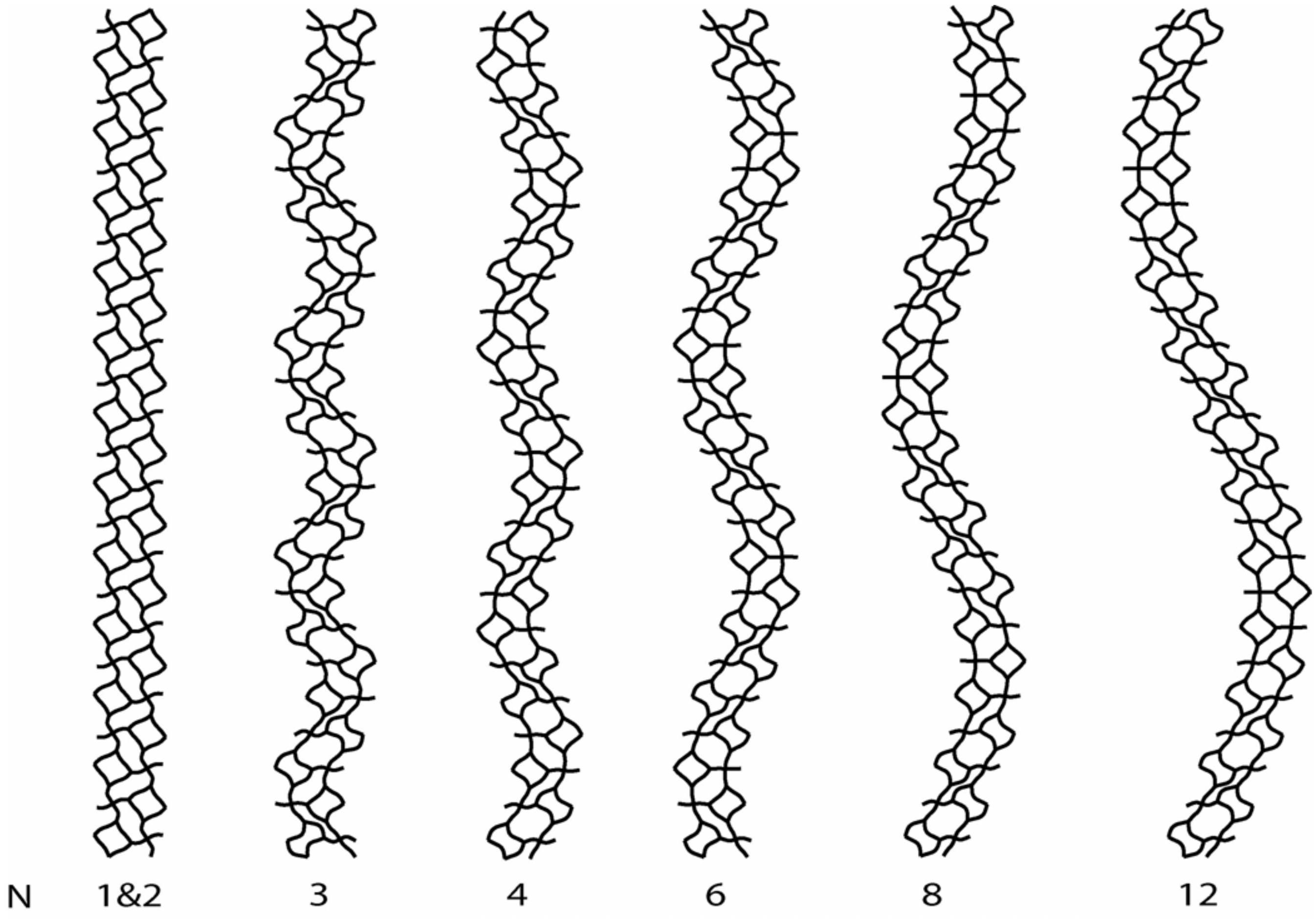

Figure 5.2 Buckling modes corresponding to fully periodic stacks of *N* Kelvin cells.

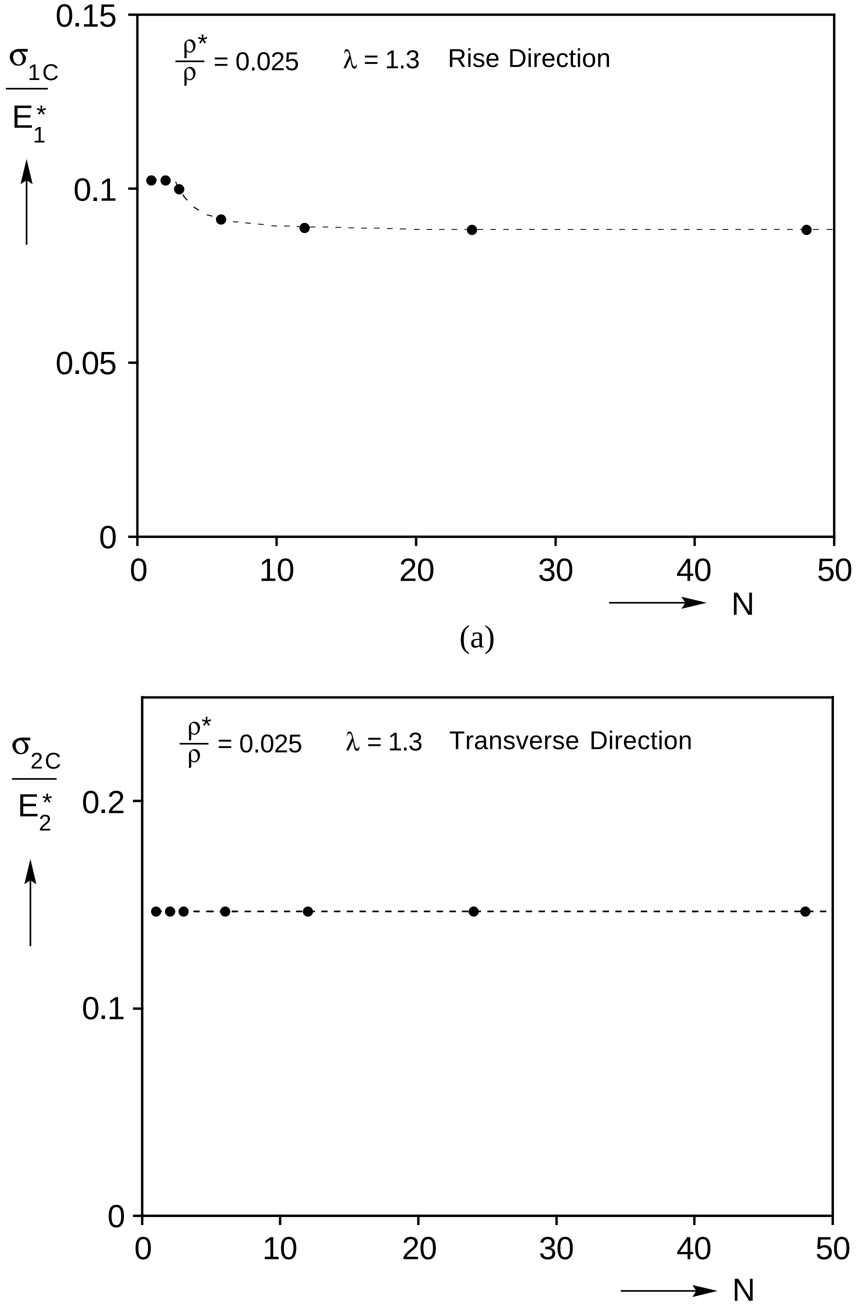

(a)

(b)

Figure 5.3 (a) Critical stress in foam rise direction as a function of number of cells in model analyzed. (b) Critical stress in foam transverse direction as a function of number of cells in model

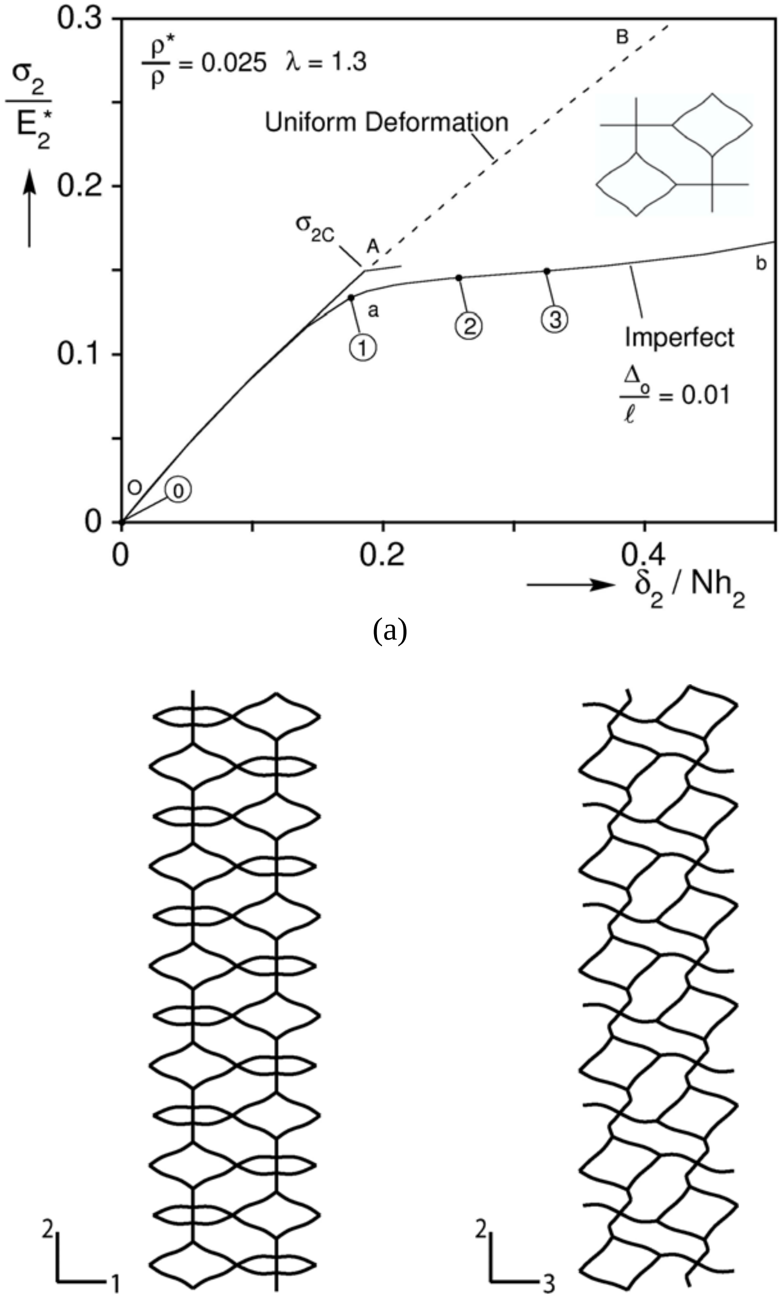

(a)

(b)

Figure 5.4 (a) Calculated transverse direction prebuckling and postbuckling stress-shortening responses for fully periodic Kelvin cells.
(b) Buckling mode of critical stress limited to cell level.

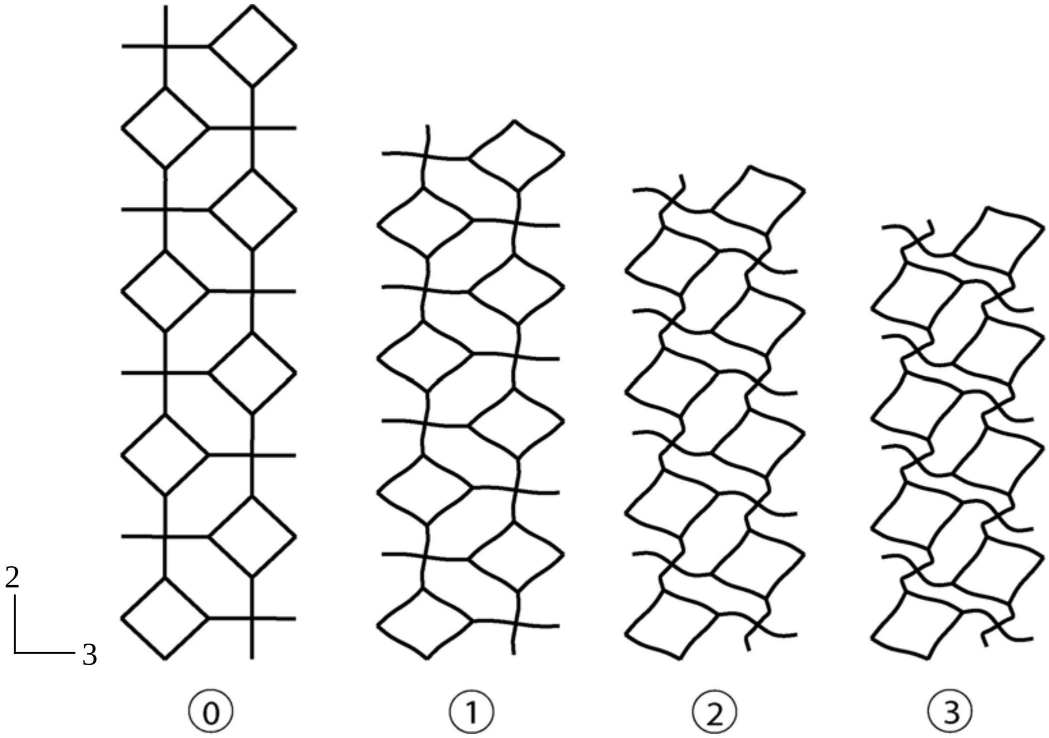

Figure 5.4 (c) Sequence of deformed configurations of cell level buckling corresponding to points marked on response in Figure 5.4a.

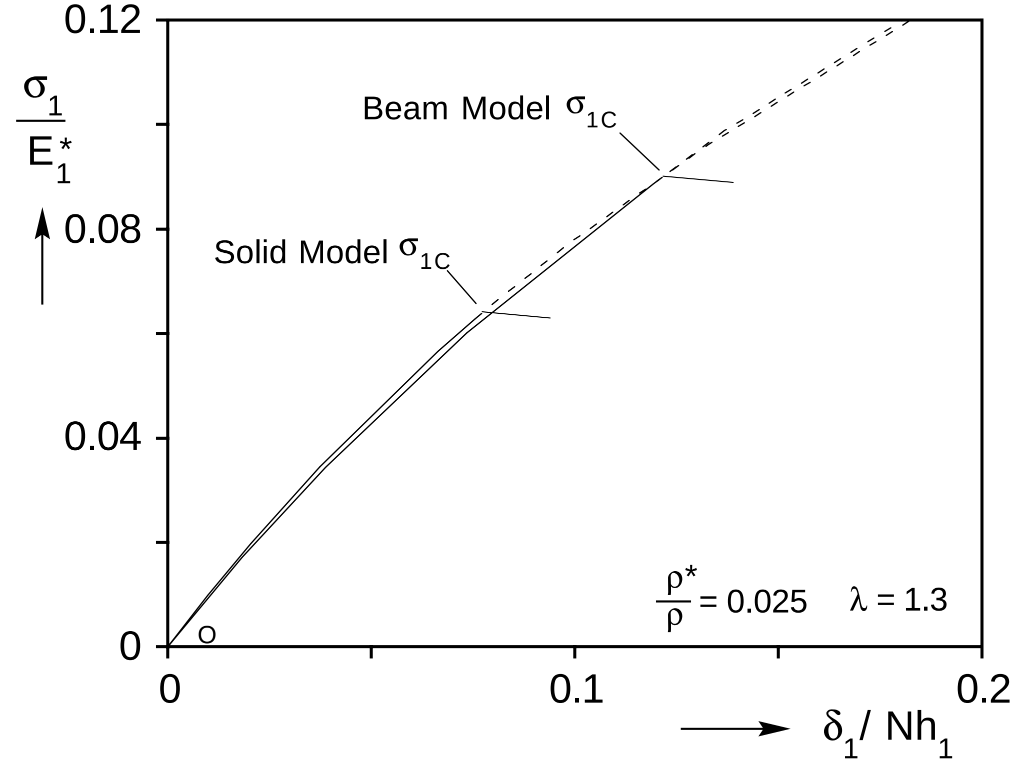

(a)

Figure 5.5 (a) Comparison of critical stresses in rise direction between beam element model and solid element model.

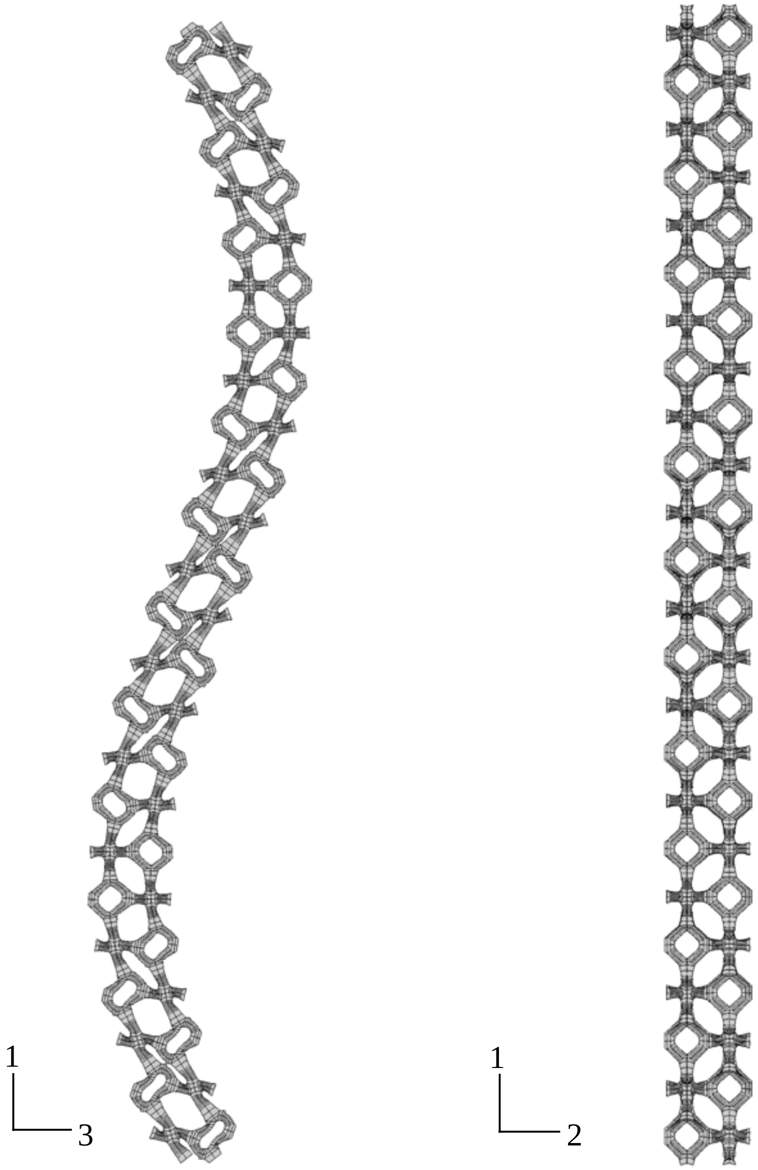

Figure 5.5 (b) Long wavelength buckling mode of critical stress in solid element model.

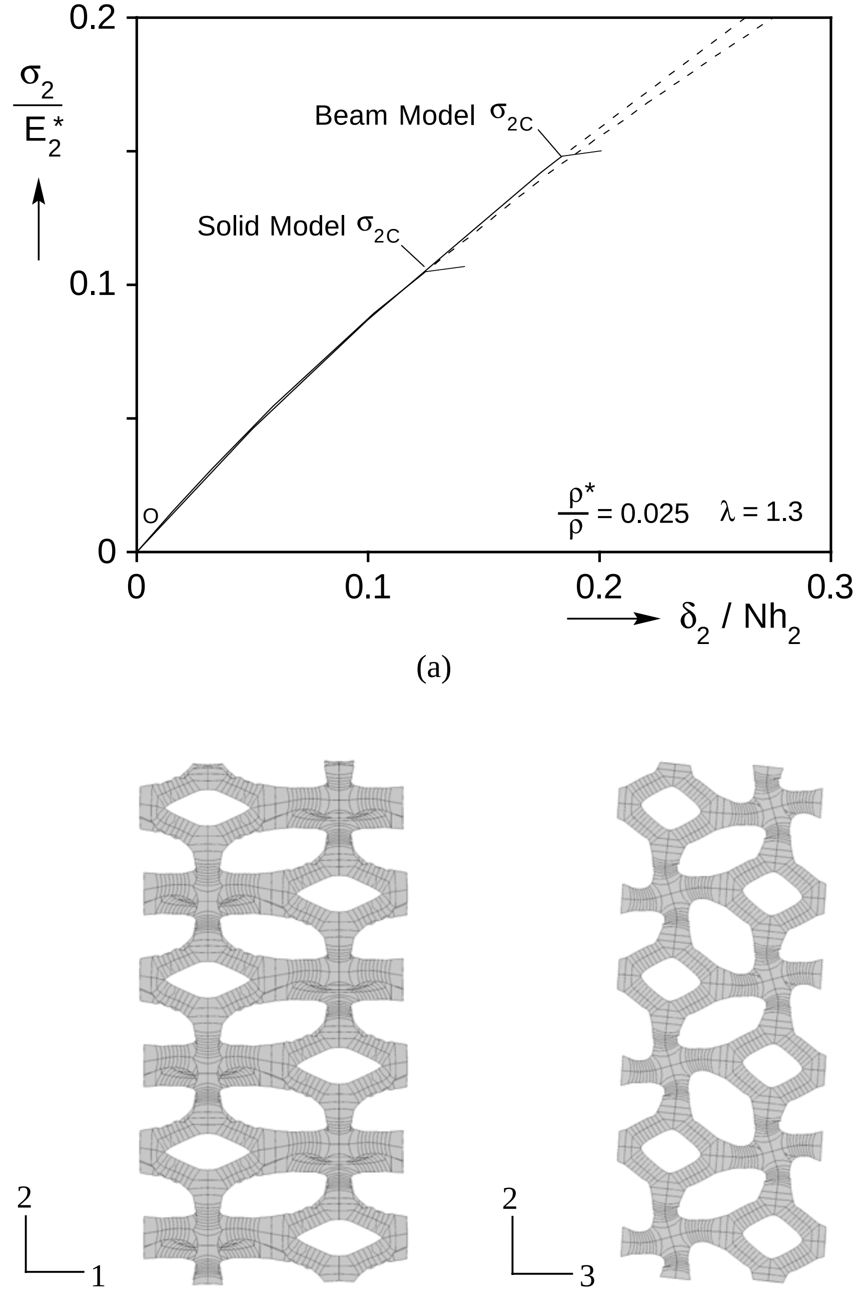

(a)

(b)

Figure 5.6 (a) Comparison of critical stresses in transverse direction between beam element model and solid element model. (b) Buckling mode of critical stress limited to cell level in solid element model.

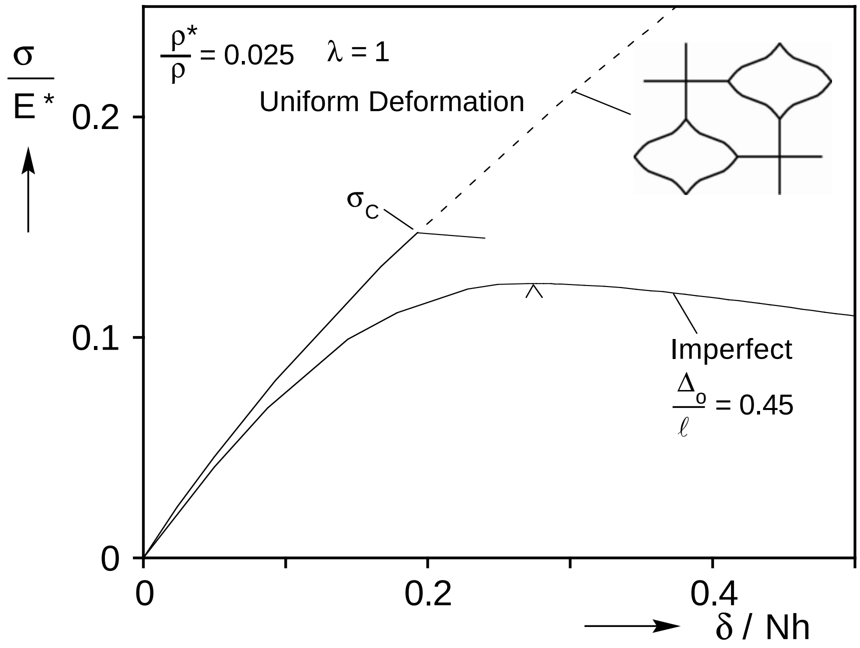

(a)

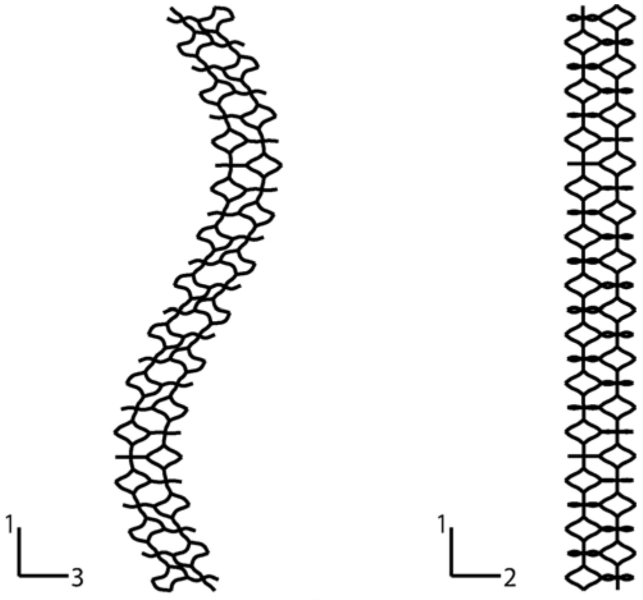

(b)

Figure 5.7 (a) Calculated prebuckling and postbuckling stress-shortening responses for fully periodic stacks of isotropic Kelvin cells. (b) Long wavelength buckling mode of critical stress.

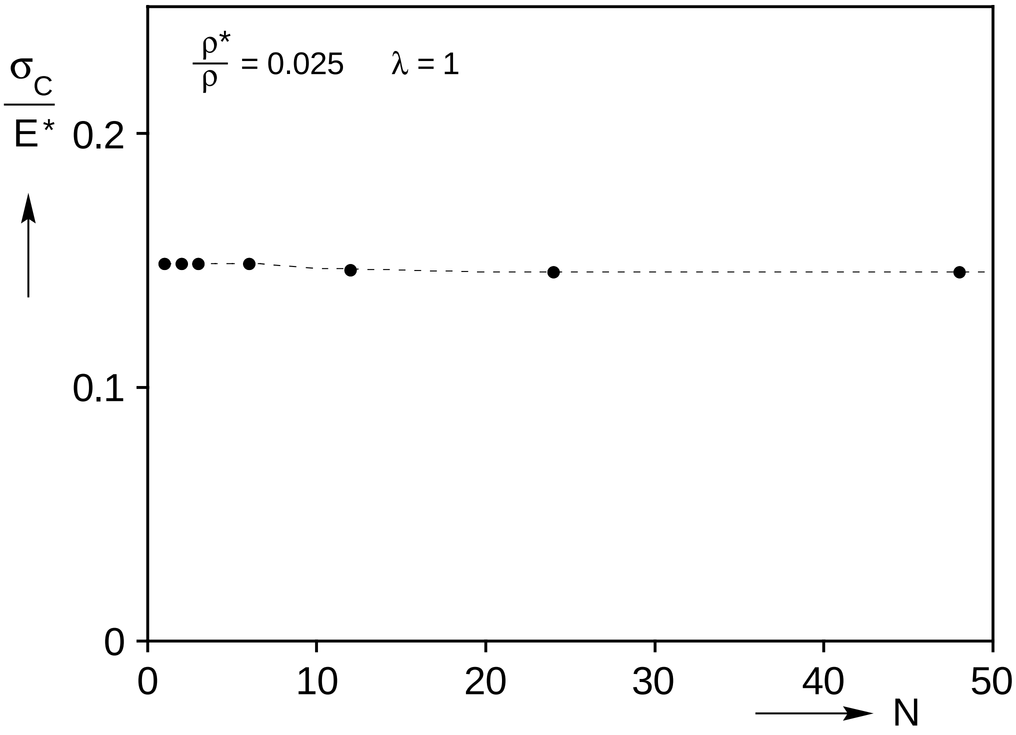

Figure 5.8 Critical stress of isotropic foam as a function of number of cells in model analyzed.

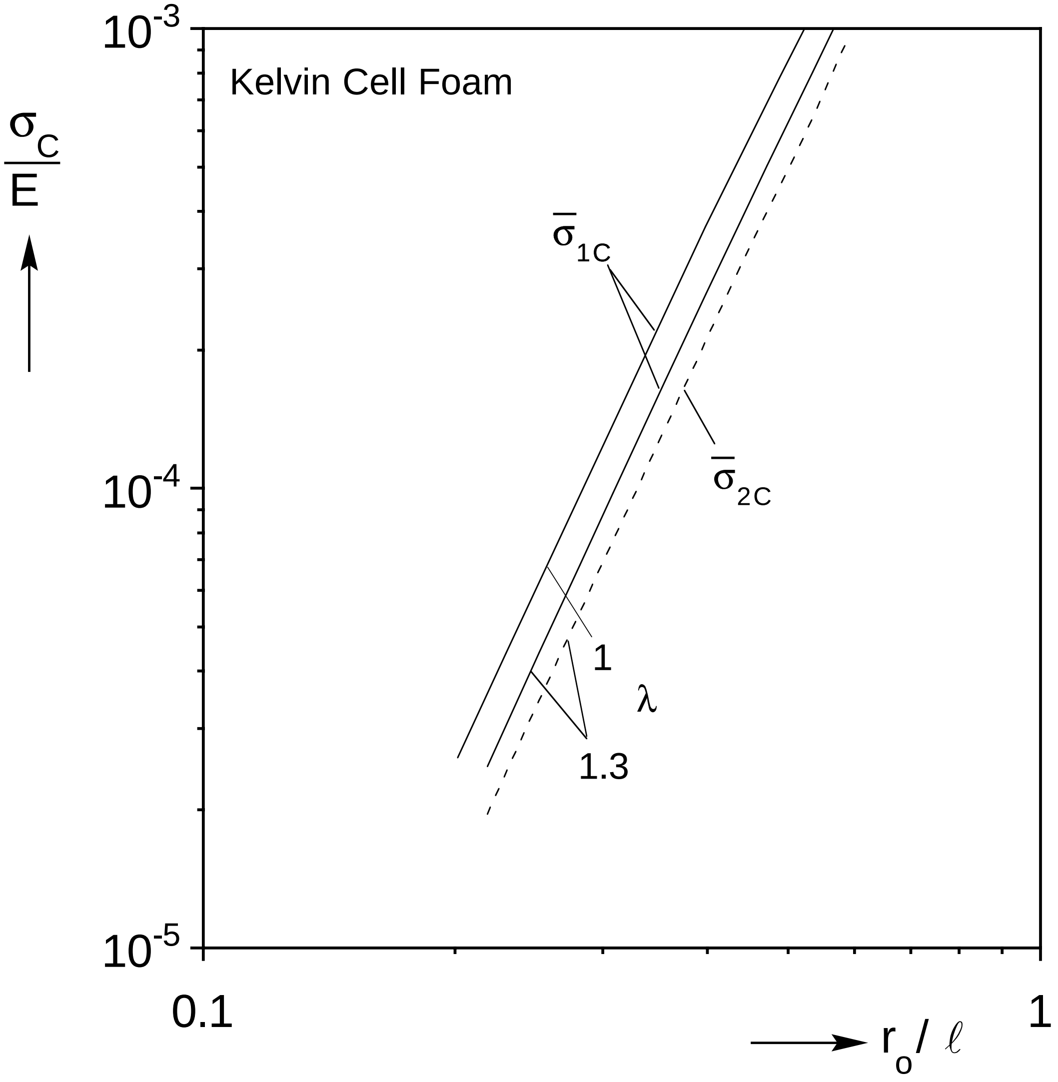

Figure 5.9 Calculated critical stress of isotropic and anisotropic foamsas a function of geometric parameter r_o/ℓ.

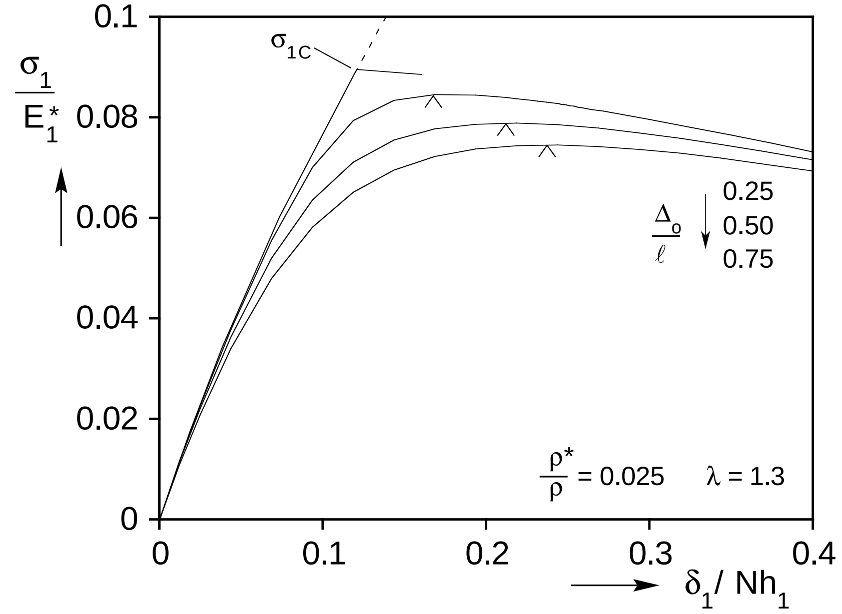

(a)

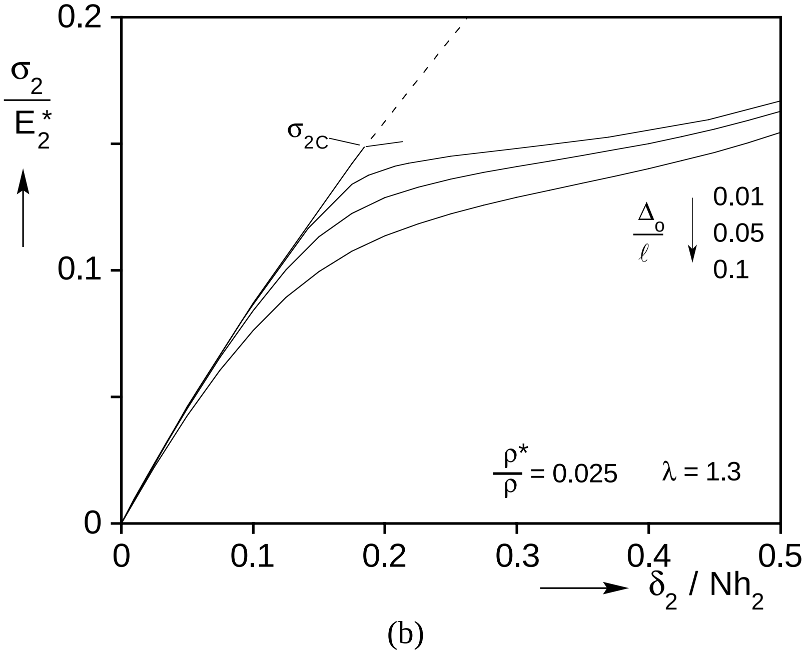

(b)

Figure 5.10 Stress-shortening responses for fully periodic stacks of Kelvin cells for different imperfection amplitudes. (a) Rise direction and (b) transverse direction.

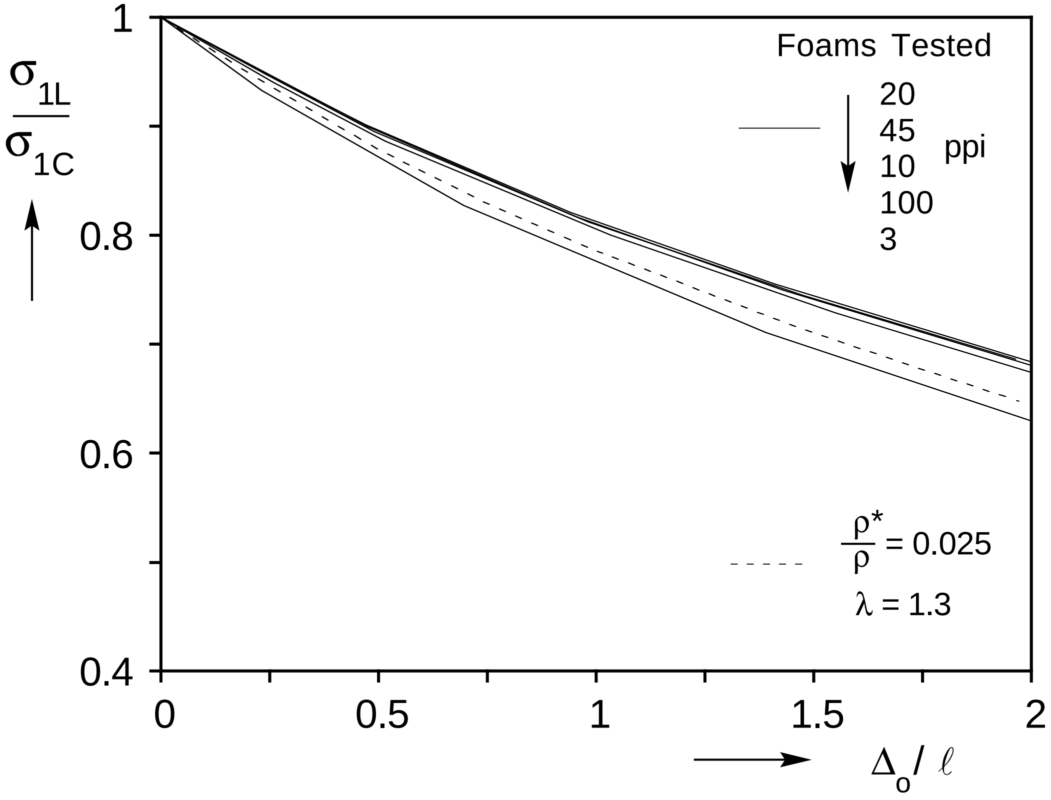

Figure 5.11 Calculated limit stress of foams used in the experiments as a function of imperfection amplitude.

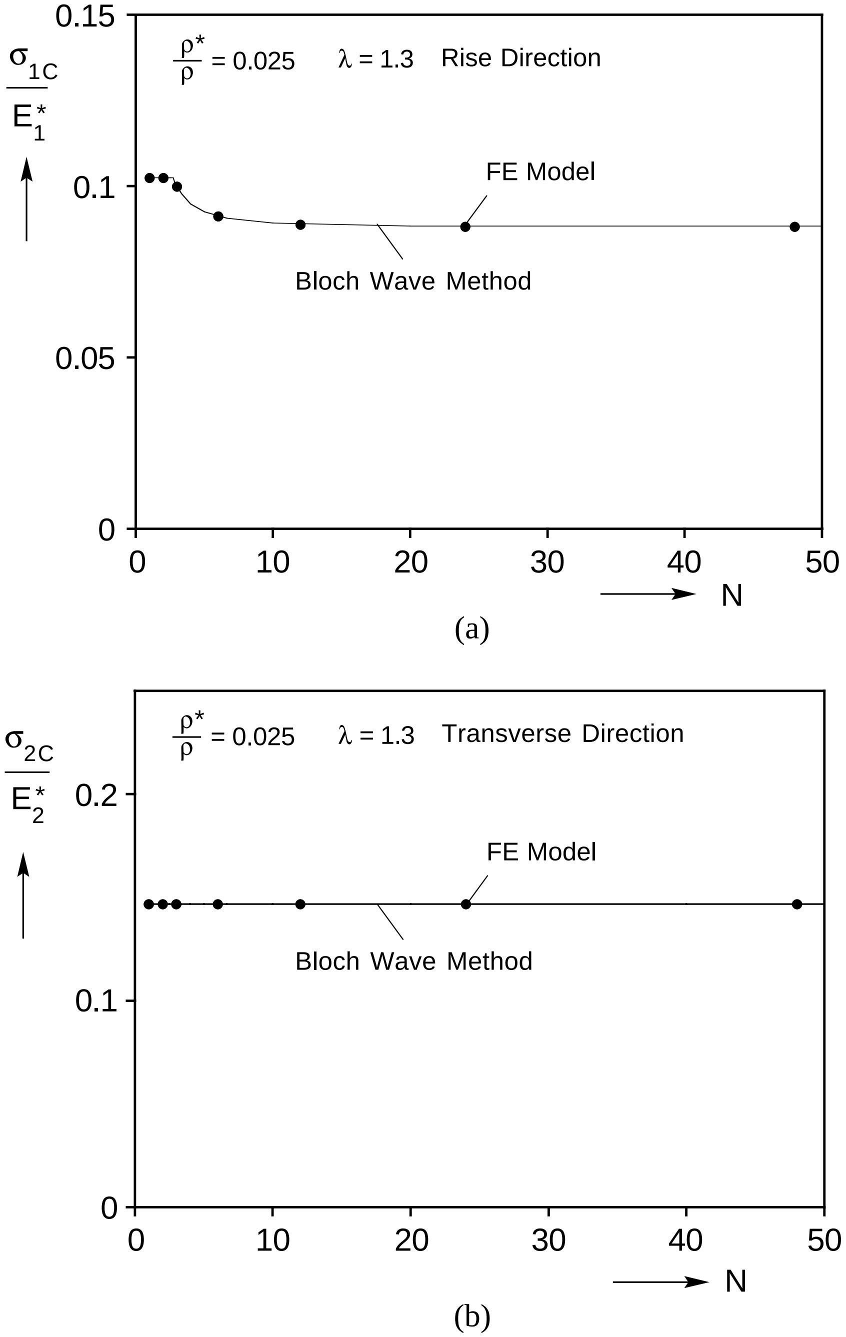

(a)

(b)

Figure 6.1 (a) Critical stress in foam rise direction as a function of number of cells in model analyzed. (b) Critical stress in foam transverse direction as a function of number of cells in model

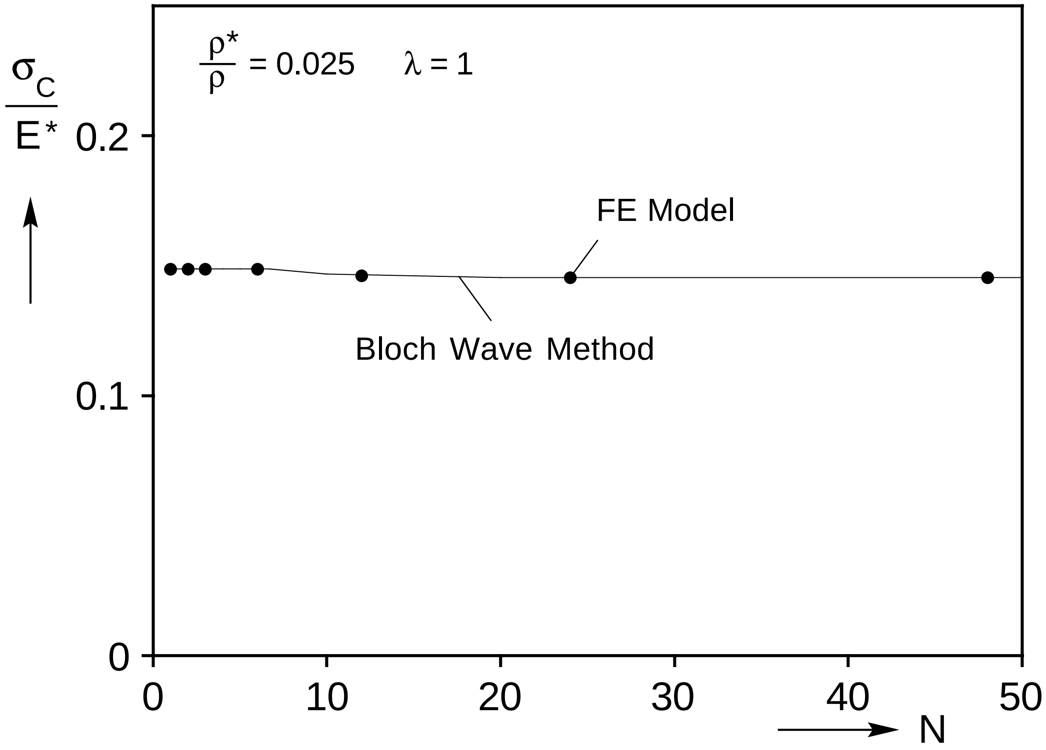

Figure 6.2 Critical stress of isotropic foam as a function of number of cells in model analyzed.

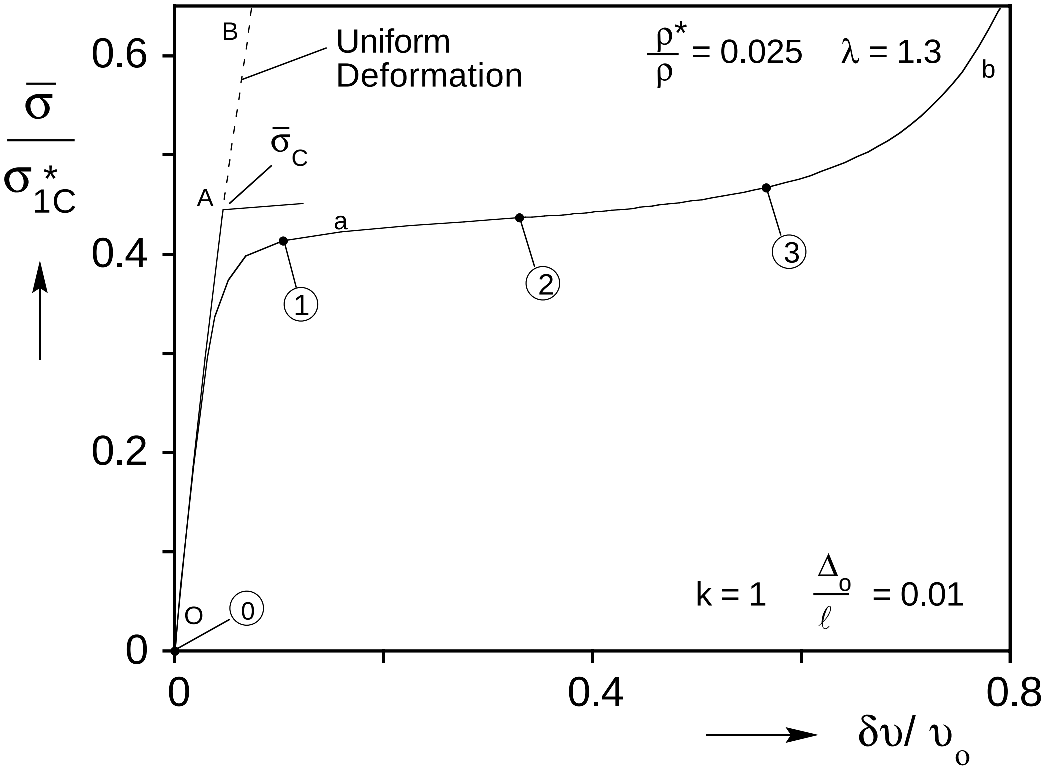

Figure 7.1 (a) Calculated prebuckling and postbuckling responses under hydrostatic pressure ($\lambda = 1.3,\ k = 1$).

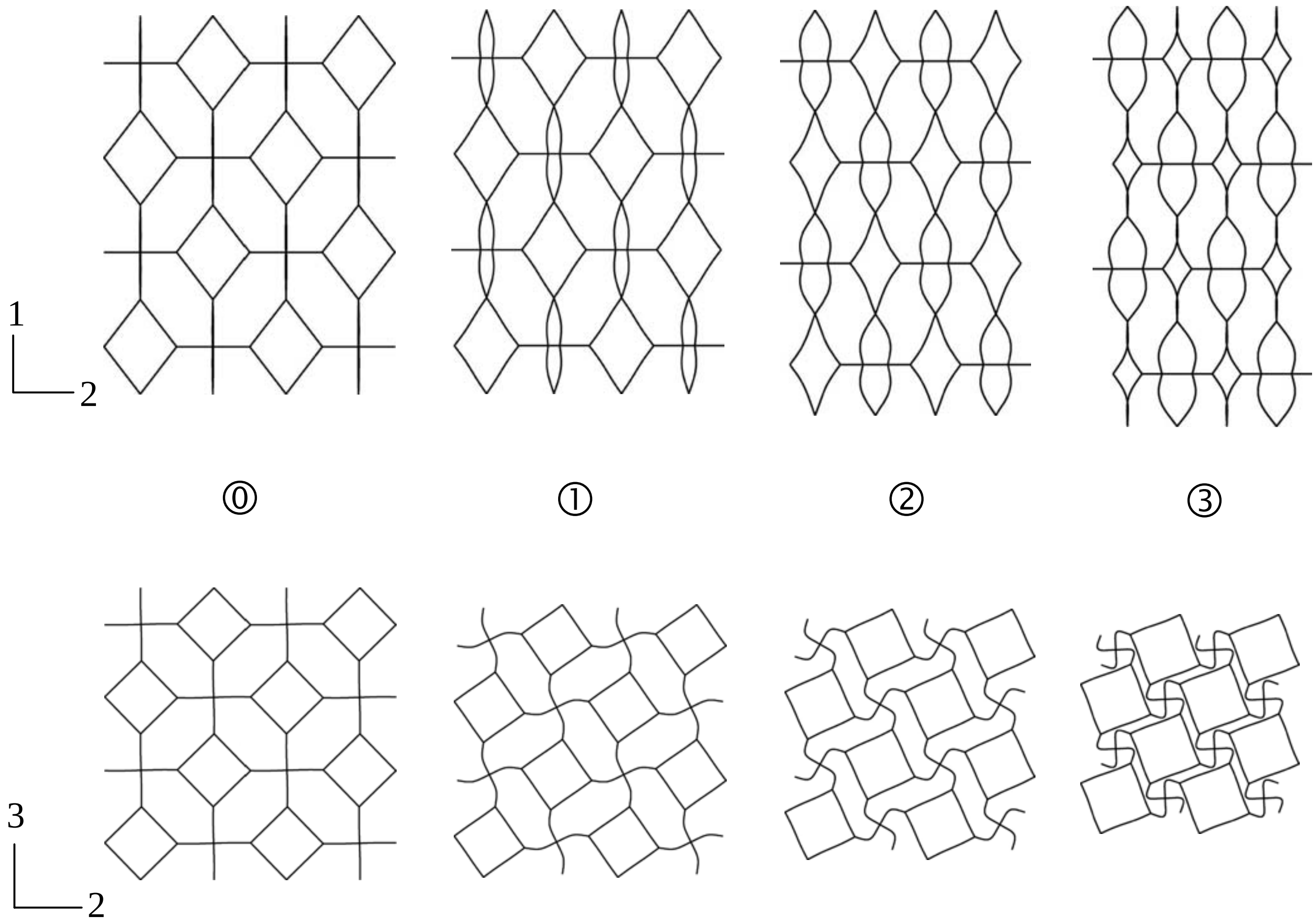

Figure 7.1 (b) Deformed configurations showing evolution of local mode corresponding to response in Figure 7.1a.

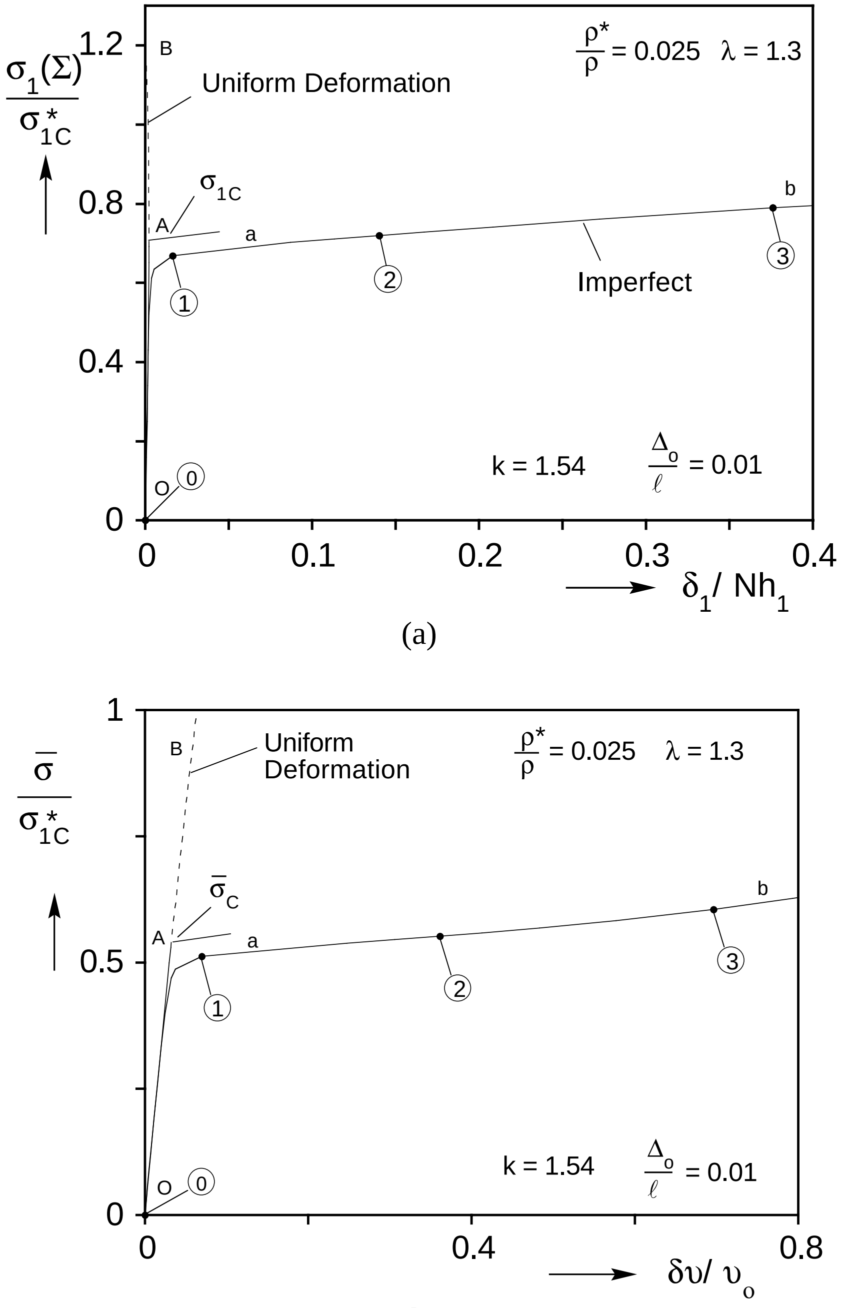

Figure 7.2 (a) Calculated axial stress-displacement prebuckling and postbuckling responses for multiaxial load ($\lambda = 1.3,\ k = 1.54$). (b) Calculated mean stress-change in volume prebuckling and postbuckling responses.

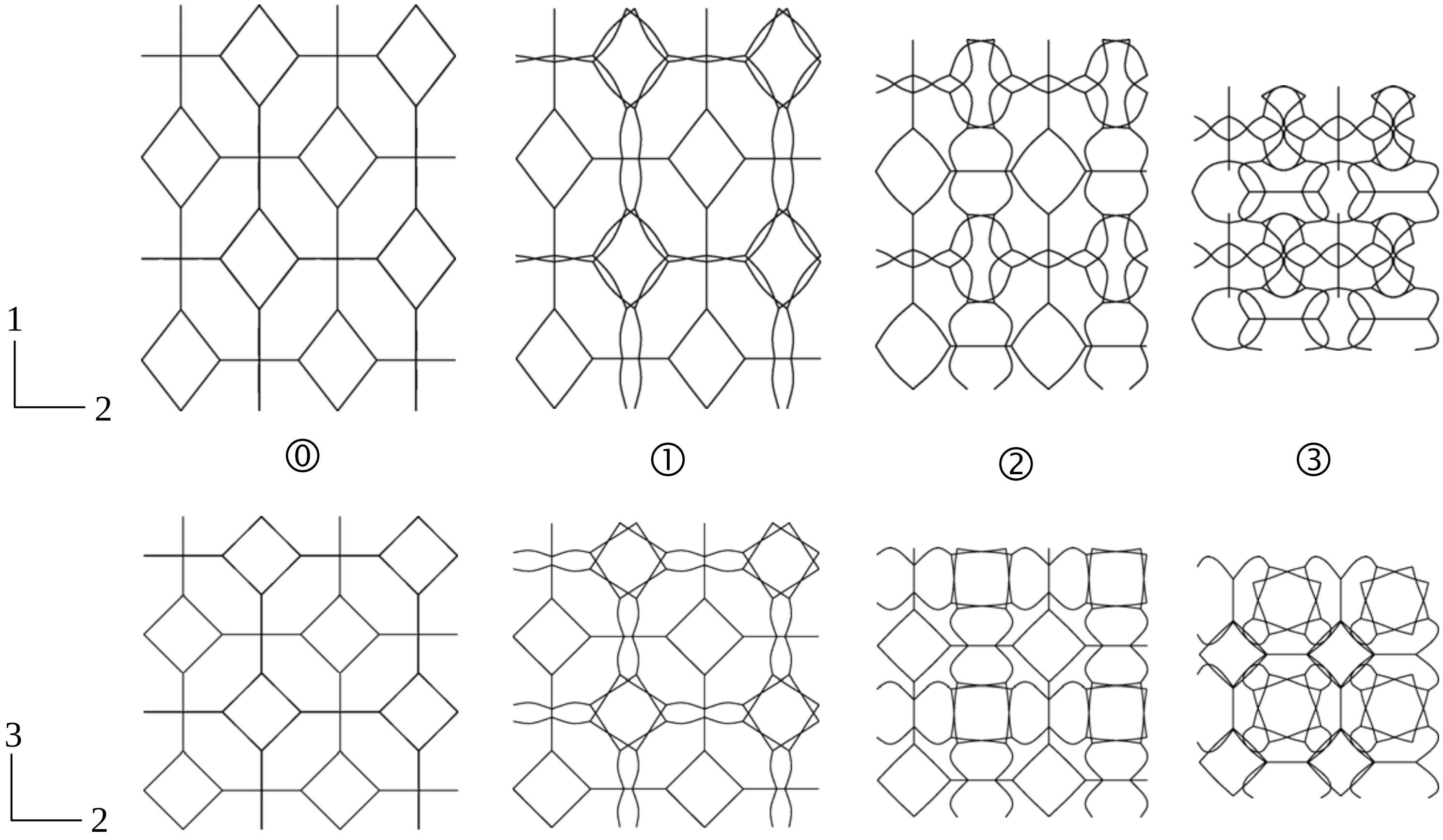

Figure 7.2 (c) Deformed configurations showing evolution of mode involving $2 \times 2 \times 2$ cell domain corresponding to response in Figures 7.2a and 7.2b.

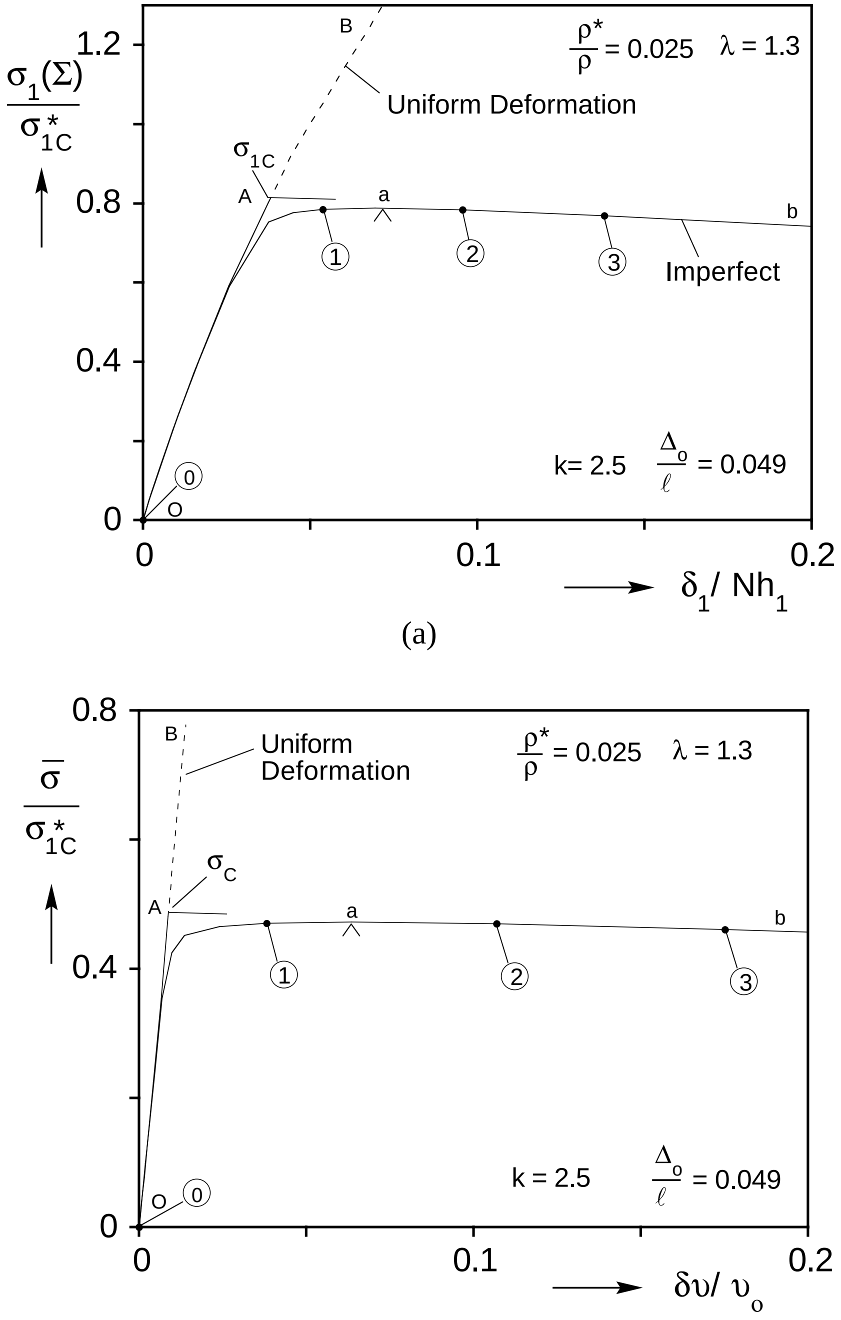

(a)

(b)

Figure 7.3 (a) Calculated axial stress-displacement prebuckling and postbuckling responses for multiaxial load ($\lambda = 1.3$, $k = 2.5$). (b) Calculated mean stress-change in volume prebuckling and postbuckling responses.

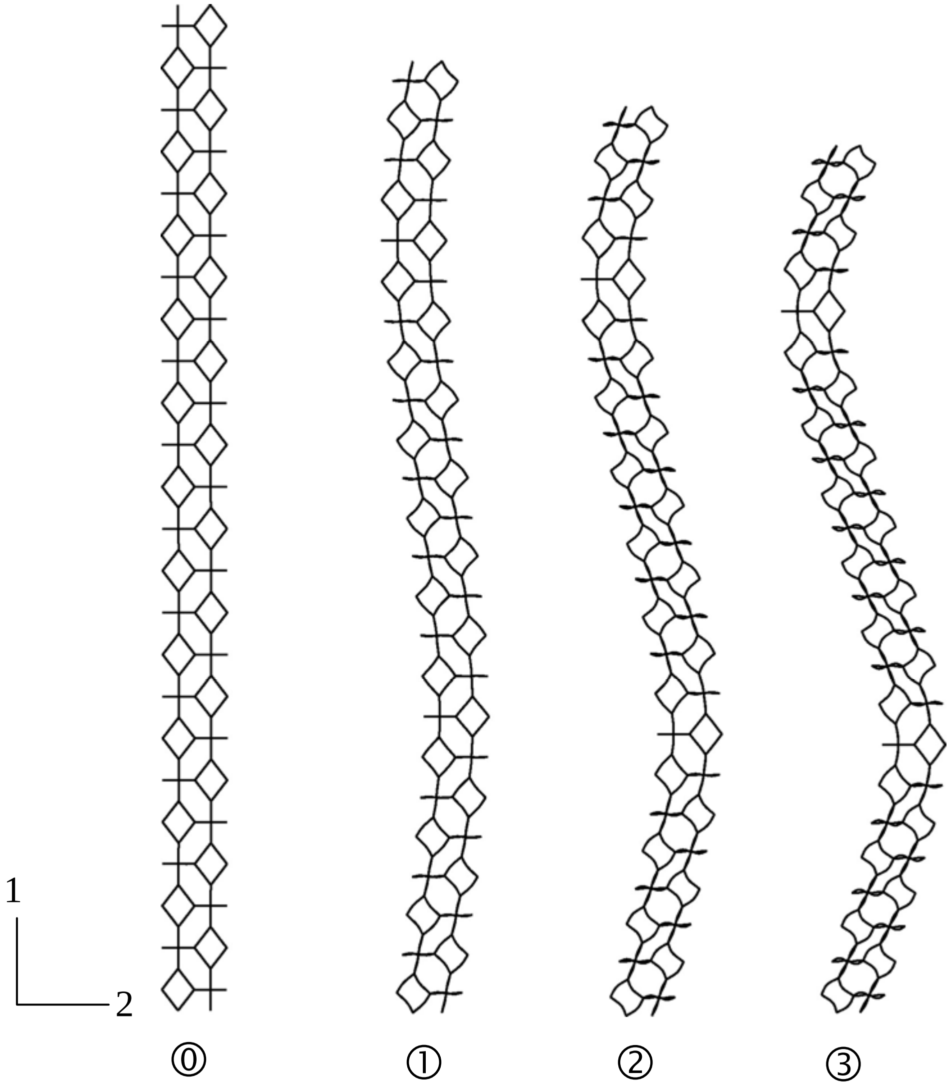

Figure 7.3 (c) Deformed configurations showing evolution of long wavelength mode corresponding to response in Figures 7.3a and 7.3b.

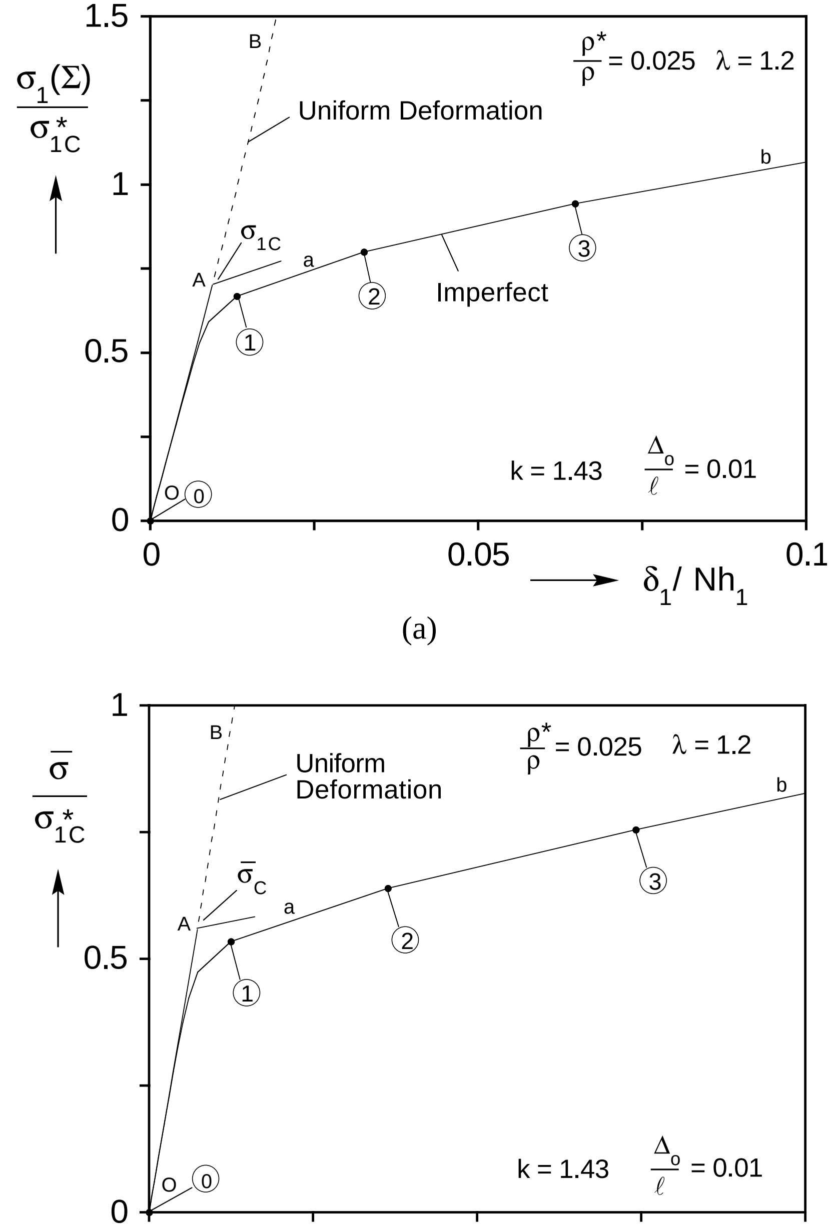

(a)

(b)

Figure 7.4 (a) Calculated axial stress-displacement prebuckling and postbuckling responses for multiaxial load ($\lambda = 1.2$, $k = 1.43$). (b) Calculated mean stress-change in volume prebuckling and postbuckling responses.

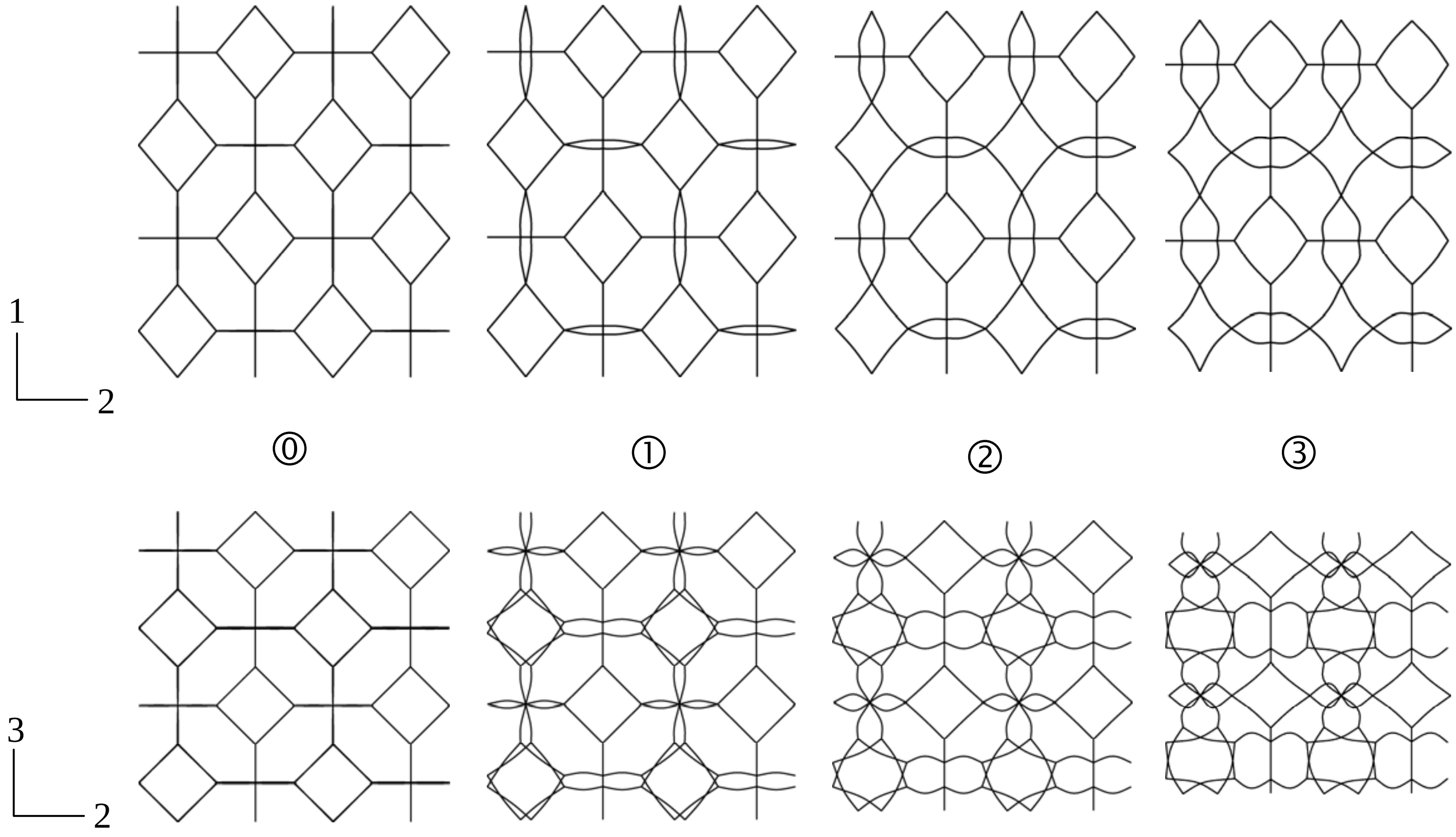

Figure 7.4 (c) Deformed configurations showing evolution of mode involving $2 \times 1 \times 2$ cell domain corresponding to response in Figures 7.4a and 7.4b.

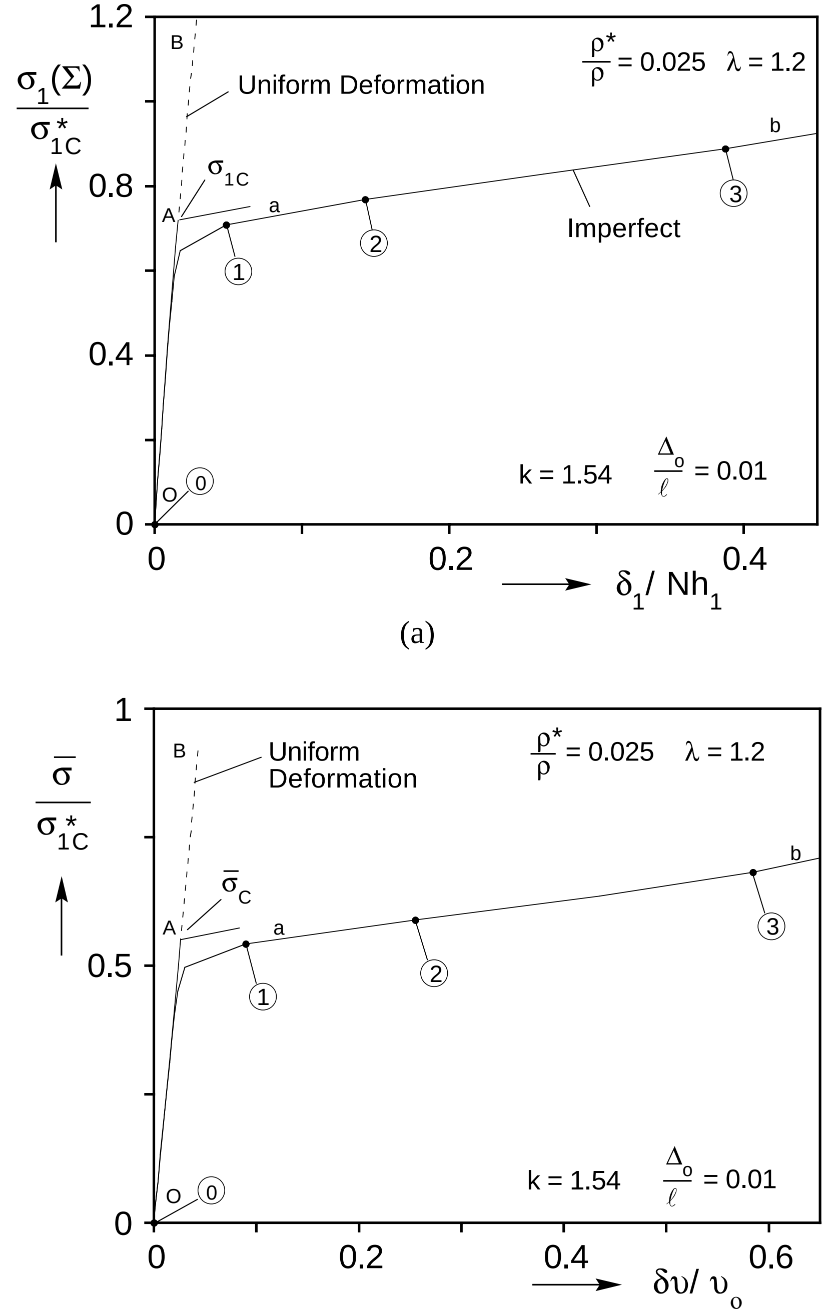

Figure 7.5 (a) Calculated axial stress-displacement prebuckling and postbuckling responses for multiaxial load ($\lambda = 1.2$, $k = 1.54$). (b) Calculated mean stress-change in volume prebuckling and postbuckling responses.

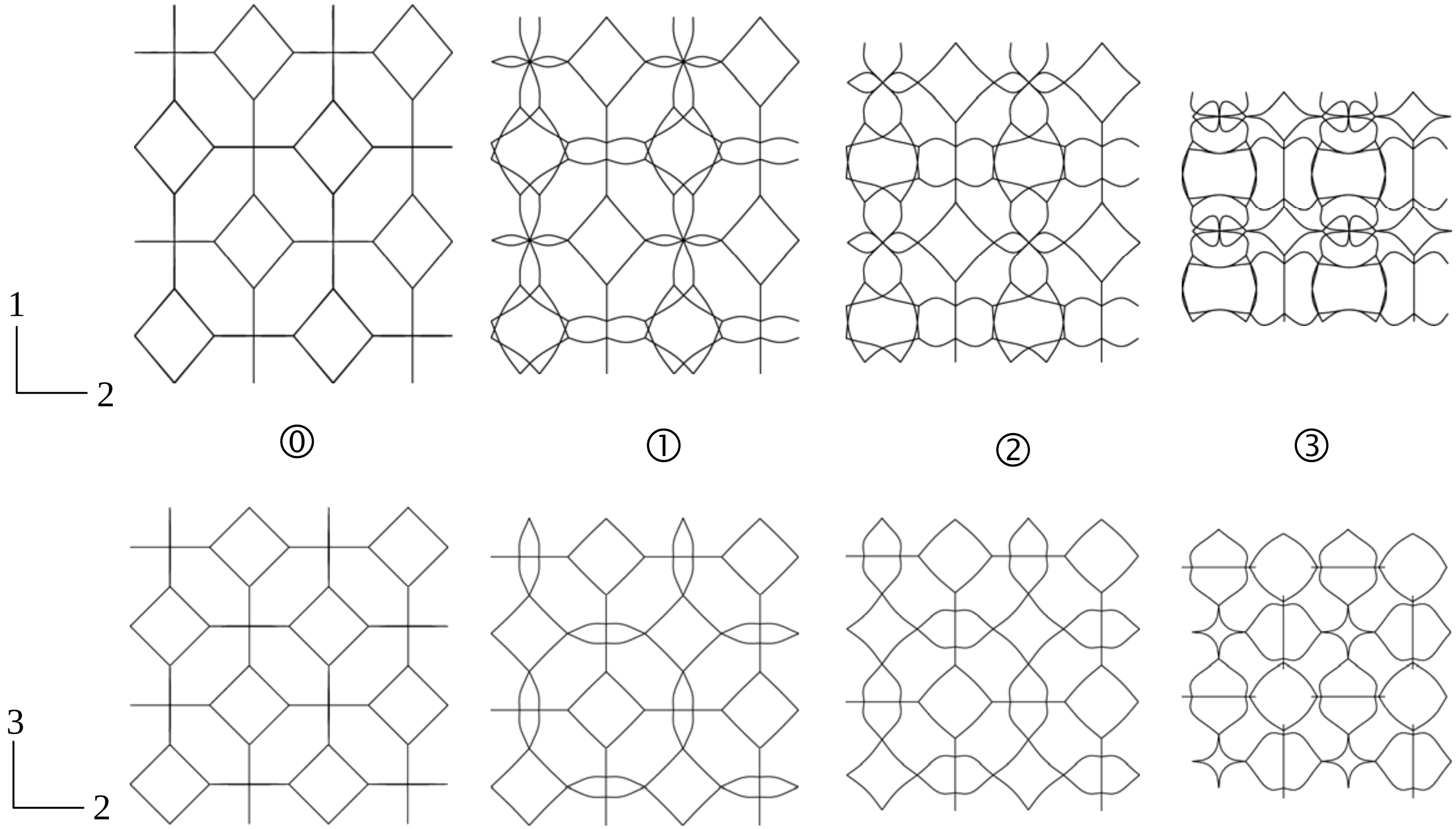

Figure 7.5 (c) Deformed configurations showing evolution of mode involving $1 \times 2 \times 2$ cell domain corresponding to response in Figures 7.5a and 7.5b.

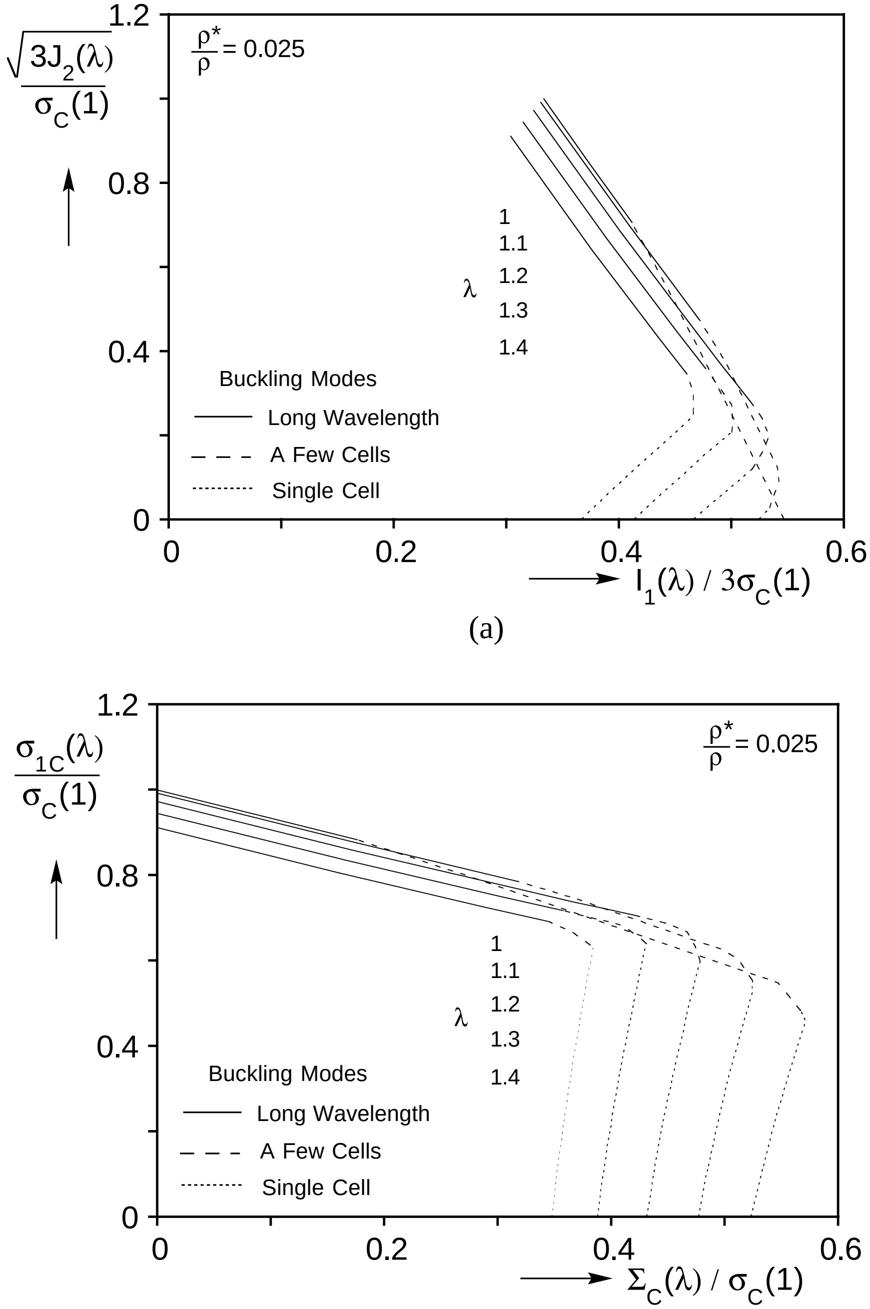

(a)

(b)

Figure 7.6 (a) Anisotropic foam failure envelopes in $\sqrt{3J_2} - I_1$ plane.
(b) Anisotropic foam failure envelopes in $\sqrt{3J_2} - I_1$ plane.

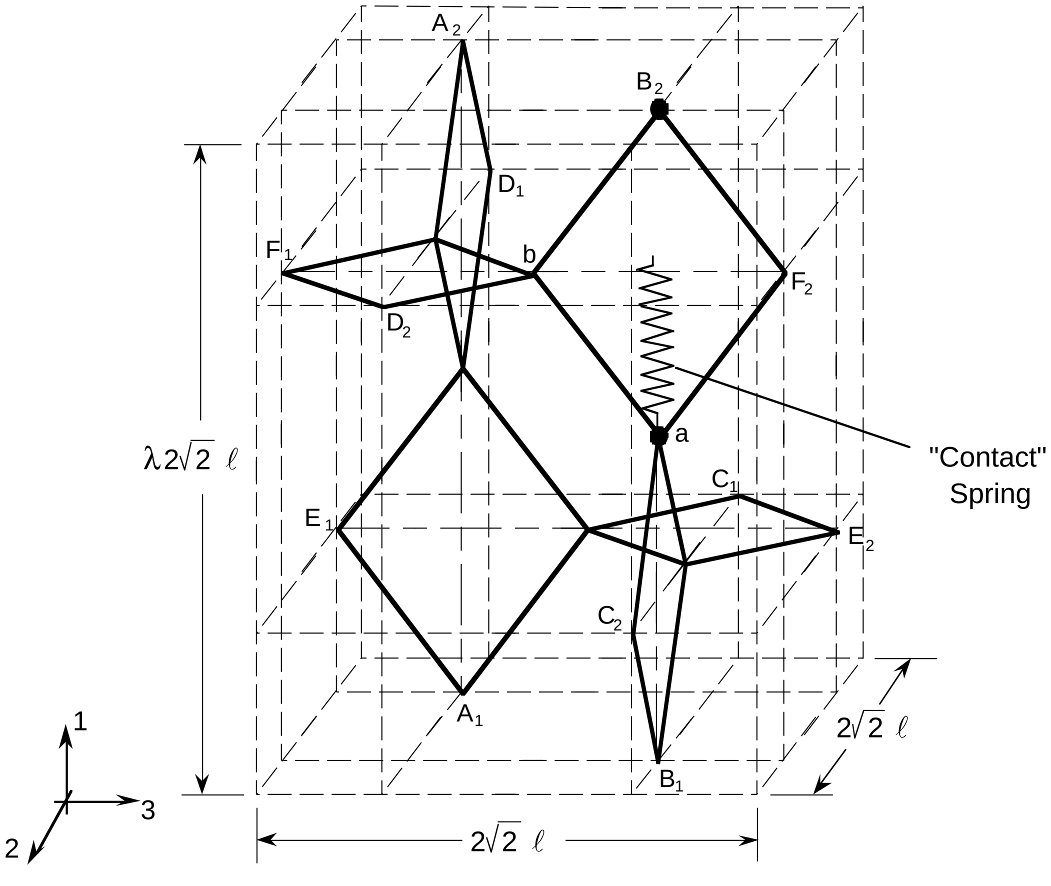

Figure 8.1 Characteristic cell showing placement of a “contact” spring introduced in direction of loading in a typical vertical rhombus.

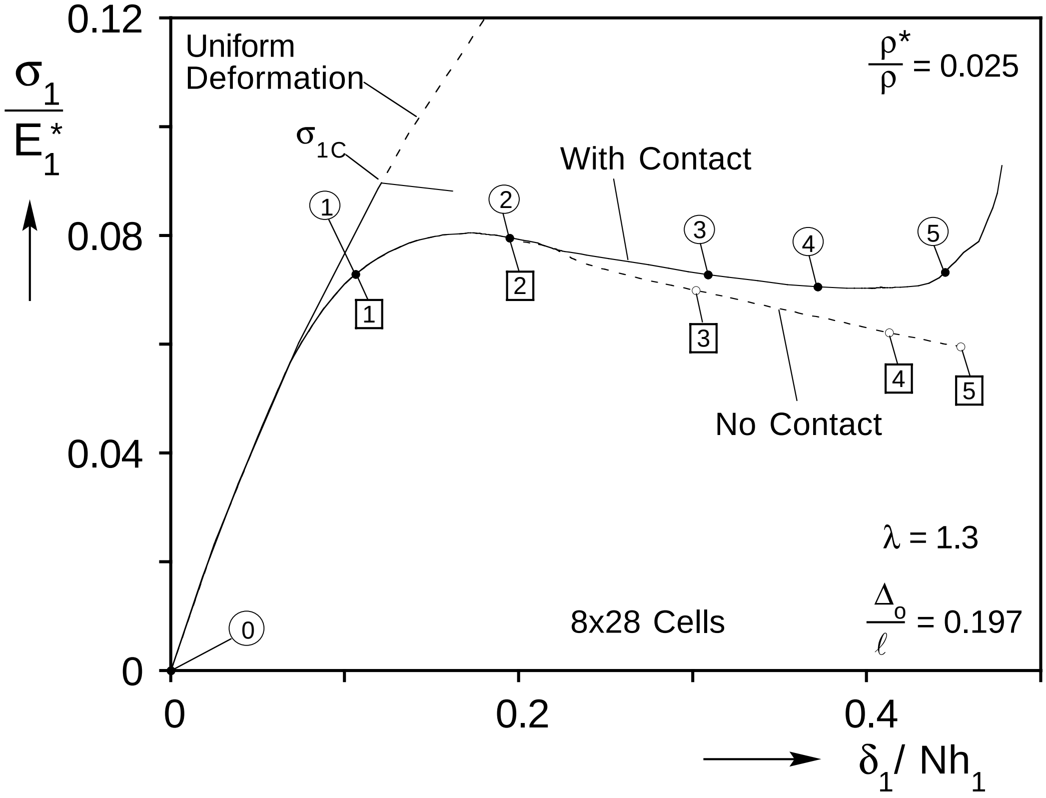

Figure 8.2 (a) Stress-displacement response of a finite size foam micro section with and without contact springs.

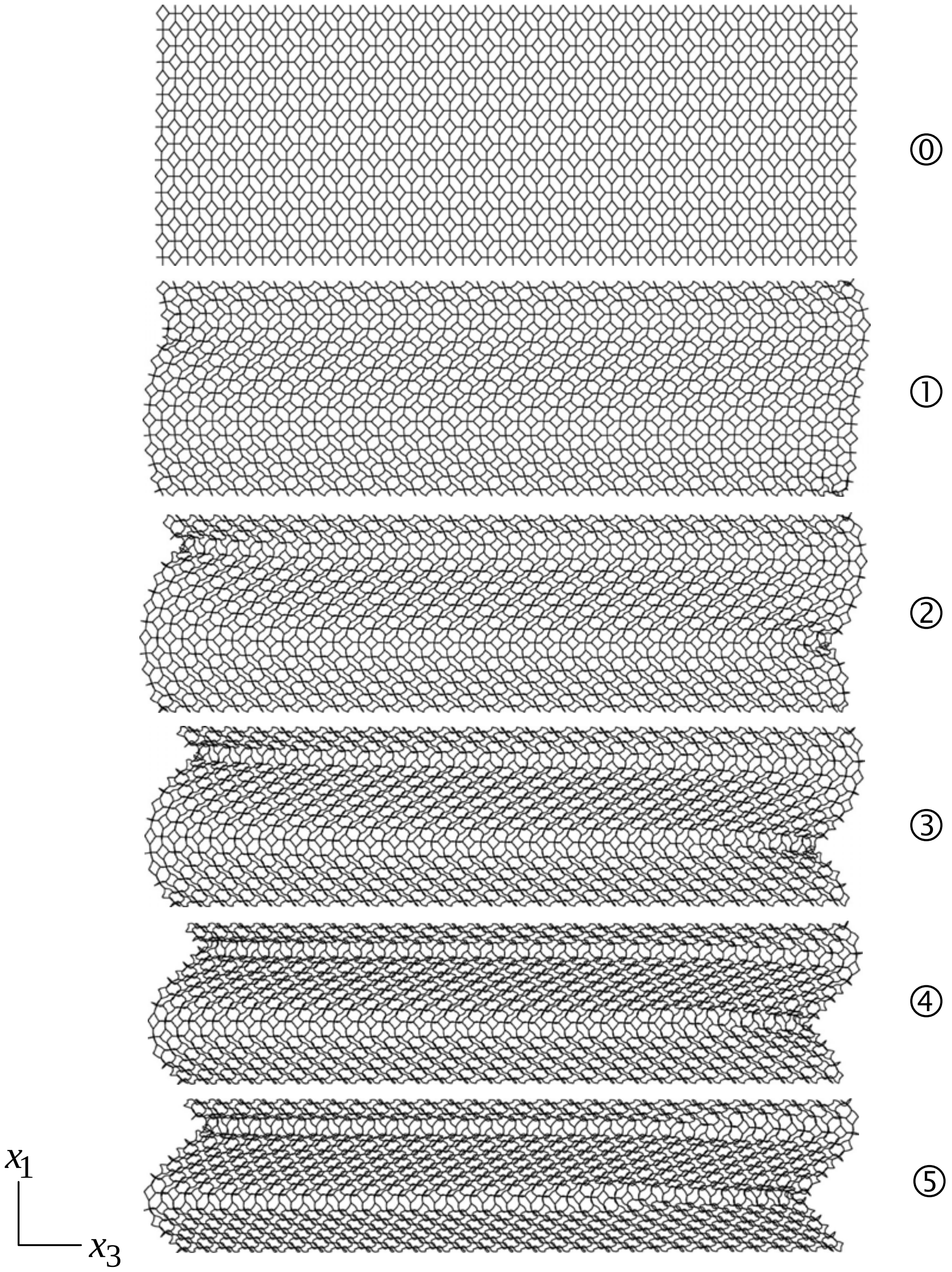

Fig.ure 8.2 (b) Sequence of deformed configurations corresponding to response in Figure 8.2a in the presence of contact springs.

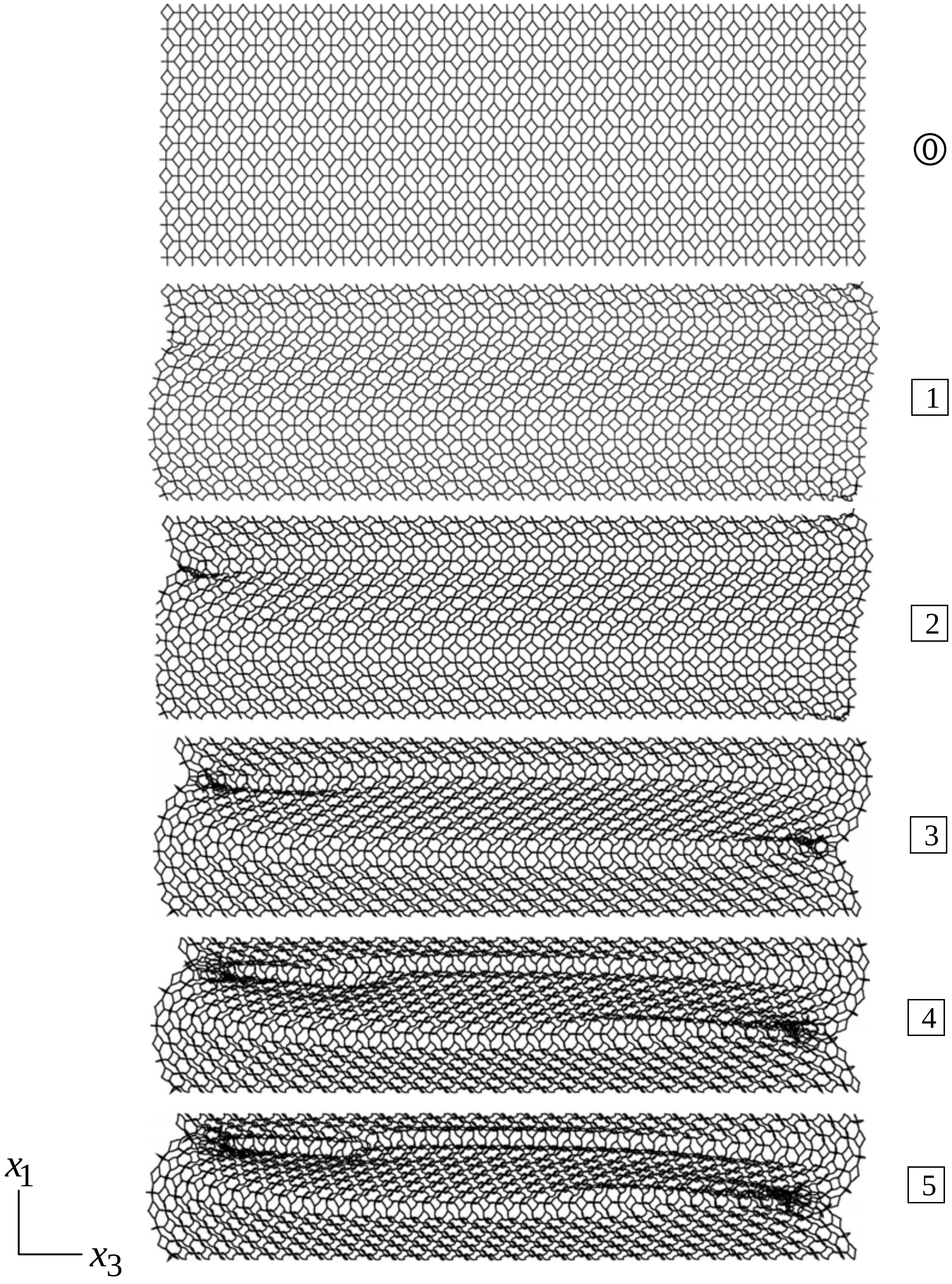

Figure 8.2 (c) Sequence of deformed configurations corresponding to response in Figure 8.2a in the absence of contact springs.

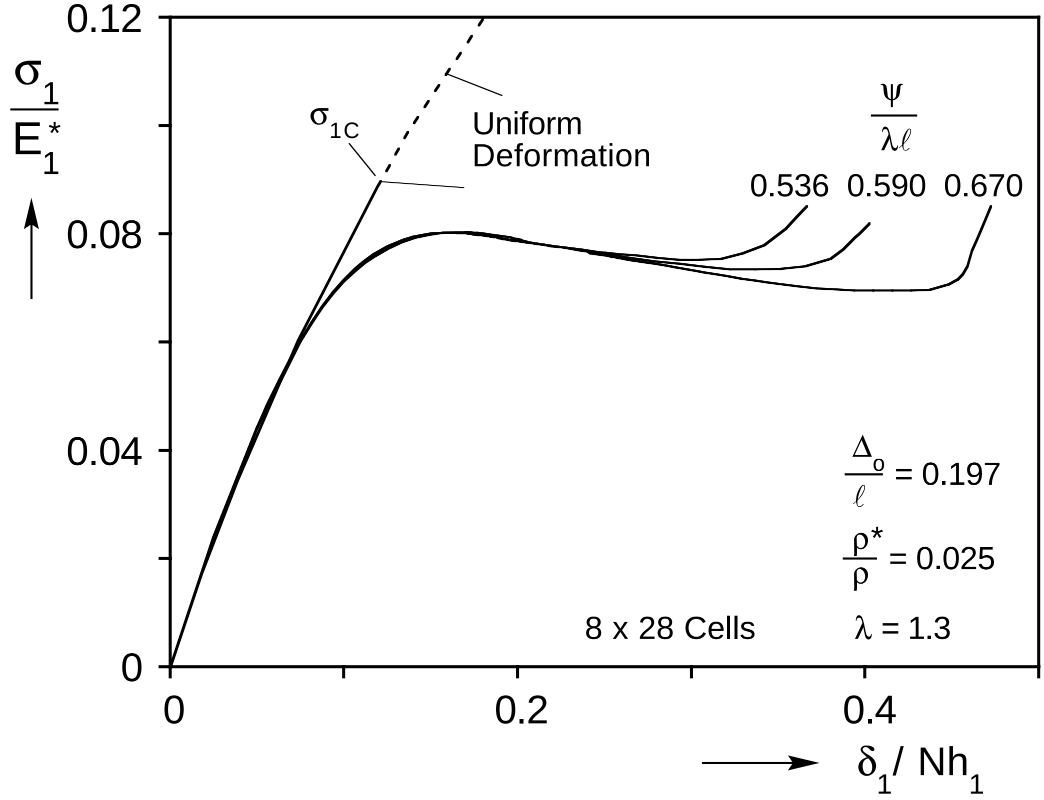

Figure 8.3 Crushing responses of a finite size foam micro section in rise direction for different values of contact variable ψ.

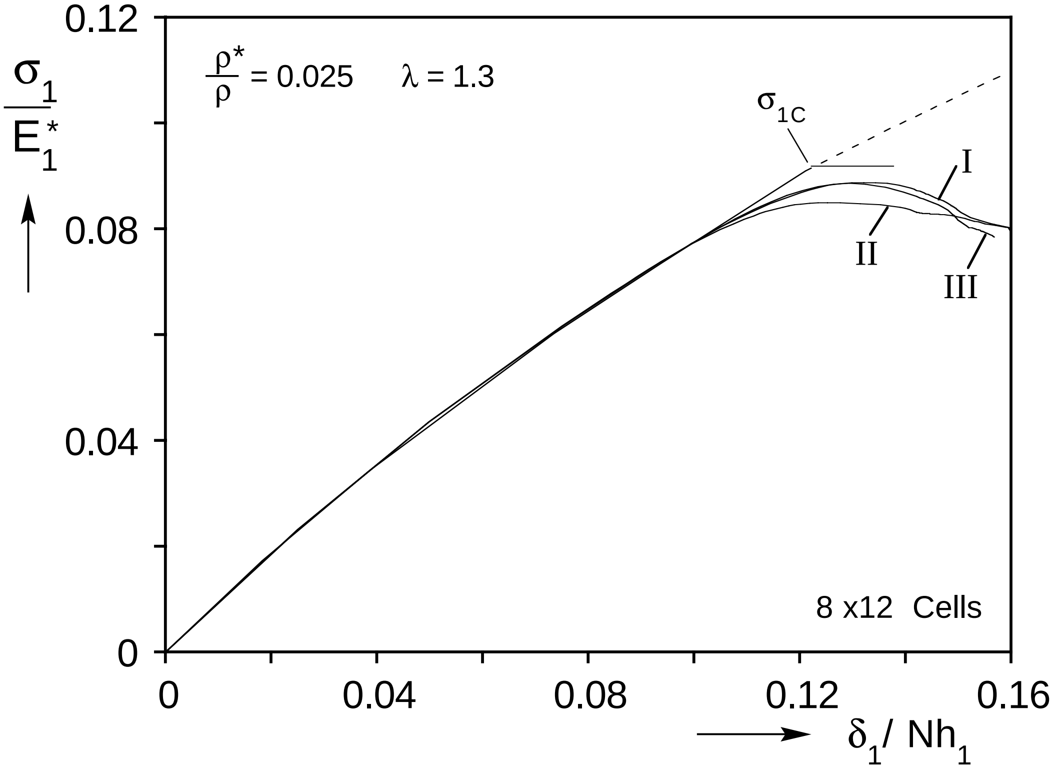

Figure 8.4 (a) Stress-displacement response of finite size foam micro sections disturbed by side forces at locations shown in Figure 8.4b

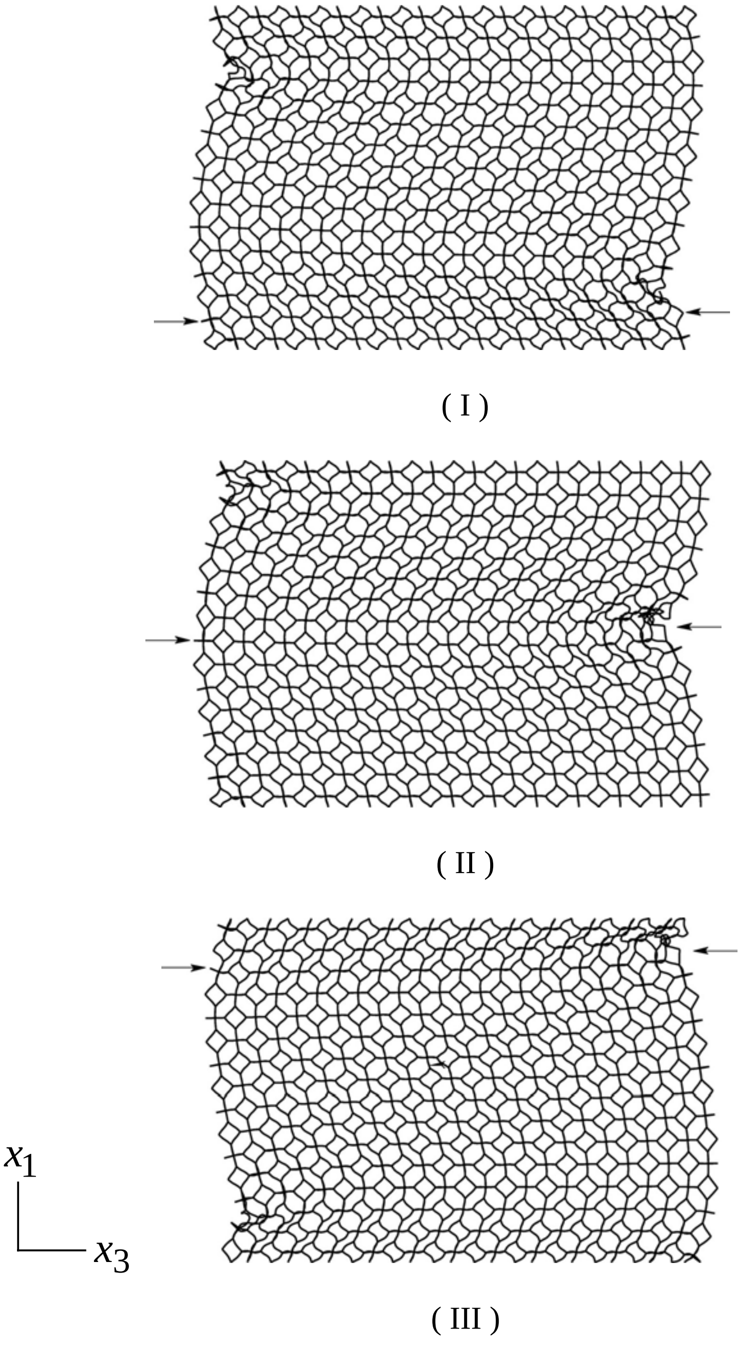

Figure 8.4 (b) Deformed configurations corresponding to points just after the limit stresses of responses “I”, “II” and “III” in Figure 8.4a.

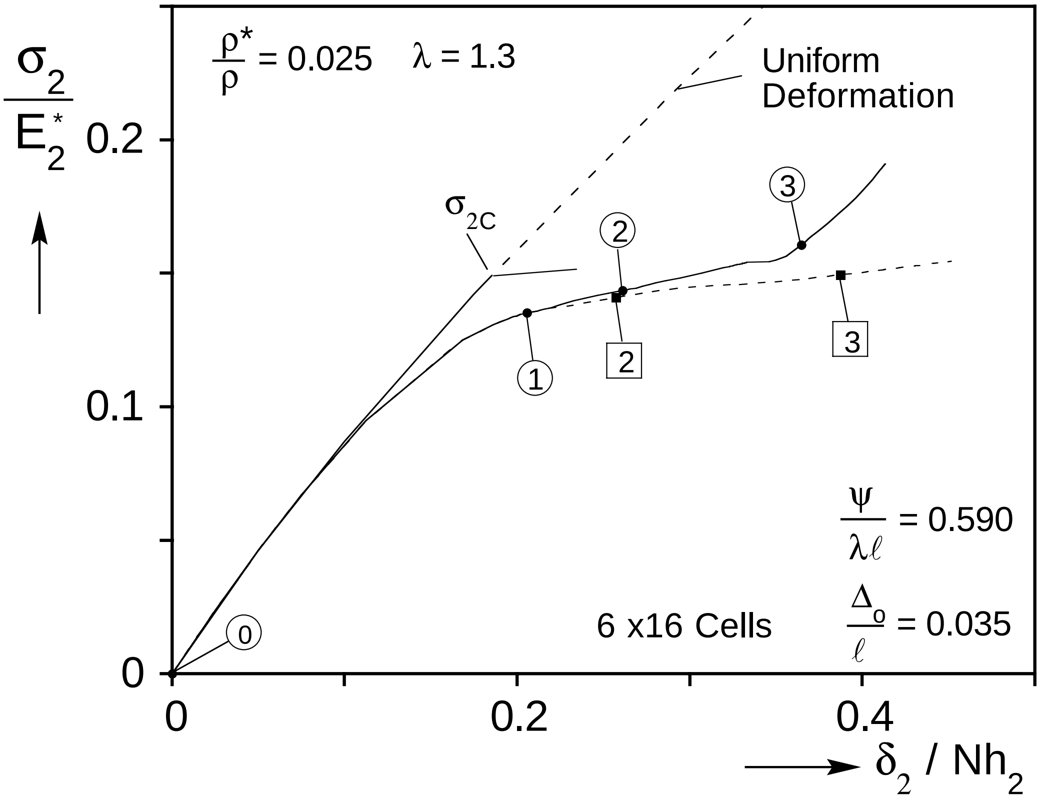

Figure 8.5 (a) Stress-displacement responses in transverse direction of a finite size foam micro section with and without contact springs.

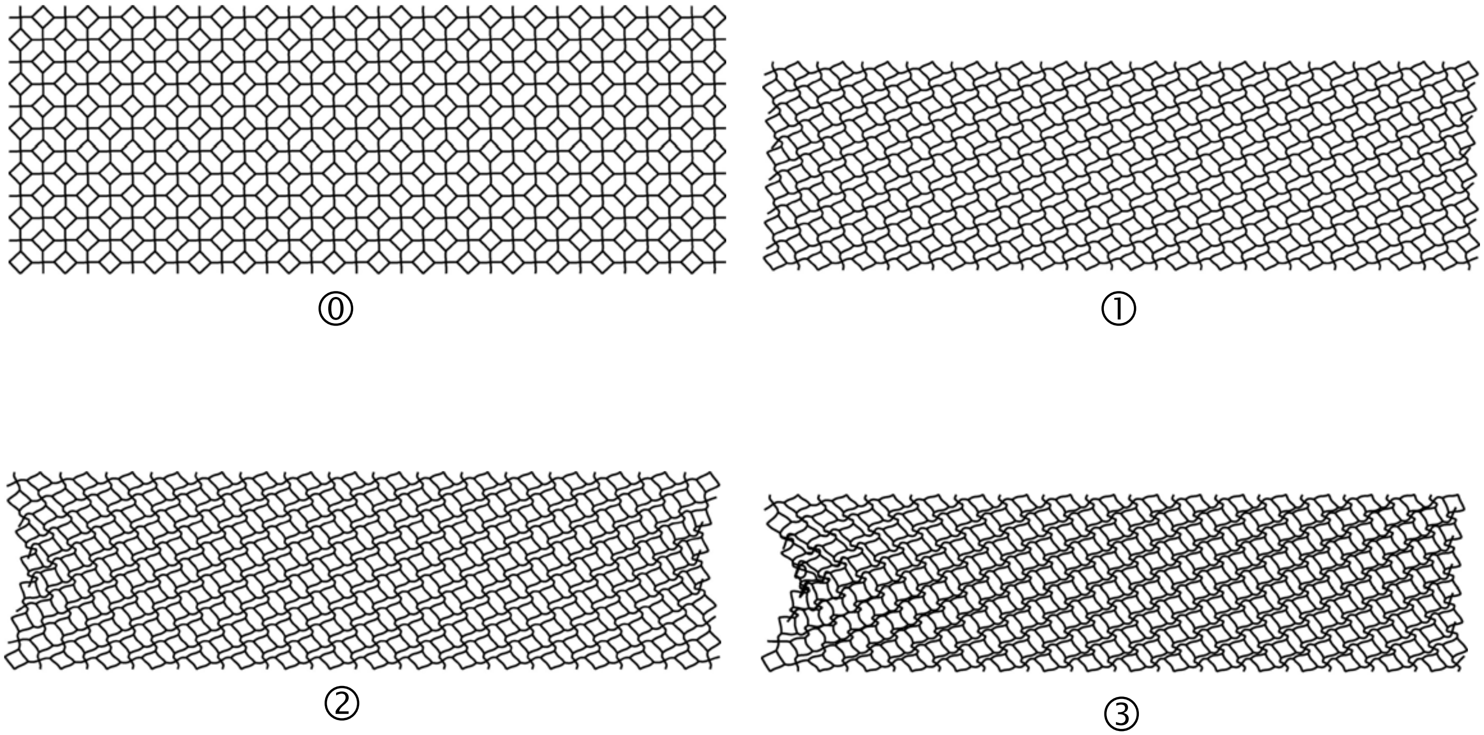

Figure 8.5 (b) Sequence of deformed configurations corresponding to response in Figure 8.5a in the presence of contact springs..

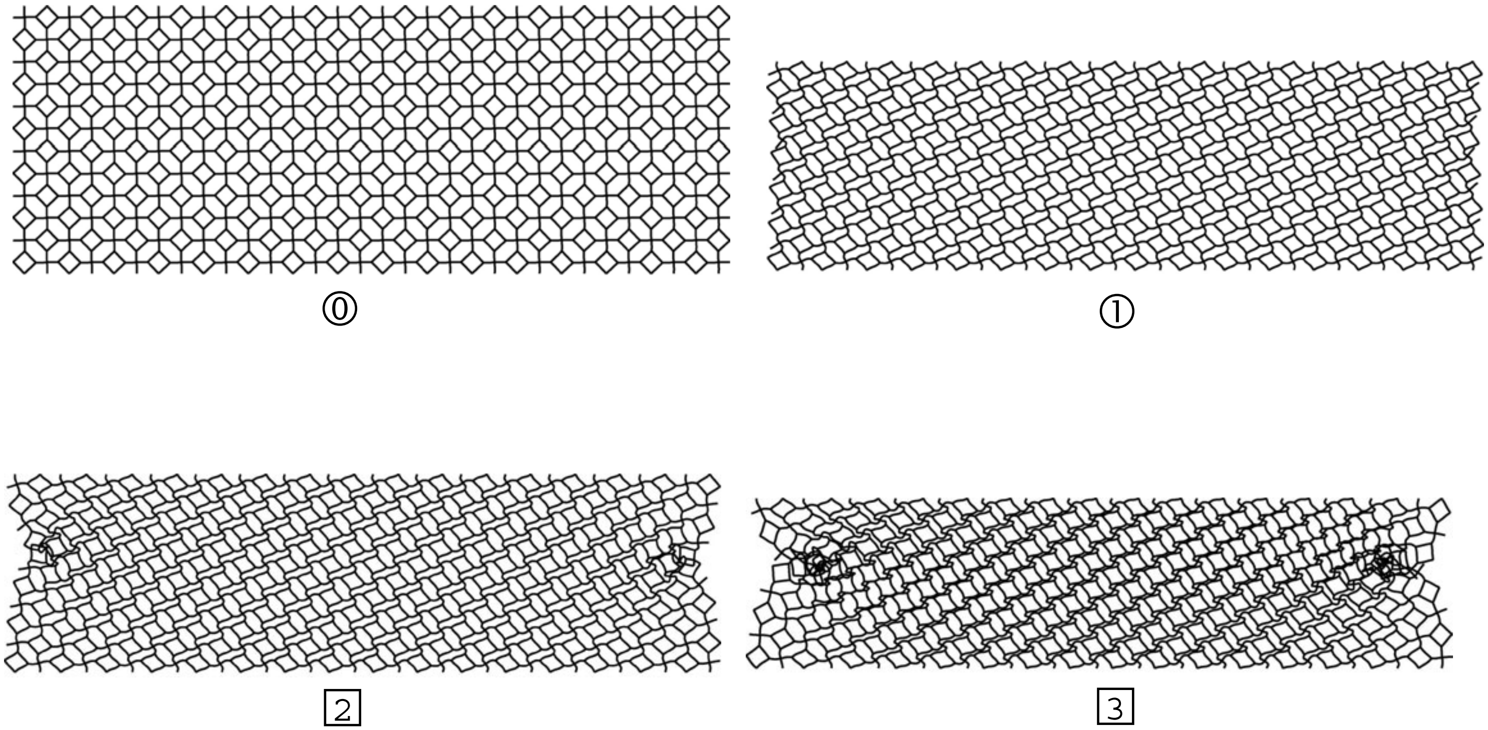

Figure 8.5 (c) Sequence of deformed configurations corresponding to response in Figure 8.5a in the absence of contact springs..

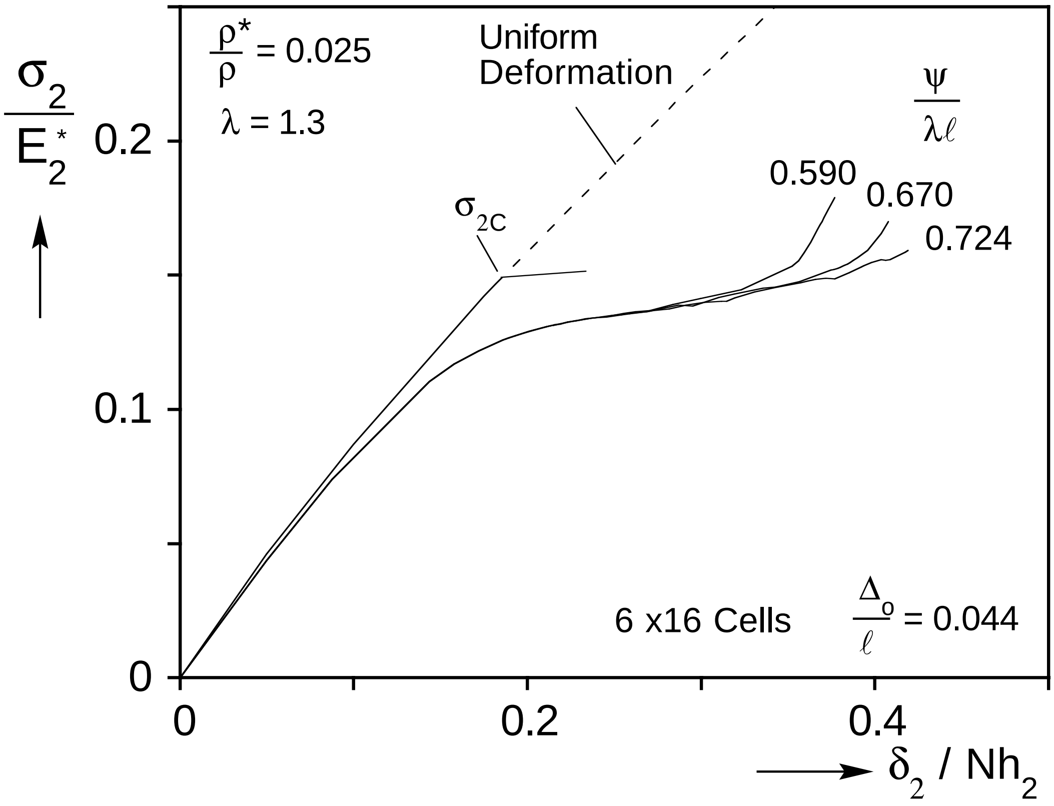

Figure 8.6 Crushing responses of a finite size foam micro section in transverse direction for different values of contact variable ψ.

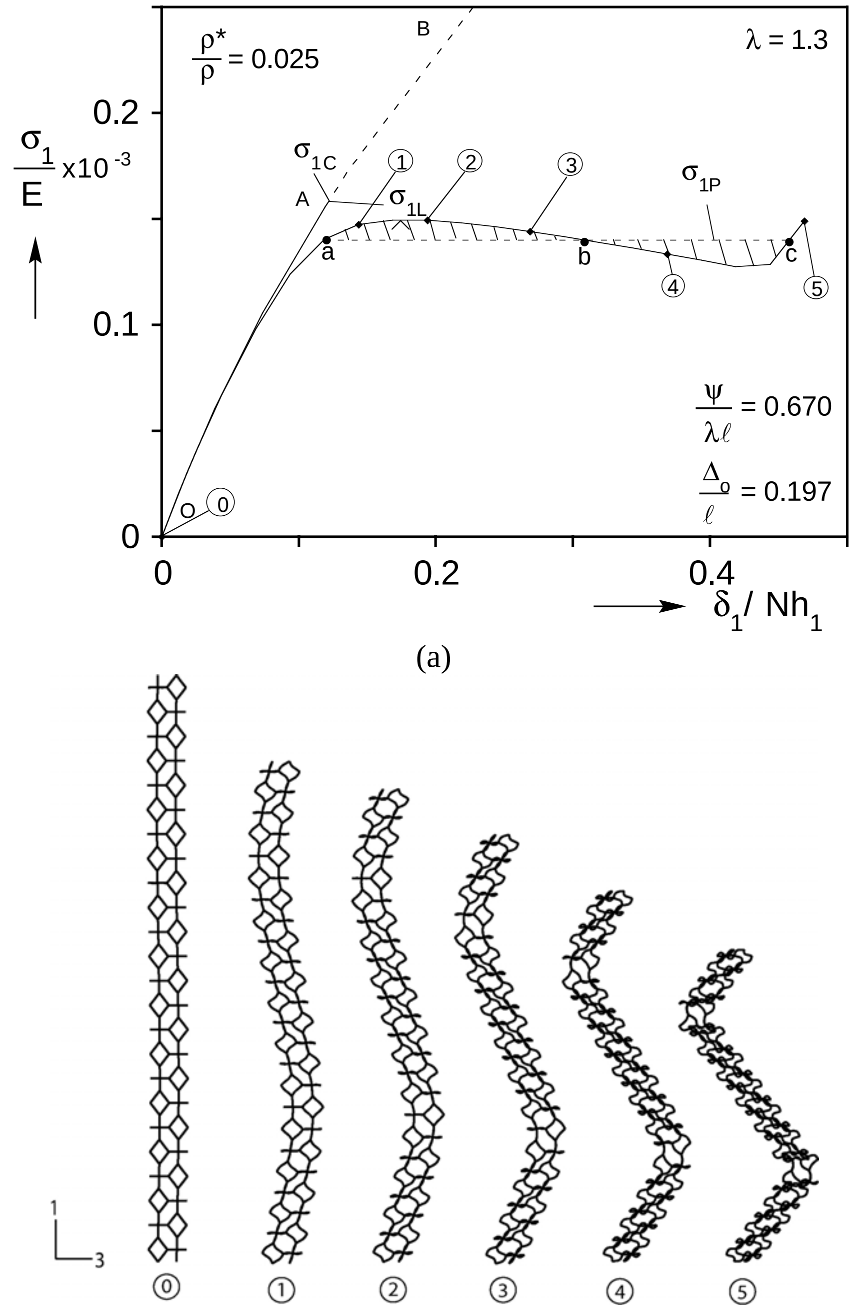

(a)

(b)

Figure 8.7 (a) Response of a fully periodic column of cells and the Maxwell construction. (b) Sequence of deformed configurations corresponding to response in Figure 8.7a.

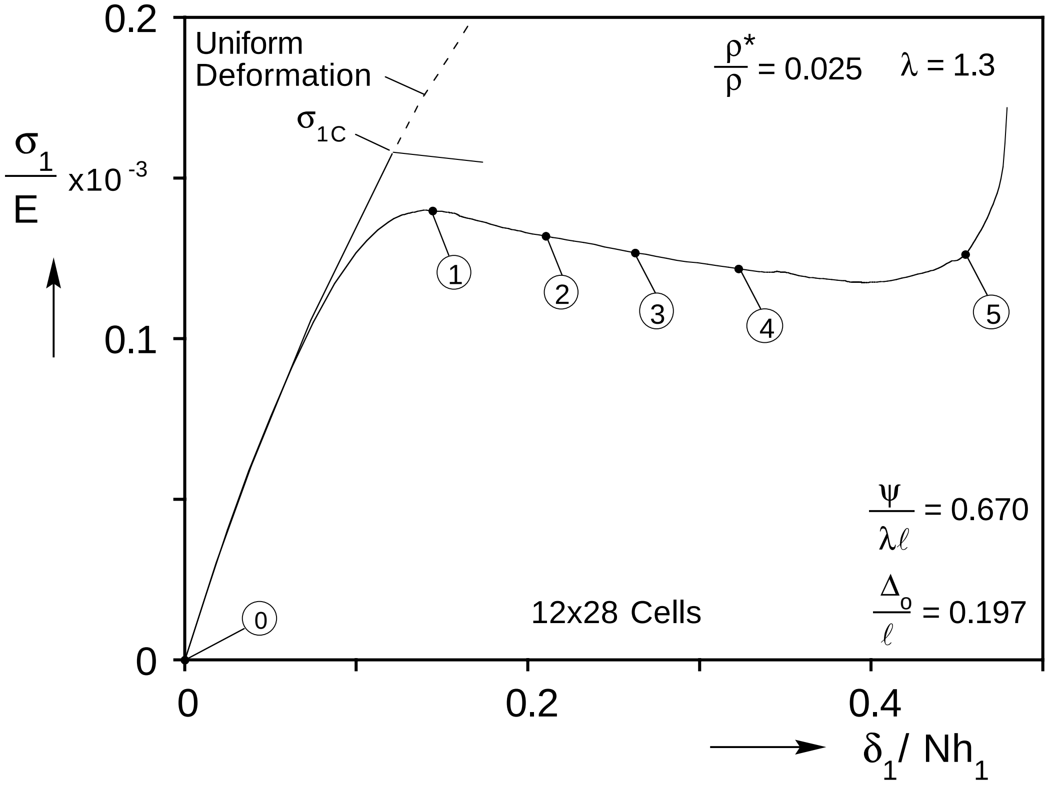

Figure 8.8 (a) Stress-displacement responses of a finite size foam microsection with contact springs.

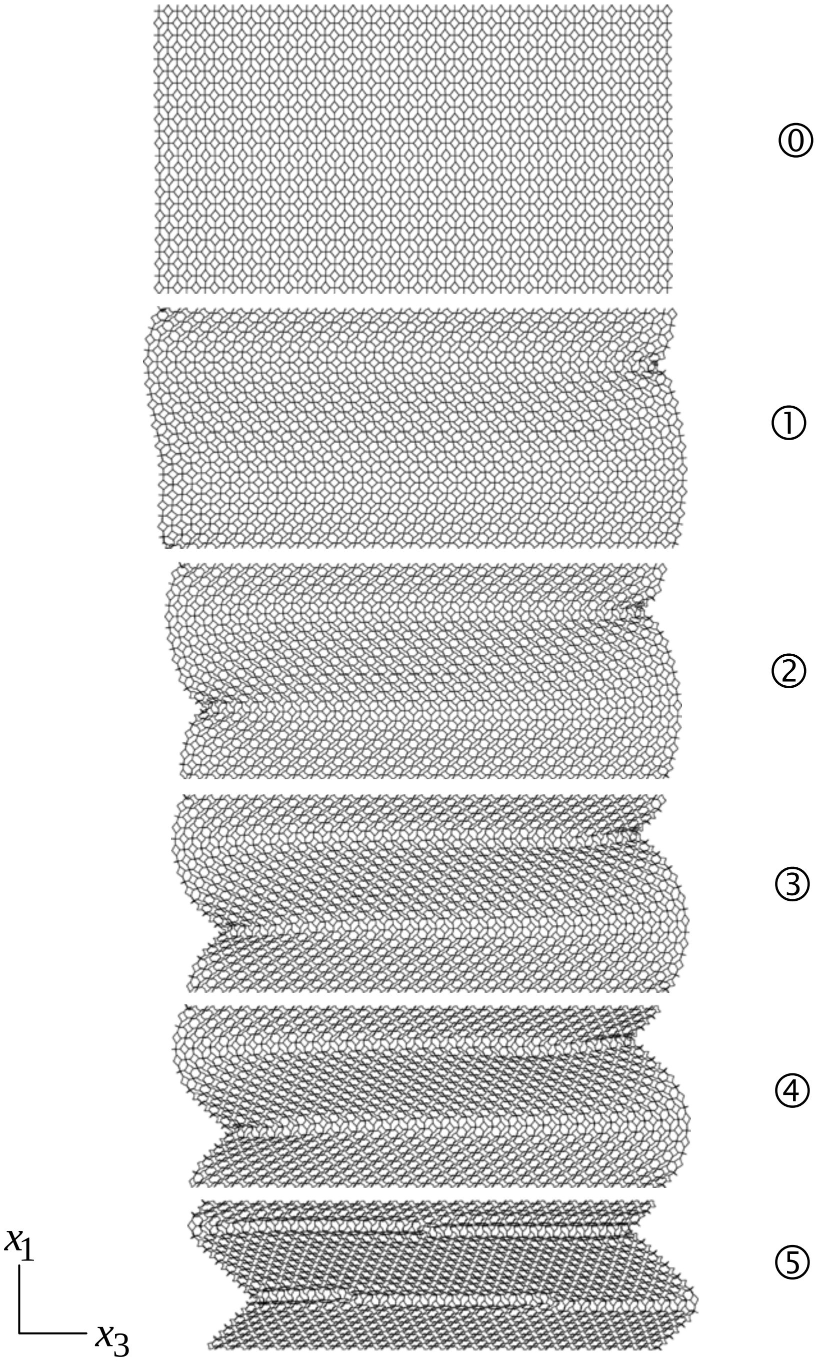

Figure 8.8 (b) Sequence of deformed configurations corresponding to response in Figure. 8.8a.

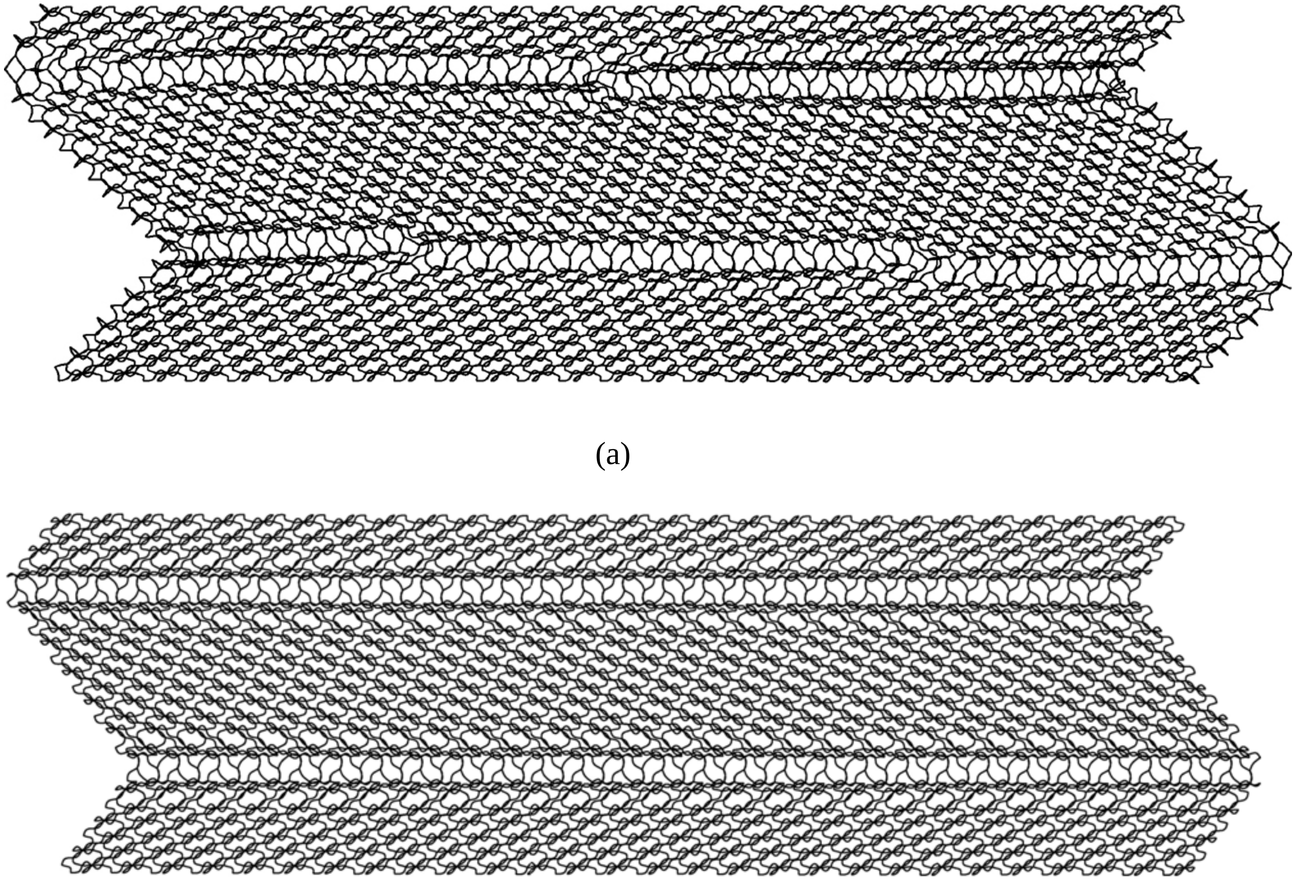

(a)

(b)

Figure 8.9 Comparison of crushed configurations from the finite width domain (a) and the fully periodic domain (b).

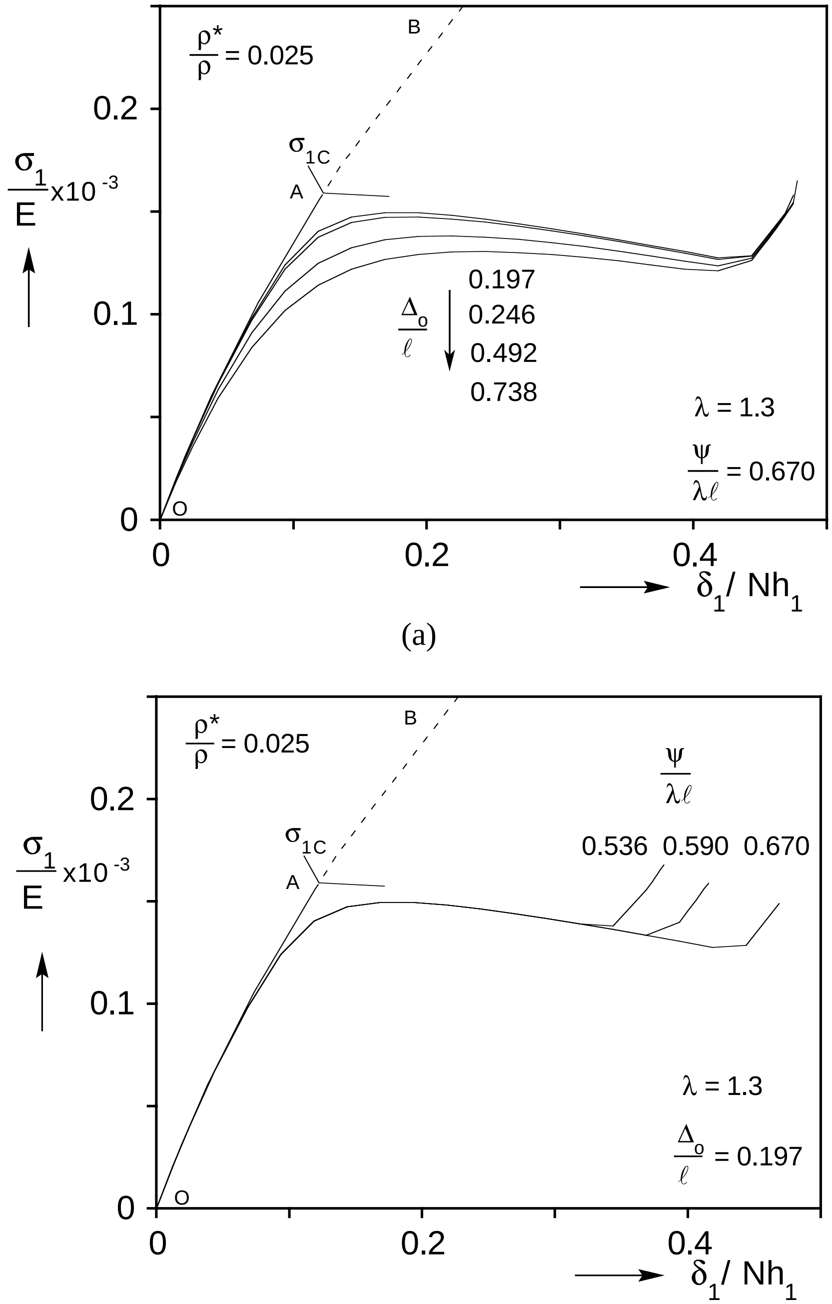

(a)

(b)

Figure 8.10 (a) Fully periodic domain responses for various imperfection amplitudes. (b) Fully periodic domain responses for various contact parameter ψ values.

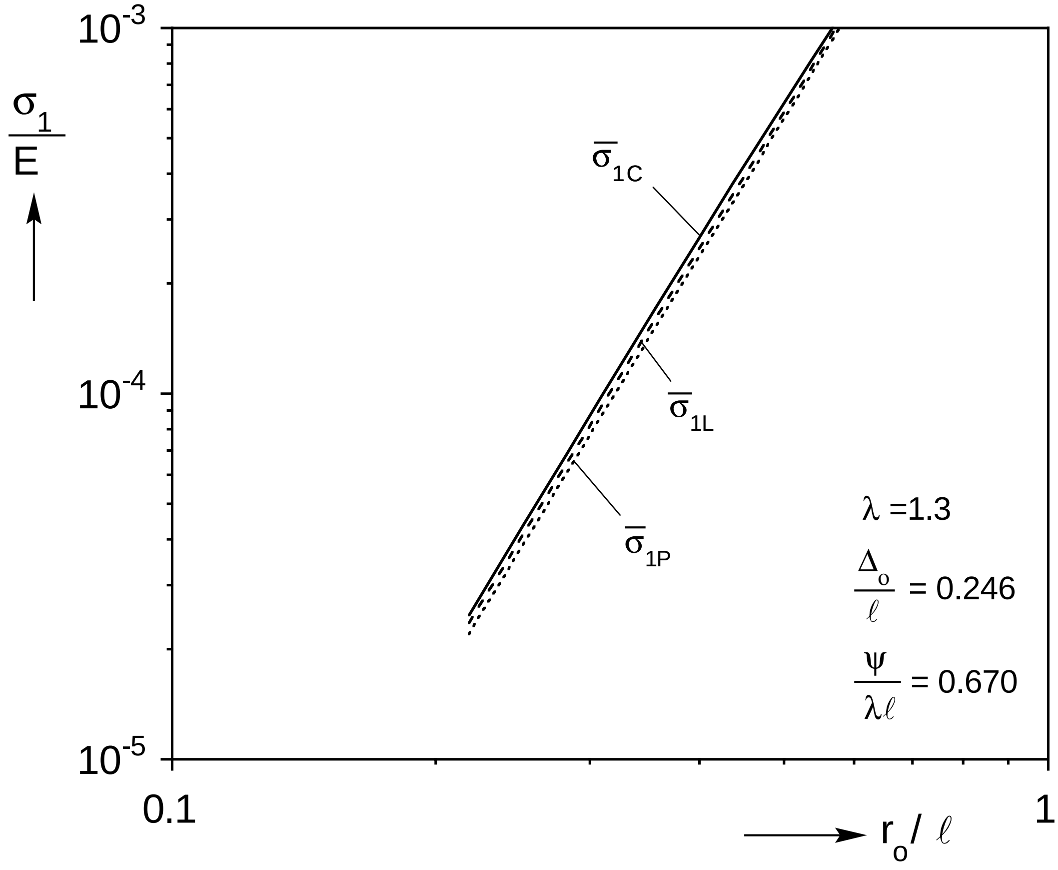

Figure 8.11 Critical stress, limit stress and crushing stress as a function of the foam geometric parameter r_o/ℓ

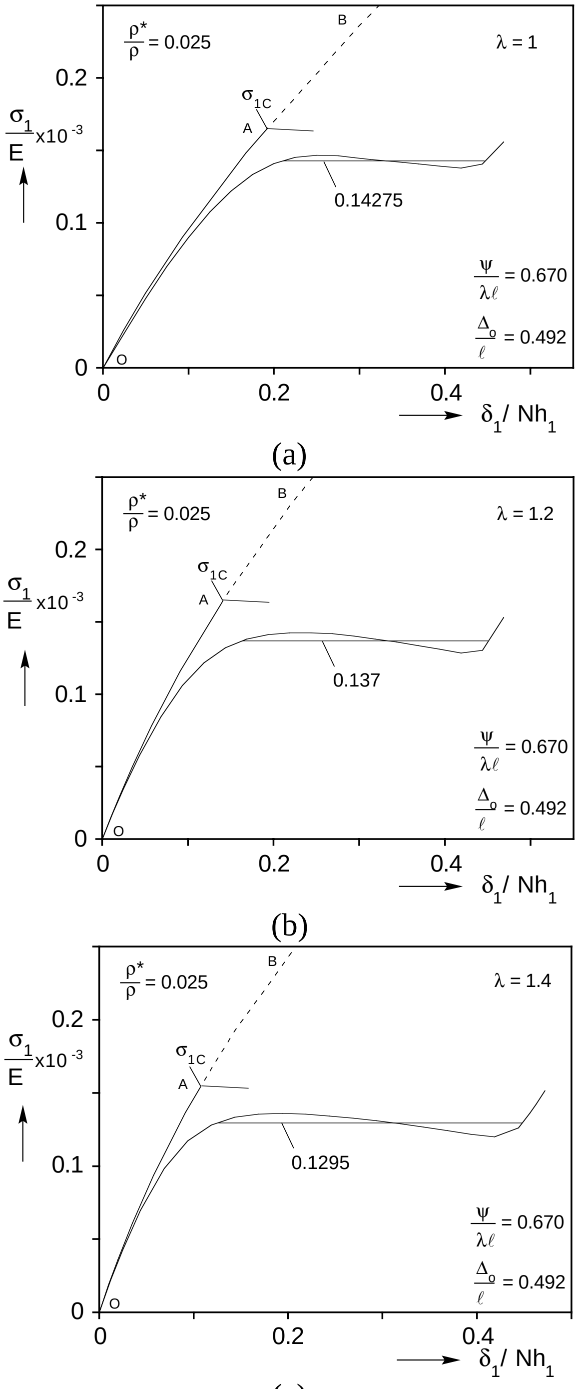

(a)

(b)

(c)

Figure 8.12 Fully periodic domain stress-displacement responses for foams of three different anisotropy values.

APPENDIX A

SECTION PROPERTIES OF PLATEAU BORDERS

Figure A.1 shows the idealized geometry of a Plateau border. ABC is the Plateau border and DEF is an equilateral triangle enclosing ABC. Let O be the center of gravity of the ABC (corresponds to cg of DEF). Let the y- and z-axes passing through O be the neutral axes of DEF. It is easy to prove that the two axes are the neutral axes of ABC also, because the centroids of the three circular sectors (ABF, BCD and ACE) are vertices of another equilateral triangle with the y-axis and z-axis being the neutral axes.

A.1 Cross Sectional Area (A)

The area of triangle DEF is: $\Delta DEF = \sqrt{3}\ \ r^2 .$ (A.1)

The area of the circular sector BCD is: $\mathrm{A}BCD = \frac{\pi}{6}\ \ r^2 .$ (A.2)

Then the area of the Plateau border ABC is calculated as:

$$\mathrm{A}ABC = \Delta DEF - 3\mathrm{A}BCD = (\sqrt{3} - \frac{\pi}{2})\ \ r^2 . \tag{A.3}$$

A.2 Moment of Inertia About the y-Axis (I_y)

$$I_y^{DEF} = \frac{\sqrt{3}}{6}\ \ r^4 . \tag{A.4}$$

$$\begin{aligned} I_y^{BCD} &= \frac{r^4}{4}(\frac{\pi}{6} + \frac{\sqrt{3}}{4}) - \frac{\pi}{6} r^2 (\frac{2r}{\pi})^2 + \frac{\pi}{6} r^2 [(\frac{2}{\sqrt{3}} - \frac{2}{\pi}) r]^2 \\ &= \frac{r^4}{8}(\frac{\pi}{3} + \frac{\sqrt{3}}{2}) + \frac{2r^4}{9}(\pi - 2\sqrt{3}) . \end{aligned} \tag{A.5}$$

$$I_y^{ABF} = \frac{r^4}{4}(\frac{\pi}{6} - \frac{\sqrt{3}}{8}) - \frac{\pi}{6}r^2(\frac{r}{\pi})^2 + \frac{\pi}{6}r^2[(\frac{1}{\sqrt{3}} - \frac{1}{\pi})r]^2$$

$$= \frac{r^4}{8}(\frac{\pi}{3} - \frac{\sqrt{3}}{4}) + \frac{r^4}{18}(\pi - 2\sqrt{3}). \tag{A.6}$$

Then moment of inertia of the Plateau border ABC about y axis is:

$$I_y^{ABC} = I_y^{DEF} - I_y^{BCD} - 2I_y^{ABF} = (\frac{5\sqrt{3}}{6} - \frac{11\pi}{24})r^4. \tag{A.7}$$

A.3 Moment of Inertia About the z-Axis (I_z)

$$I_z^{DEF} = \frac{\sqrt{3}}{6}\ r^4. \tag{A.8}$$

$$I_z^{BCD} = \frac{r^4}{4}(\frac{\pi}{6} - \frac{\sqrt{3}}{4}). \tag{A.9}$$

$$I_z^{ABF} = \frac{r^4}{4}(\frac{\pi}{6} + \frac{\sqrt{3}}{8}) - \frac{\pi}{6}r^2(\frac{\sqrt{3}r}{\pi})^2 + \frac{\pi}{6}r^2[(1 - \frac{\sqrt{3}}{\pi})r]^2$$

$$= \frac{r^4}{8}(\frac{\pi}{3} + \frac{\sqrt{3}}{4}) + \frac{r^4}{6}(\pi - 2\sqrt{3}). \tag{A.10}$$

Then,

$$I_z^{ABC} = I_z^{DEF} - I_z^{BCD} - 2I_z^{ABF} = (\frac{5\sqrt{3}}{6} - \frac{11\pi}{24})r^4. \tag{A.11}$$

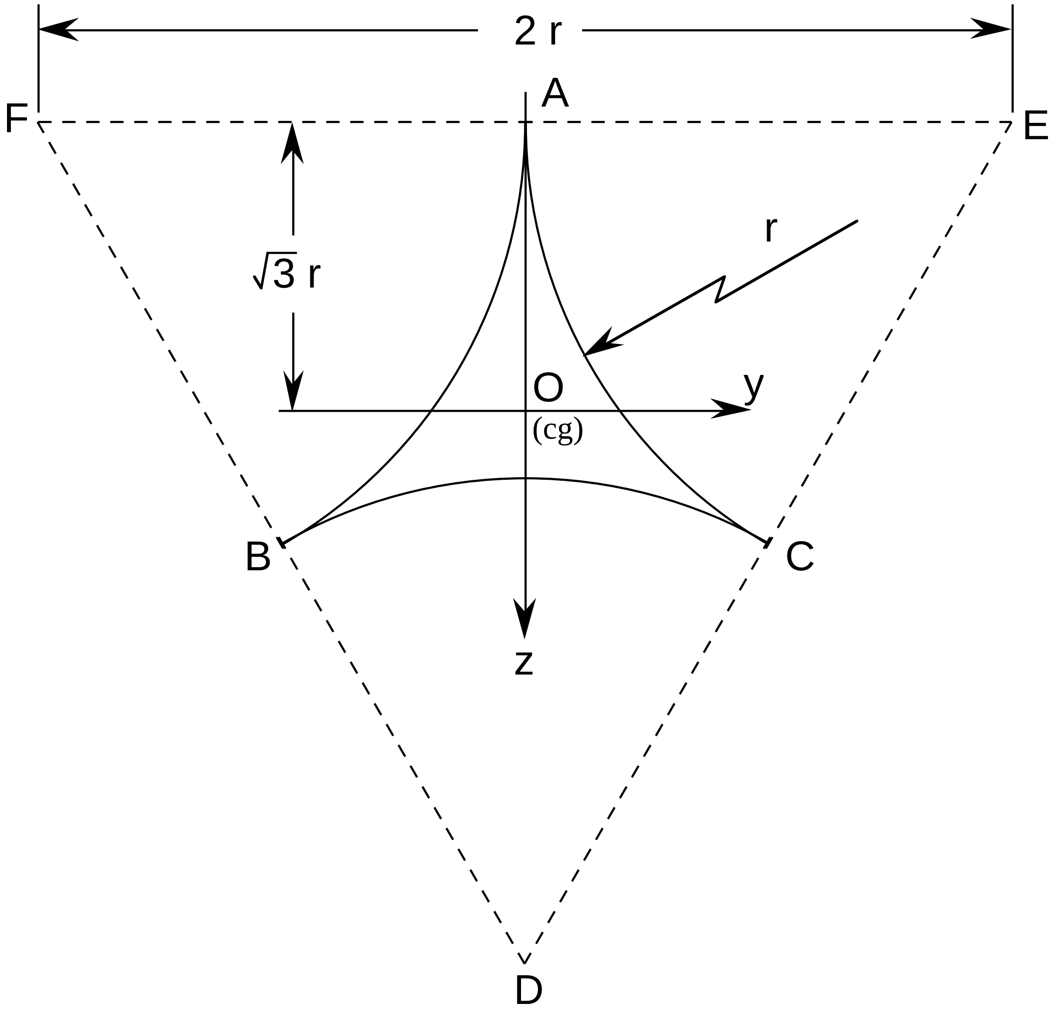

Figure A.1 Plateau border ABC and equilateral triangle DEF.

APPENDIX B

CORRECTION FOR MATERIAL AT NODES

In actual foams the nodes have smooth curved surfaces as shown in Figure 2.5. In a Kelvin cell nodes are formed by the intersection of four ligaments. When ligaments are idealized as beams, a node is formed by the intersection of four beams with their centroidal axes joining at the same point, the center of the node (Figure 4.5). It is necessary that the overlapping material be removed. At the end of a ligament, there are three curved cusp corners. Each of the corners will overlap with another ligament as shown in Figure B.1. The volume of the overlap can be approximately estimated by the following strategy. It is then subtracted for each mode of the characteristic from the total volume of solid of the cell given in (4.3).

Two ligaments CE and CF intersect at node C. The curved edges BG and DH lie in the plane formed by the axes of the two ligament. They intersect at A, where $\xi = \xi_o$ which can be determined from:

$$\tan\gamma = \frac{\sqrt{3}\left(\frac{1}{2} - \xi_o\right)}{f(\xi_o)^{1/2}}\left(\frac{\ell}{r_o}\right), \tag{B.1}$$

where $f(\xi)$ is the cross sectional area distribution function of the ligament (Eqn. (2.1)). Figure B.2b shows enlarged the intersection. The overlapping parts are corners CAB and CAD. And the volume of CAB can be evaluated from the following integration:

$$V_{CAB} = \int_{\xi_o}^{1/2} S(\xi) d\xi, \tag{B.2}$$

where $S(\xi)$ is the area of the cross-hatched part of the Plateau border shown in Figure B.2c. It can be calculated as following:

$$S(\xi) = 2r(\xi)D(\xi) - D(\xi)\left[r(\xi)^2 - D(\xi)^2\right]^{1/2} - r(\xi)^2 \sin^{-1}\left(\frac{D(\xi)}{r(\xi)}\right), \tag{B.3}$$

where

$$D(\xi) = \frac{r(\xi)}{\sqrt{3}} - \frac{\left(\frac{1}{2} - \xi\right)\ell}{\tan\gamma}. \tag{a}$$

Figure B.1 shows that it is not possible to align all edges of the four intersecting ligaments (two pairs of edges are aligned and four pairs are not). Despite this, we will apply this volume correction scheme to all ligament edges. This approximation introduces only a small error to the calculation of the volume of solid in a cell.

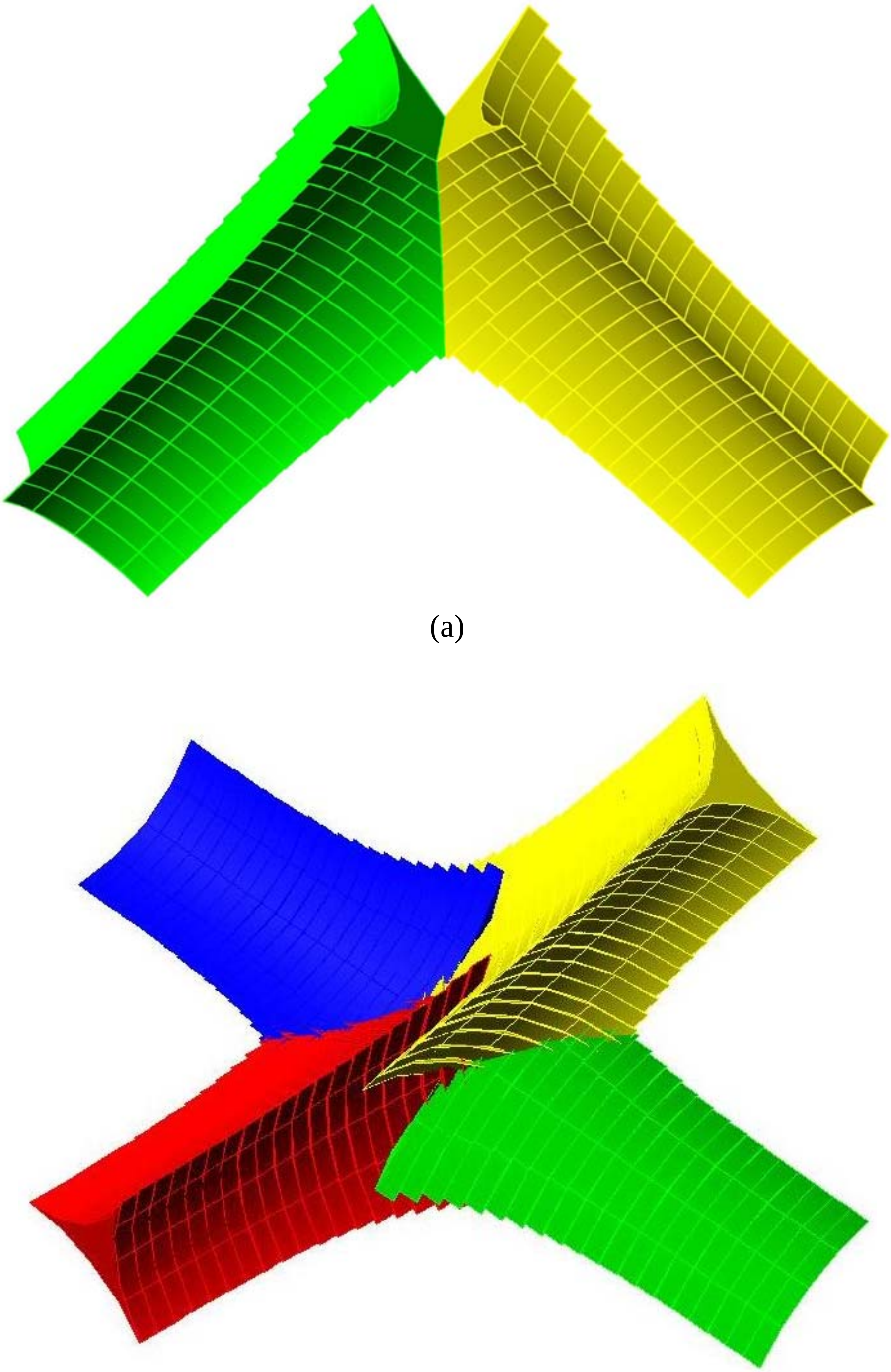

(a)

Figure B.1 (a) Two ligaments join at a node with a pair of edges aligned. (b) Four ligaments intersecting each other at a node.

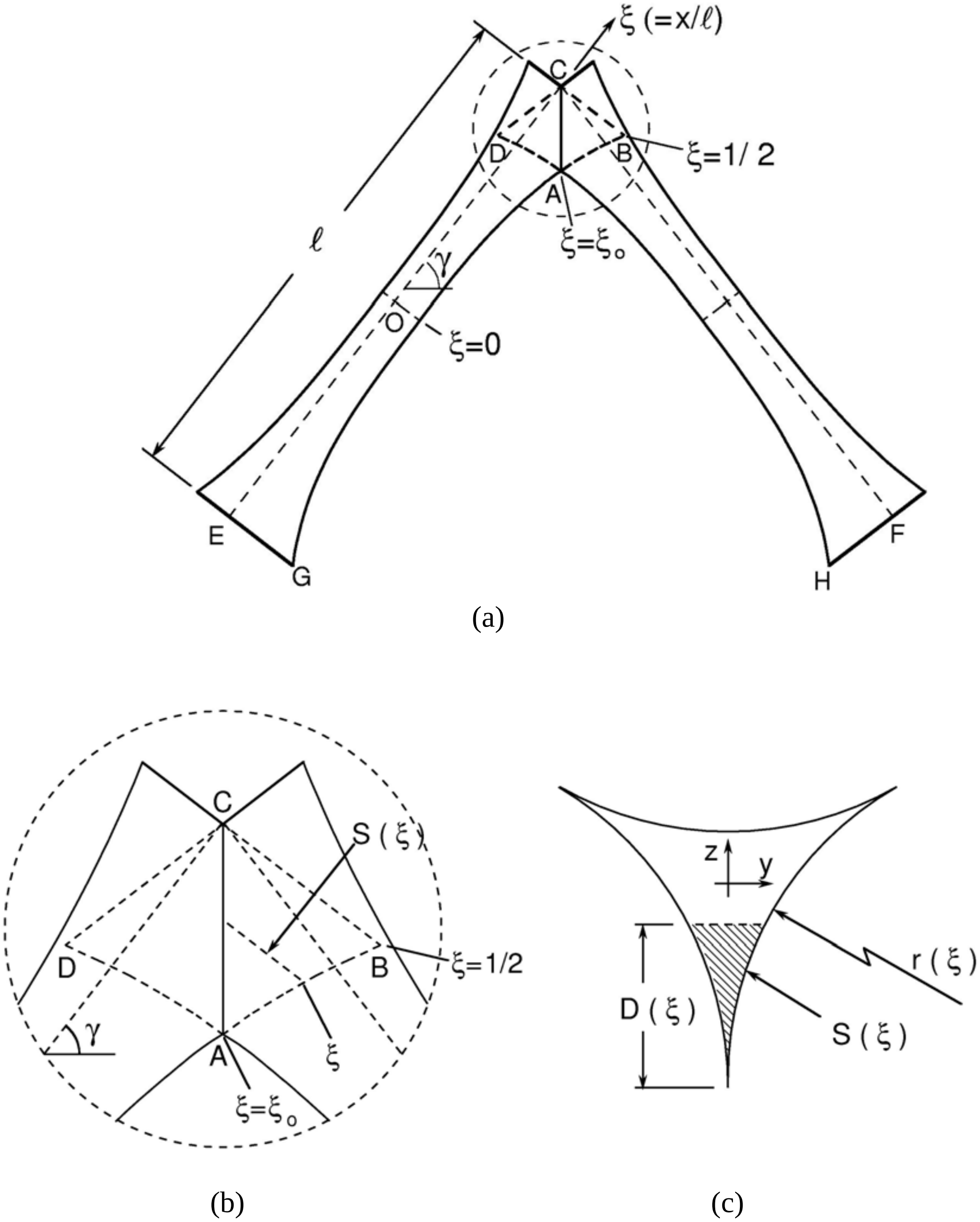

(a)

(b)

(c)

Figure B.2 (a) Two ligaments intersecting each other. (b) The enlarged intersection parts. (c) Shadow area in a cross section at ξ.

APPENDIX C

ANALYTICAL EXPRESSION FOR ELASTIC MODULUS

The initial elastic moduli ($E_1^*,\ E_2^*,\ G_{12}^*,\ G_{23}^*,\ \kappa^*,\ \nu_{12}^*,\ \nu_{21}^*,\ \nu_{23}^*$) of the anisotropic Kelvin cell foam can be calculated analytically using linear kinematics. The anisotropic Kelvin cell model was introduced in Chapter 4, Figure 4.4, where the ligaments are modeled as beams with Plateau border cross sections. The cross sectional area variation along the length is governed by the function in Eq. (2.1). The following geometric parameters will be found useful:

$$\lambda = \tan\alpha, \qquad \bar{r} \equiv \frac{r_o}{\ell}, \qquad L = \frac{\ell}{\sqrt{2}\cos\alpha}. \tag{C.1}$$

where L is the length of ligaments with projection in the rise direction and ℓ is the length of ligaments in the $x_2 - x_3$ plane.

C.1 Elastic Modulus in the rise direction (E_1^*)

In view of the symmetry and periodicity of the Kelvin cell foam, E_1^* can be evaluated by simply analyzing one ligament with projection in the rise direction as shown in Figure C.1. Figure C.1b shows the free-body diagram of a typical ligament (AB). Let P be the vertical force carried by the ligament. The following moment, axial force, shear force and torque develop in the beam

$$M(\xi) = M_o - (\frac{1}{2} - \xi)PL\cos\alpha,\ N(\xi) = -P\sin\alpha, \tag{a}$$

$$V(\xi) = P\cos\alpha \text{ and } T(\xi) = 0,$$

where $\xi = x/L$. Using the boundary condition $\theta_A = \dfrac{\partial U}{\partial M_o} = 0$

$$M_o = \frac{PL}{2}\cos\alpha. \tag{b}$$

The relative displacement between A and B in the x_1-direction is

$$\begin{aligned} \Delta_1 = u_{1B} - u_{1A} &= \frac{PL^3\cos^2\alpha}{EC_I A_o^2}C_1 + \frac{PL\sin^2\alpha}{EA_o}C_2 + \frac{\beta PL\cos^2\alpha}{GA_o}C_2 \\ &= \frac{PL^3\cos^2\alpha}{EC_I A_o^2}C_1 + \frac{PL\sin^2\alpha}{EA_o}C_2\left[1 + \frac{2\beta(1+\nu)}{\lambda^2}\right]. \end{aligned} \tag{c}$$

The foam strain and stress in the x_1-direction are respectively

$$\varepsilon_1 = \frac{\Delta_1}{L\sin\alpha} \quad \text{and} \quad \sigma_1 = \frac{P}{4L^2\cos^2\alpha}. \tag{d}$$

Thus, the elastic modulus E_1^* is given by

$$E_1^* = \frac{\sigma_1}{\varepsilon_1} = \frac{\lambda P}{4\Delta_1 L\cos\alpha}. \tag{e}$$

Substitute Δ_1 from (c) into (e),

$$\frac{E_1^*}{E} = \frac{C_I C_A^2 \sin\alpha \ \bar{r}^4}{C_1 + 2C_I C_A C_2[\sin^2\alpha + 2\beta(1+\nu)\cos^2\alpha] \ \bar{r}^2}. \tag{C.2}$$

When the shear effect is neglected ($\beta = 0$) (C.2) becomes:

$$\frac{E_1^*}{E} = \frac{C_I C_A^2 \sin\alpha \ \bar{r}^4}{C_1 + 2C_I C_A C_2 \sin^2\alpha \ \bar{r}^2}. \tag{C.3}$$

C.2 Poisson Ratio (ν_{12}^{*})

In Figure C.1b the relative displacement between A and B in the x_2-direction is

$$\Delta_2 = u_{2B} - u_{2A} = \left(-\frac{PL^3}{EC_I A_o^2} C_1 + \frac{PL}{EA_o} C_2 - \frac{\beta PL}{GA_o} C_2 \right) \sin\alpha \cos\alpha . \quad \text{(a)}$$

The foam strain in the x_2-direction is

$$\varepsilon_2 = \frac{\Delta_2}{2L\cos\alpha}. \quad \text{(b)}$$

Then the Poisson ratio ν_{12}^{*} is given by:

$$\nu_{12}^{*} = -\frac{\varepsilon_2}{\varepsilon_1} = \frac{\lambda^2}{2}\left[\frac{C_1 - 2C_I C_A C_2 \cos^2\alpha [1 - 2\beta(1+\nu)]\ \bar{r}^2}{C_1 + 2C_I C_A C_2 \cos^2\alpha [\lambda^2 + 2\beta(1+\nu)]\ \bar{r}^2} \right]. \quad \text{(C.4)}$$

When the shear effect is neglected (C.4) becomes

$$\nu_{12}^{*} = -\frac{\varepsilon_2}{\varepsilon_1} = \frac{E_1^{*}}{E} = \frac{\lambda^2}{2}\left[\frac{C_1 - 2C_I C_A C_2 \cos^2\alpha\ \bar{r}^2}{C_1 + 2C_I C_A C_2 \cos^2\alpha\ \lambda^2\ \bar{r}^2} \right]. \quad \text{(C.5)}$$

C.3 Elastic Modulus in the transverse direction (E_2^{*})

Figure C.2a shows a square and a rhombus under compressive force P in the x_2-direction. Because of the symmetry and periodicity of the Kelvin model, E_2^{*} can be evaluated by simply analyzing two ligaments, one from the rhombus (Figure C.2b) and one from the square (Figure C.2c).

The force and moment distributions in beam AB in Figure C.2b are

$$M(\xi) = M_o - (\frac{1}{2} - \xi)PL\sin\alpha, \quad N(\xi) = -P\cos\alpha, \tag{a}$$

$$V(\xi) = P\sin\alpha \text{ and } T(\xi) = 0.$$

Using the boundary condition $\theta_A = \frac{\partial U}{\partial M_o} = 0$

$$M_o = \frac{PL}{2}\sin\alpha. \tag{b}$$

The relative displacements between A and B in the x_1- and x_2-directions are

$$\varDelta_1 = u_{1B} - u_{1A} = \left(-\frac{PL^3}{EC_I A_o^2} C_1 + \frac{PL}{EA_o} C_2 - \frac{\beta PL}{GA_o} C_2 \right) \sin\alpha\cos\alpha \tag{c}$$

and

$$\varDelta_2 = u_{2B} - u_{2A} = \frac{PL^3\sin^2\alpha}{EC_I A_o^2} C_1 + \frac{PL\cos^2\alpha}{EA_o} C_2 + \frac{\beta PL\sin^2\alpha}{GA_o} C_2. \tag{d}$$

The corresponding expressions for beam CD in Figure C.2c are:

$$M(\xi) = M_o - (\frac{1}{2} - \xi)P\ell\cos 45^\circ, \quad N(\xi) = -P\cos 45^\circ = -\frac{P}{\sqrt{2}}, \tag{e}$$

$$V(\xi) = P\sin 45^\circ = \frac{P}{\sqrt{2}} \text{ and } T(\xi) = 0, \quad \xi = x/\ell.$$

From the boundary condition $\theta_C = \frac{\partial U}{\partial M_o} = 0$

$$M_o = \frac{\sqrt{2}P\ell}{4}. \tag{f}$$

The relative displacements between C and D in the x_2- and x_3-directions are

$$\overline{\varDelta}_2 = u_{2D} - u_{2C} = \frac{P\ell^3}{2EC_I A_o^2} C_1 + \frac{P\ell}{2EA_o} C_2 + \frac{\beta P\ell}{2GA_o} C_2 \tag{g}$$

and

$$\bar{\Delta}_3 = u_{3D} - u_{3C} = \frac{P}{2E}\left(-\frac{\ell^3}{C_I A_o^2} C_1 + \frac{\ell}{A_o} C_2 - \frac{\beta E \ell}{G A_o} C_2 \right). \tag{h}$$

The foam strain and stress in the x_2-direction are

$$\varepsilon_2 = \frac{\Delta_2 + \bar{\Delta}_2}{\sqrt{2}\ell} \quad \text{and} \quad \sigma_2 = \frac{P}{2\ell^2 \tan\alpha}. \tag{i}$$

Thus, the elastic modulus E_2^* is given by:

$$E_2^* = \frac{\sigma_2}{\varepsilon_2} \quad \text{resulting in} \frac{E_2^*}{E} =$$

$$\frac{2 C_I C_A^2 \cos\alpha \;\; \bar{r}^4}{\lambda\left(C_1(\lambda^2 + \sqrt{2}\cos\alpha) + C_I C_A C_2 \left(\sqrt{2}\cos\alpha + 2\cos^2\alpha + 2\beta(1+\nu)(2\sin^2\alpha + \sqrt{2}\cos\alpha) \right) \;\bar{r}^2 \right)} \tag{C.6}$$

When the shear effect is neglected (C.6) becomes:

$$\frac{E_2^*}{E} = \frac{2 C_I C_A^2 \cos\alpha \;\; \bar{r}^4}{\lambda\left(C_1(\lambda^2 + \sqrt{2}\cos\alpha) + C_I C_A C_2 \left(\sqrt{2}\cos\alpha + 2\cos^2\alpha \right) \;\bar{r}^2 \right)} \tag{C.7}$$

C.4 Poisson Ratio (ν_{21}^*)

From Figure C.2b, the foam strain in the x_1-direction is

$$\varepsilon_1 = \frac{\Delta_1}{2L\sin\alpha} \tag{a}$$

Since $\nu_{21}^* = -\dfrac{\varepsilon_1}{\varepsilon_2}$, thus

$$\nu_{21}^* = \frac{C_1 + \left(4\beta(1+\nu) - 2\right) C_I C_A C_2 \cos^2\alpha \;\; \bar{r}^2}{C_1(\lambda^2 + \sqrt{2}\cos\alpha) + (2cos^2\alpha + \sqrt{2}\cos\alpha + 2\beta(1+\nu)(2\sin^2\alpha + \sqrt{2}\cos\alpha)) C_I C_A C_2 \;\; \bar{r}^2} \tag{C.8}$$

When the shear effect is neglected (C.8) becomes

$$\nu_{21}^{*}=\frac{C_1-2C_IC_AC_2\cos^2\alpha\ \ \bar{r}^2}{C_1(\lambda^2+\sqrt{2}\cos\alpha)+(2\cos^2\alpha+\sqrt{2}\cos\alpha)C_IC_AC_2\ \ \bar{r}^2}. \tag{C.9}$$

C.5 Poisson Ratio (ν_{23}^{*})

From Figure C.2c, the foam strain in the x_3-direction is

$$\varepsilon_3=\frac{\overline{\Delta}_3}{\sqrt{2}\ell}. \tag{a}$$

Since $\nu_{23}^{*}=-\frac{\varepsilon_3}{\varepsilon_2}$, thus

$$\nu_{23}^{*}=\frac{C_1+\left(2\beta(1+\nu)-1\right)C_IC_AC_2\ \bar{r}^2}{C_1\left(1+\frac{\lambda^2}{\sqrt{2}\cos\alpha}\right)+\left(\sqrt{2}\cos\alpha+1+2\beta(1+\nu)(\sqrt{2}\lambda\sin\alpha+1)\right)C_IC_AC_2\,\bar{r}^2}. \tag{C.10}$$

When the shear effect is neglected (C.10) becomes

$$\nu_{23}^{*}=\frac{C_1-C_IC_AC_2\ \bar{r}^2}{C_1\left(1+\frac{\lambda^2}{\sqrt{2}\cos\alpha}\right)+\left(\sqrt{2}\cos\alpha+1\right)C_IC_AC_2\,\bar{r}^2}. \tag{C.11}$$

C.6 Bulk modulus (κ^{*})

Figure C.3 shows a characteristic cell under hydrostatic stress. The bulk modulus κ^{*} can be evaluated by analyzing two ligaments, AB (Figure C.3b) and CD (Figure C.3c). The force and moment distributions in beam AB are

$$M(\xi) = M_o - (\cos\alpha - \lambda\sin\alpha)\left(\frac{1}{2} - \xi\right)PL,$$

$$N(\xi) = -2P\sin\alpha,\ V(\xi) = P\cos\alpha - \lambda P\sin\alpha \ \text{ and } \ T(\xi) = 0. \tag{a}$$

The relative displacements between A and B in the x_1- and x_2-directions are:

$$\Delta_1 = u_{1B} - u_{1A} = \frac{PL^3\cos 2\alpha}{EC_I A_o^2}C_1 + \frac{2PL\sin^2\alpha}{EA_o}C_2 + \frac{\beta PL\cos 2\alpha}{GA_o}C_2 \tag{b}$$

and

$$\Delta_2 = u_{2B} - u_{2A} = \frac{\lambda PL^3\cos 2\alpha}{EC_I A_o^2}C_1 - \frac{PL\sin 2\alpha}{EA_o}C_2 + \frac{\beta\lambda PL\cos 2\alpha}{GA_o}C_2. \tag{c}$$

Referring to beam CD in Figure C.3c,

$$M(\xi) = 0,\ N(\xi) = -\sqrt{2}\lambda P,\ V(\xi) = 0 \ \text{ and } \ T(\xi) = 0. \tag{d}$$

The relative displacements between C and D in the x_2- and x_3-directions are:

$$\overline{\Delta}_2 = u_{2D} - u_{2C} = \frac{\lambda P\ell}{EA_o}C_2 \tag{e}$$

and

$$\overline{\Delta}_3 = u_{3D} - u_{3C} = \frac{\lambda P\ell}{EA_o}C_2. \tag{f}$$

The foam strains in the x_1- and x_2-directions are:

$$\varepsilon_1 = \frac{\Delta_1}{L\sin\alpha} \quad \text{and} \quad \varepsilon_2 = \frac{\Delta_2 + \overline{\Delta}_2}{\sqrt{2}\ell}. \tag{g}$$

The foam stresses are:

$$\sigma_1 = \sigma_2 = \sigma_3 = \sigma = \frac{P}{2\ell^2}. \tag{h}$$

The bulk modulus of the foam $\kappa^* = \dfrac{\sigma}{\varepsilon_{ii}}$. Thus $\dfrac{\kappa^*}{E} =$

$$\frac{C_I C_A^2 \ \bar{r}^4}{\dfrac{\cos^2 2\alpha}{\sin\alpha\cos^4\alpha} C_1 + \left((8\sin\alpha + 2\sqrt{2}\lambda) + 4\beta(1+\nu)\dfrac{\cos^2 2\alpha}{\sin\alpha\cos^2\alpha} \right) C_I C_A C_2 \ \bar{r}^2}. \quad \text{(C.12)}$$

When the shear effect is neglected (C.12) becomes

$$\frac{\kappa^*}{E} = \frac{C_I C_A^2 \ \bar{r}^4}{\dfrac{\cos^2 2\alpha}{\sin\alpha\cos^4\alpha} C_1 + (8\sin\alpha + 2\sqrt{2}\lambda) C_I C_A C_2 \ \bar{r}^2}. \quad \text{(C.13)}$$

C.7 Shear Modulus (G_{13}^*)

If we shear the Kelvin foam in the x_1- x_3 plane the shear stresses are

$$\sigma_{13} = \sigma_{31} = \frac{P}{2\ell^2}. \quad \text{(a)}$$

Figure C.4a shows the free-body diagram of a characteristic cell. M_1 and M_2 are the moments induced by the symmetry and periodicity of the microstructure. The problem reduces to analyzing the three sections shown in Figures C.4b, C.4c and C.4d. First we find the relationship between M_1 and P. In Figure C.4b, the rotations of A and B about the x_2-axis are

$$\theta_{2B} = -\theta_{2A} = \frac{C_3 M_1 L}{2 E C_I A_o^2}. \quad \text{(b)}$$

The relative displacement between B and D in the x_1-direction is

$$\Delta_1 = u_{1B} - u_{1D} = \frac{2C_2 PL}{EA_o}. \tag{c}$$

The relative displacement between A and B in the x_3-direction is

$$\Delta_3 = u_{3A} - u_{3C} = \frac{2C_2 \lambda PL}{EA_o}. \tag{d}$$

In Figure C.4c, the rotation of A about the x_2-axis is

$$\bar{\theta}_{2A} = -\left[\frac{2(1+\nu)(1+\lambda^2)}{1+2(1+\nu)\lambda^2}\right]\frac{C_3 L}{EC_I A_o^2}\left(M_1 - \frac{PL\sin\alpha}{2}\right). \tag{e}$$

In Figure C.4d, the rotation of B about the x_2-axis is

$$\bar{\theta}_{2B} = \frac{2(1+\nu)}{1+2(1+\nu)}\frac{C_3 \ell}{EC_I A_o^2}\left(2M_1 - \frac{\lambda P\ell}{\sqrt{2}}\right). \tag{f}$$

Applying compatibility condition

$$\theta_{2B} - \theta_{2A} = \bar{\theta}_{2B} - \bar{\theta}_{2A} \tag{g}$$

leads to

$$M_1 = C_M \lambda P\ell. \tag{h}$$

In Figure C.4c, the displacement of A in the x_3-direction is

$$u_{3A} = \frac{D_1 P\ell^3}{2\sqrt{2}EC_I A_o^2 \cos^3\alpha} + \frac{C_2 \beta P\ell}{\sqrt{2}GA_o \cos\alpha}. \tag{i}$$

In Figure C.4d, the displacement of B in the x_1-direction is

$$u_{1B} = \frac{D_2 \lambda P\ell^3}{EC_I A_o^2} + \frac{C_2 \beta\lambda P\ell}{GA_o}. \tag{j}$$

Then shear strain of the characteristic domain is

$$\gamma_{13} = \frac{\Delta_1 + 2u_{1B}}{2\sqrt{2}\ell} + \frac{\Delta_3 + 2u_{3A}}{2\sqrt{2}\lambda\ell} \, . \tag{k}$$

Since $G_{13}^* = \frac{\sigma_{13}}{\gamma_{13}}$, we get $\frac{G_{13}^*}{E} =$

$$\frac{2\sin\alpha\cos^2\alpha C_I C_A^2 \ \ \bar{r}^4}{D_1 + 2\sqrt{2}D_2\sin^2\alpha\cos\alpha + 2C_I C_A C_2 \ \ \bar{r}^2[1+2\beta(1+\nu)(\cos^2\alpha + \sqrt{2}\sin^2\alpha\cos\alpha)]}$$

(C.14)

When the shear effect is neglected (C.14) becomes:

$$\frac{G_{13}^*}{E} = \frac{2\sin\alpha\cos^2\alpha C_I C_A^2 \ \ \bar{r}^4}{D_1 + 2\sqrt{2}D_2\sin^2\alpha\cos\alpha + 2C_I C_A C_2 \ \ \bar{r}^2} \, . \tag{C.15}$$

C.8 Shear Modulus (G_{23}^*)

If we shear the Kelvin foam in the x_2 - x_3 plane the shear stresses are

$$\sigma_{23} = \sigma_{32} = \frac{P}{2\ell^2} \, . \tag{a}$$

Figure C.5a shows the free-body diagram of a characteristic cell. M_1 and M_2 are the moments induced by the symmetry and periodicity of the microstructure. The problem reduces to analyzing the two sections shown in Figures C.5b and C.5c. In Figure C.5b, the rotation of B about the x_1-axis is

$$\theta_{1B} = -\frac{C_3 M_1 \ell}{2EC_I A_o^2}. \qquad \text{(b)}$$

The relative displacement between B and D in the x_2-direction is:

$$\Delta_2 = u_{2D} - u_{2B} = \frac{2C_2 P\ell}{EA_o}. \qquad \text{(c)}$$

Figure C.5c shows the free-body diagrams of ligaments BE and BE' in the x_1- x_3 plane from which the following is derived:

$$M_1 = M_o \cos\alpha + T\sin\alpha. \qquad \text{(d)}$$

The rotations of B due to bending moment M_o and torque T are respectively:

$$\theta_{M_o} = \frac{C_3 L}{EC_I A_o^2}(M_o - \frac{PL}{2}) \quad \text{and} \quad \theta_T = \frac{C_3 TL}{GC_J A_o^2}. \qquad \text{(e)}$$

Due to symmetry, we have

$$\theta_{M_o}\sin\alpha - \theta_T \cos\alpha = 0. \qquad \text{(f)}$$

Substituting (e) into (f) we get:

$$M_o - \frac{EC_I}{\lambda GC_J}T = \frac{PL}{2}. \qquad \text{(g)}$$

Then the rotation of B about the x_1-axis is

$$\bar{\theta}_{1B} = \theta_{M_o}\cos\alpha + \theta_T \sin\alpha = \frac{C_3 L}{EC_I A_o^2}(M_o - \frac{PL}{2})\cos\alpha + \frac{C_3 TL}{GC_J A_o^2}\sin\alpha. \qquad \text{(h)}$$

Applying compatibility condition

$$\theta_{1B} + \bar{\theta}_{1B} = 0, \tag{i}$$

we get

$$M_o = \frac{(\sqrt{2}\lambda^2 + \sqrt{2})S + \lambda \sin\alpha}{2[(\sqrt{2}\lambda^2 + \cos\alpha + \sqrt{2})S + \lambda \sin\alpha]} PL \tag{j}$$

and

$$T = -\frac{PL \sin\alpha}{2[(\sqrt{2}\tan^2\alpha + \cos\alpha + \sqrt{2})S + \lambda \sin\alpha]}, \tag{k}$$

where

$$S = \frac{EC_I}{GC_J}. \tag{l}$$

Then the displacement of B in the x_2-direction is

$$u_{2B} = \frac{L^2}{EC_I A_o^2}[(C_1 + \frac{C_3}{4})PL - \frac{C_3}{2} M_o] + \frac{C_2 \beta PL}{GA_o} = \frac{D_3 PL^3}{EC_I A_o^2} + \frac{C_2 \beta PL}{GA_o}. \tag{m}$$

The foam shear strain becomes

$$\gamma_{23} = \frac{\Delta_2 + 2u_{2B}}{\sqrt{2}\ell}. \tag{n}$$

Finally from $G_{23}^* = \dfrac{\sigma_{23}}{\gamma_{23}}$, we get

$$\frac{G_{23}^*}{E} = \frac{\cos^3\alpha C_I C_A^2 \ \bar{r}^4}{\lambda\{D_3 + 2\sqrt{2}\cos^3\alpha C_I C_A C_2 [1 + \frac{\sqrt{2}(1+\nu)\beta}{\cos\alpha}] \ \bar{r}^2\}}. \tag{C.16}$$

When the shear effect is neglected (C.16) becomes:

$$\frac{G_{23}^*}{E} = \frac{\cos^3\alpha C_I C_A^2 \ \bar{r}^4}{\lambda(D_3 + 2\sqrt{2}\cos^3\alpha C_I C_A C_2 \ \bar{r}^2)}. \tag{C.17}$$

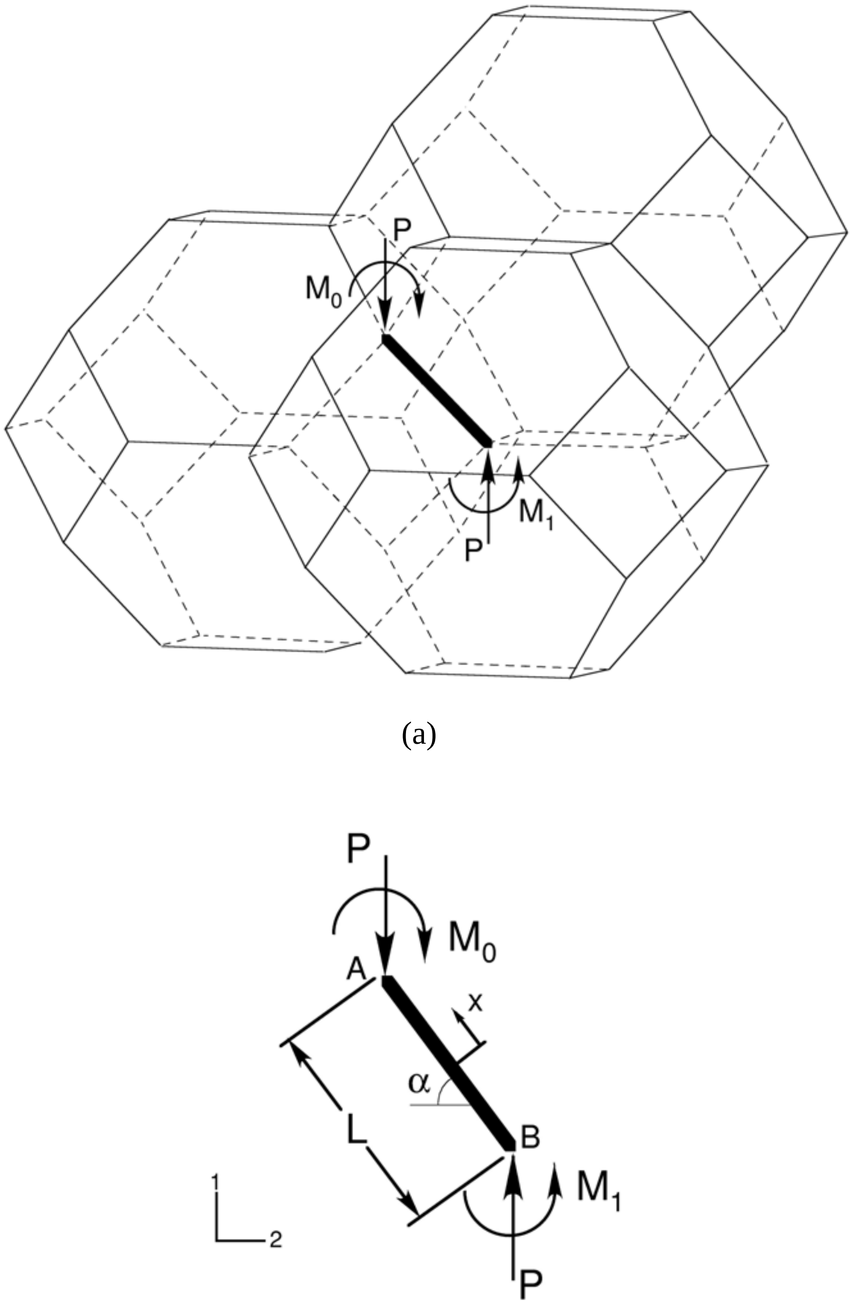

(a)

(b)

Figure C.1 Free-body diagram used to derive closed form expression of modulus E_1^* for the Kelvin cell.

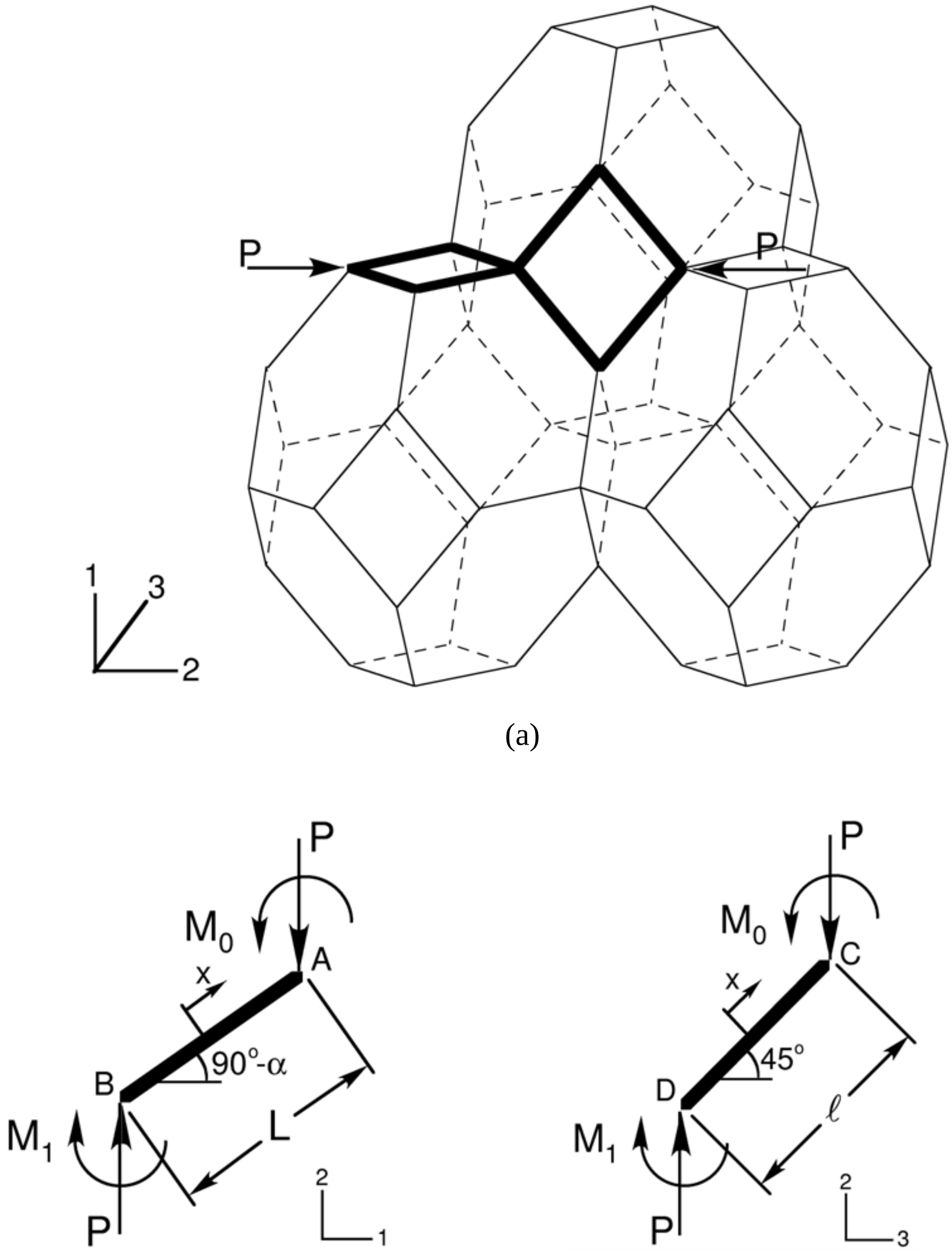

(a)

(b)

(c)

Figure C.2 Free-body diagram used to derive closed form expression of modulus E_2^*.

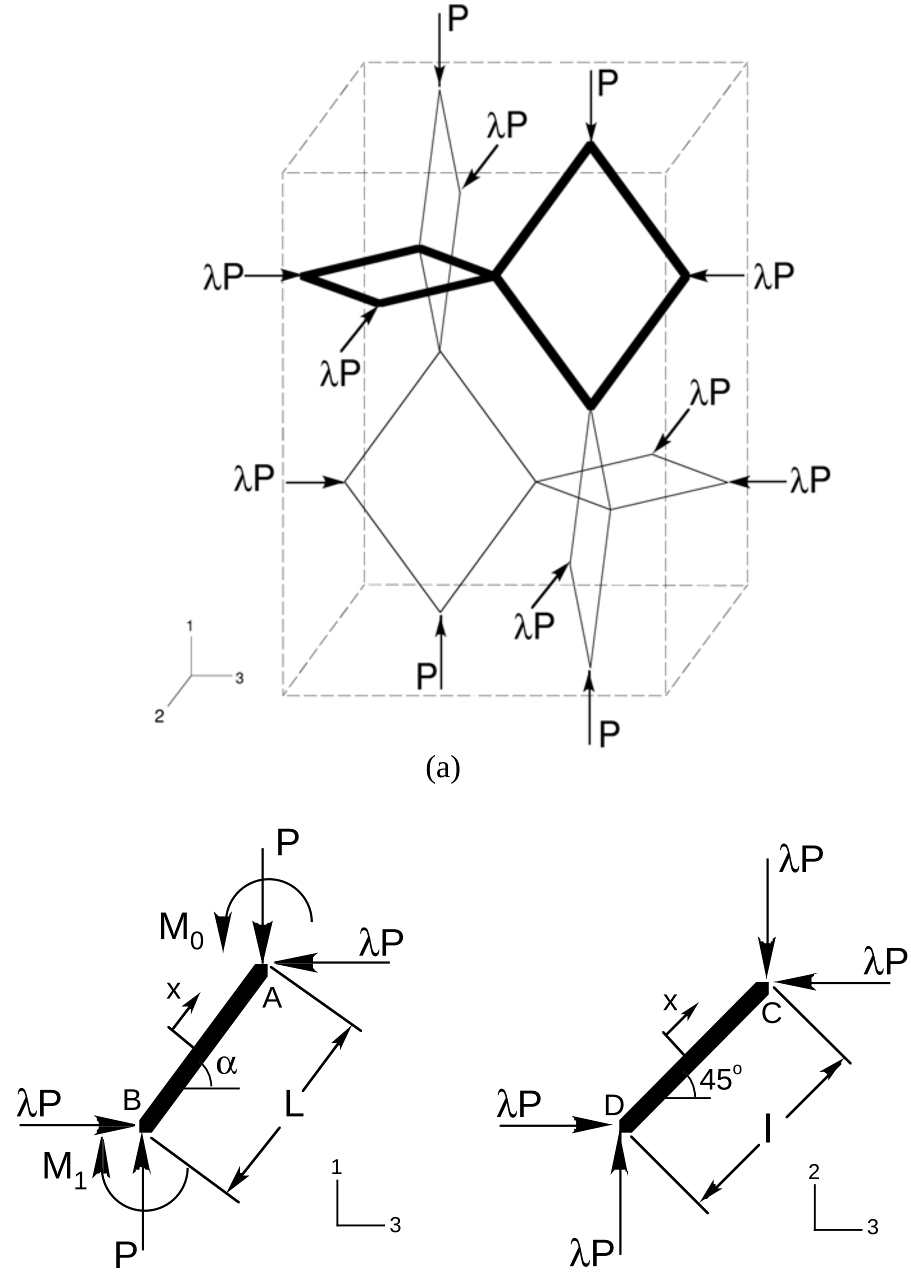

(a)

(b)

(c)

Figure C.3 (a) Free-body diagram of a characteristic cell for deriving κ^*
(b) Free-body diagram of one ligament in $x_1 - x_3$ plane.
(c) Free-body diagram of one ligament in $x_2 - x_3$ plane.

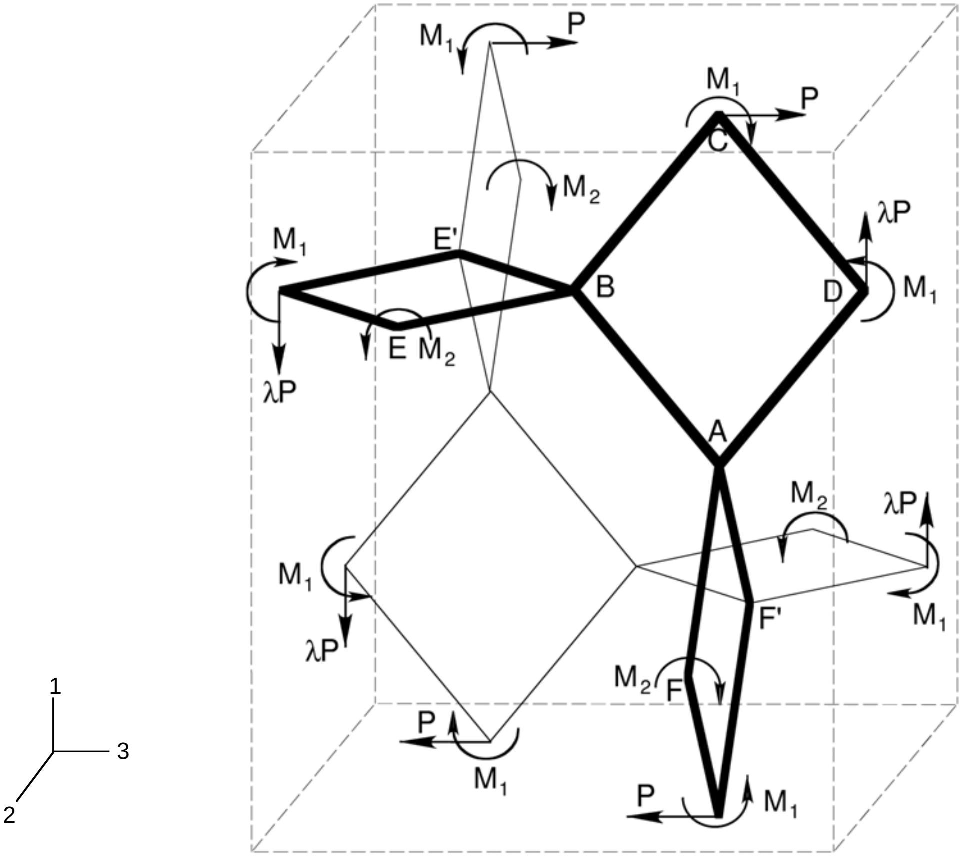

(a)

Figure C.4 Free-body diagrams for analyzing the shear modulus G_{13}^*

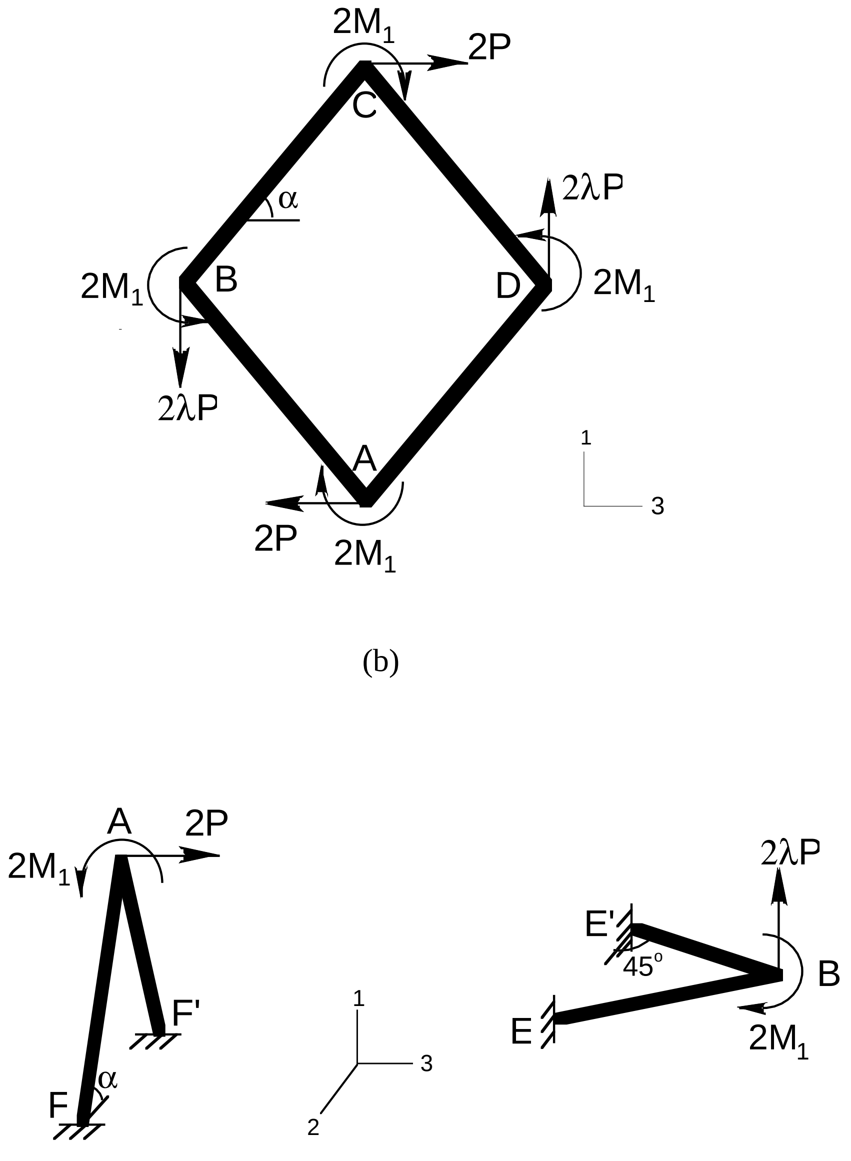

(b)

(c)

(d)

Figure C.4 Free-body diagrams for analyzing the shear modulus G_{13}^{*}

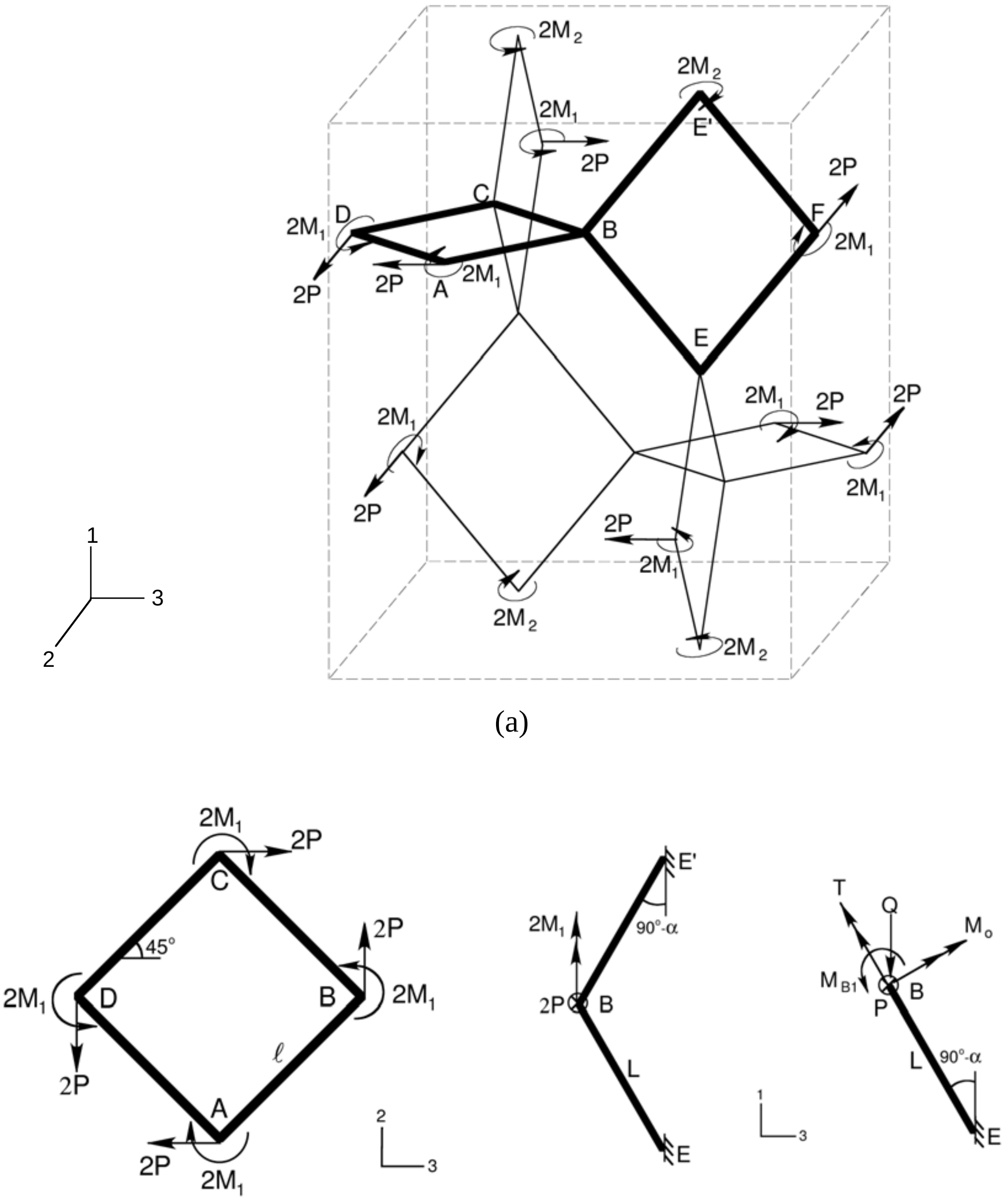

(a)

(b)

(c)

Figure C.5 Free-body diagrams for analyzing the shear modulus G_{23}^{*}.

BIBLIOGRAPHY

ABAQUS Version 6.3 (2002) Hibbit, Karlsson, and Sorenson, Inc. Pawtucket, RI.

Alderson JR., W. L. (1945). Process of obtaining cork-like products from polymers of ethylene, US Patent 2,387,730.

Allen, B. C. (1963). Method for making foamed metal, US Patent 3,087,807.

Artavia L.D. and Macosko, C.W. (1994). Polyurethane flexible foam formation. In, *Low Density Cellular Plastics: Physical Basis of Behavior*. Ed. Hilyard, N.C. and Cunningham, A. pp. 22-55. Chapman & Hall London.

Ashby, M.F., Evans, A., Fleck, N.A., Gibson, L.J., Hutchinson, J.W. and Wadley, H.N.G. (2000). Metal Foams: A Design Guide. Butterworth-Heinemann.

Ashby, M.F. (1983). The mechanical properties of cellular solids. *Metal. Trans.* **14A**, 1755-1769.

Ashcroft, N. W. & Mermin, N. D. *Solid State Physics* (Saunders, Philadelphia, 1976).

Babjak, J., Ettel, V. A. and Paserin, V. (1990). Method of forming nickel foam, US Patent 4,957,543.

Bastawros, A.-F., Bart-Smith, H. and Evans, A.G. (2000). Experimental analysis of deformation mechanisms in a closed-cell aluminum alloy foam. *J. Mech. & Physics of Solids* **48**, 301-322.

Baumeister, J. and Schrader, H. (1992). Methods for Manufacturing Foamable Metal Bodies, US Patent 5,151,246.

Bayer, O. (1947). Das di-isocyanat-polyadditionsverfahren (polyurethane), *Angewandte Chemie*, **59**, 257-272.

Block, F. (1928). Uber die quantenmechanik der elektronen in kristallgittern, *Zeitschrift fur Physik*, **52**, 555-600.

Cleland, W. J. (1962). Treatment of expanded thermoplastic polymeric material, British Patent 903,013.

Degischer, H. P. and Kriszt, B. (2002). *Handbook of Cellular Metals: Production, Processing, Applications*. Wiley-VCH, Weinheim.

Dement’ev, A.G. and Tarakanov, O.G. (1970a). Effect of cellular structure on the mechanical properties of plastic foams. *Mekhanika Polimerov* No. **4**, 594-602-865. Translation pp. 519-525.

Dement’ev, A.G. and Tarakanov, O.G. (1970b). Model analysis of the cellular structure of plastic foams of the polyurethane type. *Mekhanika Polimerov* No. **5**, 859-865. Translation pp. 744-749.

Deshpande, V. S. and Fleck, N. A. (2000). Isotropic constitutive models for metallic foams. *J. Mechanics and Physics of Solids* **48**, 1252-1283.

Elliot, J. C. (1956). Method of producing metal foam, US Patent 2,751,289.

Foamex International, Inc. (2003). Technical communication.

Forman, C. (2001). P-120X polymeric foams. Business Communication Company, Inc.

Ford, W. (1964). Method of Making Cellular Refractory Thermal Insulating Material, US Patent 3,121,050.

Frisch K. C. and Saunders J. H. (1972). *Plastic foams*, M. Dekker, New York.

Gent, A.N. and Thomas, A.G. (1963). Mechanics of foamed elastic materials. *Rubber Chemistry and Technology* **36**, 597-610.

Geymonat, G., Müller, S. and Triantafyllidis, N. (1993). Homogenization of nonlinearly elastic materials, microscopic bifurcation and macroscopic loss of rank-one convexity. *Archiv. Rational Mech. Analys.* **122**, 231-290.

Gibson, L.J. (2003). Cellular Solids. Ed., *MRS Bulletin* **28**/4, 270-306.

Gibson, L.J. and Ashby, M.F. (1997).*Cellular Solids: Structure and Properties, 2nd Ed.* Cambridge University Press.

Gibson, L.J. and Ashby, M.F. (1982). The mechanics of three dimensional cellular materials. *Proc. Royal Society of London* **A382**, 43-59.

Gibson, L.J., Ashby, M.F., Schajer, G.S. and Robertson, C.I. (1982). The mechanics of two-dimensional cellular materials. *Proc. Royal Society of London* **A382**, 25-42.

Gibson, L.J., Ashby, M.F., Zhang, J. and Triantafillou, T.C. (1989). Failure surfaces for cellular materials under multiaxial loads-I. Modeling. *Int'l J. Mechanical Sciences* **31**, 635-663.

Gioux, G., McCormac, T.M. and Gibson, L.J. (2000). Failure of aluminum foams under multiaxial loads. *Int’l J. Mechanical Sciences* **42**, 1097-1117.

Googin, J., Napier, J. and Scrivner, M. (1967). Method for Manufacturing Foam Carbon Products, US Patent 3,345,440.

Hager, J. W., Newman, J. W., Johannes, N. and Turrill, F. H. (2000). Carbon Artifacts and Compositions and Processes for Their Manufacture, US Patent 6,013,371.

Hilyard, N.C. and Cunningham, A. eds. (1994). *Low Density Cellular Plastics: Physical Basis of Behavior.* Chapman & Hall London.

Huber, A.T. and Gibson, L.J. (1988). Anisotropy in foams. *J. Materials Science* **23**, 3031-3040.

Hubscher M. (1954). *Silikattechnik*, **5**(6), 243-247.

ICI Ltd. (1971). Polyamides foamed with N-substituted carbamic ester blowing agents, British Patent 1,228,474.

ICI Australia & New Zealand Ltd. (1969). Process of foaming a polymerizable cyclic vinyl ether composition, British Patent 1,157,904.

Klempner, D. and Frisch, K.C. (1991). *Handbook of Polymeric Foams and Foam Technology*. Oxford University Press, New York.

Klett, R. D. (1975). High Temperature Insulating Carbonaceous Material, US Patent 3,914,392.

Klintworth, J.W. and Stronge, W.J. (1988). Elasto-plastic yield limits and deformation laws for transversely crushed honeycombs. *Int'l J. Mechanical Sciences* **30**, 273-292.

Ko, W.L. (1965). Deformations of foamed elastomers. *J. Cellular Plastics* **1**, 45-50.

Kraemer JR., W. C. and Eckardt C. R. (1967). Chlorinated polyethylene foam, US Patent 3,335,101.

Kraynik, A.M. (2003). Foam structure: From soup froth to solid foams. *MRS Bulletin* **28**/4, 275-278.

Kyriakides, S. (1993). Propagating instabilities in structures. In, *Advances in Applied Mechanics* **30**, Ed. J.W. Hutchinson and T.Y. Wu, 67-189. Academic Press, Boston.

Kyriakides, S. (2001). Propagating instabilities in materials. In, Materials Science for the 21th Century, Society of Materials Science, Japan, Vol. 1, pp. 316-325, May 2001

Laroussi, M., Sab, K. and Alaoui, A. (2002). Foam mechanics: Nonlinear response of an elastic 3D-periodic microstructure. *Int'l J. Solids & Structures* **39**, 3599-3623.

Lee, S.T. and Ramesh N.S. (2004). *Polymeric Foams: Mechanism and Materials*. CRC Press, Boca Raton, Fla.

Matzke, E.B. (1946). The three-dimensional shape of bubbles in foam-An analysis of the role of surface forces in three-dimensional shape determination. *American Journal of Botany* **33**, 58-80.

Menges, G. and Knipschild, F. (1975). Estimation of mechanical properties for rigid polyurethane foams. *Polymer Engineering and Science* **15**, 623-627.

Mullins, L. (1948). Effect of stretching on the properties of rubber. *Rubber Chemistry and Technology* **21**, 281-300.

Mullins, L. (1969). Softening of rubber by deformation. *Rubber Chemistry and Technology* **42**, 339-362.

Papka, S.D. and Kyriakides, S. (1994). In-plane compressive response and crushing of honeycomb. *J. Mechanics & Physics of Solids*, **42**, 1499-1532.

Papka, S.D. and Kyriakides, S. (1998a). In-plane crushing of a polycarbonate honeycomb. *Int'l J. Solids & Structures* **35**, 239-267.

Papka, S.D. and Kyriakides, S. (1998b). Experiments and full-scale numerical simulations of in-plane crushing of a honeycomb. *Acta Materialia* **46**, 2765-2776.

Papka, S. D. and Kyriakides, S. (1998c). In-plane crushing of a polycarbonate honeycomb. In, *Proc. IUTAM Symposium Material Instabilities in Solids*, June 1997, Delft, Ed. R. de Borst and E. van der Giessen, Wiley, Chichester, England, pp. 159-183.

Papka, S.D. and Kyriakides, S. (1999a). In-plane biaxial crushing of honeycombs: Part I Experiments. *Int'l J. Solids & Structures* **36**, 4367-4396.

Papka, S.D. and Kyriakides, S. (1999b). In-plane biaxial crushing of honeycombs: Part II Analysis. *Int'l J. Solids & Structures* **36**, 4397-4423.

Patel, M.R. and Finnie, I. (1970). Structural features and mechanical properties of rigid cellular plastics. *J. Materials* **5**, 909-932.

Plateau, J.A.F. (1873). Statique experimentale et theorique des liquides soumis aux seules forces moleculaires. 2 Volumes, Gauthier-Villars, Paris

Pradel, F. (1998). Homogeneisation del milieux discrets periodiques orientes: Une application aux mousses. PhD Thesis, Ecole Nationale des Ponts et Chaussees, Camps-sur-Marne.

Priester, R.D. and Turner, R.B. (1994). The morphology of flexible polyurethane matrix polymers. In, *Low Density Cellular Plastics: Physical Basis of Behavior*. Ed. Hilyard, N.C. and Cunningham, A. pp. 78-103. Chapman & hall London.

Rice, J.R. (1976). The localization of plastic deformation. *Proc. ICTAM 1976*, Delft, Ed. W.T. Koiter, pp.207-220, North Holland Publishing Co.

Richard, K. B., Hugh, P. O., Robert, T. H. and Brian, W. E. (1992). High Temperature Resistant Reticulated Foam Structure and Process, US Patent 5,154,970.

Saggio-Woyansky, J. and Scott, C. E. (1992). Processing of Porous Ceramics, *American Ceramic Society Bulletin*, **71**(11), 1674-82.

Schraad, M.W. and Triantafyllidis, N. (1997a). Scale effects in media with periodic and nearly periodic microstructures, Part I: Macroscopic properties. *ASME J. Applied Mechanics* **64**, 751-762.

Schraad, M.W. and Triantafyllidis, N. (1997b). Scale effects in media with periodic and nearly periodic microstructures, Part II: Failure mechanisms. *ASME J. Applied Mechanics* **64**, 763-771.

Schwartzwalder, K. and Somers, A. V. (1963). Method of Making Porous Ceramic Articles, US Patent 3,090,094.

Schwencke E. H. (1954). Methods of producing a cellular structure in a plasticized vinyl ester resin, US Patent 2,666,036.

Shaw, M.C. and Sata, T. (1966). The plastic behavior of cellular materials. *Int'l J. Mechanical Sciences* **8**, 469-478.

Shim, V.P.-W. and Stronge, W.J. (1986). Lateral crushing of tightly packed arrays of thin-walled tubes. *Int'l J. Mechanical Sciences* **28**, 709-728.

Shroyer, H. F. (1960). Cavityless casting method, British Patent 850,331.

Sosnik, B. (1948). Process for making foamlike mass of metal, US Patent 2,434,775.

Stuart, F. W. (1959). Method for Preparing a Catalytic Metal Foam and Use Thereof, US Patent 2,895,819.

Thompson, W. (Lord Kelvin) (1887). On the division of space with minimal partitional area. *Philos. Magazine* **24**, 5th Series 503-514.

Triantafillou, T.C., Zhang, J., Shercliff, T.L., Gibson, L.J. and Ashby, M.F. (1989). Failure surfaces for cellular materials under multiaxial loads-II. Comparison of models with experiment. *Int'l J. Mechanical Sciences* **31**, 665-678.

Triantafyllidis, N. and Schraad, M. (1998). Onset of failure in aluminum honeycombs under general in-plane loading. *J. Mechanics & Physics of Solids* **46**, 1089-1124.

Wang, T. G. (1982). Method and Apparatus for Producing Gas-filled Hollow Spheres. US Patent 4,344,787.

Wang, Y., Gioia, G. and Cuitino, A.M. (2000). The deformation habits of compressed open-cell solid foams. *ASME J. Engineering Materials & Technology* **122**, 376-378.

Warren, W.E. and Kraynik, A.M. (1997). Linear elastic behavior of a low-density Kelvin foam with open cells. *ASME J. Applied Mechanics* **64**, 787-793.

Warren, W.E., Nielsen, M.K. and Kraynik, A.M. (1997). Torsional rigidity of a plateau border. *Mechanics Research Communications* **24**, 667-672.

Weaire, D. and Hutzler, S. (1999). *The Physics of Foams*, Oxford University Press, Oxford.

Wong, R. S. and Mahoney, C. L. (1994). Low moisture absorption syntactic foam. European Patent 0,588,437.

Zhu, H.X., Knott, J.F. and Mills, N.J. (1997). Analysis of the elastic properties of open-cell foams with tetrakaidecahedral cells. *J. Mechanics & Physics of Solids* **45**, 319-343.

VITA

Lixin Gong was born in Beijing, China on November 22, 1966, the son of Yuying Fu and Zhiyong Gong. After graduating from Beijing Experimental High School in 1985, he attended the Beijing University of Aeronautics and Astronautics where he received the degree of Bachelor of Science in Aerospace Engineering in July, 1989. In September, 1989, he entered the graduate school at the 2nd Institute of Aerospace Ministry, where he achieved the Master degree of Science in Aerospace Engineering in March, 1992. After that he worked as an engineer of structure design. In August, 1998, he entered Graduate School at The University of Texas at Austin for his Ph.D. He has co-authored the following papers:

Gong, L., Kyriakides, S. (2005). On the crushing stress of open-cell foams. ASME *Journal of Applied Mechanics* (submitted).

Gong, L., Kyriakides, S. and Triantafyllidis, N. (2005). On the stability of Kelvin cell foams under compressive loads. *J. Mechanics and Physics of Solids* **53**/4, 771-794.

Gong, L., Jang, W.-Y and Kyriakides S. (2005). Compressive response of open-cell foams, part I: morphology and elastic properties. *Int'l Journal of Solids & Structures* **42**/5-6, 1355-1379.

Gong, L., and Kyriakides S. (2005). Compressive response of open-cell foams, part II: initiation and evolution of crushing. *Int'l Journal of Solids & Structures* **42**/5-6, 1381-1399.

Gong, L., and Kyriakides S. (2004). On the crushing response of open-cell foams. *Proc. ICTAM 04*, Warsaw, Poland, ISBN 83-89687-01-1.

Permanent address: 16-1-302 Wu Shen Xi Li, Beijing, China 100021

This dissertation was typed by the author.